米日

U.S. - JAPAN COORDINATED PROGRAM

FOR

MASONRY BUILDING RESEARCH

PB93-214559

Report No. 3.1(c)-2

IN-PLANE SEISMIC RESISTANCE OF TWO-STORY CONCRETE MASONRY SHEAR WALLS WITH OPENINGS

by

Gilberto Leiva
Richard E. Klingner

Supported by:

National Science Foundation
Grant No. ECE-8611860

PHIL M. FERGUSON STRUCTURAL ENGINEERING LABORATORY
Department of Civil Engineering/Bureau of Engineering Research
The University of Texas at Austin

PMFSEL Report No. 91-2

August 1991

This report presents the results of a research project which was part of the U.S. Coordinated Program for Masonry Building Research. The program constitutes the United States part of the United States - Japan Coordinated Masonry Research Program conducted under the auspices of the Panel on Wind and Seismic Effects of the U.S.-Japan Natural Resources Development Program (UJNR).

This material is based on work supported by the National Science Foundation under the direction of Program Director, Dr. S.C. Liu.

Any opinions, findings, and conclusions or recommendations expressed in this publication are those of the authors and do not necessarily reflect the views of the National Science Foundation and/or the United States Government.

IN-PLANE SEISMIC RESISTANCE OF TWO-STORY CONCRETE MASONRY SHEAR WALLS WITH OPENINGS

by

Gilberto Leiva

and

Richard E. Klingner

Report on a Research Project
Sponsored by
National Science Foundation
Grant No. ECE-8611860

PHIL M. FERGUSON STRUCTURAL ENGINEERING LABORATORY

Department of Civil Engineering
BUREAU OF ENGINEERING RESEARCH
THE UNIVERSITY OF TEXAS AT AUSTIN

August 1991

GENERAL REMARKS ON NOTATION

Throughout this report, variables are defined as they are used. Notation is generally consistent with that of the 1988 Uniform Building Code [19]. For example, the subscript "n" is used to refer to nominal capacity.

Two items regarding notation are especially worthy of note:

1. Notation for masonry strength. Masonry strength, measured by compressive prism strengths, is often denoted by f_m. The specified strength, normally denoted by f_m' is less than most measured values of f_m. Formulas for predicting masonry capacity are often expressed in terms of f_m. When such formulas are placed into codes, f_m' is substituted for f_m so that the predicted capacity will be conservative (low). That practice is continued in this report. The nomenclature f_m' denotes two strengths: the measured strength (when used in formulas derived from laboratory results); and the specified strength (when used in formulas for codes).

2. Notation for maximum strength. Throughout this report, maximum strength is referred to as "ultimate."

TABLE OF CONTENTS

LIST OF FIGURES

Page

LIST OF TABLES

Table Page

1. INTRODUCTION

1.1 General

During recent years, increasing attention in the United States has been devoted to performance and design of masonry structures. In the area of serviceability, consideration has been given to subjects such as durability, water permeance, differential movements, and life cycle cost. In the area of structural strength, work has began in the development of the basic framework of a strength design code for masonry. This work has been oriented principally towards seismic zones, in which strength design approaches are very appropriate.

As part of this process, a large amount of experimental information has been obtained on the behavior of reinforced concrete masonry elements under cyclic loads. This information has permitted the development of some strength design provisions for reinforced masonry, such as those recently adopted in the United States by the 1988 UBC [19] for reinforced masonry walls. However, there are still several areas in which considerable effort is needed to obtain a better understanding of the mechanisms governing the strength and deformation capacity of reinforced masonry elements.

The U.S. Coordinated Program for Masonry Building Research, funded by the National Science Foundation and directed by the Technical Coordinating Committee for Masonry Research (TCCMAR), consists of a set of separate but coordinated tasks, intended to address the basic issues of masonry material and structural response to gravity and seismically induced loads. The program is divided into 10 research categories: 1) materials; 2) mathematical models; 3) walls; 4) intersections; 5) floors; 6) construction; 7) small-scale models; 8) design methods; 9) full-scale building; and 10) design recommendations and criteria development [46].

The research described here, and identified as Task 3.1(c) of the TCCMAR Program, is concerned with the in-plane seismic resistance of two-story reinforced concrete masonry walls. During this program, 6 full-scale reinforced concrete masonry walls, each two stories high, were designed, constructed, tested, analyzed, and evaluated at the Phil M. Ferguson Structural Engineering Laboratory of the University of Texas at Austin. All specimens were of fully grouted hollow concrete masonry. Two specimens were single walls with door and window openings, and four specimens were pairs of walls, each coupled by a different floor system, with and without lintels.

The single walls with openings, termed Type 1 specimens, were intended to represent walls in a two-story building, perforated by window and door openings. According to the particular design philosophy used, each specimen was intended to show a different response to lateral load excitations.

The pairs of coupled walls, termed Type 2 specimens, were intended to represent coupled walls in a two-story building. Each specimen had a different combination of floor and coupling systems.

1.2 Scope and Objectives

The overall objectives of Task 3.1(c) were to examine how the in-plane seismic resistance of multistory concrete masonry walls is affected by:

a) floor-wall joints,

b) wall openings, and

c) floor elements.

The specific objectives of the Type 1 specimen tests were:

a) to examine the cyclic shear resistance of the perforated wall system which each specimen represented

b) to compare the effectiveness of two different philosophies for designing perforated wall systems, and

c) to test the analytical models developed in this and in other TCCMAR tasks

The specific objectives of the Type 2 specimen test were:

a) to examine the cyclic shear resistance of the coupled wall system which each specimen represented

b) to examine the shear strength and in-plane response of the floor-wall joints

c) to examine the coupling effectiveness (under reversed cyclic loads) of plank floor systems, with and without masonry lintels, and

d) to test the analytical models developed in this and in other TCCMAR tasks

Results of the test of the first two Type 2 specimens have been completely described in Reference 13. However, to give completeness to this report, the most important features of those results have been repeated here.

This report is organized as follows: In Chapter 2, the different forms of masonry walls are described, and the parameters influencing their behavior are discussed, with emphasis on the different modes of failure. A complete description of each specimen is given in Chapter 3. Test equipment and procedure are described in Chapter 4. Chapter 5 describes the expected behavior of the perforated wall specimens as a function of design philosophy, including predictions for the behavior and lateral load capacities. Test results for perforated wall specimens are described in Chapter 7, and Chapter 8 includes a discussion of the test results for those specimens. Test results for coupled wall specimens are described and discussed in Chapter 9. Analytical results obtained using the computer program SCAM, developed as part of this project, are described and discussed in Chapter 10. A proposed model to predict the shear strength of masonry walls is presented in the same Chapter. A summary of the results, conclusions, and recommendations for further research are presented in Chapter 11. Appendix A describes the design for Type 1 specimens. A complete description of the computer program SCAM to predict the load-displacement response of masonry structures under monotonically increasing imposed displacements is given in Appendix B. The proposed model to predict the shear strength of masonry walls, and its development are presented in Appendix C.

2. BACKGROUND

Masonry buildings are normally characterized by large number of walls. These walls act primarily as vertical load-resisting elements, and also carry the building's lateral loads. In this chapter the behavior of masonry walls and their components is reviewed. Different forms of masonry walls are described, and the parameters influencing their behavior are discussed, with emphasis on their various modes of failure.

2.1 General

It is well known that the forces associated with the linear elastic response of a structure to severe ground motion, are several times larger than typical code seismic loads [19]. However, it is also known that most code-designed structures so designed have been able to survive severe earthquake excitations. This behavior has been attributed to factors such as inelastic energy dissipation, increased structural damping due to damage, and soil-structure interaction.

When code design forces are less than the elastic forces associated with the elastic response, the structure is expected to remain stable under seismic excitations while responding inelastically after reaching its load capacity. The inelastic response of the structure is associated with inelastic deformations of so-called critical elements. These elements must be able to deform inelastically after reaching their strength without excessive deterioration of strength and stiffness. This characteristic is commonly known as "ductility" [24].

Because of these requirements, it is usually intended that flexural behavior control the formation of a structural mechanism, in which most of the inelastic action is due to large, ductile flexural deformations of the end sections of critical elements. According to the capacity design philosophy, each such element must be designed to prevent undesirable brittle modes of failure such as diagonal tension, diagonal compression, sliding shear, anchorage failure, and buckling of compression reinforcement or part of the wall, when subjected to the forces associated with the development of the actual flexural strength of the system. The actual flexural strength, or flexural overstrength, is based on the probable (i.e., expected) strength of the materials, including such aspects as strain hardening of the reinforcement.

To accomplish this design approach, it is necessary to know the load-deformation behavior of the structural materials, elements, and assemblages. A large amount of experimental information on the behavior of reinforced concrete masonry elements under cyclic loads has been obtained during recent years [14,17,43,44,12,1]. This information has permitted the development of some strength design provisions for reinforced masonry, such as those recently adopted in the United States by the 1988 UBC [19] for reinforced masonry

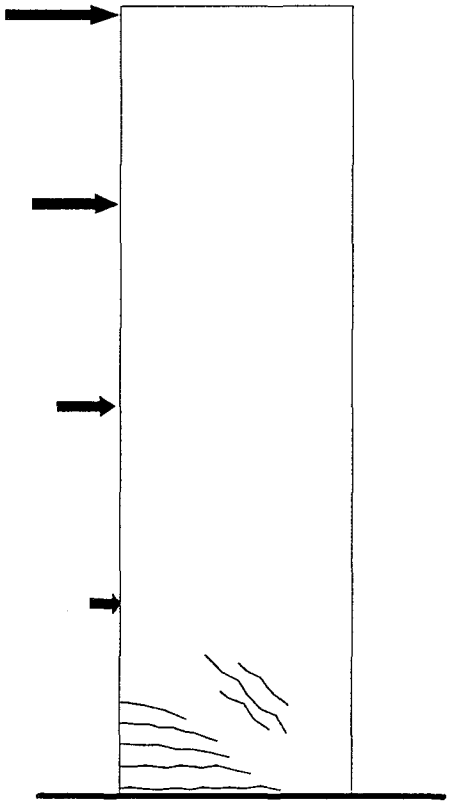

Figure 2.1 Cantilever masonry wall under seismic loading.

walls. However, there are still several areas in which considerable effort is needed to obtain a better understanding of the mechanism governing strength and deformation capacity of reinforced masonry elements. A review of the behavior of masonry structures and elements is given in the following sections.

2.2 Masonry Structures

The simplest type of masonry structure consists of cantilever walls, connected through floor slabs flexible enough so the basic cantilever action is not affected. Most inelastic action under lateral loads occurs at plastic hinges at the base of the walls, as shown in Fig. 2.1.

More typical masonry construction consists of perforated walls like those shown in Fig. 2.2, in which window and door openings define pier and spandrel elements. The inelastic behavior of the wall will depend on the relative capacity of piers and spandrels. Window openings usually define a pier-dominated type of behavior in which most of the inelastic action occurs in the piers, in a column-type sidesway mechanism at one or more story levels, as shown in Fig. 2.2(a). Door openings usually define a coupled wall type of behavior in which most of the inelastic action takes place at the ends of the coupling elements and at the base of the coupled walls, in a beam-type sidesway mechanism, as shown in Fig. 2.2(b).

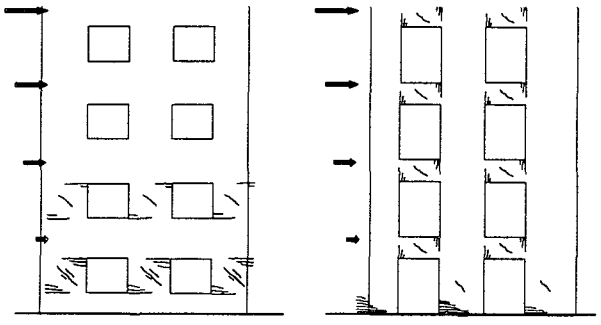

Figure 2.2 Masonry walls under seismic loading.

As previously mentioned, the inelastic response of the structure is governed by the inelastic deformations of some critical elements. It is then essential to relate the demands on those elements with their capacities. The available

ductility of an element dominated by flexural behavior depends on the rotation capacity of its hinging regions, which in turn depends on the section's curvature capacity and the plastic hinge length ℓ_p. The ductility demand on that element depends on the structural form and the external actions. An accurate assessment of the ductility demand on the elements of an structure subjected to some particular ground motion, can be obtained by performing a nonlinear dynamic analysis. However, analysis of the inelastic deformations of the structure's collapse mechanism under equivalent static lateral loads [19] can indicate regions of high deformation demand. Similarly, the shear demand on each element depends on the maximum expected flexural capacity of that element, the structural form, and the load distribution. Shear forces can be calculated from the plastic collapse mechanism as previously described. However, during actual seismic excitation, the M/V ratio at a given section varies continuously during the response of the structure, and the calculated values of the shear demand must be amplified to consider the effects of higher modes [22,30] and ground motion intensity [2] on structural response.

Several criteria have been proposed for selecting the most appropriate masonry structural form. Priestley [22] has suggested that the best structural form for masonry wall structures is the simple cantilever wall. Moment transfer between walls should be minimized by using flexible coupling elements and openings in the walls should be small enough so they do not affect the cantilever action of the walls. This approach is based on calculated levels of available ductility in cantilever masonry walls using a plastic hinge length of $\ell_w/2$ at the base of the walls. In addition to imposing architectural limitations, the assumed value of the plastic hinge length seems to be too large compared with test observations [1,13], which would lead to overestimates of the available ductility levels. A second approach, suggested by Hidalgo and Lüders [7], consists simply in recognizing that some walls will have a shear-dominated behavior, and that this fact must be taken into account in design by inducing a "ductile-shear" failure [12] and by increasing seismic design forces. This approach tends to ignore evidence regarding the available ductility of masonry walls, and the extent of the proposed increase in design forces is not clear. To investigate different design approaches further, the inelastic behavior of each type of masonry wall must be examined in more detail. That is the purpose of the following sections.

2.2.1 Cantilever Wall. In a cantilever wall, energy dissipation occurs only at plastic hinges at the base of the wall, as shown in Fig. 2.3 (a); this makes it easier to properly detail those zones. The distribution of curvature at ultimate can be idealized into elastic and plastic regions [21], as shown in Fig. 2.3(b). Strictly speaking, this idealization is valid only for a cantilever with a concentrated load at the top. However, a multi-story system with loads at each story can be thought of as a cantilever under the action of the resultant force. The plastic hinge region, a zone in which curvature exceeds the yielding value ϕ_y and reaches the ultimate value ϕ_u, is assumed to have a length ℓ_p. Wall rotations and

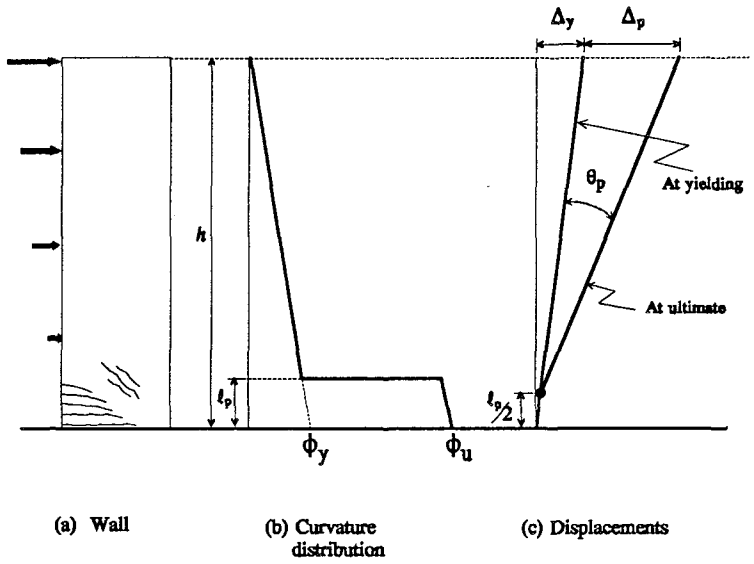

Figure 2.3 Curvature and displacement distribution in a cantilever wall.

displacement can be calculated by integrating the curvature distribution over the wall height h:

$$\Delta_y = \frac{1}{3}\phi_y h^2 \tag{2.1}$$

$$\theta_p = (\phi_u - \phi_y)\,\ell_p \tag{2.2}$$

$$\Delta_u = \Delta_y + \Delta_p = \frac{\phi h^2}{3} + (\phi_u - \phi_y)\left(h - \frac{\ell_p}{2}\right)\ell_p \tag{2.3}$$

where Δ_y and Δ_u are the displacement at the top of the wall at the first yielding and at ultimate respectively.

The same results can be obtained using the idealized model in Figure 2.3(c)[23], in which the inelastic deformations θ_p and Δ_p are assumed to be produced by a concentrated rotation of the wall at a height $\ell_p/2$. For a required overall ductility $\mu = \Delta_u/\Delta_y$, the

curvature ductility demand μ_ϕ at the base of the cantilever wall can be easily estimated using this model:

$$\mu_\phi = \frac{\phi_u}{\phi_y} = \frac{h^2(\mu - 1)}{3\ell_p (h - 0.5\ell_p)}$$

As shown in Eq. 2.4, the curvature ductility demand μ_ϕ tends to increase rapidly as the value of ℓ_p decreases [21]. Experimental results [1,17] have shown that the plastic hinge length in masonry walls is shorter than that of otherwise similar reinforced concrete elements.

For a cantilever wall subjected to a code-type linear distribution of lateral forces, as shown in Fig. 2.1, the maximum expected shear is equal to the flexural capacity at the base of the wall, divided by the height of the lateral force resultant. However, as previously mentioned, this value must be amplified to consider the effect of higher modes and ground motion intensity on the response.

2.2.2 Pierced Wall. In this type of walls, openings are arranged in such a way that spandrel beams are stronger than piers. In a wall dominated by pier behavior, inelastic deformation predominantly occurs at the piers of one or more story levels, as shown in Fig. 2.4(a). Plastic deformations after yielding are usually concentrated in a single story, defining a column sidesway mechanism as shown in Fig. 2.4(b). The wall displacement distribution is idealized in Fig. 2.4(c) [23]. In that model, displacements are assumed to increase linearly with height until yield, after which, the inelastic displacements are concentrated at the soft story. Because shear deformations are an important part of the total deformation of the usually squat piers, it makes more sense to work with the displacement ductility of the piers rather than rotational or curvature ductilities. For an overall ductility demand $\mu = \Delta_u/\Delta_y$, it can be demonstrated that the required pier displacement ductility μ_p is:

$$\mu_p = \frac{n}{(\alpha+\beta)} (\mu - 1) + 1 \qquad (2.5)$$

where h is the story height, αh the height of the pier, βh the height of the window sill, and n the number of stories. The high ductility demand on the piers, especially for taller buildings, is clearly evident from this equation. This is a typical characteristic of "soft-story" mechanisms [30].

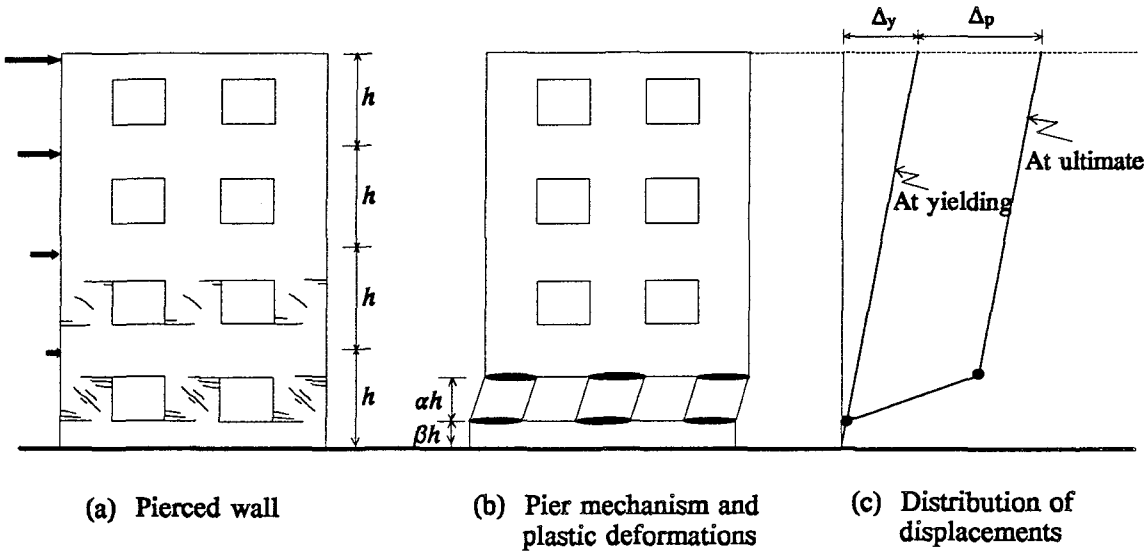

Figure 2.4 Plastic mechanism and displacement distribution in a pierced wall.

Because of the usually low span to depth ratio of the piers, high shear forces are associated with the development of their lateral load capacities. It is therefore necessary to minimize the piers' flexural capacity and provide them with high ratios of transverse reinforcement to prevent shear failure. It can then be expected that the inelastic deformation capacity of the piers will be limited by possible fracture of the jamb bars, by diagonal compression, or by shear transfer at the pier-wall connections. Large shearing forces must be transmitted between the piers and the wall in a zone usually highly deteriorated by the action of reversed load cycles, as shown in Fig. 2.5. It is also conceivable that the occurrence of large inelastic deformations of the piers could lead to undesirable damage and out-of-plane instability of the pier regions.

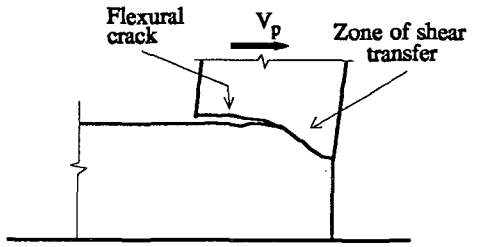

Figure 2.5 Zone of shear transfer at pier - wall connection.

2.2.3 Coupled Walls. In a wall dominated by coupled wall type of behavior, inelastic deformation occurs at the bases of the coupled walls and at the ends of the coupling elements, as shown in Fig. 2.6(a). The collapse mechanism is defined by the formation of plastic hinges at those locations, as shown in Fig. 2.6(b). Assuming that all plastic deformations are concentrated at the plastic hinges, and that the walls rotate about their compression toes, the distribution of plastic displacements is as

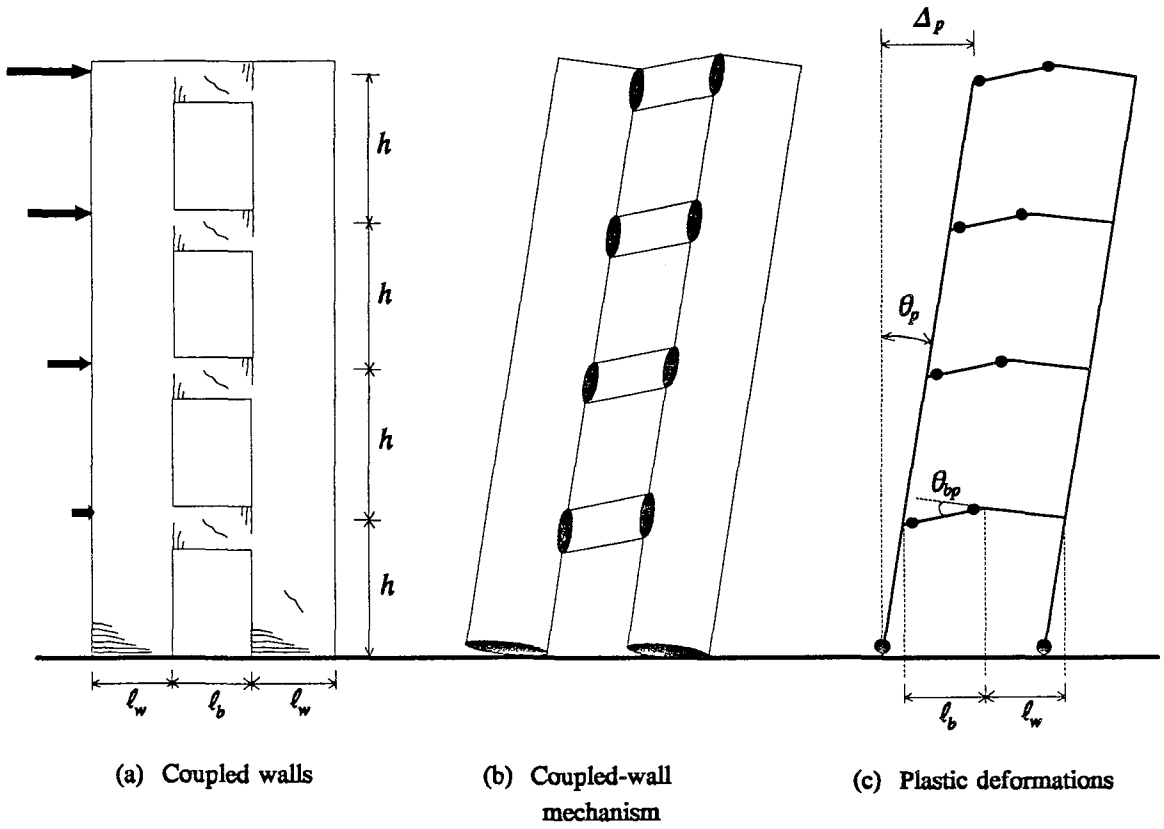

Figure 2.6 Plastic mechanism and displacement distribution for coupled walls.

shown in Fig. 2.6(c). The coupling beam plastic rotation θ_{pb} is:

$$\theta_{pb} = (1 + \ell_w/\ell_b)\,\frac{\Delta_p}{nh} \tag{2.6}$$

where ℓ_w is the wall cross section length, ℓ_b the beam span, h the story height, n the number of stories, and Δ_p the plastic displacement at the top of the wall.

From Eq. (2.6), the rotational ductility demand on the coupling bemas, $\mu_{\theta b} = \theta_{ub} / \theta_{yb}$, is:

$$\mu_{\theta b} = \frac{(1 + \ell_w/\ell_b)}{nh} \frac{\Delta_y}{\theta_{yb}} (\mu - 1) + 1 \qquad (2.7)$$

where μ is the overall required ductility, Δ_y is the top displacement at first yielding, and θ_{yb} is the beam rotation at first beam yielding. Note that Δ_y and θ_{yb} do not necessarily occur at the same time.

Because of the lintels' low shear span to depth ratio, high shear forces are associated with the development of their flexural capacity. Because of the characteristics of the masonry, it is usually not possible to provide all the required transverse reinforcement in those elements. As a result, even when the minimum flexural reinforcement is used, shear damage and early degradation can be expected to occur in the lintels, limiting the effectiveness of the coupling system. If the coupled masonry walls are long in plan, formation of plastic hinges at their bases produces large strains in wall longitudinal reinforcement. This condition has often been observed to cause fracture of longitudinal reinforcement under reversed cyclic loads, and has also been associated with in-plane and out-of-plane slip of the walls at their bases, limiting the deformation capacity of the structure [13].

In an ideal coupled wall system, energy dissipation is provided by large inelastic deformations, first of the coupling elements (lintels), and later, of the walls themselves. This behavior permits a great part of the inelastic action to take place before the walls start to suffer damage.

2.3 Masonry Walls and Piers

The influence of wall panels and piers in the response of masonry assemblages has been clearly identified. Considerable research has been carried out in this area in recent years. In this and the following sections, some of the most important findings in this area are described.

Two basic load-deformation and failure mechanisms have commonly been identified in reinforced masonry wall panels [4,12]: a flexural mechanism, characterized by large deformations of flexural reinforcement and/or crushing of masonry at the compression toe; and a shear mechanism, characterized by diagonal tensile cracking. While the flexural mechanism exhibits considerable ductility, shear failure is sudden and brittle.

A third failure mechanism, involving sliding, has been frequently observed in walls subjected to reversed loading cycles. A sliding plane of failure can be defined either by a

flexural crack continuous along an horizontal course (sliding-flexure failure) [12,17], or between two diagonal cracks as in the case of squat walls (sliding-shear failure) [8,12]. While some authors define sliding as an independent mode of failure [12], it always occurs simultaneously with the development of some of the other mechanisms previously described.

A description of the behavior of concrete masonry walls and piers, with emphasis on the different modes, is given in the next sections. Most of the results are valid for all types of masonry, but the reader must be aware that this work emphasizes fully grouted concrete masonry walls.

2.3.1 Flexural Behavior. It has been widely recognized that the flexural behavior of lightly reinforced, fully grouted concrete masonry elements is well described by the simple flexure theory developed for reinforced concrete members [1,17,22,4.7,4.8], which is based on the plane-section assumption. Some test results [3] have shown that the plane-section assumption is no longer valid when the section is close to its flexural capacity, and that the neutral axis lies closer than assumed to the extreme compression fiber of the section. This means that the plane section assumption could lead to an underestimation of moment capacity, and that shear demand could be larger than predicted. However, the difference does not seem to be significant.

Computer programs based on a fiber model for the cross-section, and also on the plane-section assumption, have been satisfactorily used to predict the flexural behavior of sections of fully grouted concrete masonry walls [1,13]. Flexural strength of these sections has been accurately predicted using formulas based on the assumption of an equivalent rectangular stress block [1,22].

Wall displacement can be calculated by integrating curvatures over the wall height. Test results have shown that the inelastic deformations of masonry walls tend to concentrate at the base of the wall [1,13,17,18], resulting in a plastic hinge length ℓ_p shorter than that expected in otherwise similar reinforced concrete elements. Plastic hinge lengths averaging $0.2\ \ell_w$ were obtained from tests on slender walls as described in Ref. 17. Tests on square panels described in Ref. 1 showed plastic hinge lengths of about $0.15\ \ell_w$. Because of these relatively small values of ℓ_p, large curvature ductility levels are required to satisfy a given displacement ductility demand.

Wall flexural deformations are increased by base uplift due to bond slippage, and by deformation of the steel embedded in the foundation [1]. Lap splices at the base of the wall in the plastic hinge region affect wall behavior in two ways [17]: the plastic hinge length is reduced due the existence of an overreinforced zone at the middle of the lap splice; in addition, effectiveness of grouting is reduced, vertical splitting cracking occurs early, and bond failure of flexural steel occurs.

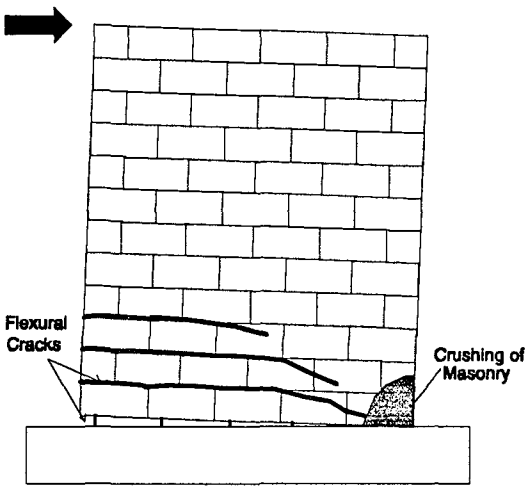

Figure 2.7 Flexural type of failure.

Axial load level has an important influence on flexural behavior. Under increasing axial load, the lateral load capacity and stiffness of the wall are increased, but available ductility is decreased [1]. Higher axial load produces a more rapid load degradation due to more severe toe crushing, but it produces a higher unloading stiffness [3]. The increase in flexural capacity produced by the increase in axial load can change the mode of failure from ductile flexure to brittle shear [1,12].

As previously mentioned, flexural failure is characterized by large deformations of flexural reinforcement and/or crushing of masonry at the compression toe, as shown in Fig. 2.7. Crushing of masonry usually starts as vertical splitting; the block shell then spalls off; and finally, extensive crushing of grout occurs. Inelastic flexural hinging at the bases of long walls can lead to fracture of the extreme bars [13].

2.3.2 Shear Behavior. When the principal diagonal tensile stress exceeds the masonry tensile strength, the shear mode of failure is initiated by a crack along the diagonal in the center part of the wall. The diagonal cracking strength of the grouted wall depends on the diagonal tensile strength of masonry (which can be taken as proportional to $\sqrt{f'_m}$). It also depends on the applied axial stress, and on the aspect ratio of the panel [4,11].

Before cracking, the wall can be considered elastic and homogeneous, and the contribution of the reinforcement can be assumed negligible. Shear stiffness properties of the element can be calculated using the gross area of the cross section [1]. This assumption is no longer valid after flexural cracking has occurred. Before diagonal cracks develop along the main diagonal, vertical and horizontal loads can be assumed taken by a diagonal strut mechanism [1]. This strut model can be used to estimate shear stiffness.

After diagonal cracking, lateral load action is resisted by a new mechanism shown in Fig. 2.8. Shear strength is provided by the masonry strength at the compression toe, by aggregate interlock forces between the sides of the crack, and by the action of the longitudinal and transverse reinforcement crossing the crack [4,8]. Under these conditions, the wall becomes more flexible than before cracking. The following parameters have been recognized as influencing the shear strength after diagonal cracking: masonry compressive

strength; aspect ratio; amount of transverse reinforcement; vertical load; and amount of vertical reinforcement [1,12].

It has been usual to express the shear strength V_n after diagonal cracking as the sum of two different effects: the residual masonry shear strength V_m; plus the shear resistance V_s provided by transverse reinforcement [19].

$$V_n = V_m + V_s \qquad (2.8)$$

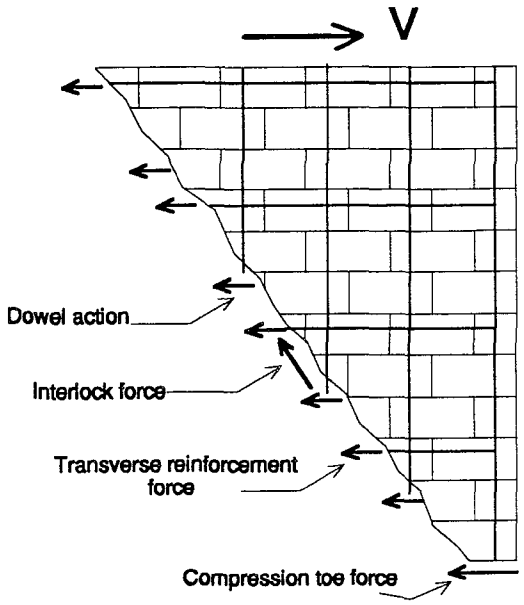

Figure 2.8 Shear resistance mechanism after diagonal cracking.

V_m is provided by the masonry shear resistance of the compression toe, by aggregate interlock, and by dowel action of the longitudinal steel crossing the crack. V_m tends to increase with the ratio of longitudinal reinforcement, and with the magnitude of the axial compressive stress [1,10]. The aggregate-interlock mechanism depends on the extent of crack opening, which depends in turn on the axial stress and the amount of flexural reinforcement. Axial load increases aggregate interlock, but tends to produce more crushing of masonry [11]. Because they develop their maximum capacities at different displacement levels, the mechanisms of compression toe resistance, aggregate interlock, and dowel action are not fully additive. It has been suggested [23] that the residual shear strength of the masonry decreases with increased flexural ductility demand.

Shear strength V_s is provided by the tensile capacity of the horizontal steel crossing the diagonal crack (Fig. 2.8). Design provisions like those of the 1988 UBC [19] give an expression for V_s based on the assumption that all the transverse reinforcement crossing a 45-degree diagonal crack is able to reach yielding [22], as in the case of reinforced concrete elements. However, the extent of the effectiveness of the transverse reinforcement in resisting shear forces has been subject of considerable discussion. Experimental results have shown that shear strength does not increase proportionally to the increase in transverse reinforcement ratio [4,6,7,12]. There is evidence of problems with anchorage of transverse bars, with lack of ductility in steel used for joint reinforcement (truss- or ladder-type wire mesh), and with non-simultaneous occurrence of the maximum capacity of masonry and steel. Test results have shown that 180-degree hooks around the extreme longitudinal bar are the best way to anchor transverse reinforcement resulting in improved shear capacity

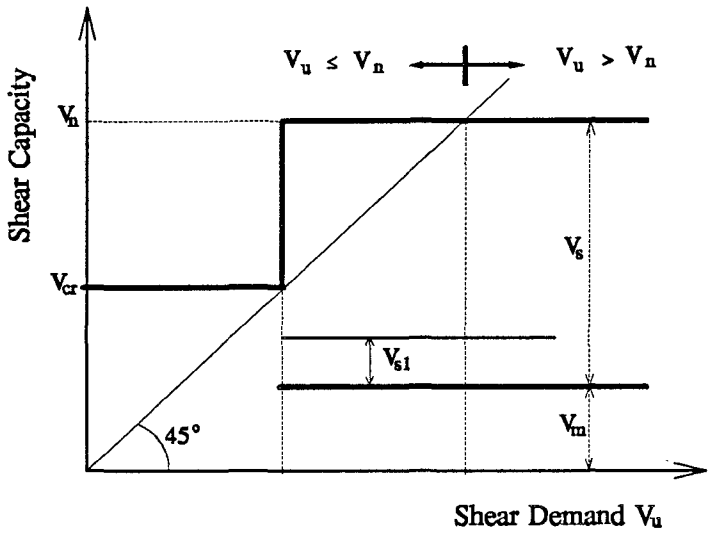

Figure 2.9 Shear resistance mechanisms of masonry walls.

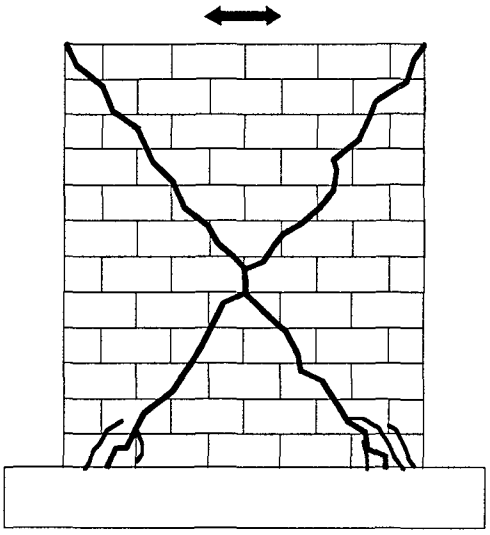

Figure 2.10 Brittle shear failure

and more gradual shear degradation [1,10,12,14].

The available shear strength of the wall for different levels of shear demand V_u is shown schematically in Fig. 2.9. Before diagonal cracking, available shear capacity is the cracking strength V_{cr}. After diagonal cracking, V_m and V_s become effective. Because the residual masonry shear strength V_m is lower than V_{cr}, the behavior of the wall after diagonal cracking will depend on the amount of transverse reinforcement. If the shear strength provided by transverse reinforcement is insufficient, like V_{s1} in Fig. 2.9, then the shear capacity provided by the new mechanism is lower than the cracking strength, the diagonal crack opens extensively, and the failure is sudden and brittle (Fig. 2.10). In this case, the maximum lateral capacity of the wall is given by its cracking load, and its deformation capacity is very limited [4,8,11,12]. In walls with larger transverse reinforcement ratios, the strength of the new mechanism is higher than the cracking strength (like V_s in Fig. 2.9), and new diagonal cracks develop and spread over the diagonals of the wall as displacement increases. Transverse reinforcement limits crack opening, and enhances aggregate interlock. Failure ($V_u = V_n$ in Fig. 2.9) generally occurs by crushing of masonry at cracked portions of the diagonals, as shown in Fig. 2.11. This mechanism has been termed a "ductile shear failure" [12].

During recent years, several expressions have been proposed for calculating the shear capacity of masonry walls [1,7,8,10,20,22]. Most are empirical, and include in different ways some or all of the above aspects influencing shear strength of masonry walls.

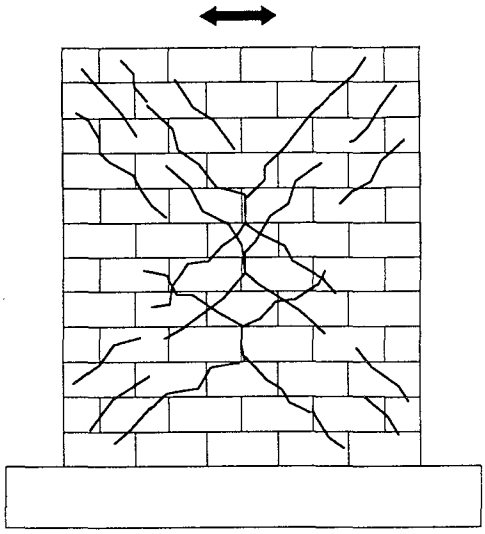

Figure 2.11 Ductile shear failure

In general, deformation capacity of a panel dominated by shear is lower than that of a panel dominated by flexure [1], and the rate of load degradation is higher. Ductility can be improved by increasing the amount of transverse reinforcement. An empirical expression to calculate the overall shear stiffness of a wall panel under normal load conditions is given in Ref. [1]. That expression, based on the secant stiffness at first major diagonal cracking, is conservative up to that level; and its validity for slender walls is unknown. An expression to evaluate strength degradation under cyclic loading due to a shear mechanism is proposed in the same Ref. 1.

2.3.3 Sliding Mode of Failure. A third mechanism of failure, sliding, has frequently been observed in walls with large amounts of transverse reinforcement but light longitudinal reinforcement, and subjected to reversed cyclic loading [12,13,14]. A sliding plane of failure can be defined either by a flexural crack continuous along an horizontal course (sliding-flexure failure) [12,17], or between two diagonal cracks as in the case of squat walls (sliding-shear failure) [8,12].

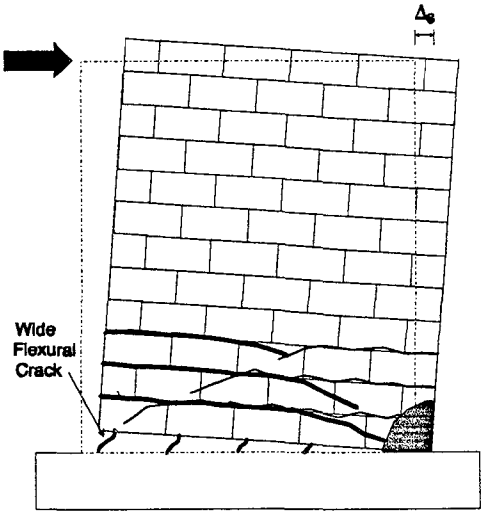

Figure 2.12 Sliding mode of failure.

The sliding flexural mechanism, shown in Fig. 2.12, has been described in Ref. [14]. After complete cycles of reversed displacement of large amplitude, the longitudinal reinforcement at both ends of the wall yields, and a wide crack propagates through the length of the section, generally at the base of the wall. Lateral load is resisted only by dowel action of the longitudinal reinforcement crossing that crack, and by aggregate interlock. However, due to the characteristics of the "cold joint" at the base of the wall, and to the wide opening of

the crack, aggregate interlock is almost ineffective at this stage. On the other hand, dowel action will not develop until large displacements have occurred. As displacement increases, dowel action becomes effective, and the crack will eventually close at one end of the wall, enhancing aggregate interlock action and defining a shear transfer zone at the compression toe. In a pure sliding type of failure, damage occurs only at the interface zone, and failure occurs by crushing of masonry along the sliding plane [12].

Interface shear capacity has been usually calculated using traditional concepts of shear friction. Reinforcement normal to the sliding plane produces the clamping force necessary to develop aggregate interlock, and provides dowel action [13,21]. This mechanism is more efficient if the longitudinal reinforcement is uniformly distributed.

2.3.4 Available Ductility. Some authors [1,17] have pointed out that in calculating ductility, it is more convenient to define the ultimate flexural displacement as that corresponding to some given percentage of the flexural strength after toe crushing, instead of the displacement at ultimate strain of masonry, as conventionally defined. Analytical [15,16] and experimental [1,12,17] results have shown that available ductility so defined decreases with increasing axial load and aspect ratio of the wall, but increases with increasing compressive strength of masonry. Increases in flexural reinforcement ratio and yield strength decrease ductility when defined conventionally, but do not affect the ductility defined as above. Confining plates at the compression toes of the wall are helpful in increasing deformation capacity of the walls [16]. Because of the relatively small values of the plastic hinge length ℓ_p for masonry walls, large curvature ductility levels are required to satisfy a given displacement ductility demand.

3. SPECIMEN DESCRIPTION

In this chapter, the specimens built and tested during this program are described in detail. The specimens are described as part of a prototype building. Structural details of each specimen, including reinforcement and construction details of walls, floors, and lintels, are discussed in the following sections. Results of standard material tests are given.

3.1 Overall Description

3.1.1 General. Each specimen was a two-story concrete block wall system 16.67 ft (5.08 m) long, 17.33 ft (5.28 m) high, and 5-5/8 in. (143 mm) thick, resting on a reinforced concrete base beam. Type 1 specimens were perforated walls with one door opening and one window opening per story. Type 2 specimens were coupled walls with one central opening per story. Each specimen had a floor system 8 in. (200 mm) thick, extending 3.0 ft (0.91 m) from each lateral face of the wall. The wall element designations are shown in Fig. 3.1. The walls were denoted as first-story and second-story walls; and with the base of the wall considered the first floor, the floor slabs were designated as the second floor and the roof.

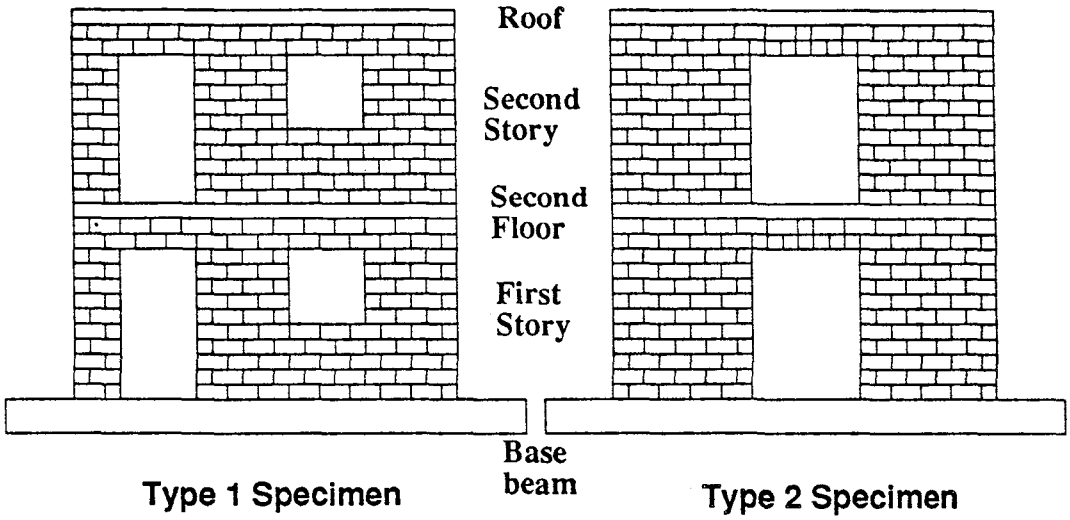

Figure 3.1: Wall element designations.

The specimens were intended to represent a wall subassemblage system in a two-story prototype building [35], shown in Fig. 3.2 for the case of Type 2 specimens. The walls were assumed to be 20 ft (6.10 m) apart. Depending on the characteristics of each wall system, the floor slabs spanned either perpendicular or parallel to the plane of the walls. As shown in Fig. 3.3, the second floor and roof were represented in the specimens by a floor slab

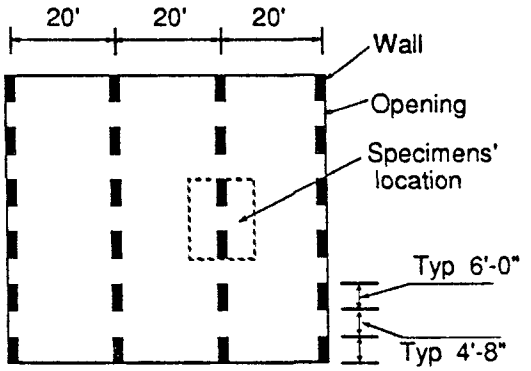

Figure 3.2: Prototype building floor plan.

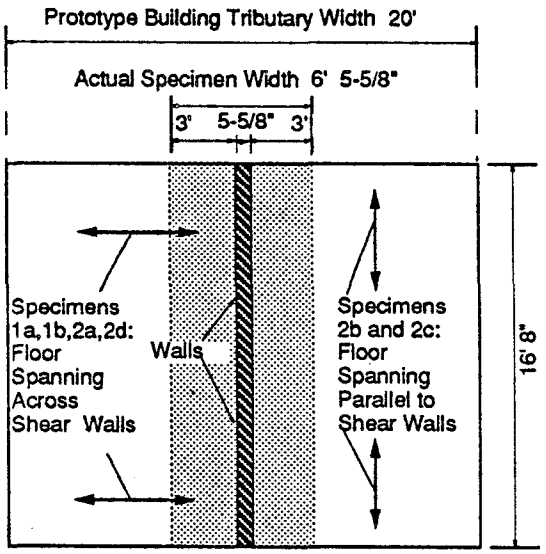

Figure 3.3: Specimen location in prototype building.

extending 3.0 ft (914 mm) from each face of the wall. The effective floor width contributing to the stiffness and strength of the wall was assumed to lie within this width. The walls of the prototype building were assumed to be rigidly connected to an immovable foundation.

The walls were constructed of hollow lightweight concrete masonry units measuring 6 in. thick by 8 in. high by 16 in. long (152 x 203 x 406 mm) for full units, and 8 in. long (203 mm) for half units. Units were laid in running bond, and the walls were fully grouted. To allow the placement of transverse reinforcement and to improve grout continuity, all walls except those at the second story of Specimen 2b were built using full units consisting of open-end bond-beam units. In the case of the second story walls of Specimen 2b, bond-beam units were used only in courses with transverse reinforcement.

The specimens had reinforcement meeting ASTM A615, Grade 60. Transverse reinforcement had 180-degree hooks around the extreme longitudinal reinforcement. Vertical dowels were placed in the foundation beam when Specimens 2a and 2b were constructed. Dowels for the remaining specimens were epoxy-anchored to the foundation beam. Longitudinal reinforcement was anchored to the roof slab using 90-degree hooks. When necessary, $40d_b$ lap-splices were used. Bars were cold-bent in the laboratory. Because the units were only 6 in. thick, the inside bend diameter was usually less than that specified by *ACI 318-89* [45] for transverse reinforcement.

3.1.2 Design. To use consistent criteria throughout the project, all specimens were designed for gravity and lateral loads as specified in the 1985 *Uniform Building Code* [34], acting on the wall as part of the prototype building [35]. Lateral load-resisting elements were provided with enough flexural and shear strength to satisfy UBC requirements for Zone 4. The lateral load capacity of each specimen was predicted using a plastic collapse analysis. All wall elements were then re-designed to satisfy the requirements consistent with the development of the expected collapse mechanism. In all specimens, the wall capacity was assumed to be controlled by flexural behavior. According to a capacity design

philosophy, elements were provided with shear capacities larger than shear forces associated with the development of flexural strength of the system.

Depending on the characteristics of each wall system, the floor slabs spanned either perpendicular or parallel to the to the plane of the walls. If the slabs spanned perpendicular to the plane of the walls, the tributary floor load would be carried completely by the walls in the prototype building, as shown in Fig. 3.3. If the floors spanned parallel to the plane of the walls, the floor load would not be carried by the walls in the prototype building, as shown in Fig. 3.3. In either case, the floor loads on the prototype walls were accurately considered in design and represented in the test setup. Appendix A gives a detailed description of the design of Type 1 specimens. Design of Type 2 specimens is described in Ref. 13.

3.2 Structural Details of Type 1 Specimens

3.2.1 General. Typical block layout and dimensions for Type 1 specimens are shown in Fig. 3.4. The specimens were perforated walls with one door opening 3.33 ft (1.02 m) wide and 6.67 ft (2.03 m) high, and one window opening 3.33 ft (1.02 m) wide and 3.33 ft (1.02 m) high, per story. Lintels 2 courses deep were placed below the slab over each opening.

3.2.2 Walls. Because of the different design philosophies used with Type 1 specimens, the structural detailing of the lateral load resisting elements was different for each specimen.

Pier-Based Specimen 1a

Structural details of Specimen 1a, designed by the pier-based philosophy, are shown in Fig. 3.5. Reinforcing details for this specimen were characterized by light longitudinal reinforcement in piers, #3 (10 mm) jamb bars (ρ_v = 0.08%), and columns, 2#3 (10 mm) bars (ρ_v = 0.16%); heavy transverse reinforcement in first story piers, 1#3 (10 mm) and 1#4 (13 mm) bars at every course (ρ_h = 0.73%); and heavy horizontal reinforcement in the base of the wall and the 2nd floor horizontal element between piers, 2#4 (13 mm) bars at every course (ρ_h = 0.97%). Roof lintels had 1#4 (13 mm) bar as top longitudinal reinforcement and 2#4 (13 mm) bars as bottom longitudinal reinforcement. The second floor lintel had 6#4 (13 mm) bars as total longitudinal reinforcement. Transverse reinforcement in the lintels consisted of #3 (10 mm) U ties placed at 8-in. (203 mm) centers. As shown in Fig. 3.6, the bottom course of the lintels was constructed with bond beam units placed in an inverted position. To improve sliding shear capacity between the wall and base beam, smooth shear keys in the form of truncated cones (3.25 in. in diameter and 1.5 in. deep) were drilled in the base beam, coinciding with the positions of the wall cells with no longitudinal reinforcement.

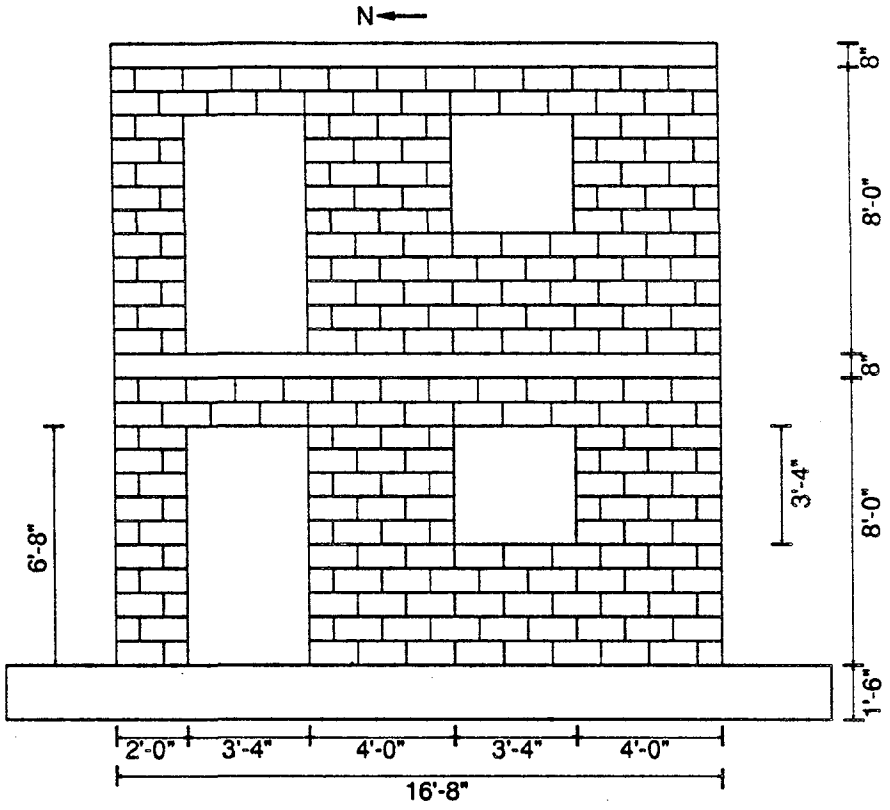

Figure 3.4: Typical Type 1 Specimen.

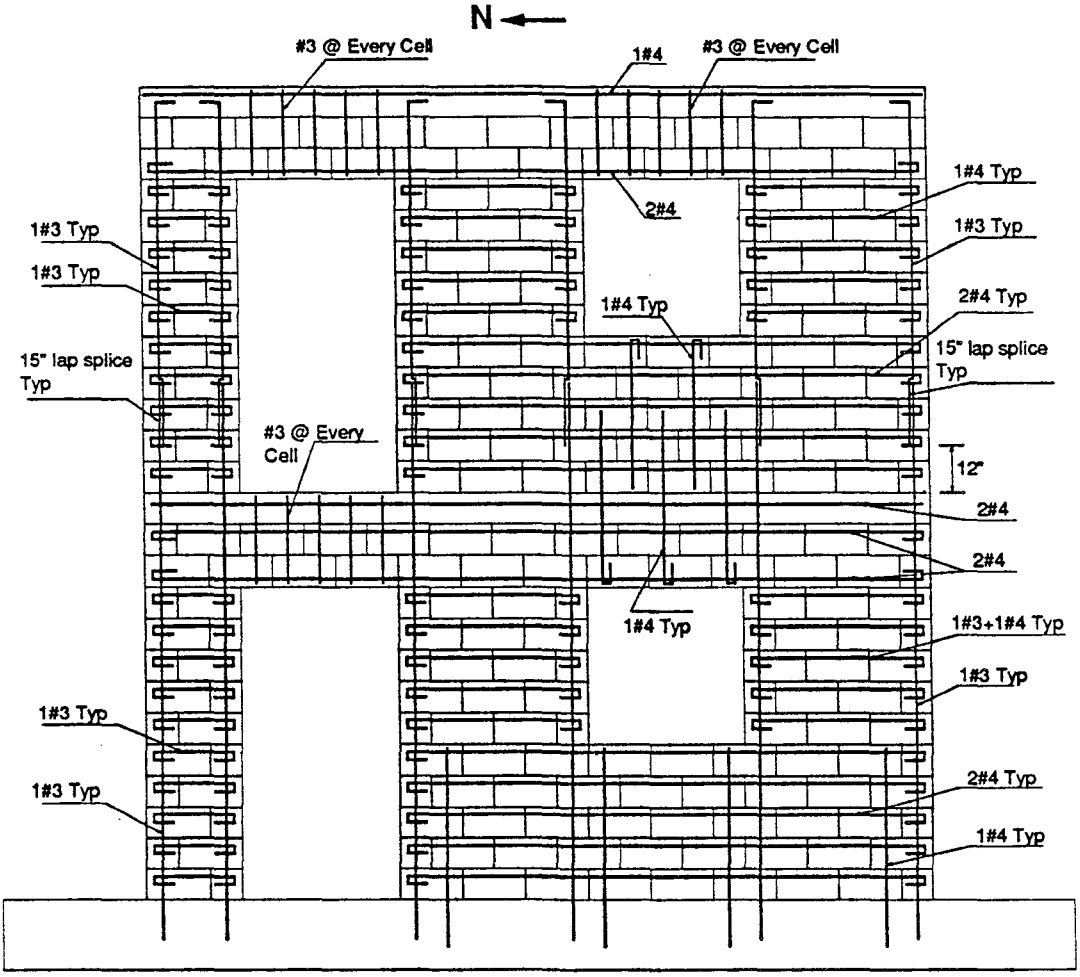

Figure 3.5: Specimen 1a wall reinforcement.

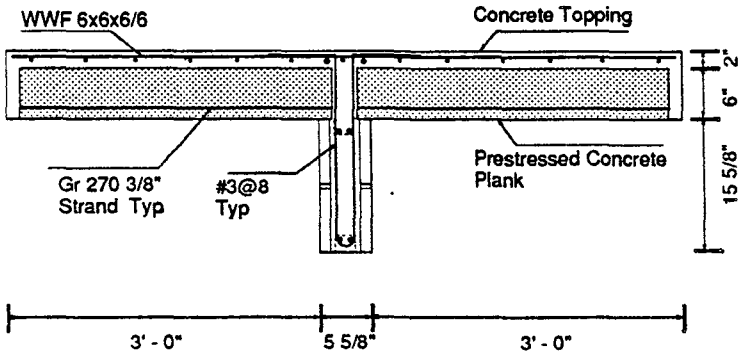

Figure 3.6: Type 1 Specimen: floor slab reinforcement detail.

Coupled Wall-Based Specimen 1b

Structural details of Specimen 1b, designed by the coupled wall-based philosophy, are shown in Fig. 3.7. Reinforcing details for this specimen were characterized by heavy longitudinal reinforcement in the first story piers, #3 (10 mm) jamb bars plus 6#6 (19 mm) bars distributed in each pier (ρ_v = 1.06%); heavy longitudinal reinforcement in columns, 3#5 (16 mm) bars (ρ_v = 0.69%); heavy transverse reinforcement in first story piers, 1#3 (10 mm) and 1#4 (13 mm) bars at every course (ρ_h = 0.73%); light longitudinal reinforcement in the base of the wall, 4#3 (10 mm) bars (ρ_v = 0.06%); heavy horizontal reinforcement in the base of the wall and the second floor horizontal element between piers, 2 #4 (13 mm) bars at every course (ρ_h = 0.97%); and lighter longitudinal reinforcement in the lintels, 1#3 (10 mm) bar as a top and bottom reinforcement. Transverse reinforcement in the lintels consisted of #3 (10 mm) U ties placed at 8-in. (203 mm) centers. As shown in Fig. 3.6, the bottom course of the lintels was constructed with inverted bond beam units. To improve the deformation characteristics of the wall, the flexural reinforcement was debonded in the lowest 8 in. of the wall (Fig. 3.7). To improve sliding shear capacity between the wall and base beam, smooth shear keys in the form of truncated cones (3.25 in. in diameter and 1.5 in. deep) were drilled in the base beam, coinciding with the positions of the wall cells with no longitudinal reinforcement.

3.2.3 Floors. As is typical of this type of construction, the floors of the prototype building were assumed as precast, prestressed concrete planks, 6 in. (152 mm) thick and 4 ft (1.22 m) wide, with a 2-in. (50 mm) thick reinforced topping of cast-in-place concrete. For the Type 1 specimens, the planks were assumed to span perpendicular to the plane of the walls. As shown in Figs. 3.6 and 3.8, the specimens' floors were built of 3-ft (914 mm) long plank segments resting 1.5 in. (51 mm) inside the walls on each side of the specimen. Reinforcement requirements of the slabs were based on the 1985 UBC [34] gravity load requirements on the floors of the prototype building and on ACI 318-86 [34] provisions for reinforced concrete elements. Longitudinal reinforcement for the precast planks, as shown in Fig. 3.6, consisted of four Gr 270 3/8-in. strands (10 mm) (ρ^* = 0.00152). Topping reinforcement, provided for shrinkage and temperature steel requirements for the prototype building, consisted of WWF 6 x 6 x 6/6 (152mm x 152mm x 4.8mm/4.8mm), placed approximately at the mid-depth of the 2-in. topping slab. To provide better structural integrity, #4 (13 mm) bars at 18 in. (457 mm) were run continuously through the cells of planks at opposite sides of the wall. Those plank cells containing reinforcement, and also those crossed by bolts from the lateral loading system, were filled with concrete at the time the topping was cast. To improve punching shear capacity of the wall-slab joint, additional pieces of welded wire fabric reinforcement were added to the topping in the wall areas, as shown in Fig. 3.9.

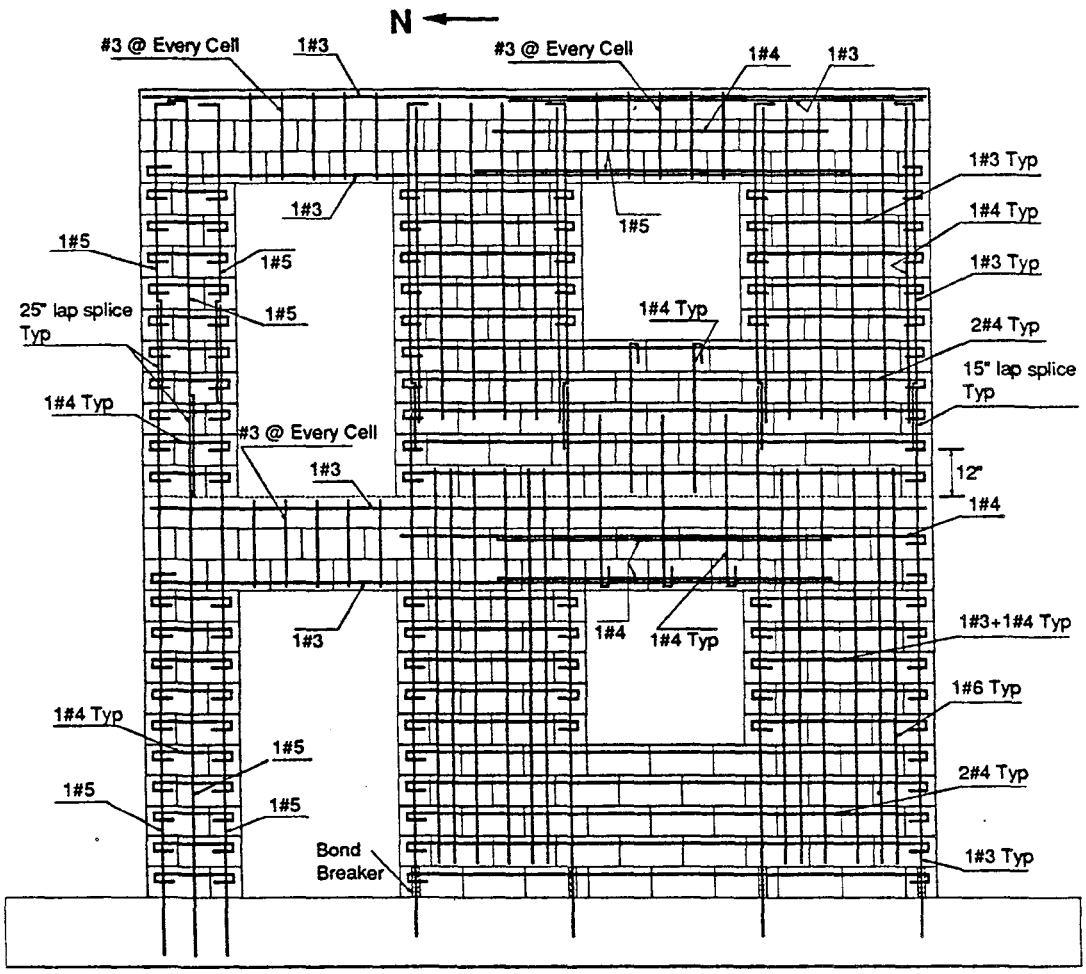

Figure 3.7: Specimen 1b wall reinforcement.

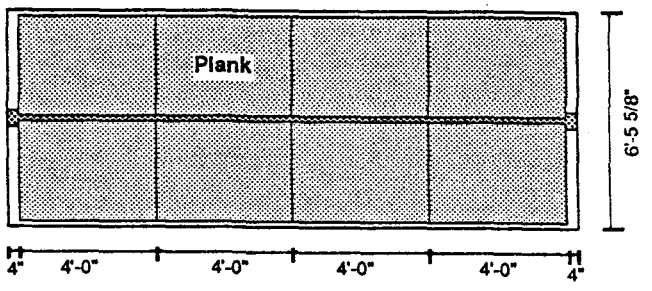

Figure 3.8: Type 1 Specimen floor layout.

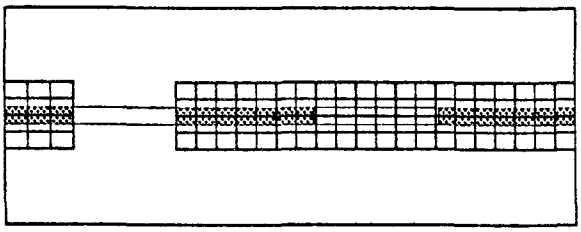

Figure 3.9: Additional WWF reinforcement in Type 1 Specimens.

3.3 Structural Details of Type 2 Specimens

3.3.1 General. As shown in Figs. 3.10 to 3.13, the Type 2 specimens were coupled walls with one central opening 4.67 ft (1.42 m) wide. They were two-story concrete block walls 8.0 ft (2.44 m) high, 6.0 ft (1.83 m) long, with an actual thickness of 5-5/8 in. (143 mm). Block layout and dimensions for Specimens 2a and 2b are shown in Figs 3.10 and 3.11 respectively. As shown in Figs. 3.12 and 3.13, Specimens 2c and 2d had a lintel 2 courses deep under the slab over the openings.

3.3.2 Walls. Wall reinforcement was the same for all four Type 2 specimens. However, due to the presence of lintels, and to improve the behavior of the walls, the structural detailing was slightly modified for the last two Type 2 specimens.

Specimens 2a and 2b

Wall reinforcement was arranged as shown in Fig. 3.14 for Specimens 2a and 2b. Longitudinal reinforcement consisted of 5 #4 bars (13 mm) placed at 16 in. centers (406 mm) in each wall (ρ_v = 0.248%). Vertical reinforcement was lap spliced to dowels in the base, using a $40d_b$ lap (20 in. or 510 mm). Transverse reinforcement in the first story consisted #4 bars (13 mm) at every course (ρ_h = 0.44%). Transverse reinforcement in the second story was #4 bars in every other course (ρ_h = 0.22%).

Specimens 2c and 2d

Walls of Specimens 2c and 2d were almost identical to those of Specimens 2a and 2b. However, as shown in Fig 3.15, vertical reinforcement was lap spliced to dowels at the mid-height of the walls. Longitudinal reinforcement in the lintels consisted of two #4 (13 mm) bars in each face. Transverse reinforcement consisted of #3 (10 mm) U ties placed at 8-in. (203 mm) centers. As shown in Fig. 3.16, the bottom course of the lintels was constructed with half units. To improve sliding shear capacity between the wall and base beam, 4-in. diameter and 1.5-in. deep shear keys were drilled in the base beam coinciding with the positions of the wall cells with no longitudinal reinforcement.

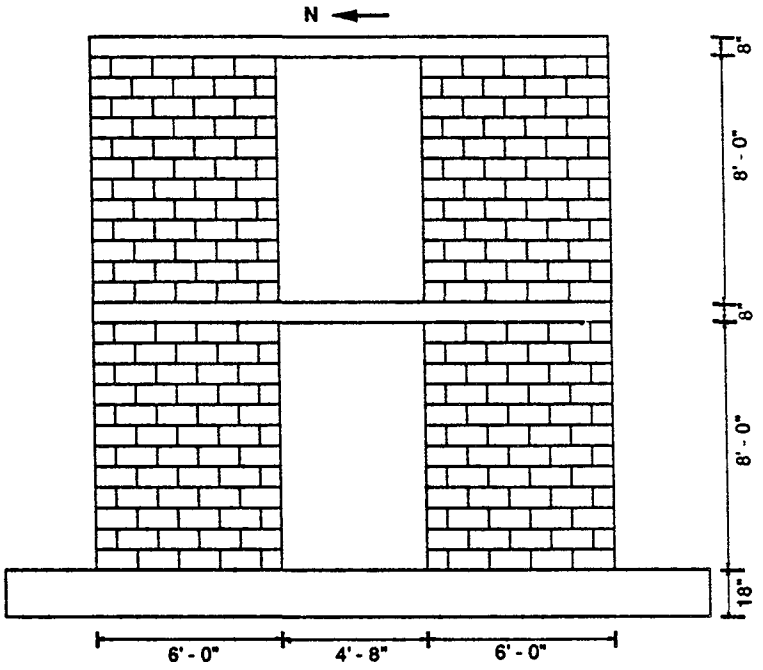

Figure 3.10: Specimen 2a.

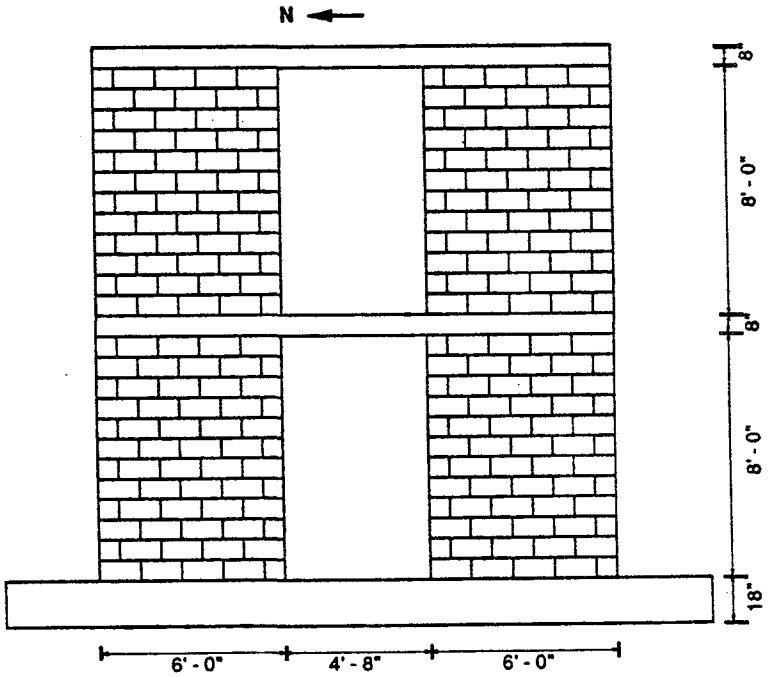

Figure 3.11: Specimen 2b.

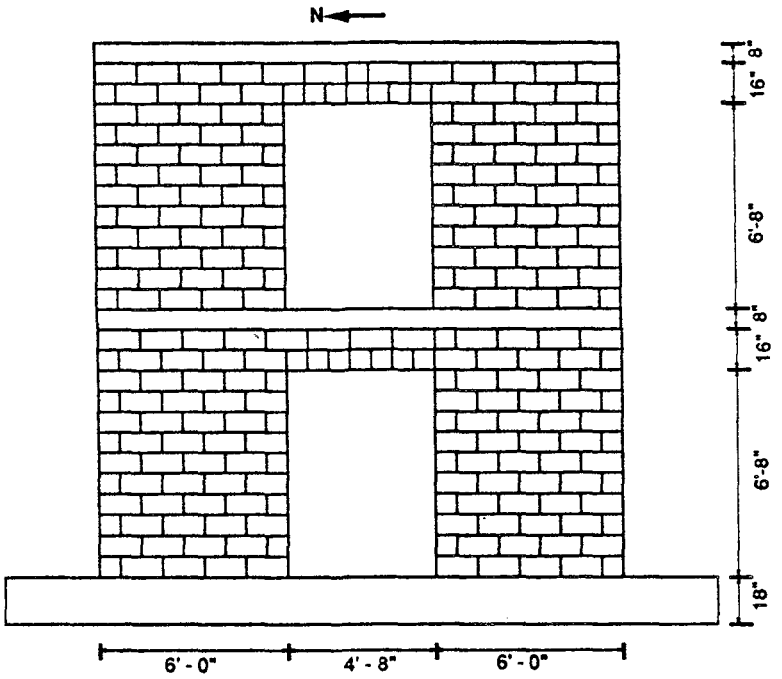

Figure 3.12: Specimen 2c.

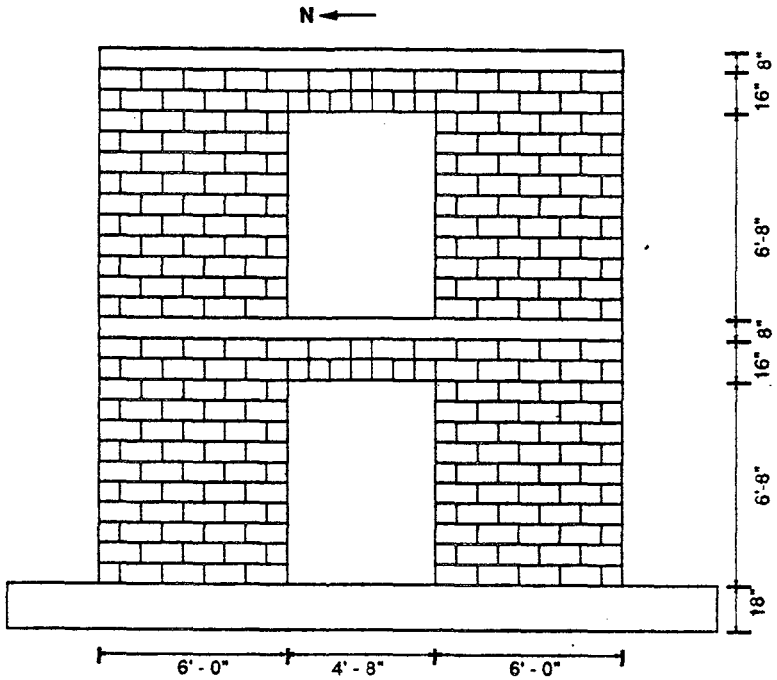

Figure 3.13: Specimen 2d.

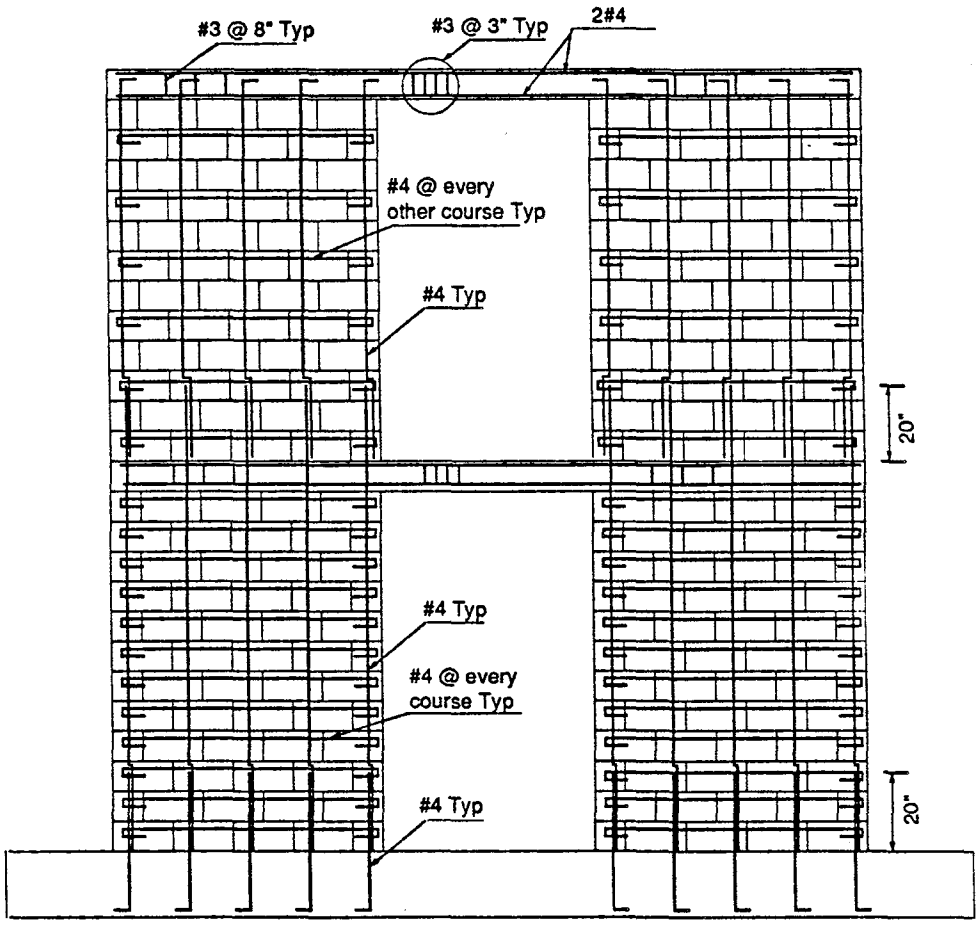

Figure 3.14: Specimens 2a and 2b, wall reinforcement.

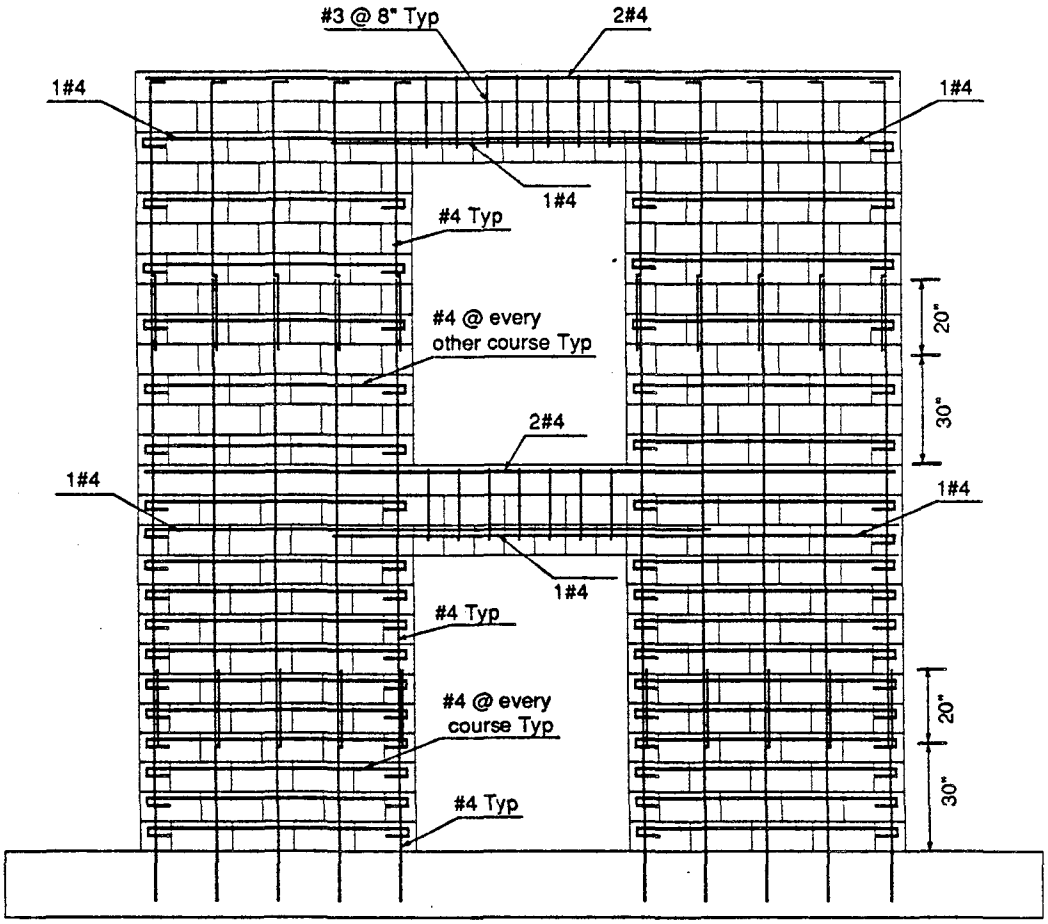

Figure 3.15: Specimens 2c and 2d, reinforcement.

Figure 3.15: Specimens 2c and 2d, reinforcement.

3.3.3 Floors. As described in this section, each of the Type 2 specimens was used to study the behavior of a different floor-coupling beam system in the prototype building.

Specimen 2a

In this case, the floor system of the prototype building was assumed as a cast-in-place reinforced concrete flat slab, 8 in. (200 mm) thick. Given the characteristics of the prototype building (Fig. 3.2), the floors were assumed to span perpendicular to the coupled walls. As shown in Fig. 3.16, transverse reinforcement in the top of the slab consisted of #5 bars (16 mm) spaced at 10 in. (254mm) with $\rho' = 0.00388$, and in the bottom of the slab, of #4 bars (13 mm) spaced at 10 in. (254 mm) with $\rho = 0.00250$. Transverse reinforcement requirements were governed by the required flexural capacity, in the prototype building, of a continuous slab spanning 20 ft. (6.01 m) between the shear walls [25]. Longitudinal reinforcement requirements were governed by shrinkage and temperature steel requirements for the prototype building. Longitudinal reinforcement consisted of #3 bars (10 mm) spaced at 12 in. (305 mm). As shown in Fig. 3.16, additional longitudinal reinforcement, consisting of four #4 bars (13 mm), was placed in the slab directly over the shear walls to provide extra flexural strength in the portion of the slab which was envisioned to act as a coupling beam between the two walls ($\rho = \rho' = 0.00206$). These #4 bars were enclosed by #3 ties (10 mm) placed at 3-in. centers (76 mm) between the walls, and at 8-in. centers (203 mm) on the walls.

Specimen 2b

As with the Type 1 specimens, the floors of the prototype building were assumed as precast, prestressed concrete planks, 6 in. (152 mm) thick and 3 ft (914 mm) wide, with a 2-in (50 mm) thick reinforced topping of cast-in-place concrete. Since there were no lintels at the wall openings, the planks were assumed to span parallel to the plane of the walls. As shown in Fig. 3.16, the specimen's floors were built of two precast planks measuring 6 in. (152 mm) thick, 16.67 ft. long (5.08 m) and 3 ft. (914 mm) wide. Reinforcement of the planks and the cast-in-place topping was the same as described for Type 1 specimens. However, no additional pieces of welded wire fabric were used in the vicinity of the walls. As shown in Fig. 3.16, additional longitudinal reinforcement, consisting of four #4 bars (13 mm), was placed between the precast planks directly over the shear walls to provide extra flexural strength and ductility in the portion of the slab which coupled the two walls. These #4 bars were enclosed by #3 ties (10 mm) placed at 3-in. centers (76 mm) between the walls, and at 8-in. centers within the walls.

Specimen 2c

Floor planks and topping were identical to those of Specimen 2b. However, as shown in Fig. 3.16, Specimen 2c had lintels constructed of two courses of concrete masonry below the coupling slabs over the openings. To improve punching shear capacity of the wall-slab joint, additional pieces of welded wire fabric reinforcement were added to the topping in

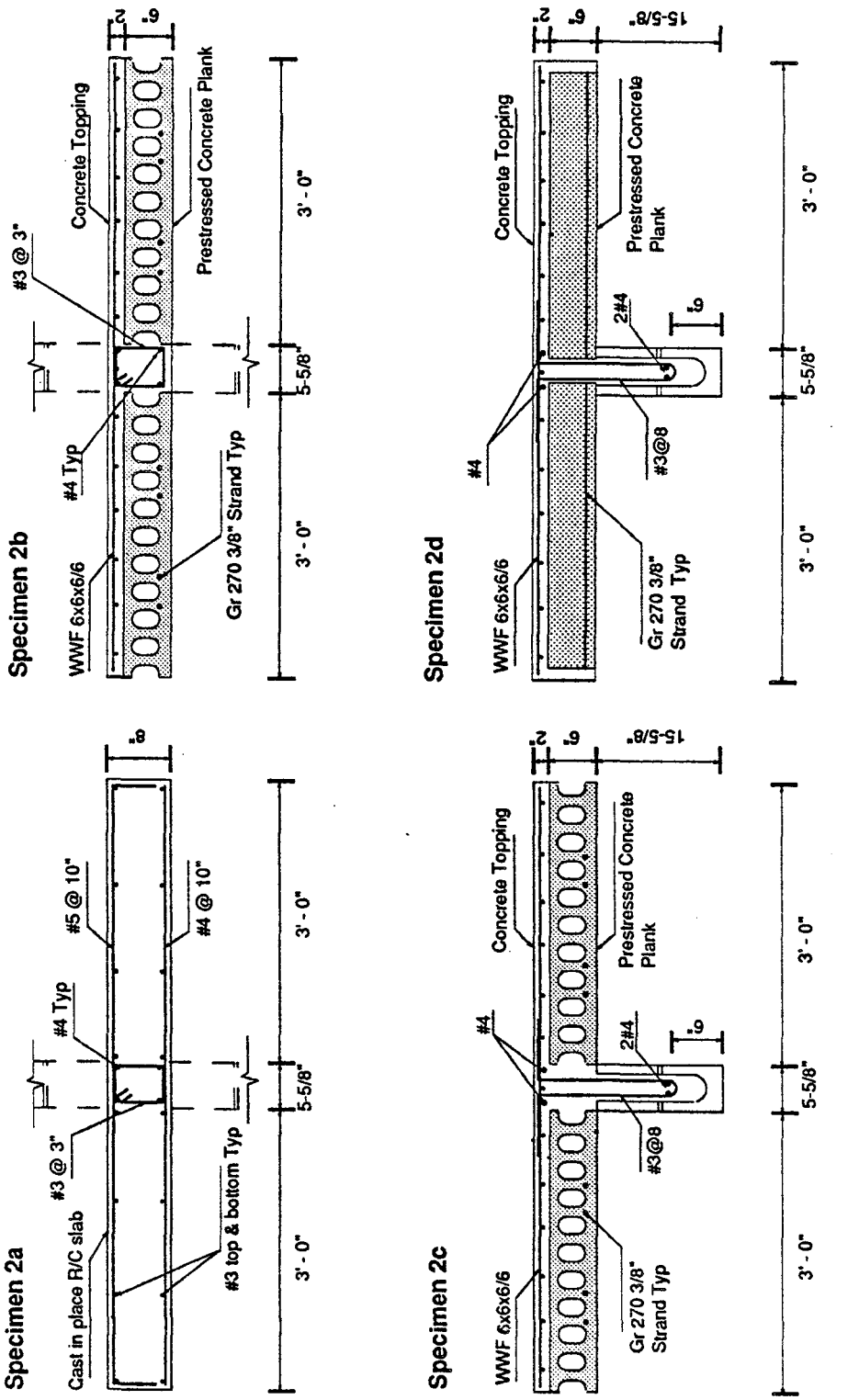

Figure 3.16: Type 2 Specimens, floor slab reinforcement detail.

the wall areas, as shown in Fig. 3.17. To improve the behavior of the specimen's floor system, steel clamps intended to simulate the restraining effect of the rest of the floor in the prototype building, were used to keep the planks from separating at the ends of the wall, as shown in Fig. 3.18.

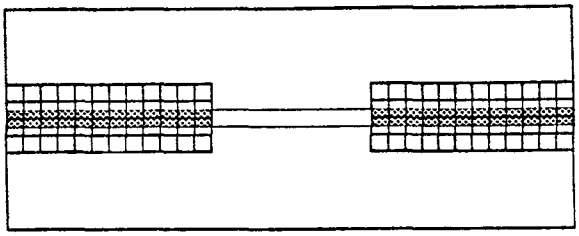

Figure 3.17: Additional WWF reinforcement in Specimens 2c and 2d.

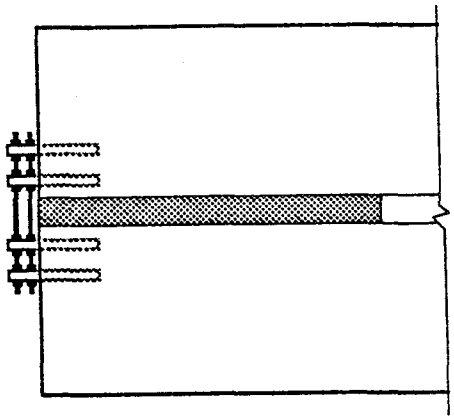

Figure 3.18: Specimen 2c, floor clamps.

Specimen 2d

Floor planks and topping were identical to those of Type 1 specimens. To improve punching shear capacity of the wall-slab joint, additional pieces of welded wire fabric reinforcement were added to the topping in the wall areas, as shown in Fig. 3.17.

3.4 Material Tests

3.4.1 General. In this section, results of standard tests conducted on the materials used to construct the masonry walls are described. Masonry components, concrete, and reinforcement were tested according to specifications mentioned in the subsequent sections. In order to obtain representative material properties, most tests were performed immediately after completion of the wall tests.

3.4.2 Concrete Masonry Unit Tests. To ensure basic material uniformity, all concrete units for this and other TCCMAR experimental specimens were manufactured by Blocklite (Selma, California). The units were specified to be Type I units (moisture-controlled), and to conform to the requirements of ASTM C90 (Hollow Load-Bearing Concrete Masonry Units). All specimens were constructed from a single production run of blocks.

Unit weight of two full-sized hollow units was determined by measuring the weight of sand required to fill the unit holes. Knowing the bulk specific weight of the sand, the net volume of the unit was calculated as the difference between its gross volume and the sand volume. The units were 15-9/16 in. long, 5-5/8 in. wide, and 7-1/2 in. high. Their average area ratio (net volume/gross volume) was 0.6, and their average unit weight, as shown in Table 3.1, was 99.0 lb/ft^3. No saturation or absorption tests were run.

To determine compressive strength, 4 units were capped and tested in accordance with ASTM C140 (Sampling and Testing Concrete Masonry Units). Compressive strength was calculated using both the gross and the net area. Results are given in Table 3.1.

Table 3.1 Results of Concrete Block Unit Tests

Test	Units	Average	COV %
Unit Weight (pcf)	2	99.0	-
Compressive Strength (psi)			
Net Area	4	2750	9
Gross Area		1650	9

3.4.3 Mortar Tests. The mortar conformed to the proportion specification for Type S mortar of ASTM C270 (Mortar for Unit Masonry). It was proportioned by volume to have 1 part of Portland cement, 1/2 part hydrated lime, and 4-1/2 parts masonry sand.

a) Portland cement conformed to Type I (general purpose) of ASTM C150 (Portland Cement).
b) Lime conformed to Type S of ASTM C207 (Hydrated Lime for Masonry Purposes).
c) Sand was natural, and was specified to conform to ASTM C144 (Aggregate for Masonry Mortar). It was not tested for conformance with the gradation requirements of that specification.

Tests were conducted on the mortar used in the specimen (referred to here as "field" mortar), and on separate mortar batches mixed for that purpose (referred to here as "laboratory" mortar). Before building the specimens, flow tests were conducted on

laboratory mortars, to establish a water content giving a flow of just over 110. Two-in. mortar cube specimens were taken from this mix and tested to provide a value of relative mortar strength and quality to enable a comparison to be made with similarly tested mortars used by other researchers. Results are summarized in Table 3.2.

Table 3.2 Laboratory Mortar Test Results

Specimens		Age	Average Compressive Strength	Coeff. of Variation
No.	Size	(days)	(psi)	
3	2-in. cubes	14	3260	4%
3	2-in. cubes	31	3380	3%

During construction of each story of the specimens, flow tests were conducted on field mortars taken form the mason's board. Two-in. (51 mm) cube specimens were taken and tested in accordance with ASTM C780 (Preconstruction and Construction Evaluation of Mortars for Plain and Reinforced Concrete Masonry). In some cases, additional 3 x 6-in. (76 x 152-mm) cylinders and 2 x 4-in (51 x 102-mm) cylinders were taken and tested. Results are summarized in Table 3.3. In that table the designation "test" refers to the age of the material specimen at the time of the test of the wall specimen. Differences between compressive strengths of both mortars are due to the fact that the flow of the field mortar is higher than that of the laboratory mortar, about 110.

3.4.4 Grout Tests. The grout conformed to the coarse grout specification of ASTM C476 (Grout for Masonry). Proportions by volume were 1 part portland cement to 3 parts masonry sand to 2 parts pea gravel. To control water loss and shrinkage of the grout, Type 2 Grout-Aid, manufactured by Sika, was used at a dosage of one pound of Grout-Aid to one bag of cement, with a maximum of six pounds of Grout-Aid to one cubic yard of grout. Sand and pea gravel conformed to ASTM C404 (Aggregates for Masonry Grout).

During the grouting of each story, 3 x 3-in. (76 x 76-mm) grout prisms were formed in absorptive molds in accordance with ASTM C1019. They were subsequently tested in accordance with ASTM C39 (Standard Method of Test for Compressive Strength of Cylindrical Concrete Specimens). Additional 2-in. and 3-in. cylinders were taken from grout poured in hollow units using a core drill and were then tested. Results are summarized in Table 3.4. The change in drill sizes was due to availability of core drills in the testing laboratory.

3.4.5 Prism Tests. During the construction of each story the mason constructed several full unit prisms, each 3 units high. The prisms were laid against a vertical surface.

Table 3.3 Field Mortar Test Results

Sample	Specimens		Age	Average Compressive Strength (psi)	Coeff. of Variation
	No.	Size	(days)		
Sp-2a Story 1	3	2-in. cubes	16	800	3%
	2	3-in. cyl.	16	600	--
	3	2-in. cubes	28	690	10%
	5	3-in. cyl.	113 (test)	1150	5%
Sp-2a Story 2	3	2-in. cubes	76 (test)	1230	2%
Sp-2b Story 1	9	2-in. cubes	156 (test)	1640	13%
	4	2-in. cyl.	156 (test)	1330	4%
Sp-2b Story 2	9	2-in. cubes	100 (test)	1770	9%
	7	2-in. cyl.	100 (test)	1650	10%
Sp-2c Story 1	12	2-in. cubes	93 (test)	3160	14%
Sp-2c Story 2	9	2-in. cubes	65 (test)	1880	13%
Sp-2d Story 1	9	2-in. cubes	130 (test)	3640	2%
Sp-2d Story 2	9	2-in. cubes	106 (test)	3010	23%
Sp-1a Story 1	9	2-in. cubes	109 (test)	1900	16%
Sp-1a Story 2	9	2-in. cubes	81 (test)	1660	19%
Sp-1b Story 1	6	2-in. cubes	88 (test)	3100	22%
Sp-1b Story 2	9	2-in. cubes	67 (test)	1600	19%

Table 3.4 Grout Test Results

Sample	Specimens		Age	Average Compressive Strength	Coeff. of Variation
	No.	Size	(days)	(psi)	
Sp-2a Story 1	3 1 5	3-in. prism 3-in. prism 3-in. core	28 104 (test) 104 (test)	5320 5410 4040	5% -- 19%
Sp-2a Story 2	4 4	3-in. prism 3-in core	69 (test) 69 (test)	4690 4420	8% 10%
Sp-2b Story 1	4 3	3-in. prism 2-in. core	154 (test) 154 (test)	5480 3250	6% 9%
Sp-2b Story 2	4 3	3-in. prism 2-in. core	88 (test) 88 (test)	4930 2470	10% 27%
Sp-2c Story 1	4 3	3-in. prism 2-3/4-in. core	87 (test) 87 (test)	1640 4540	35% 8%
Sp-2c Story 2	4 4	3-in. prism 2-3/4-in. core	52 (test) 52 (test)	4570 3660	37% 15%
Sp-2d Story 1	4 4	3-in. prism 2-3/4-in. core	123 (test) 123 (test)	6180 3280	9% 10%
Sp-2d Story 2	4 4	3-in. prism 2-3/4-in. core	99 (test) 99 (test)	4990 4190	9% 18%
Sp-1a Story 1	4 4	3-in. prism 2-3/4-in. core	98 (test) 98 (test)	5010 3260	7% 6%
Sp-1a Story 2	4 3	3-in. prism 2-3/4-in. core	77 (test) 77 (test)	6060 3470	10% 11%
Sp-1b Story 1	4 5	3-in. prism 2-3/4-in. core	83 (test) 83 (test)	5610 5140	9% 11%
Sp-1b Story 2	4 4	3-in. prism 2-3/4-in. core	62 (test) 62 (test)	5270 4867	7% 10%

No other jigs were used to aid construction. All prisms were laid using stretcher units. The prisms were grouted simultaneously with the walls, consolidated using the same mechanical vibrators, and cured under the same conditions as the walls. The ends of the prisms were capped using hydrostone, according to the following procedure: with the prism standing in vertical position, wooden molds were placed around the top end; once the verticality of the lateral faces of the prism had been checked, hydrostone was poured inside the molds. Once the hydrostone hardened, the process was repeated for the other end. Loads were applied using a 1-in. thick steel plate, with 1-by-3-inch welded stiffeners. The vertical centroid of each prism specimen could be aligned visually with the axis of the testing machine. Compression tests were performed in accordance with ASTM E447 (Compressive Strength of Masonry Prisms). Results are summarized in Table 3.5.

3.4.6 Concrete Tests. All concrete used was generally in accordance with the requirements of ACI 318-83 [15]. Concrete for the base beams had a specified compressive strength of 6,000 psi (41.4 MPa). Concrete for the floor slabs had a specified compressive strength of 4,000 psi (27.6 Mpa). During the pouring of each floor slab, 6-in. (152-mm) diameter cylinder specimens were taken in accordance with ASTM C31 (Making and Curing Concrete Test Specimens in the Field), and were subsequently tested in accordance with ASTM C39. Results are summarized in Table 3.6.

3.4.7 Reinforcement Tests. Reinforcement conformed to Grade 60 of ASTM A615 (Deformed and Plain Billet Steel Bars for Concrete Reinforcement).

Within each bar size, all reinforcement for each specimen was intended to be taken from the same heat. However, due to an oversight in ordering materials, the reinforcement in Specimen 2a came from multiple heats. For that specimen, test were conducted on steel from each heat.

For all specimens, reinforcement from each heat was tested in tension, and stress-strain curves were obtained. Deformations were measured using a Tinius-Olsen extensometer over an 8-in. gauge length. Typical stress-strain curves are given in Fig. 3.19 to 3.30. Data are summarized in Table 3.7.

3.4 Construction of Specimens

The specimens were constructed in the Phil M. Ferguson Structural Engineering Laboratory, located at the Balcones Research Center of the University of Texas at Austin. Construction methods and techniques were the same as typically used in the field for this type of structure.

The foundation dowels for the first-story of the first two specimens (2a and 2b) were cast in place with the base beams. The beams were re-used for subsequent tests. After the first two specimens were tested and removed, the old foundation dowels were cut off flush

Table 3.5 Prism Test Results

Sample	Specimens	Age (days)	Average Compressive Strength (psi)	Coeff. of Variation
Sp-2a Story 1	3 prisms	104 (test)	2020	19%
Sp-2a Story 2	4 prisms	69 (test)	2340	8%
Sp-2b Story 1	4 prisms	154 (test)	3090	10%
Sp-2b Story 2	3 prisms	88 (test)	2510	14%
Sp-2c Story 1	4 prisms	87 (test)	2950	11%
Sp-2c Story 2	3 prisms	52 (test)	2820	10%
Sp-2d Story 1	4 prisms	123 (test)	3170	11%
Sp-2d Story 2	3 prisms	99 (test)	2970	14%
Sp-1a Story 1	3 prisms	98 (test)	2810	12%
Sp-1a Story 2	4 prisms	77 (test)	2790	8%
Sp-1b Story 1	4 prisms	83 (test)	3500	2%
Sp-1b Story 2	4 prisms	62 (test)	3150	8%

Table 3.6 Slab Concrete Test Results

Sample	Specimens		Age	Average Compressive Strength (psi)	Coeff. of Variation
	No.	Size	(days)		
Sp-2a Floor 2	3 3	6-in. Cyl. 6-in. Cyl.	7 90 (test)	4250 5280	12% 1%
Sp-2a Roof	5	6-in. Cyl.	57 (test)	3660	9%
Sp-2b Floor 2	6	6-in. Cyl.	117 (test)	5220	2%
Sp-2b Roof	5	6-in. Cyl.	65 (test)	3670	6%
Sp-2c Floor 2	12	6-in. Cyl.	73 (test)	4450	2%
Sp-2c Roof	10	6-in. Cyl.	46 (test)	5670	4%
Sp-2d Floor 2	6	6-in. Cyl.	112 (test)	5320	2%
Sp-2d Roof	6	6-in. Cyl.	88 (test)	5210	3%
Sp-1a Floor 2	8	6-in. Cyl.	100 (test)	4680	5%
Sp-1a Roof	8	6-in. Cyl.	75 (test)	4540	1%
Sp-1b Floor 2	7	6-in. Cyl.	76 (test)	5000	4%
Sp-1b Roof	7	6-in. Cyl.	55 (test)	4420	3%

with the base. For subsequent tests, holes were drilled in the base beam, and new foundation dowels were inserted and secured with Epcon, an epoxy-based structural adhesive made by ITW Ramset.

All masonry walls were laid by an experienced mason in running bond pattern. Clean-out openings were used in the bottom courses of the walls in both stories. After the walls were built to their full story height of 8.0 ft (2440 mm) and the formwork was erected, all cores were grouted using a single lift. Grout was consolidated using 3/4-in. electric vibrators. The vibrators were placed in the cores and turned on. Grout was placed in the cores, and the vibrators were slowly withdrawn during the grouting operation. Grout and slab concrete was placed using a bottom-opening bucket lifted into place by a travelling overhead crane.

After construction of each story was completed, sway braces were connected to that story slab. Once the specimen was built, the elements of the lateral and vertical loading systems were installed, and all hydraulic and electric connections were made.

A complete description of the construction process is given in Ref. 13.

Table 3.7 Reinforcing Bar Test Results (Refer to Fig. 3.19)

Reinforcement	f_y (Ksi)	E (Ksi)	ϵ_{sh}	E_{sh} (Ksi)	f_u (Ksi)	ϵ_u	Refer to:
Sp 2a - 2b Dowel Reinf.	62.6	29,000	---	---	106.4	0.125	Fig. 3.20
Sp 2a Vert. Reinf. 1st Story	64.9	32,000	0.0093	1040	104.3	0.13	Fig. 3.21
Sp 2a #3 Slab Reinf.	68.2	29,000	0.0051	644	106.4	0.12	Fig. 3.22
Sp 2b Vert. Reinf. 1st Story	70.6	30,700	0.0075	1570	113.1	0.127	Fig. 3.23
Sp 2c #4 Reinf.	72.2	28,200	0.0046	1140	113.6	0.10	Fig. 3.24
Sp 2c - 2d #3 Stirrup	66.4	29,600	0.0118	1040	104.5	0.137	Fig. 3.25
Sp 2d #4 Reinf.	65.2	28,300	0.0138	1130	97.2	0.148	Fig. 3.26
Sp 1a - 1b #3 Reinf.	74.2	29,100	0.0145	1210	106.9	0.113	Fig. 3.27
Sp 1a - 1b #4 Reinf.	67.3	27,600	0.0048	1110	107.2	0.116	Fig. 3.28
Sp 1a - 1b #5 Reinf.	74.8	29,600	0.0104	1240	110.6	0.114	Fig. 3.29
Sp 1a - 1b #6 Reinf.	67.2	29,800	0.0075	1440	111.9	.0120	Fig. 3.30

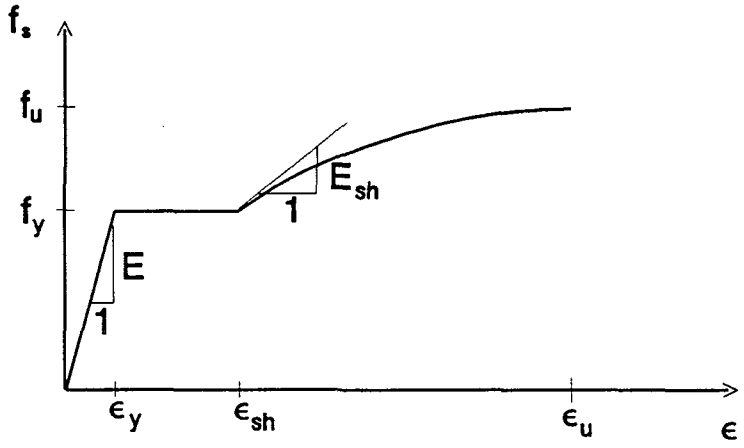

Figure 3.19: Typical stress-strain curve for reinforcement.

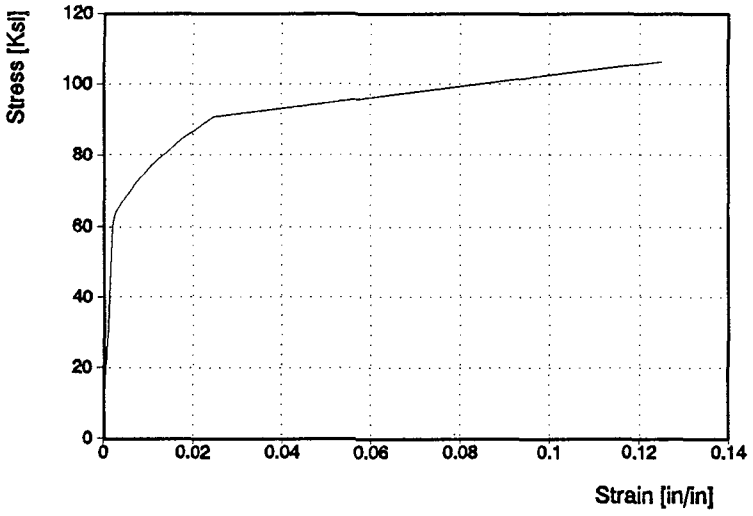

Figure 3.20: Typical stress-strain curve for Specimens 2a and 2b dowel reinforcement.

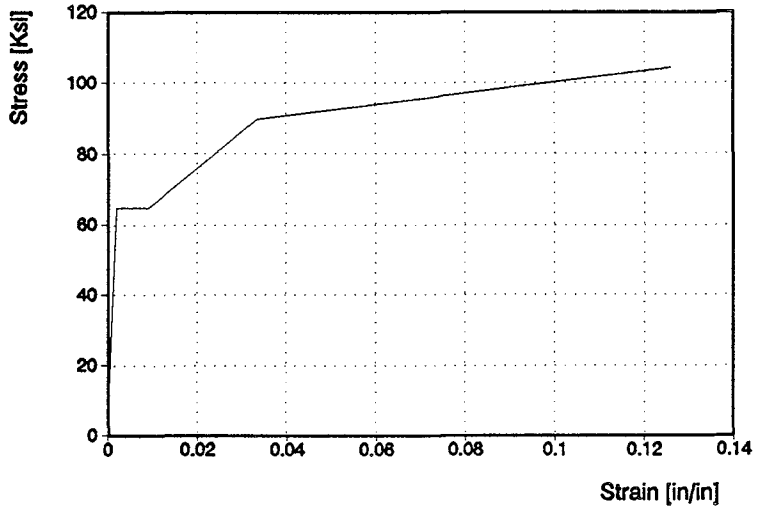

Figure 3.21: Typical stress-strain curve for Specimen 2a vertical reinforcement.

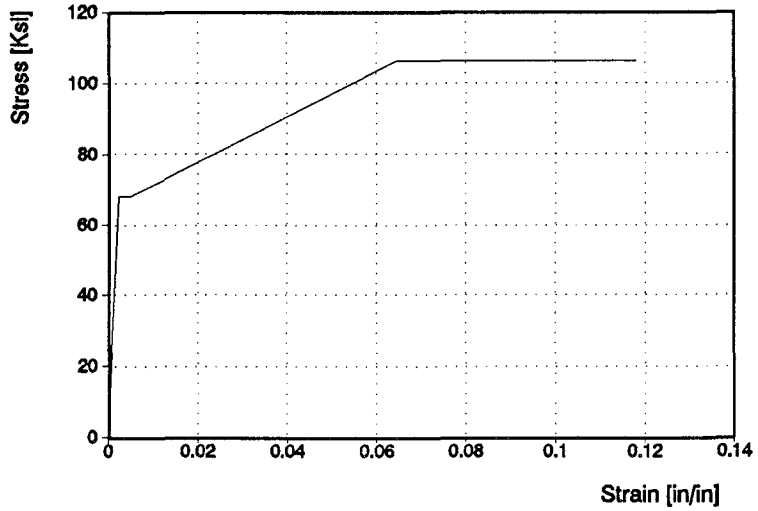

Figure 3.22: Typical stress-strain curve for Specimen 2a longitudinal reinforcement of slabs.

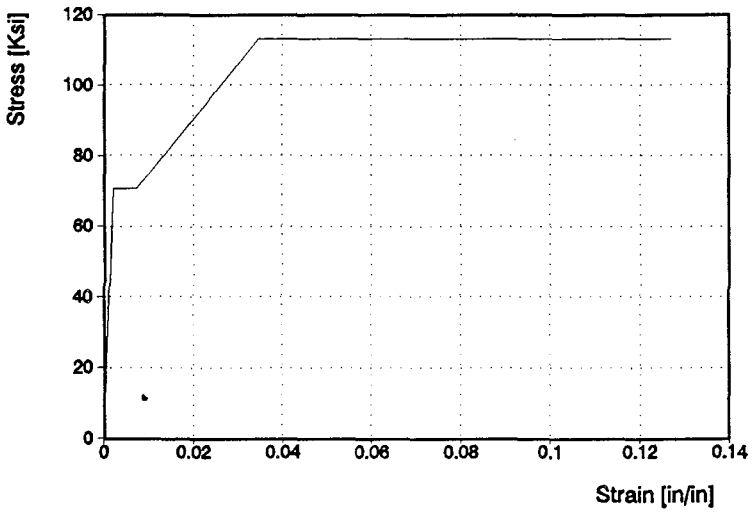

Figure 3.23: Typical stress-strain curve for Specimen 2b reinforcement except dowels.

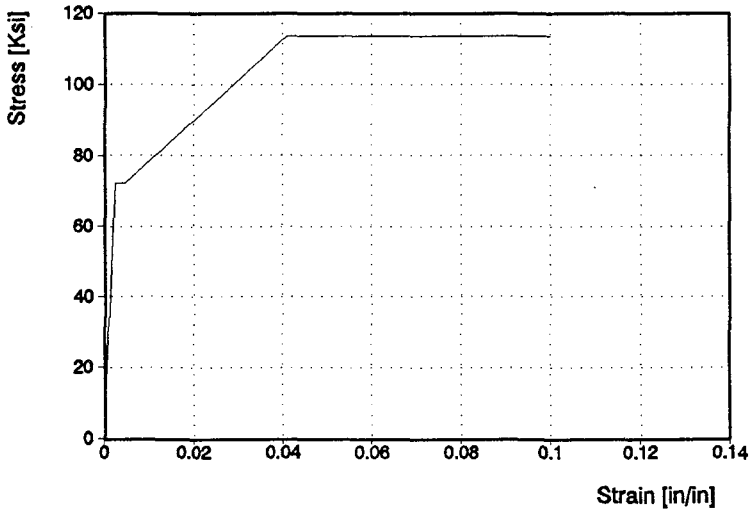

Figure 3.24: Typical stress-strain curve for Specimen 2c reinforcement.

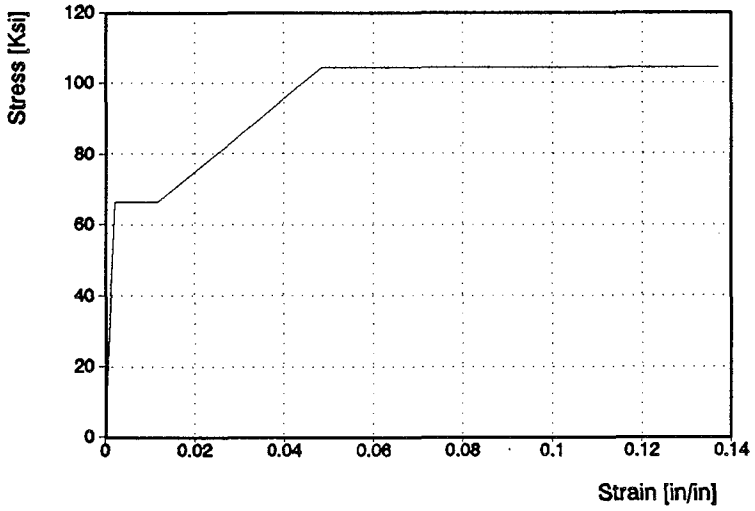

Figure 3.25: Typical stress-strain curve for Specimens 2c and 2d lintel transverse reinforcement.

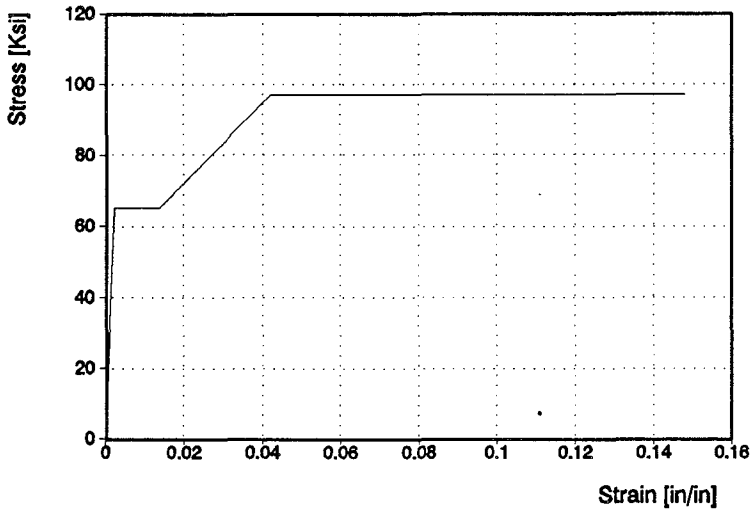

Figure 3.26: Typical stress-strain curve for Specimen 2d reinforcement.

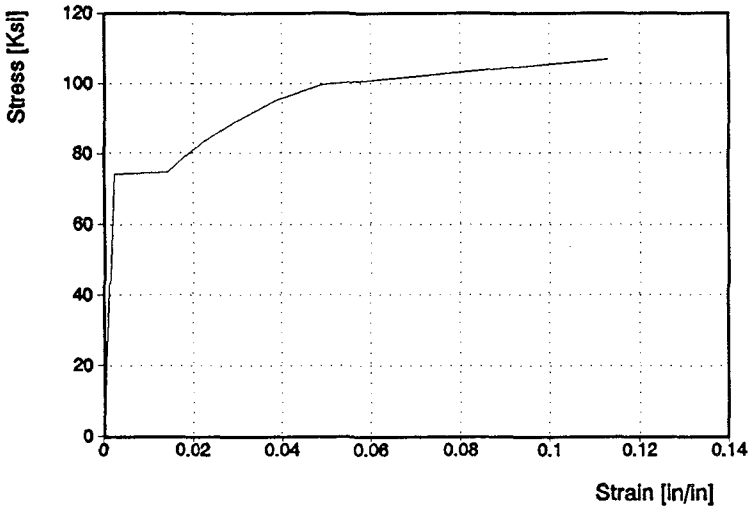

Figure 3.27: Typical stress-strain curve for Specimens 1a and 1b #3 reinforcement.

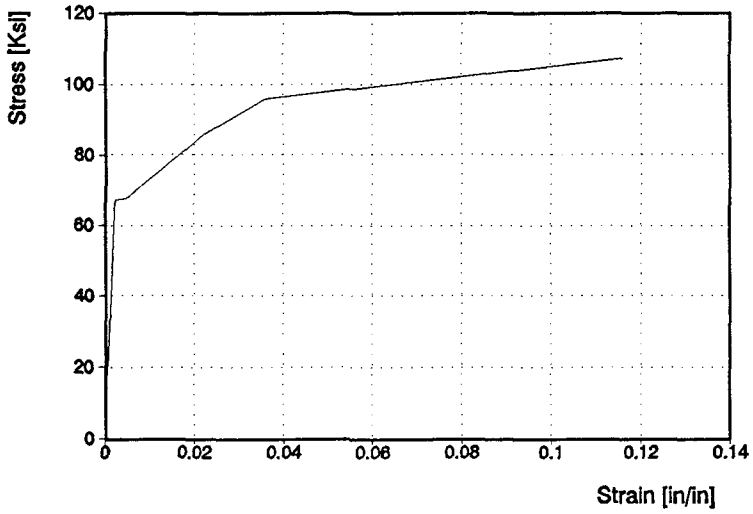

Figure 3.28: Typical stress-strain curves for Specimens 1a and 1b #4 reinforcement.

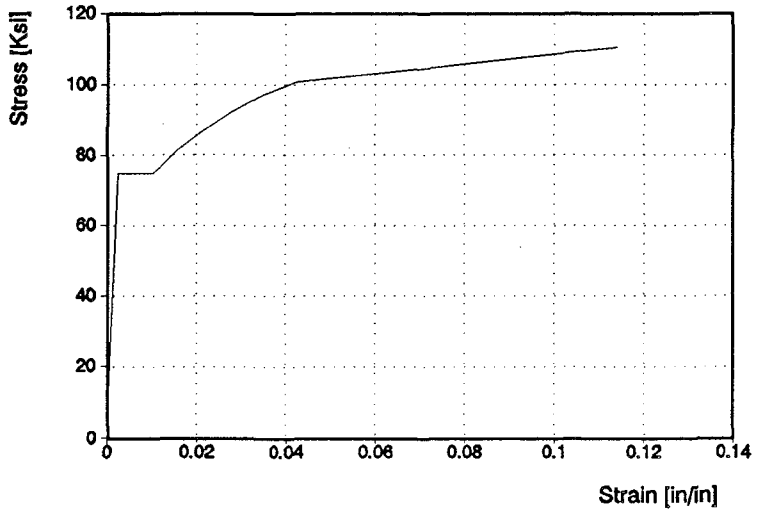

Figure 3.29: Typical stress-strain curve for Specimens 1a and 1b #5 reinforcement.

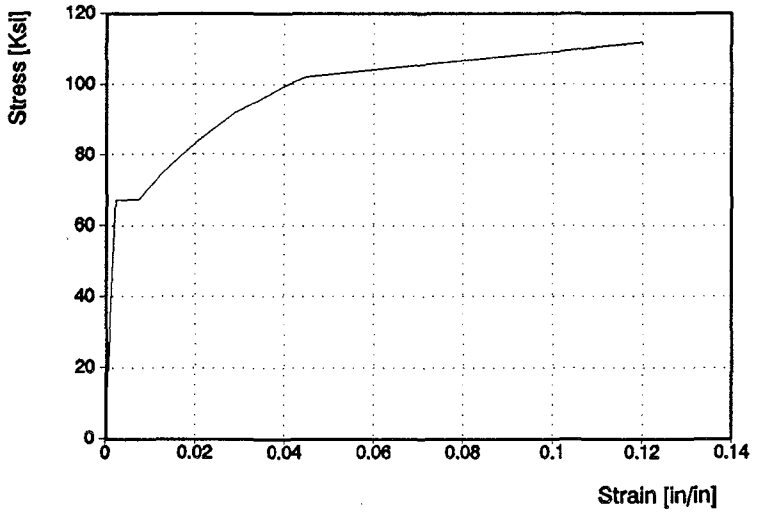

Figure 3.30: Typical stress-strain curve for Specimens 1a and 1b #6 reinforcement.

4. TEST EQUIPMENT AND PROCEDURE

This chapter contains a description of the test setup, the instrumentation of the specimens, the loading and data acquisition systems, and the testing procedure.

4.1 Test Setup

The test setup, shown in Figures 4.1 to 4.3, was intended to simulate the conditions imposed on the specimens as part of a building under earthquake excitations. The overall test setup consisted of the following elements:

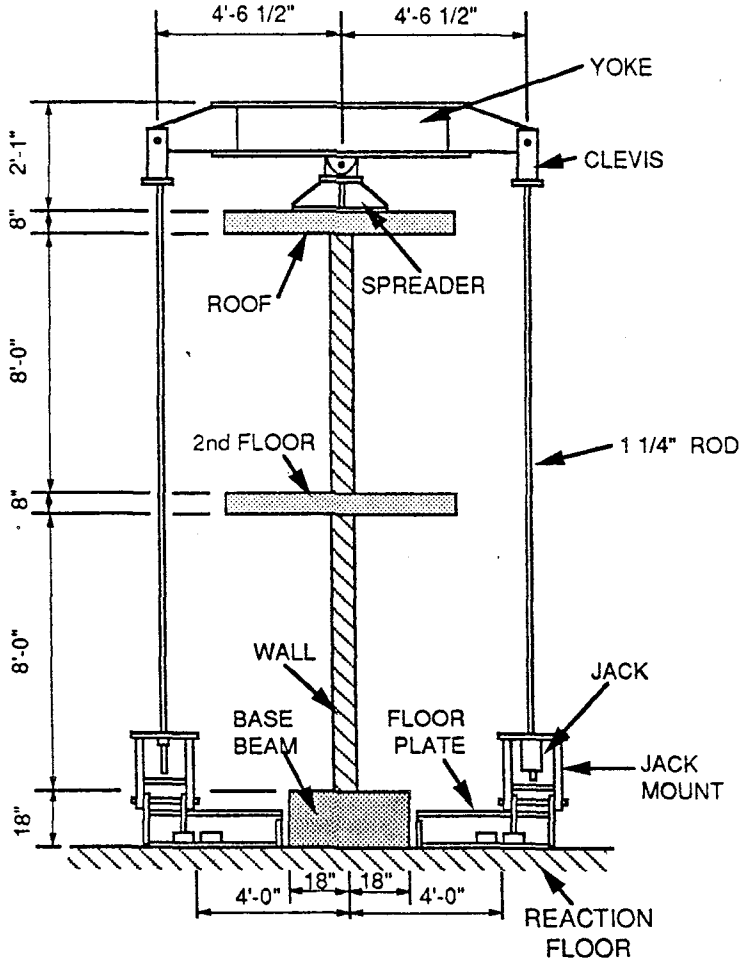

Figure 4.1 Vertical load system.

1) reaction system
2) precast base beams
3) vertical loading frames

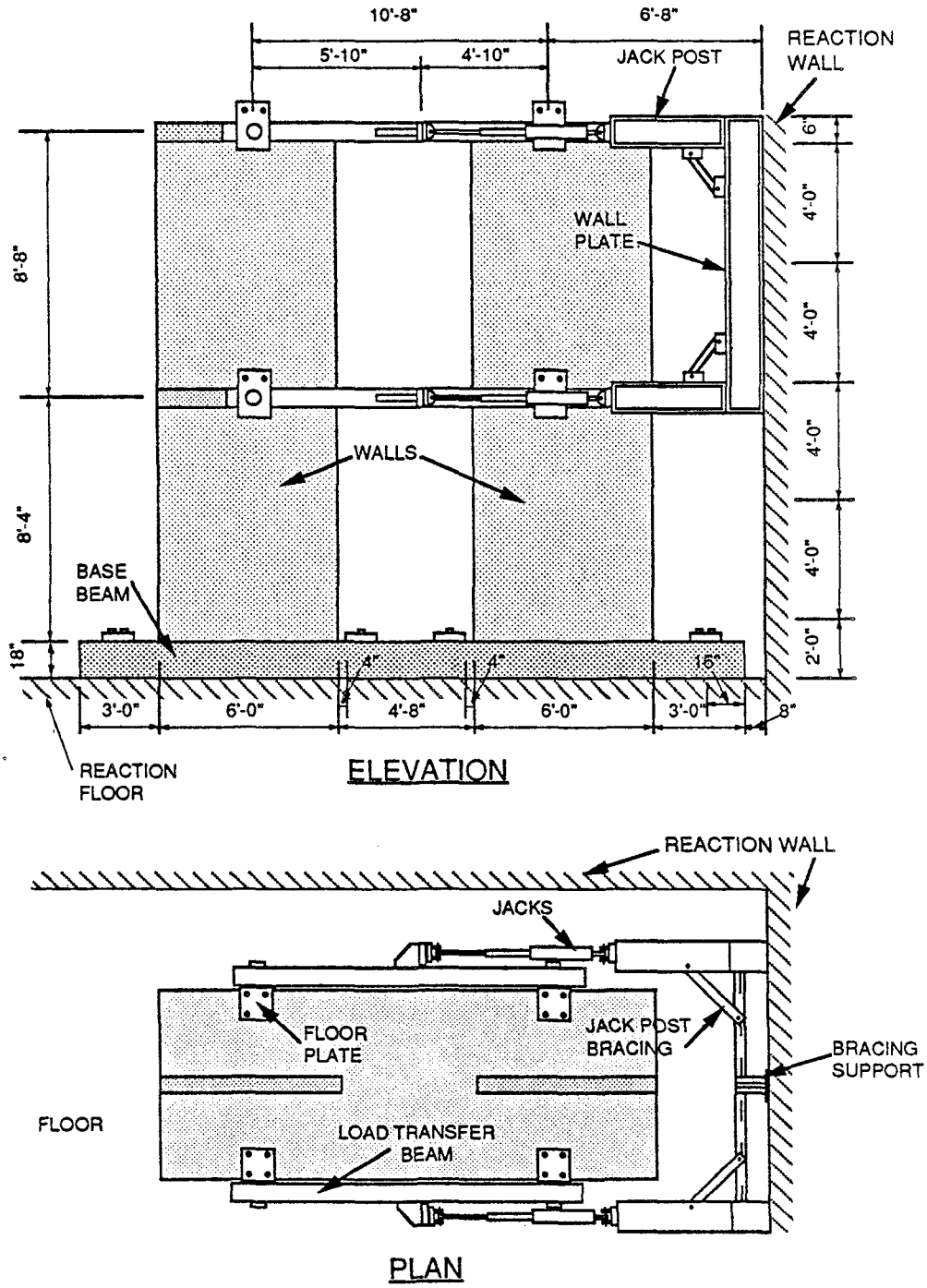

Figure 4.2 Lateral load system.

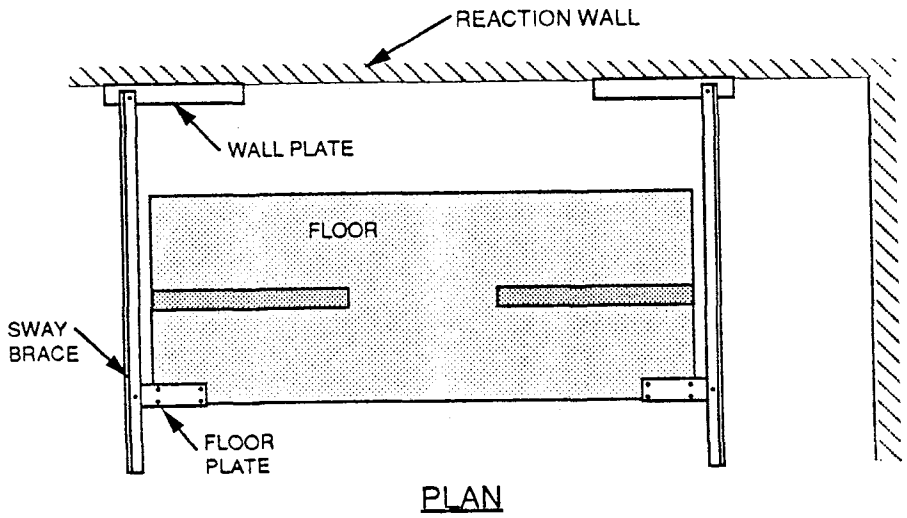

Figure 4.3 Sway bracing system.

4) lateral loading frame
5) sway bracing

To simulate the actual conditions in a building under seismic excitation in which load result from floor and roof masses, lateral loads were applied at the lateral edges of the slabs rather than directly on walls. Those loads were applied by hydraulic actuators attached to steel frames mounted on the reaction wall. Simple steel link sway bracing was attached to the outer edges of the second-floor and the roof slabs, and was anchored to the reaction wall running parallel to the specimen's in-plane centerline.

Vertical loads, when needed to represent floor and roof gravity loads transferred from the slabs to the walls in the prototype building, were applied to the top of each coupled wall or piers by hydraulic actuators attached to a steel frame mounted on the reaction floor. The elements comprising the test setup are described the following sections. A detailed description of the design of the test setup system is given in Ref. 25, and a description of the reaction system is given in Ref. 26.

Reaction System. This consisted of a massive reinforced concrete floor and two walls, 19 ft. (5790 mm) high, and joined at right angles. The floor and walls have anchor bolt locations, each with four anchor bolts, on a 4-ft. (1219 mm) square grid. Each floor anchor bolt location has an allowable vertical loading of plus or minus 200 kips (890 KN), and each wall anchor bolt location has an allowable horizontal loading of plus or minus 100 kips (445 KN) [17].

Concrete Base Beam. The concrete base beam was intended to simulate the action of a rigid foundation and provided anchorage for the vertical reinforcement of the specimens. It was connected to the testing floor using 12 prestressing rods, each consisting of a 1-1/4 in. (32 mm) diameter ASTM 193 B7 rod prestressed to 25 kips (111 KN).

Prestressing provided adequate lateral frictional resistance between the base beam and the reaction floor without allowing any slippage or shear forces in the tie-down rods.

Vertical Loading Frame. As shown in Fig. 4.1, the vertical load was applied by a steel frame located at the out-of-plane centerline of each of the two walls in the case of the coupled wall specimens, and at the out-of-plane centerlines of the two piers in the case of the perforated specimens. A spreader beam was used to distribute the load into the top slab along the in-plane centerline of each of the vertical elements. The spreader beam was attached with a pinned coupling to a yoke going across the specimen. Using a long 1-inch diameter rod, one end of the yoke was connected to an anchor plate attached to the reaction floor. Using another long 1-inch diameter rod, the other end of the yoke was connected to a hydraulic actuator mounted on an anchor plate attached to the floor. Load was controlled by an Edison servo-mechanical load maintainer. All connections between the spreader beam and the yoke, the yoke and the rods, and the rods and the anchor plates were designed as pinned to allow for up to ±6 in. (152 mm) of horizontal movement, and 1 in. (25 mm) of vertical movement of the wall during the test.

Lateral Loading Frame. As shown in Fig. 4.2, lateral loads were applied to the specimens using 4 two-way hydraulic actuators, each with a capacity of 112 kips (498 KN) and a maximum stroke of ±6 in. The stationary ends of the actuators were attached to a steel frame bolted to the reaction wall, and oriented perpendicular to the plane of the specimens. The other end of each actuator was attached to the center of a steel beam with a pinned connection at each end. The pinned connections were bolted to the outer edge of each floor slab. The purpose of the pinned connections was to allow for independent vertical, horizontal and rotational movements of each of the coupled walls during the test.

Sway Bracing. The sway bracing system, shown in Figure 4.3, was designed to control out-of-plane movement of the specimens during testing. Four simple braces connected one outer corner of each floor slab with the reaction wall running parallel to the in-plane centerline of the specimen. This system was modified to permit the out-of-plane displacements induced during the test of Specimen 1a.

4.2 Instrumentation

Lateral loads were measured using 50-kip capacity load cells placed on the actuators at each floor level, and monitored continually during testing using a X-Y plotter connected to one of the load cells.

Vertical loads were measured using a 50-kip capacity load cell placed on one of the rods, and monitored continually during testing monitored using the pressure gauge on the load maintainer.

As shown in Figs. 4.4 to 4.10, each specimen was fully instrumented to measure displacements and deformations. A brief description of the instrumentation is given in the next paragraphs.

Wall lateral displacements were measured using linear potentiometers at each end of each floor level. At the south end of the roof slab, three linear potentiometers were connected to the specimens. The first was used for the data acquisition system. The second was connected to a plotter to continuously monitor the top floor displacement during the test. The third was used for the load control phase of the test. In the case of Type 1 Specimens, all the linear potentiometers to measure wall overall lateral displacements were attached to the reaction wall. In the case of Type 2 Specimens, the linear potentiometers at the north end of the wall were attached to an steel pole bolted to the floor. In all cases, readings from those potentiometers represent absolute wall displacements.

Flexural deformations of walls and piers were measured using sets of linear potentiometers on the extreme fibers of each element.

Shearing deformations of walls and piers were measured using sets of crossed linear potentiometers along two diagonals of the element.

Linear potentiometers were used to measure relative horizontal movement between the base beam and the laboratory floor, between the walls and the base beam, between the walls and the slabs at each face of the slabs, and between the piers and the rest of the wall for Type 1 Specimens.

End rotations of coupling elements with respect to walls were measured by sets of linear potentiometers placed at each end of each coupling beam.

Strains in reinforcement were measured using electrical resistance strain gauges placed on the reinforcement at some critical zones. The concrete slab had strain gauges on longitudinal reinforcement. Specimen 2a also had strain gauges placed on the concrete surface of the slabs, as shown in Fig. 4.7.

4.3 Control and Data Acquisition Systems

Vertical loading system. The hydraulic actuators for each vertical loading frame were operated in parallel under control of an Edison load maintainer, so that as the specimen rocked under the lateral loading, the vertical load was held constant and at the same value for both actuators.

Lateral loading system. Lateral loads were applied using a hand-operated servo-controlled closed-loop system. The four hydraulic actuators were operated in parallel

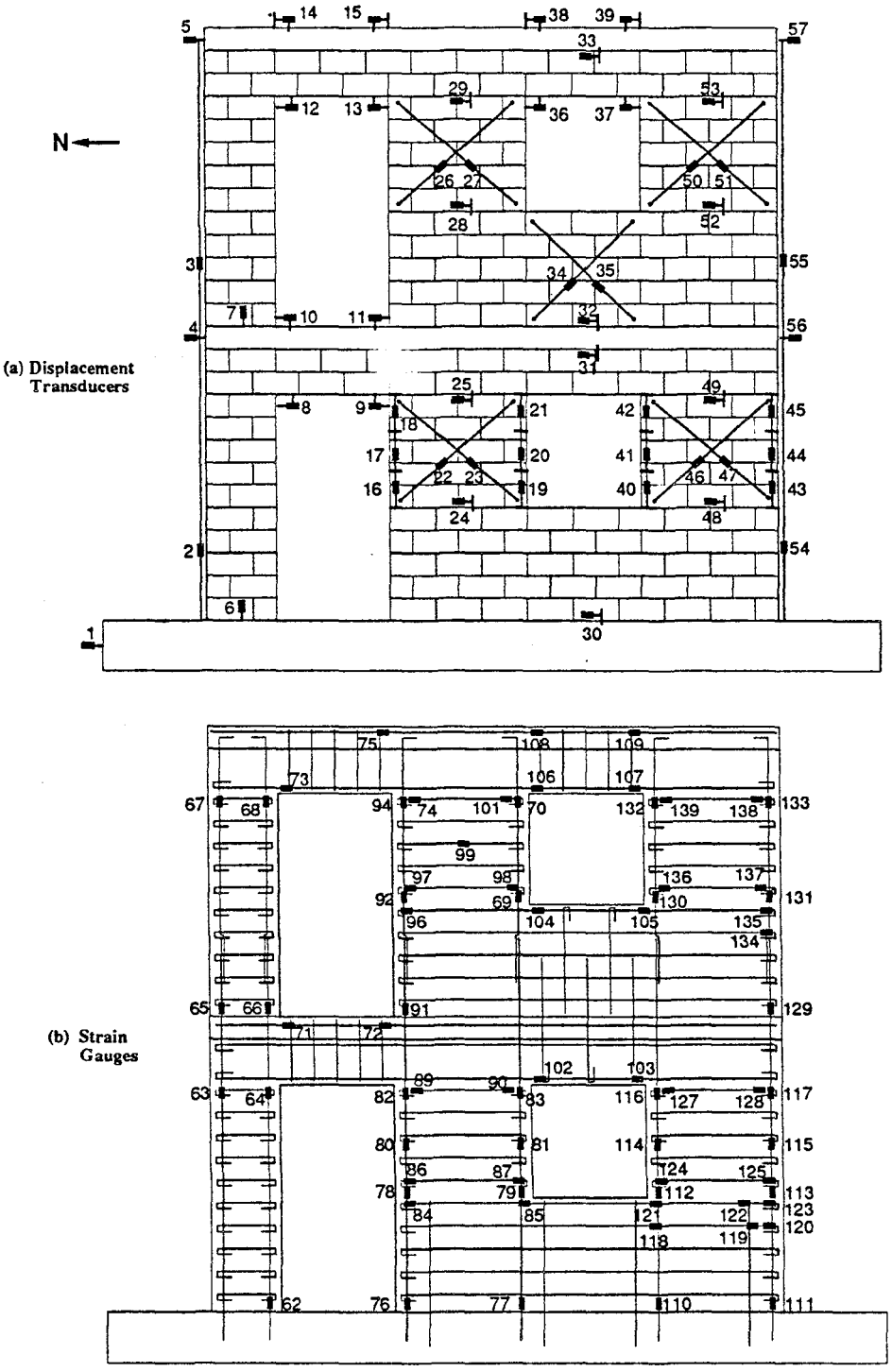

Figure 4.4 Specimen 1a instrumentation.

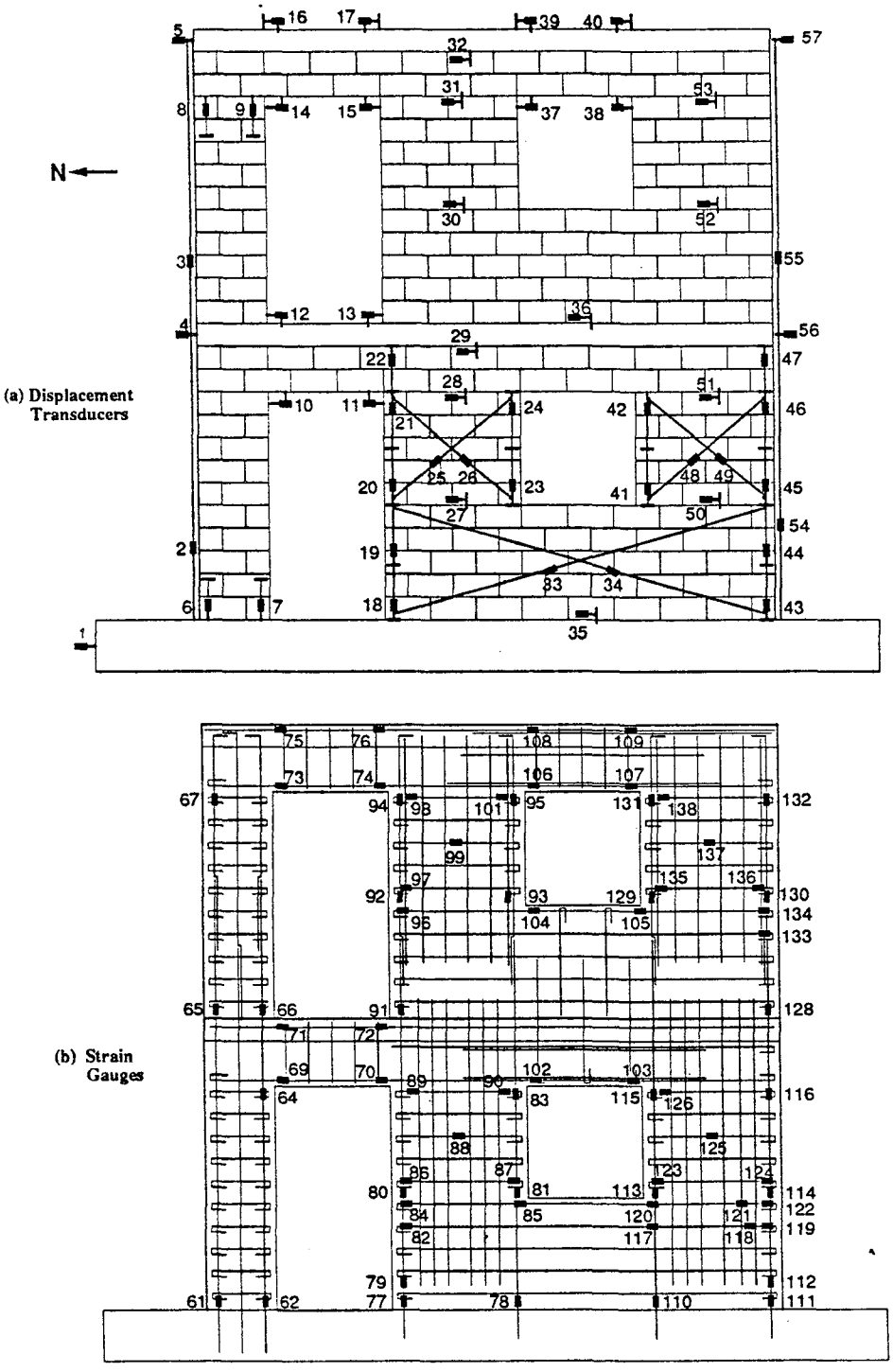

Figure 4.5 Specimen 1b instrumentation.

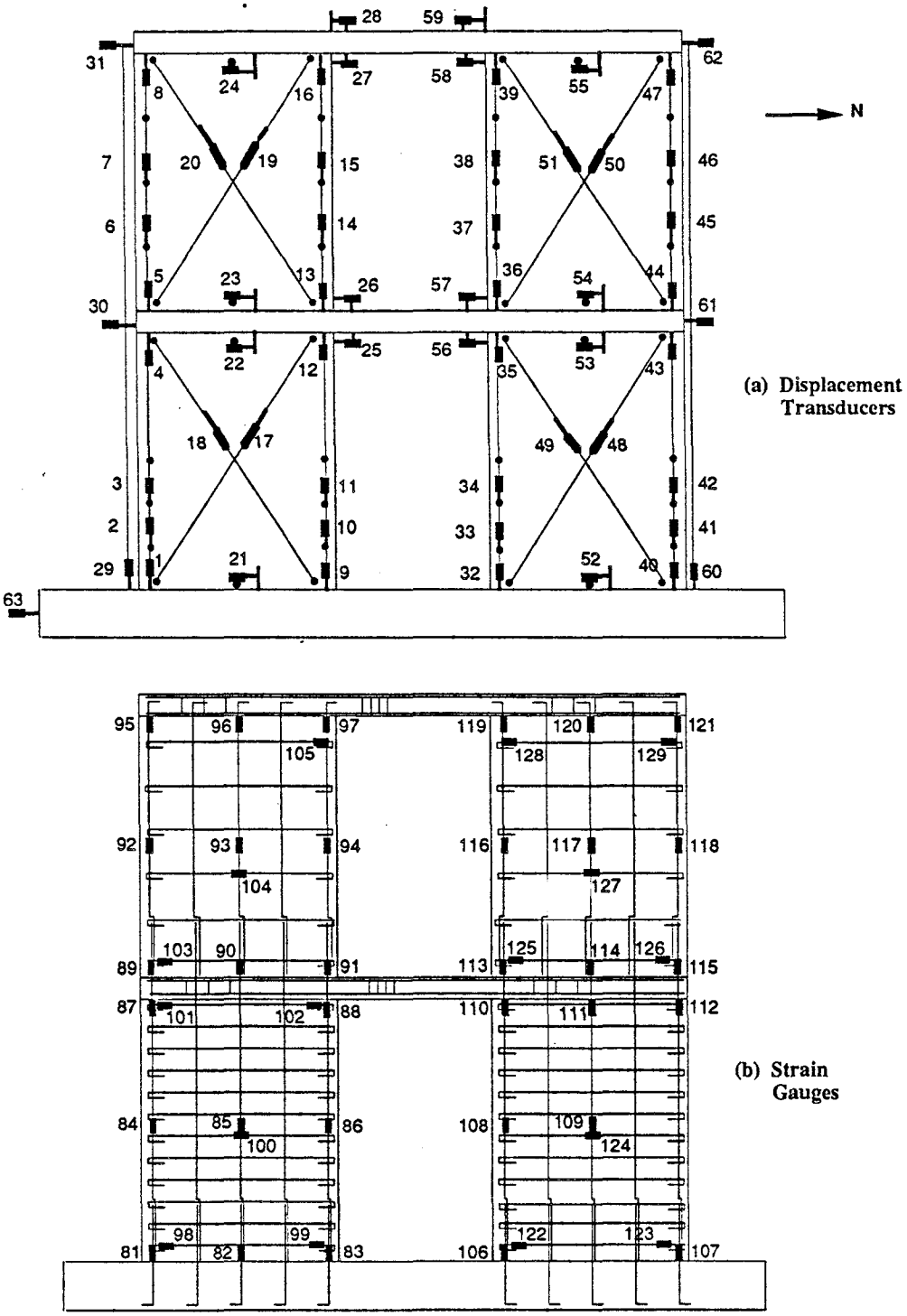

Figure 4.6 Specimen 2a instrumentation.

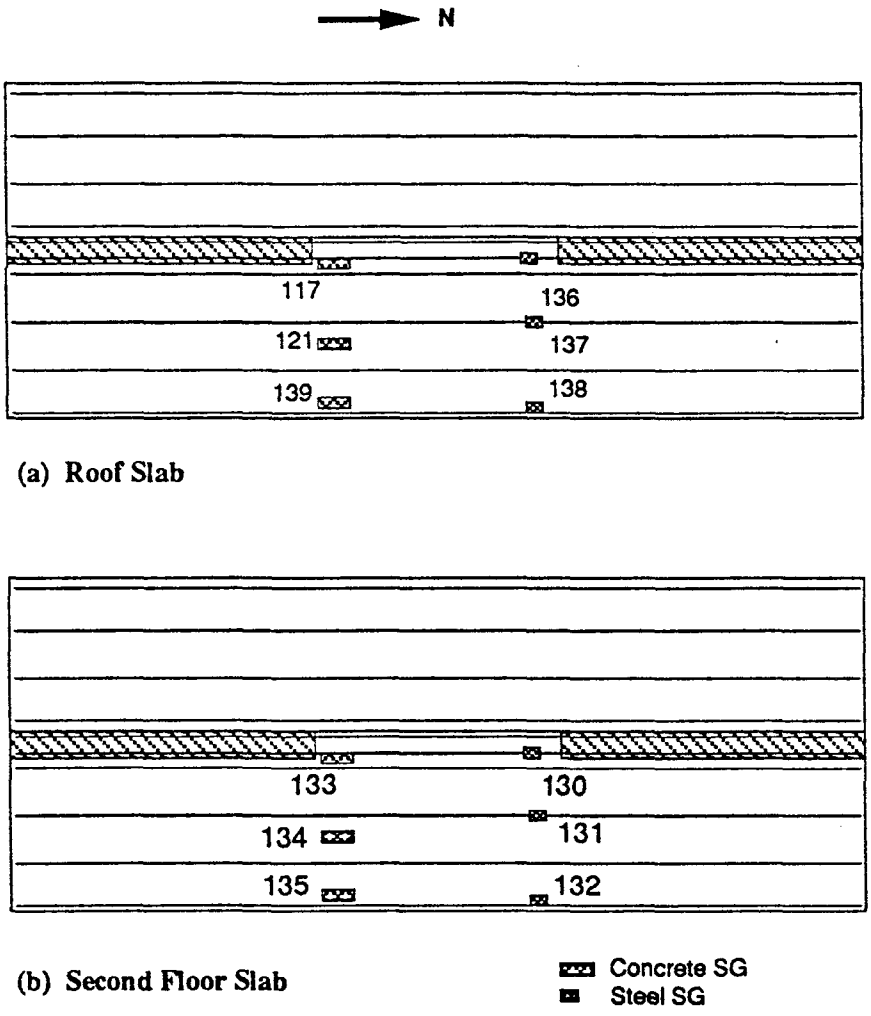

Figure 4.7 Specimen 2a floor instrumentation.

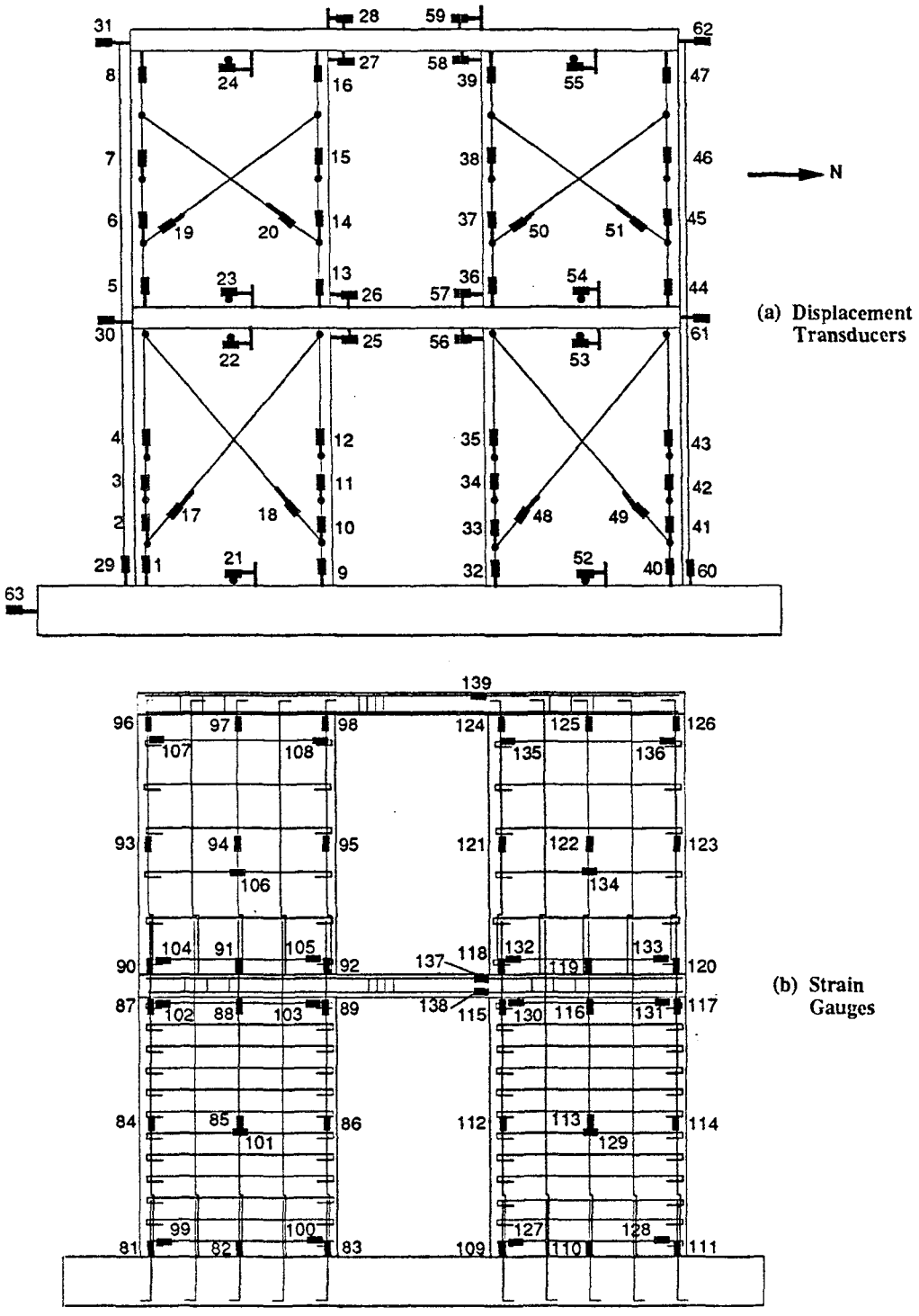

Figure 4.8 Specimen 2b instrumentation.

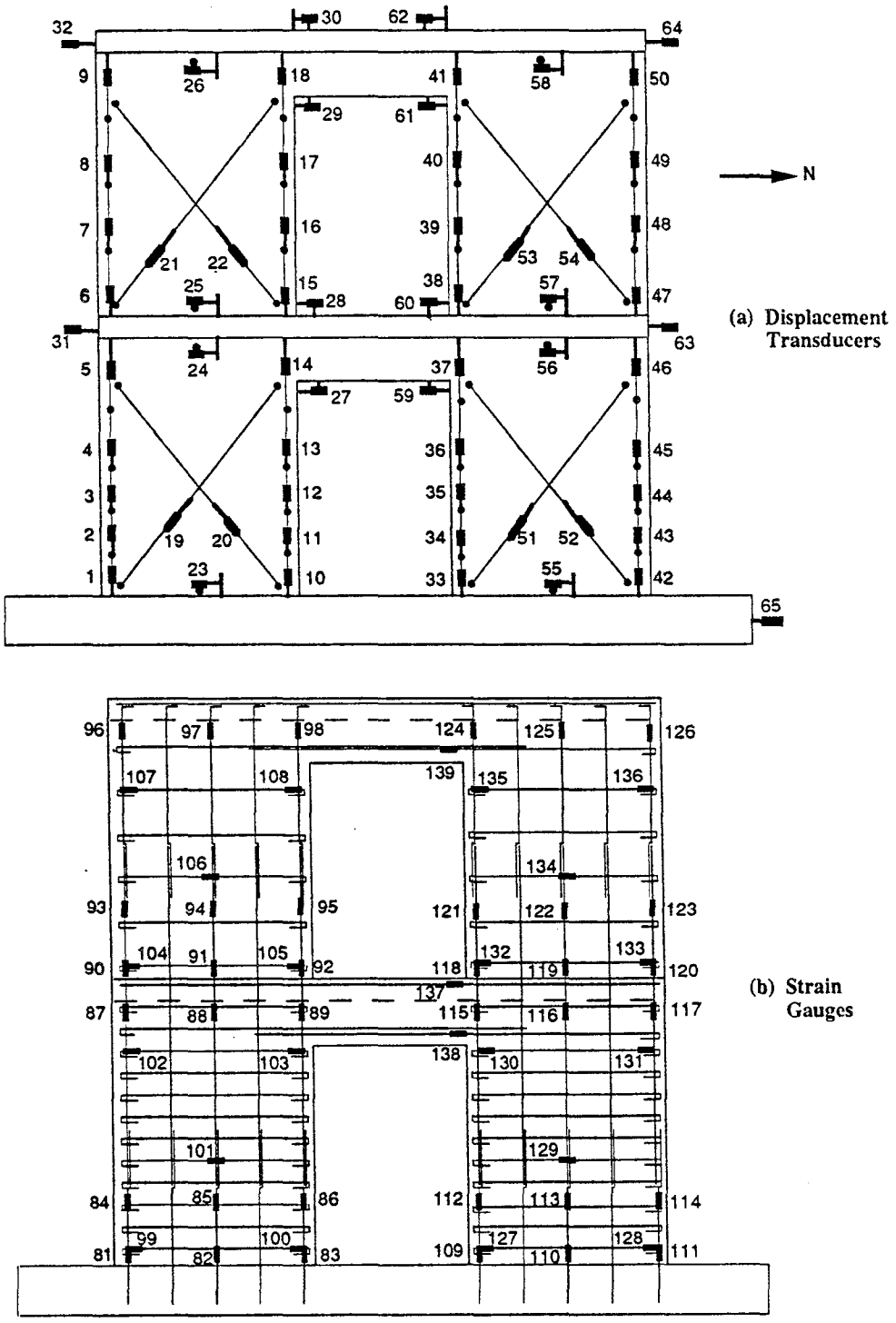

Figure 4.9 Specimen 2c instrumentation.

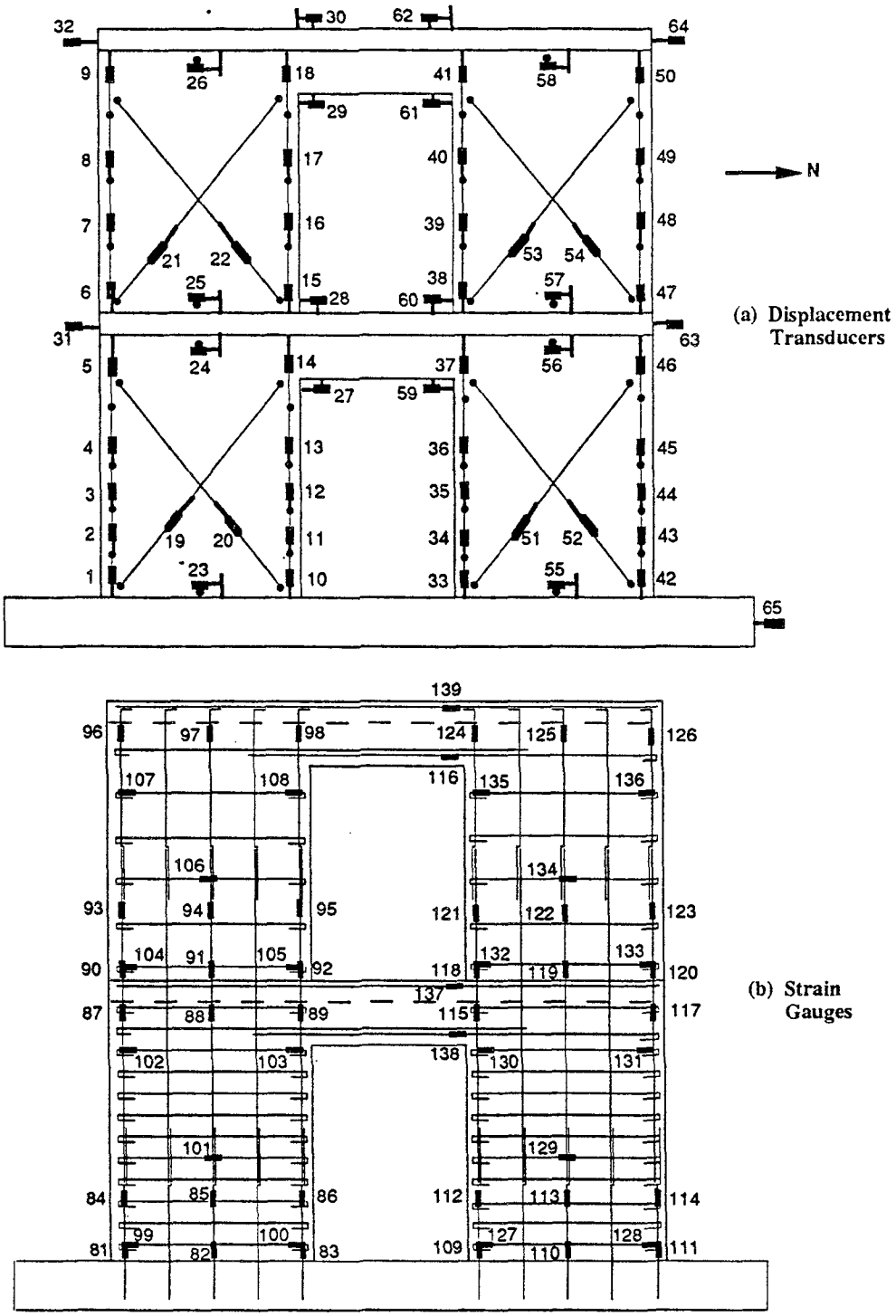

Figure 4.10 Specimen 2d instrumentation.

under control of a single servovalve and powered by an electric motor-driven pump. The flowchart of the control system is shown in Fig. 4.11. The function of each component is briefly described in the following paragraphs.

The input command was hand-generated by the system operator. The feedback signal was obtained either from a load cell attached to one of the actuators (in the case of a load-controlled test phase) or from a displacement transducer measuring the

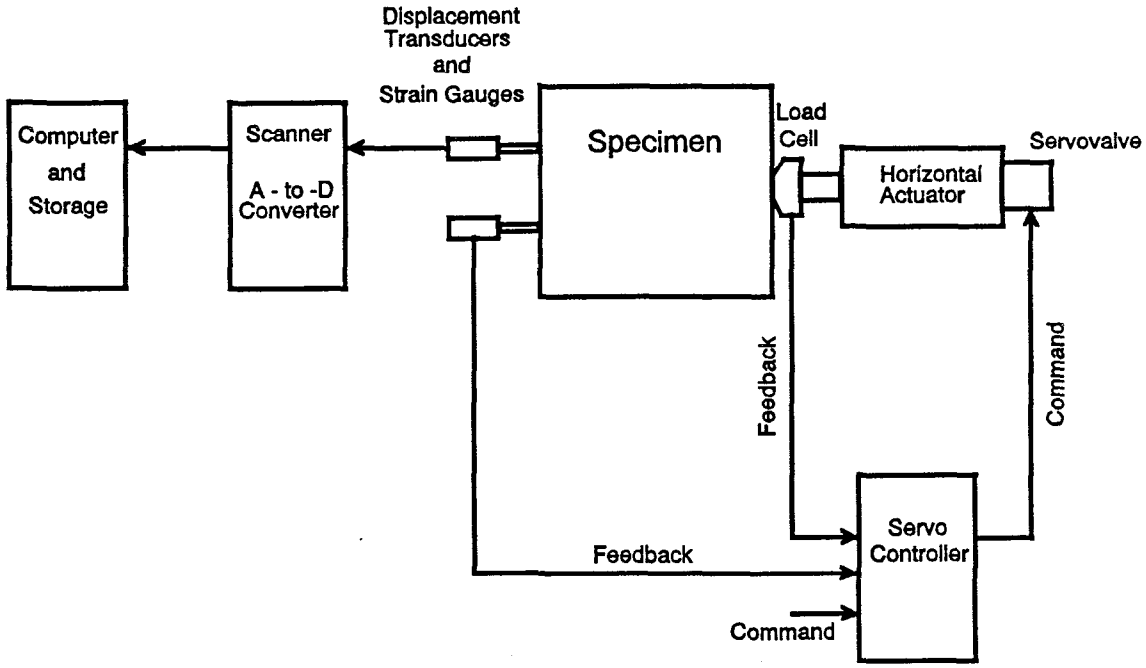

Figure 4.11 Flowchart of control and data acquisition systems.

absolute roof displacement (in the case of a displacement-controlled test phase). The feedback signal was conditioned and compared to the command signal by the Pegasus servo-controller. The calculated error is used to generate a command output from the servo-controller to the servovalve, which regulates the fluid pressure on the actuators. The loop operates to keep the error within a preset tolerance.

Data Acquisition System. The data acquisition system consisted of a 140-channel capacity model HP 3852 scanner connected to an IBM-PC type computer via a HPIB bus. The flowchart of the data acquisition system is shown in Fig. 4.11. The command signal to scan all the channels is manually sent by the operator, using the computer program that controls the data acquisition system. One by one, the voltage signals from the instrumentation channels are read, converted from analog to digital format, and sent to the computer. Data are displayed, printed if necessary, and stored in a hard disk

unit by the computer. A second computer program is used to reduce the data to a format compatible with standard microcomputer spreadsheet programs.

4.4 Testing Procedure

The loading history followed during the tests was based on the TCCMAR standard Sequential Phased Displacement (SPD) loading history [27] shown in Figure 4.12. The SPD loading history begins as a series of three reversed load cycles to the same displacement amplitude. This series is repeated increasing the maximum displacement up to a point denoted as the First Major Event (FME). The First Major Event corresponds to some significant event of the specimen behavior, such as first flexural cracking or first yielding of the reinforcement of the walls. After reaching the FME, the SPD loading history consists of a series of seven reversed load cycles. The first one is a cycle with a peak amplitude equal to that one of the FME amplified by a given factor. It is followed by three cycles of decreasing amplitude, and finally by three cycles of the same peak amplitude. This series is repeated increasing the peak value according to a prescribed history, until the end of the test. The particular history of increasing peaks for each test is discussed in the test result sections of this work.

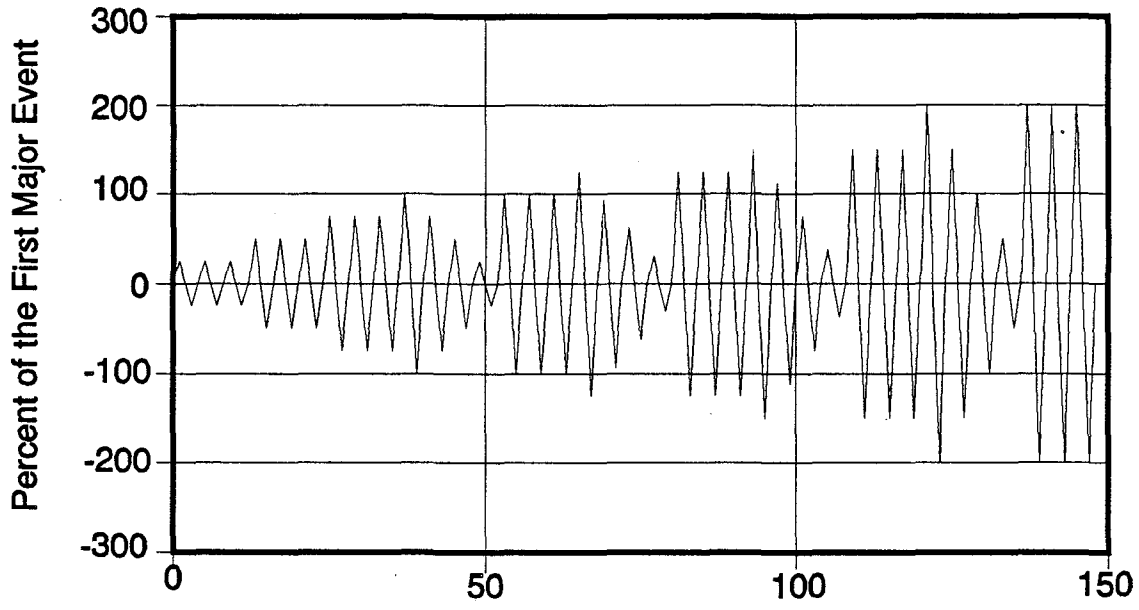

Figure 4.12 Sequential phased displacement load history.

Due to the high initial stiffness of the specimens, testing began under load control for all specimens. Base shears were keyed to the base shear corresponding to the First Major Event (FME). Once the lateral displacement at the top of the wall was large enough, the loading system was switched to displacement control. The subsequent loading history was then based on the First Major Event displacement.

Selected channels were monitored during each test. At each load point, readings from all channels were scanned, stored, and in some cases, printed. During the first and last cycles at each displacement level and at some important events, the walls were visually inspected, all cracks were marked and photographs were taken. Videotape recordings were made during the first cycle at each of the higher displacement levels for some of the tests.

Test were considered finished when the damage suffered by the specimen seemed large enough to endanger the stability of all or part of the system.

5. EXPECTED BEHAVIOR OF PERFORATED WALL SPECIMENS AS A FUNCTION OF DESIGN PHILOSOPHY

In this chapter, expected behavior and lateral load capacity calculations of the two perforated wall Type 1 specimens (Fig. 3.4) are described. The results obtained are discussed, with emphasis on the differences resulting from the two different design philosophies used for these specimens [31]. In each case, lateral load-resisting elements were provided with enough flexural and shear strength to satisfy UBC requirements. The lateral load capacity of each specimen was predicted using a plastic collapse analysis. All wall elements were then re-designed to satisfy the requirements consistent with the development of the expected collapse mechanism.

As usually intended in designing seismic resistant elements, the wall capacity was assumed to be controlled by flexural behavior. According to a capacity design philosophy, elements were provided with shear capacities larger than shear forces associated with the development of flexural strength of the system. The elements were also assumed to have enough deformation capacity to develop a collapse mechanism with no deterioration of strength.

5.1 Design Criteria

Estimated values of the material properties were based on the results of previous tests in the same project [13,32]. The properties of the Grade 60 reinforcing steel used in these calculation are: yielding f_y = 72 Ksi; modulus of elasticity E_s = 29,000 Ksi; tensile capacity f_u = 114 Ksi; and ultimate strain ϵ_u = 12%. A masonry compressive strength f'_m = 2000 psi was used, and concrete compressive strength was f'_c = 4000 psi. The stress-strain behavior of the masonry and concrete was modeled using the curve given by Kent and Park for unconfined concrete [33].

To use consistent criteria throughout the project, Type 1 Specimens were designed for gravity and lateral loads as specified in the 1985 UBC [34], acting on the wall as part of the prototype building [35]. A wall density of 121 pcf was used. The floor dead and live loads were 107 and 43 psf respectively. The tributary width of the wall in the prototype building was taken as 20 ft. The resulting base shear acting on the wall was 15.6 Kips. The actual specimens are loaded vertically by constant loads representing the gravity loads on the wall's tributary area.

5.2 Code Design

The code-type design was the same for both specimens. Essentially, an allowable stress design was performed on the lateral load-resisting elements under the service-level code loads. Required longitudinal reinforcement in piers was #3 jamb bars, which, when extended to the foundation, provided the required longitudinal reinforcement for the wall at its base. One #3 bar at each course was required as transverse reinforcement in these elements. A detailed description of the code design is given in Appendix A.

The final design of the walls, described in Appendix A, was completed based on the actual lateral load capacity of each specimen, computed according to its respective design philosophy.

5.3 General Expected Behavior of Specimens

Both specimens were designed to behave in an essentially flexural mode, in which most of the inelastic action is due to large flexural deformations at the end sections of critical elements. Each element was designed to resist the forces associated with the predicted lateral load capacity of the specimen. Reinforcement ratios and detailing were intended to prevent undesirable modes of failure such as diagonal tension, diagonal compression, sliding shear, anchorage failure, and buckling of compression reinforcement.

The lateral load capacity of each specimen was expected to be defined by a predominantly flexural collapse mechanism associated with the development of plastic hinging regions at the ends of some elements, with the position of the plastic hinges depending on the elements' relative flexural capacity. The expected collapse mechanism configuration depended on the design philosophy adopted. A plastic analysis was performed on the flexural collapse mechanism for each wall. In performing the plastic collapse analysis, all elements were assumed to have enough deformation capacity to develop the collapse mechanism with no strength deterioration. Assuming that the actual element strength could not exceed the values used, and because the assumed hinge configuration might not be critical, each calculated collapse load constituted an upper bound to the true solution [36]. Both cases are discussed in detail in later sections.

Since, as previously mentioned, a predominantly flexural type of lateral load resisting behavior was desired for both specimens, it was necessary to develop a model capable of describing the flexural behavior of the elements' sections. It has been widely recognized that the flexural behavior of lightly reinforced, fully grouted concrete masonry elements is well described by the theory developed for reinforced concrete members [1,22,37]. The wall specimens of this study were analyzed using the general methodology developed for reinforced concrete sections under eccentric axial load, which is based on the plane-section assumption.

Because of good agreement with results of tests performed on pier specimens similar to those analyzed here [38], it was decided to use the shear strength model proposed by Blondet et al. [20]. In that model, the cracking strength v_{cr0} of the masonry in the absence of axial stresses is:

$$v_{cr0} = (3.5 - 1.75 M/Vd)\sqrt{f'_m} \qquad for \qquad M/Vd \le 1$$
$$v_{cr0} = 1.75\sqrt{f'_m} \qquad for \qquad M/Vd > 1 \tag{5.1}$$

The influence of axial compressive stress f_a is included based on a principal stress criterion:

$$v_{cr} = \sqrt{v_{cr0}^2 + \frac{v_{cr0} f_a}{1.5}} \tag{5.2}$$

The shear strength v_n is taken as the sum of the contributions of the masonry, v_{cr}, and the transverse reinforcement, $\frac{1}{2}v_s$. The latter is calculated assuming that only 1/2 of the steel is effective in resisting shear. If ρ_h is the transverse reinforcement ratio, the shear strength will be:

$$v_n = v_{cr} + \frac{1}{2}v_s = v_{cr} + \frac{1}{2}\rho_h f_y \tag{5.3}$$

Because the end sections of the flexural elements may be subjected to large rotations, wide cracks will probably develop there. It is necessary to check the interface shear transfer capacity at these sections. The resisting mechanism is provided by aggregate interlock and by dowel action. Reinforcement normal to the sliding plane produces clamping force necessary to develop aggregate interlock action and provides dowel action. The interface shear capacity V_f is usually computed using traditional concepts of shear friction:

$$V_f = \mu(N + A_s f_y) \tag{5.4}$$

where μ is the friction coefficient, A_s is the distributed reinforcement normal to the sliding plane, and N is the net axial load acting on the wall. Previous experimental results obtained in the same project [13,32] showed that the coefficient of friction could be taken equal to one.

5.4 Behavior of "Pier-Based" Specimen 1a

5.4.1 Expected Behavior of Pier-Based Specimens. In a pier-based design, inelastic deformation predominantly occurs in a column-type sidesway mechanism at one or more story levels. In each story mechanism, plastic hinges form at the top and bottom of all piers, as shown schematically in Fig. 5.1. The pier elements are intended to be constrained to ductile flexural failure modes by the use of a capacity design approach for shear.

The specimen designed according to the pier-based design philosophy was expected to experience most of its inelastic deformation in the lower story. As a result, a high deformation demand was expected in the first story piers. In addition, in a pier-based design, the energy dissipation occurs through large inelastic deformations of the vertical load bearing elements. This behavior can conceivably lead to undesirable damage and out-of-plane instability of the pier regions.

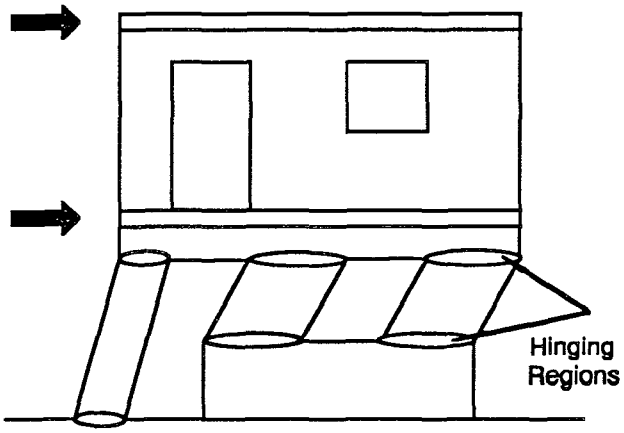

Figure 5.1: Collapse mechanism "Pier-based" design philosophy (Specimen 1a).

The force distribution among the different lateral load resisting elements depends on the stage of the loading process. In the case of Specimen 1a, analysis based on the uncracked elastic properties of the elements indicated that 48% of the base shear would be taken by each pier, and 2% taken by the column [35]. After cracking, the relative lateral stiffness of the piers and column depends on their axial load levels, which in turn depend on their gravity load and overturning force.

The design of Specimen 1a was governed by the requirement to force ductile flexural behavior in the piers. Because of their low height to length ratio, high shear forces are associated with the development of their flexural capacity. As a result, it was necessary to minimize the flexural reinforcement of the piers using only the #3 jamb bars required by code design.

Because of their low flexural reinforcement ratio, it was expected that the deformation capacity of the piers would be limited by possible fracture of the jamb bars. On the other hand, heavy transverse reinforcement was expected to prevent diagonal tension failure of the piers. However, there was a strong potential for failure by diagonal compression.

Shear transfer at the pier-wall connection at the base of the wall was also a significant factor in the behavior of this specimen. As shown in Fig. 5.2, wide flexural cracks were expected to develop at the base of the pier. The pier shear V_p must be transmitted to the base of the wall through the compressed toe of the pier and must be resisted by the "drag" bars crossing a potential crack under the base of the pier. Design of this reinforcement was governed by the conditions at the critical compression toe of the downwind pier. For design purposes, that crack was conservatively assumed to be inclined at 45°.

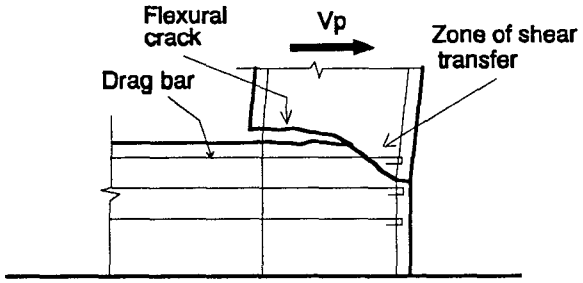

Figure 5.2: Shear transfer mechanism between pier and wall at base.

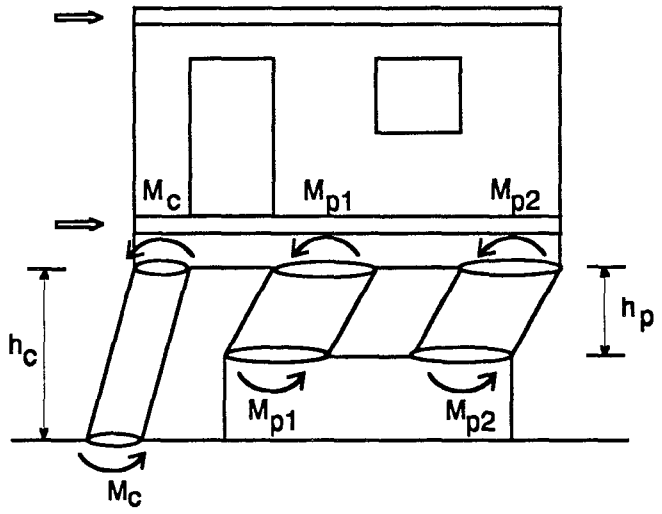

Figure 5.3: Forces acting on the collapse mechanism of the "pier-based" Specimen 1a.

5.4.2 Lateral Load Capacity of Pier-Based Specimen 1a. By either applying the principle of virtual displacements, or by imposing equilibrium conditions on the collapse mechanism when equal lateral loads are applied at each floor (Fig. 5.3), the following expression is derived for the lateral load capacity V_b of the specimen:

$$V_b = \frac{2M_c}{h_c} + \frac{2}{h_p}(M_{p1} + M_{p2}) \qquad (5.5)$$

where

M_c = Flexural capacity of column
M_{p1}, M_{p2} = Flexural capacity of center and extreme pier respectively
h_c = Clear height of column = 80 in
h_p = Clear height of piers = 40 in

Note that this expression for the lateral load capacity of the specimen is valid for load acting in either direction. However, since flexural capacities of the piers and column depend on the axial force level on each element, which in turn depends on the gravity loads and overturning forces in the wall, this expression cannot be applied directly to obtain the lateral load capacity of the specimen. As explained in the next sections, a satisfactory upper-bound solution must satisfy global equilibrium of forces, and the flexural and shear capacities of the elements must not be exceeded.

In addition to its own weight, the specimen was subjected to vertical forces intended to simulate gravity loads on the floors of the prototype building. Those forces were applied on the roof level at the center of each pier. The total weight of the specimen and the test setup was calculated as 28.4 kips. The vertical load applied on each pier at the roof was 40.8 kips. According to an uncracked elastic analysis, the axial forces produced by these loads on the column, center pier, and extreme pier at the first story were respectively:

N_{gc} = 10.3 Kips (Column)
N_{g1} = 49.6 Kips (Center pier)
N_{g2} = 50.1 Kips (Extreme pier)

To keep the specimen's lateral load capacity within the limits imposed by the test setup, it was decided to keep #3 jamb bars as the only flexural reinforcement in the piers and column, as determined from the code design (Appendix A). Both first story piers were provided with 1 #4 plus 1 #3 bars at each course as transverse reinforcement.

Moment-axial force interaction diagrams for piers and column were obtained using the RCCOLA computer program [39], using a maximum compressive masonry strain of 0.003. For axial load values below the balance point, the interaction diagrams could be approximated by:

$$M = 13.138N + 527.24 \qquad \textit{(Pier in compression)} \qquad (5.6)$$

$$M = 6.71N + 219.19 \qquad \textit{(Column in compression)} \qquad (5.7)$$

$$M = 219.19 - 8.73N \qquad \textit{(Column in tension)} \qquad (5.8)$$

The shear-axial force interaction diagram for piers, given by Eq. (5.9), was obtained using Eqs. (5.1) to (5.3), with:

M/Vd = 0.46
v_{cr0} = $(3.5 - 1.75 \times 0.46)\sqrt{2000} = 2.69\sqrt{2000} = 120$ psi (Eq. 5.1)
f_a = $N_p/(47.63 \times 5.63)$
v_s = $\rho_h f_y = 0.69\% \times 72000 = 497$ psi
Shear capacity: $V_n = (v_{cr} + \frac{1}{2}v_s)\, bd$, or:

$$V_n = 60.69 + 29.32\sqrt{1 + 0.0207N} \tag{5.9}$$

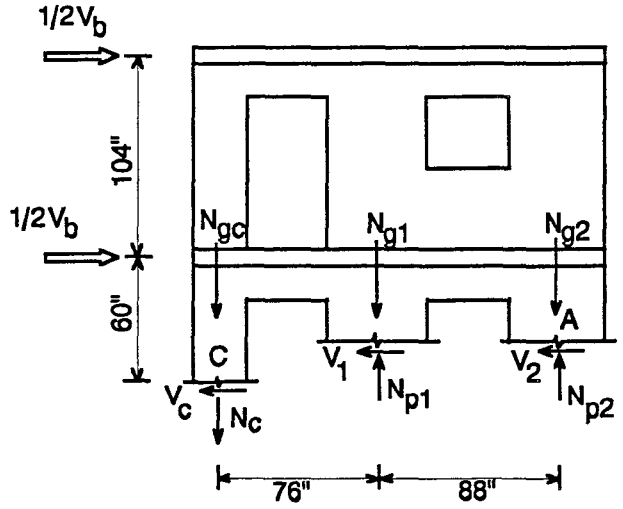

Figure 5.4: Forces acting on Specimen 1a under southward lateral loads.

Lateral Load Capacity: Load to the Right (Southward)

Forces acting on the specimen under southward lateral loads are shown in Fig. 5.4. Equations (5.10) to (5.12) describe the specimen's equilibrium under vertical forces, lateral forces, and moments about point A (center of extreme pier), respectively:

$$N_{p1} + N_{p2} - N_c = 110 \tag{5.10}$$

$$V_1 + V_2 + V_c = V_b \tag{5.11}$$

$$92V_b + 88N_{p1} + 20V_c - 164N_c = 6054 \qquad (5.12)$$

Note that if Eq. (5.11) is expressed in terms of end moments on elements assumed to be in double curvature, the result is Eq. (5.5).

The system of Equations (5.10) to (5.12) contains 7 unknowns. If the elements are assumed to be at their flexural capacity, Eqs. (5.6) to (5.8) and the assumption of double curvature permit axial forces to be expressed in terms of shear forces. Eq. (5.9) permits the same for elements acting at their shear capacity. Since 4 unknowns still remained in the system, it was necessary to make an additional assumption with respect to the distribution of forces in the specimen. After several trials, it was found that if the center pier was assumed to experience an axial force equal to its tensile axial capacity, a solution could be obtained under which the column reached its flexural capacity and the extreme pier reached its shear capacity. In this case:

N_{p1} = -25.1 Kips (tensile axial capacity)
M_{p1} = 0
V_1 = 0
M_c = $219.19 - 8.73N_c$ (from Eq. 5.8)
V_c = $2M_c/h_c$ (column in double curvature)
V_2 = $60.69 + (1 + 0.0207N_{p2})^{1/2}$ (from Eq. 5.9)

Replacing these expressions in Eqs. (5.10) to (5.12), the lateral load capacity V_b of Specimen 1a when loaded to the South was calculated:

$$V_b = 122.1 \text{ Kips}$$

This value is an upper bound to the actual lateral load capacity.

The rest of the forces on the elements were:

N_c = 18.3 Kips (tensile force) < Tensile capacity = 25.1 Kips
M_c = 59.4 Kip-in
V_c = 1.5 Kips
V_2 = 120.6 Kips (shear capacity)
N_{p2} = 153.4 Kips (compressive force)
M_{p2} = $20V_2$ = 2413 K-in < Flexural capacity = 2543 K-in

In summary, Specimen 1a was expected to reach its southward lateral load capacity when the extreme pier developed its shear capacity, the center pier developed its axial tensile capacity, and the column developed its flexural capacity.

Lateral Load Capacity: Load to the Left (Northward)

Forces acting on the specimen under northward lateral loads are shown in Fig. 5.5. Equations (5.13) to (5.15) describe the specimen's equilibrium under vertical forces, lateral forces, and moments about point C (center of column), respectively:

$$N_{p1} - N_{p2} + N_c = 110 \tag{5.13}$$

$$V_1 + V_2 + V_c = V_b \tag{5.14}$$

$$112V_b + 76N_{p1} - 164N_{p2} - 20V_1 - 20V_2 = 11986 \tag{5.15}$$

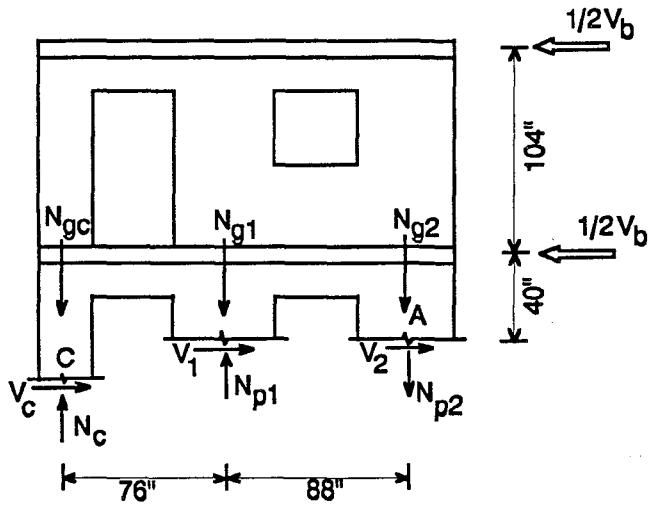

Figure 5.5: Forces acting on Specimen 1a under northward lateral loads.

The system of equations was solved in the same way previously described, combining Eqs. (5.13) to (5.15) with Eqs. (5.6) to (5.9). In this case, it was assumed that the lateral pier reached its axial tensile capacity and the center pier and the column reached their flexural capacities:

N_{p2} = 25.1 Kips (tensile axial capacity)
M_{p2} = 0
V_2 = 0
M_c = $219.19 + 6.71N_c$ (from Eq. 5.7)
V_c = $2M_c/h_c$ (column in double curvature)
M_{p1} = $13.138N_{p1} + 527.24$ (from Eq. 5.6)

V_1 = $2M_{p1}/h_p$ (pier in double curvature)

Replacing these expressions in Eqs. (5.13) to (5.15), the lateral load capacity V_b of Specimen 1a when loaded to the North was calculated:

V_b = 98.3 Kips

This value is an upper bound to the actual lateral load capacity.

The rest of the forces on the elements were:

M_c = 524.0 Kip-in (flexural capacity)
N_c = 45.4 Kips (compressive force)
V_c = 13.1 Kips
M_{p1} = 1704.0 Kip-in (flexural capacity)
V_1 = 85.2 Kips < Shear capacity = 110.2 Kips
N_{p1} = 89.6 Kip (compressive force)

In summary, Specimen 1a was expected to reach its northward lateral load capacity when the extreme pier developed its axial tensile capacity, and the center pier and the column developed their flexural capacities.

5.5 Behavior of "Coupled Wall-Based" Specimen 1b

5.5.1 Expected Behavior of Coupled Wall-Based Specimens. In a coupled wall-based design, inelastic deformation occurs in a beam-type sidesway mechanism in which plastic hinges form at the base of the coupled walls and at the ends of coupling elements, as shown schematically in Fig. 5.6. The elements are intended to be constrained to ductile flexural failure modes by the use of a capacity design approach for shear. The flexural capacity of the piers must not be exceeded under the lateral loads associated with this mechanism.

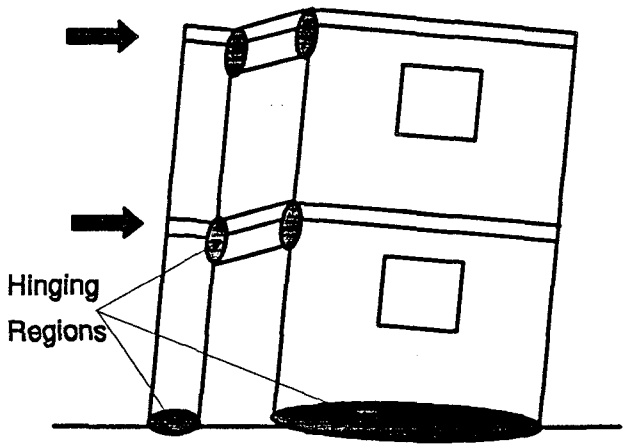

Figure 5.6: Collapse mechanism of "Coupled wall-based" design philosophy (Specimen 1b).

Since no large inelastic deformations are expected to develop in the piers, design of these elements is based on elastic behavior assuming low values of the shear-to-moment

ratio. Due to their higher axial loads, downwind piers will be stiffer (after cracking) than the center piers, and will take most of the lateral forces. These assumptions lead to high calculated moments and heavy required longitudinal reinforcement in the downwind piers. In some cases, such as the downwind pier of Specimen 1b, it was not possible to provide the element with the flexural capacity required by design, and a potential plastic hinge was expected to develop at the base of the pier. Even though this behavior would probably not affect the lateral capacity of the specimen, it showed that the piers can still suffer some potential damage.

If the masonry walls are long in plan, formation of plastic hinges at their bases produces large strains in the walls' longitudinal reinforcement. This condition has often been observed to cause fracture of longitudinal reinforcement under reversed cyclic loads, and has also been associated with in-plane and out-of-plane slip of the walls at their bases [13]. In order to avoid these undesirable effects, it was decided to use a bond breaker around the flexural reinforcement at the base of the wall of Specimen 1b, up to 8 in. above the foundation beam.

Because their low shear span to depth ratio, high shear forces are associated with the development of the flexural capacity of the lintels. Because of the physical limitations produced by the size and location of the masonry cells, it is usually not possible to provide all the required transverse reinforcement in those elements. As a result, even when the minimum flexural reinforcement is used, some shear damage can be expected to occur in the lintels. However, as found in previous tests [32], the floor-lintel system should develop a shear capacity higher than expected, and shear damage should be controlled. In the case of Specimen 1b, one #3 bar was used as top and bottom flexural reinforcement in the lintels.

Similarly to pier-based Specimen 1a, due to the high levels of shear in the piers, Specimen 1b has a strong potential for damage of the piers by diagonal compression, and for damage at the pier-wall connection by sliding-shear.

In a coupled wall-based design, energy dissipation is provided by large inelastic deformations, first of the horizontal elements (lintels), and later, of the vertical load bearing elements. This behavior permits a great part of the inelastic action to take place before the vertical load bearing elements start to suffer damage.

5.5.2 Lateral Load Capacity of Coupled Wall-Based Specimen 1b. By either applying the principle of virtual displacements, or by imposing equilibrium conditions to the collapse mechanism when the same lateral load is applied on each floor (Fig. 5.7), the following expression is derived for the lateral load capacity V_b of the specimen:

$$V_b = \frac{2}{h_2 + h_r}[M_c + M_w + N_t \ell] \qquad (5.16)$$

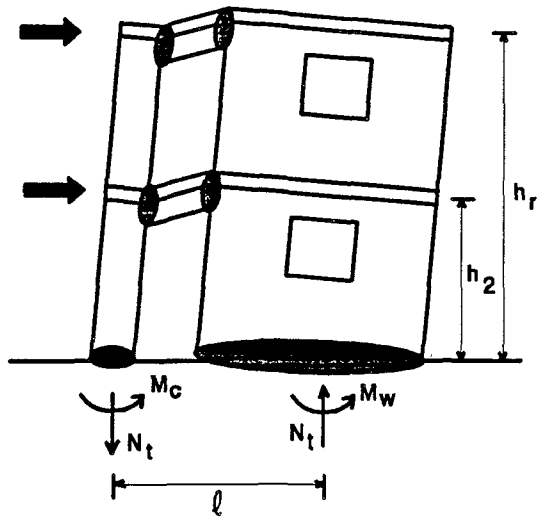

Figure 5.7: Forces acting on the collapse mechanism of the "coupled wall-based" Specimen 1b.

Where

M_c = Flexural capacity of column

M_w = Flexural capacity of wall at base

N_t = Total vertical force transmitted through the coupling elements

ℓ = Distance between plastic centroids of coupled walls = 120 in

h_2 = 2nd floor height = 100 in

h_r = Roof height = 204 in

Note that the expression for the lateral load capacity of the specimen is valid for load acting in both directions. Flexural capacities of wall at base and column depend on the axial load acting on each element, which in turn depends on the gravity load level and overturning forces in the wall.

If the vertical elements (piers and column) are provided with enough longitudinal reinforcement to prevent axial tensile failure, the occurrence and location of the plastic hinges in the coupling elements will depend on the ratio between the flexural capacity of the coupling elements and that of the vertical elements. After studying several possible combinations of relative strengths, it was concluded that plastic hinges would develop at all but one of the expected locations: a plastic hinge would develop at the column instead of at the lintel in the lintel-column connection at the roof (Fig. 5.8). The total vertical force N_t transmitted through the wall is governed by the shear forces in the lintels associated with the failure mechanism.

According to a tributary area criterium, 1/4 of the specimen's own weight was assumed to be taken by the column, and the rest of by the wall. The external vertical load, applied directly on the top of the piers, was assumed to be carried entirely by the wall. The assumed distribution differs from that one in an actual building, in which the floor gravity loads are more likely to be distributed according to the tributary areas on each vertical load bearing element.

Lateral Load Capacity: Load to the Right (Southward)

Reinforcement of the wall consisted of #3 jamb bars in the piers, passing continuously through the base beam, as determined by the code design. After several trials with different lintel/column strength ratios, it was decided to use three #5 bars to reinforce

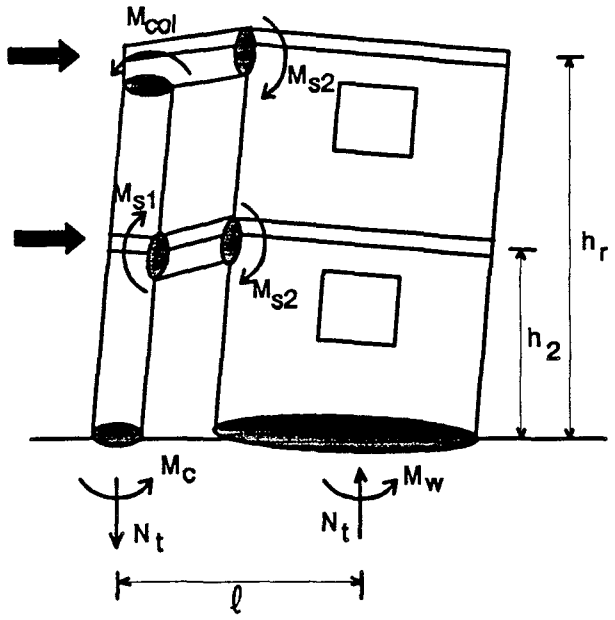

Figure 5.8: Forces acting on the expected mechanism of the "coupled wall-based" Specimen 1b.

the column, and one #3 bar as top and bottom reinforcement in the lintels. Flexural capacity of the elements was calculated as previously described. The coupling system had 6x6 No. 6 welded wire fabric in the topping, plus the lintel reinforcement. The flexural capacity of the coupling system (Fig. 5.8) was:

M_{s1} = 267 Kip-in
M_{s2} = 991 Kip-in

Under lateral load to the right, overturning produces a tensile force N_t on the column and a compressive force of the same value N_t on the wall (Fig. 5.9). These forces must be combined with gravity forces N_{gc} and N_{gw} acting on the column and wall respectively, resulting in net axial forces N_c and N_w respectively. The total vertical force N_t transmitted through the wall is governed by the shear forces at the lintels associated with the failure mechanism in Fig. 5.8. For the 2nd floor lintel this force is:

$$V_2 = (M_{s1} + M_{s2})/40 = (267 + 991)/40 = 31.5 \text{ Kips}$$

In the case of the roof lintel, the hinge was expected to occur at the column, whose flexural capacity $M_{n\,col}$ (Fig. 5.10) depends on the axial load N_{col} acting on that section. On the other hand, this axial load must be in equilibrium with the rest of the vertical loads acting on that connection (Fig. 5.10). Solving by iterations,

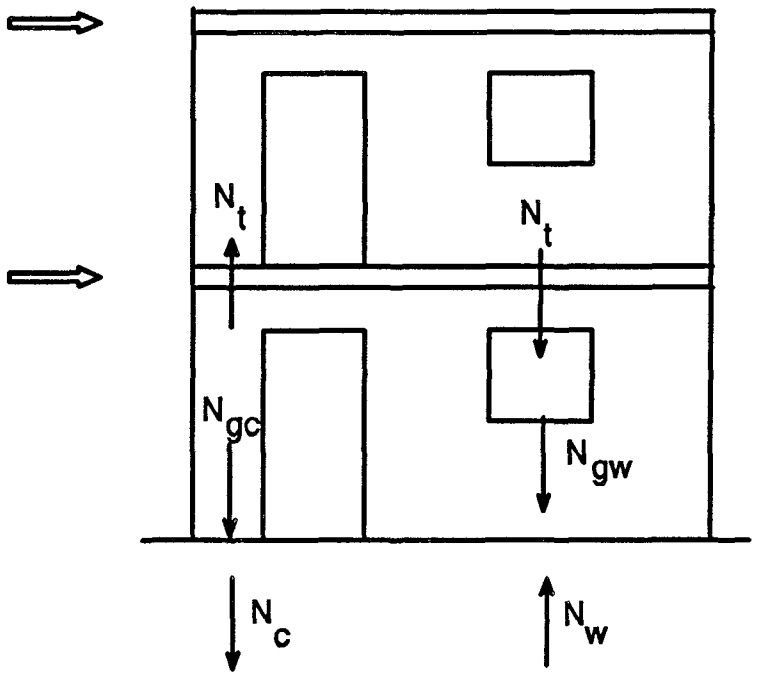

Figure 5.9: Axial forces acting on vertical elements of "coupled wall-based" Specimen 1b.

$M_{n\,col}$ = Section flexural capacity = 437 Kip-in
V_{col} = 10.9 Kips
N_{col} = 27.3 Kips (tens. force)
M_{lint} = 208 Kip-in < Section flexural capacity = M_{s1} = 267 Kip-in
V_{lint} = V_r = 30.0 Kips

The vertical force N_t transmitted through the specimen is:

$$N_t = V_r + V_2 = 30.0 + 31.5 = 61.5 \text{ Kips}$$

The net axial forces acting on the column and the wall are:

$N_c = N_t - N_{gc}$ = 61.5 - 5.4 = 56.1 Kips (Tension)
$N_w = N_t + N_{gw}$ = 61.5 + 108.1 = 169.6 Kips (Compression)

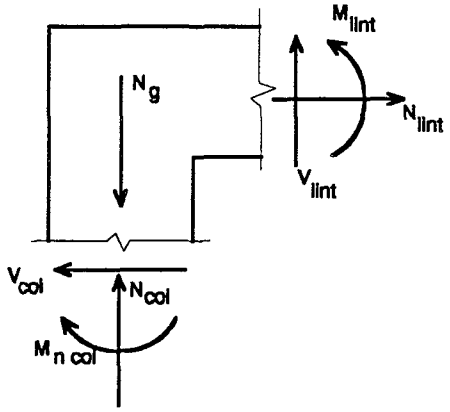

Figure 5.10: Forces acting on the roof lintel-column connection of Specimen 1b under southward loads.

For the given values of the axial loads, the flexural capacities of the column and wall sections are:

M_c = 273 Kip-in
M_w = 12,040 Kip-in

Substituting those values in Eq. 5.16, the lateral load capacity V_b of Specimen 1b when loaded to the South was calculated as:

$$V_b = 2/(100 + 204)\ [273 + 12{,}040 + 61.5 \times 120)] = 130 \text{ Kips}$$

This value is an upper bound to the actual lateral load capacity.

Lateral Load Capacity: Load to the Left (Northward)

Similarly to the previous case, in the lintel-column connection at the roof, the hinge was expected to occur at the column, whose flexural capacity $M_{n\,col}$ (Fig. 5.11) depends on the axial load N_{col} acting on that section. On the other hand, this axial load must be in equilibrium with the rest of the vertical loads acting on that connection. Solving by iterations:

$M_{n\ col}$	=	Section flexural capacity = 752 Kip-in
V_{col}	=	17.9 Kips
N_{col}	=	26.4 Kips (Comp. force)
M_{lint}	=	682 Kip-in < Section flexural capacity = M_{s2} = 991 Kip-in
V_{lint}	=	V_r = 23.7 Kips

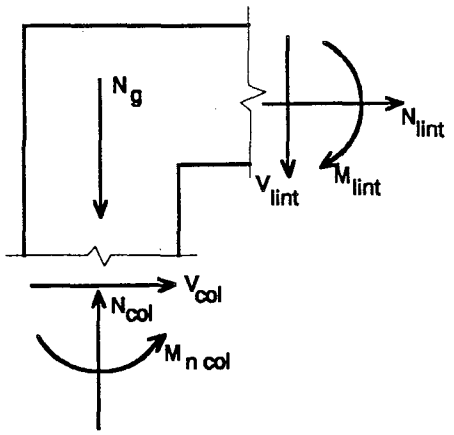

Figure 5.11: Forces acting on the roof lintel-column connection of Specimen 1b under northward loads.

The vertical force N_t transmitted through the specimen is:

$$N_t = V_r + V_2 = 23.7 + 31.5 = 55.2 \text{ Kips}$$

The net axial forces acting on the column and the wall are:

$N_c = N_t - N_{gc} = 55.2 + 5.4 = 60.6$ Kips (Comp. force)
$N_w = N_t + N_{gw} = 108.1 - 55.2 = 52.9$ Kips (Comp. force)

For the given values of the axial loads, the flexural capacities of the column and wall sections are:

M_c = 890 Kip-in
M_w = 5897 Kip-in

Substituting those values in Eq. 5.16, the lateral load capacity V_b of Specimen 1b when loaded to the North was calculated as:

$$V_b = 2/(100 + 204)\,[890 + 5897 + 55.2 \times 120)] = 88 \text{ Kips}$$

This value is an upper bound to the actual lateral load capacity.

5.6 Capacity Design

Each structural element of the walls was designed to resist the forces associated with the lateral load capacity of the specimen. Those elements expected to develop large inelastic deformations were provided with shear capacities larger than the shear forces associated with the development of their flexural strengths. A detailed description of the capacity design calculations is given in Appendix A.

As previously mentioned, the flexural behavior of reinforced concrete masonry elements was modeled using the general methodology developed for reinforced concrete sections under eccentric axial load. Flexural capacity of the masonry member sections were calculated using the RCCOLA computer program [39] considering a maximum compressive masonry strain of 0.003.

Each element was provided with enough shear capacity to resist the shearing forces associated with the development of the collapse mechanism. No explicit strength reduction coefficient were used in shear design. However, the elements were provided with shear capacities that ranged between 10% and 56% larger than the respective shear demands. The shear strength of the masonry elements, as previously described, was calculated using the model proposed by Blondet et al. [20]. It was assumed that shear strength would govern the behavior of sections where plastic hinges would not develop. The contribution of masonry to the shear strength was always considered in addition to that of the transverse reinforcement. Shear behavior of plastic hinging regions was assumed to be essentially a problem of interface shear transfer. Sections in which plastic hinges were expected to develop were checked for sufficient interface shear transfer capacity.

The resulting reinforcement and detailing for both Type 1 specimens have been completely described in Chapter 3.

5.7 Structural Details for Type 1 Specimens

5.7.1 Structural Details of Pier-Based Specimen 1a. Structural details of Specimen 1a, designed by the pier-based philosophy, are described in Chapter 3 and shown in Fig. 3.5. Reinforcing details for this specimen are characterized by light longitudinal reinforcement in piers and columns; heavy transverse reinforcement in the first story piers; and heavy horizontal reinforcement in the base of the wall and the 2nd floor horizontal element between piers.

5.7.2 Structural Details of Coupled Wall-Based Specimen 1b. Structural details of Specimen 1b, designed by the coupled wall-based philosophy, are described in Chapter 3 and shown in Fig. 3.7. Reinforcing details for this specimen are characterized by heavy longitudinal reinforcement in piers and columns; heavy transverse reinforcement in first story piers; heavy horizontal reinforcement in the base of the wall and the 2nd floor horizontal element between piers; and lighter reinforcement in the lintels.

5.8 Comparison between Expected Behavior of Each Specimen

Both specimens were intended to develop their lateral load capacity in a predominantly flexural mode. According to a capacity design philosophy, elements were provided with shear capacities larger than the shear forces associated with the development of flexural strength of the system. The elements were also assumed to have enough deformation capacity to develop a collapse mechanism with no strength deterioration.

As expected, capacity calculations for both specimens showed larger lateral capacity under load to the South. Moreover, similar lateral load capacities were obtained for both specimens: 98.3 and 122.1 kips for Specimen 1a under northward and southward loads respectively, and 88.0 and 130.0 kips for Specimen 1b under northward and southward loads respectively.

Both specimens had similar overall amounts of reinforcement. However, reinforcement was more uniformly distributed among the different elements in Specimen 1a. As previously discussed, two of the most critical aspects of the specimens' behavior and design were the shear forces in the piers, and the transfer of this shear to the wall. Even though the collapse mechanism was different for each specimen, the design shear force for the critically loaded pier was almost the same in both specimens, resulting in a similar amount of transverse reinforcement in all vertical elements. Because of the differences in required flexural capacity, longitudinal reinforcement ratios were very different in the two specimens. Piers of Specimen 1a had minimum longitudinal reinforcement, whereas those of Specimen 1b were reinforced with the maximum practical amount of steel. Conversely, lintels of Specimen 1a were heavily reinforced, while those of Specimen 1b had only minimum steel.

Because it involves large inelastic deformations of only the piers of the structure, the expected collapse mechanism for pier-based Specimen 1a is potentially undesirable. Being squat, these piers have a tendency for shear-dominated failure and consequent loss of axial capacity. Other potentially critical aspects of this design are the possible diagonal compression failure of the piers, shear transfer at the pier-wall joints, and excessive inelastic deformation demand on the piers.

In coupled wall-based Specimen 1b, energy dissipation is provided by large inelastic deformations, first of the horizontal elements (lintels), and later, of the vertical load bearing elements. This behavior permits a great part of the inelastic action to take place before the vertical load bearing elements start to suffer damage. Critical aspects in this design are the potential development of hinging regions at the vertical elements (piers and column at lintel-column joint), shear damage of lintels, and high deformation demand at the base of the wall.

The objective of the different design philosophies is to direct the behavior and damage of the structure to some desired pattern compatible with the design requirements imposed on that structure. However, as indicated in the design of both specimens, the design philosophy can sometimes only influence damage progression, but cannot control it completely. This makes damage more likely to occur in some designated locations; however, damage can still occur in some other undesirable locations.

6. TEST RESULTS FOR PERFORATED WALL SPECIMENS

6.1 General

Test results of the perforated wall Type 1 specimens are presented in this chapter. The results are described in terms of the load-displacement response of the specimens, displacements and deformations measured at some critical areas of the specimens, crack pattern and yielding maps at some selected displacement points, and a description of the significant event sequence during the test.

The load-displacement response is presented in the form of base shear-overall drift ratio curves. The overall drift ratio is defined as the in-plane displacement at the mid-depth of the roof slab divided by the height at that point above the top of the beam foundation, equal to 204 in. Displacements and deformations measured in critical zones of the specimen are presented for different stages of the test. Instrumentation channels are designated according to the description given in Section 4.3. Plots of readings obtained from displacement transducers (DT) and strain gauges (SG) have been cut at the point when each instrument stopped working properly.

The crack pattern and yielding maps progressive damage at given stages of each test. They provide a good indication of the response of the specimen: zones of concentration of stresses; load transfer patterns; and the failure mechanism.

Description of the results is based on visual observations, on the load-displacement curves obtained directly during the test, and on readings from the data acquisition system. Events during the test are described in terms of base shear and overall drift ratio at each load point, identified by its corresponding scan number. The events described include cracking in the elements, yielding of reinforcement, crushing of masonry, fracture of reinforcement, and other particular events. The nomenclature described in Fig. 6.1 has been used in describing the results of the tests.

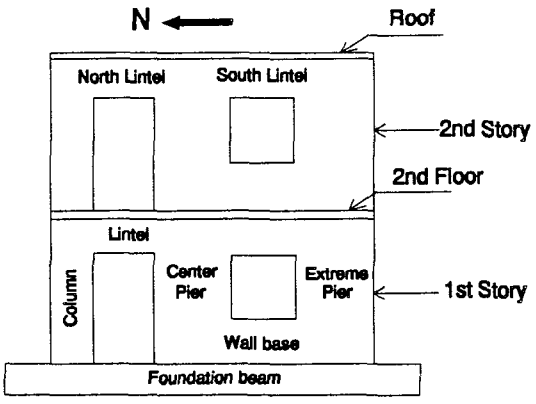

Figure 6.1: Perforated wall element designation.

The displacement sequence pattern used during the tests was described in Section 4.4. According to the particular characteristics of each specimen, slight modifications were introduced in each test. Within each load-displacement series, the peaks are defined as shown in Fig. 6.2: "first peak", "second peak",

and "last peak" are respectively the peak values corresponding to the first time, the second time, and the last time the peak is reached in a particular series. "Next peak" indicates the point at which the peak value of the last series is reached when loading up to a higher value in the next series.

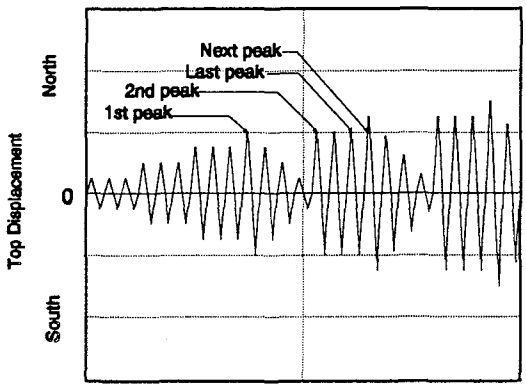

Figure 6.2: Peak value designations in SPD diagram.

6.2 Test Results for Specimen 1a

6.2.1 Test Result Summary. Specimen 1a was subjected to the roof in-plane displacement history shown in Fig. 6.3. To check potential out-of-plane instability after the 1st story piers had been subjected to considerable in-plane deformations, the specimen was subjected to a constant distribution of out-of-plane displacements, applied simultaneously with the last cycles of loading, as shown in Fig. 6.3.

Constant vertical loads of 40.8 kips were applied on the roof at the top of each 2nd story pier, making a total externally applied vertical load of 81.6 kips.

Because of the specimen's high initial stiffness, the test of Specimen 1a was initiated under load control. The test was switched to displacement control when the overall drift ratio was 0.059% (0.12 in. top displacement).

The First Major Event (FME) was defined as the first yielding of the pier longitudinal reinforcement. It occurred when the wall was being loaded in the north direction, at an overall drift ratio of 0.069% (0.14 in. top displacement) and a base shear of 77.6 kips, as shown in Fig. 6.3. At that stage, the extreme longitudinal bar of the south first story pier yielded.

Lateral load capacity of the specimen was 98.2 kips, at an overall drift ratio of 0.39% (0.80 in. top displacement) when loaded to the north, and 104.5 kips, at an overall drift ratio of 0.39% (0.79 in. top displacement) in the south direction.

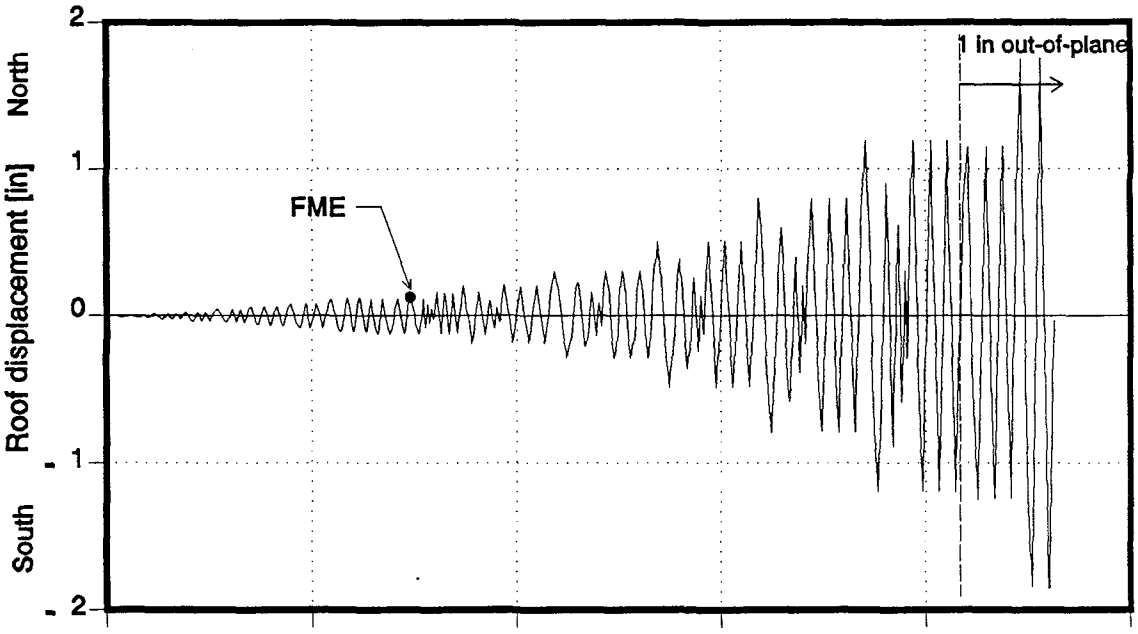

Figure 6.3: Specimen 1a: Roof displacement history.

The test was stopped due to damage of the specimen, specially in the areas of the connection between the first story piers and the base of the wall, as shown in Fig. 6.35. The maximum overall drift ratio was 0.86% (1.75 in. top displacement) when loaded in the north direction with 59.8 kips, and 0.91% (1.85 in. top displacement) when loaded in the south direction with 73.6 kips.

The most significant events that occurred during the test have been summarized in Tables 6.1 and 6.2 for northward and southward loading respectively.

6.2.2 Load-Displacement History and Deformations. The overall load-displacement history, and displacements and deformations measured in some critical areas of the specimen, are presented in this section. Since most inelastic deformation and damage occurred in the 1st story, the description of results is concentrated on the behavior of the elements of that story.

The base shear-overall drift ratio history for the entire test is shown in Fig. 6.4. The envelope of the first peaks of the hysteresis loops is shown in Fig. 6.5. Lateral roof displacement was measured with displacement transducer (DT) 57.

Table 6.1: Specimen 1a test: significant events, northward loading

Load Point	Test Event	Base Shear Kips	Top Displ. in	Overall Drift Ratio %
76	Flexural cracking of wall base; Bed joint cracking at 1st story extreme pier and column.	29.8	0.018	0.009
218	Cracking at the 1st story lintel - pier connection	70.1	0.11	0.052
258	Horizontal cracking at base wall under extreme pier	68.5	0.11	0.055
297	FME, yielding of longitudinal reinforcement in extreme pier	73.6	0.14	0.069
348	Diagonal cracking at wall base under center pier	77.9	0.20	0.10
538	Cracking at bottom face of slab in the 2nd story lintel - pier connection	94.0	0.50	0.24
620	Splitting crack at north end of window sill; Cracking at the bottom face of slab in the 1st story lintel - pier connection	88.9	0.50	0.25
636	Diagonal cracking at center pier	95.6	0.70	0.34
637	Maximum lateral load capacity	98.2	0.80	0.39
673	Vertical splitting of masonry at column base	65.1	0.40	0.20
739	Crushing of masonry at column base	86.5	0.90	0.44
834	1-inch out-of-plane displacement is imposed at top of specimen			
840	Fracture of longitudinal bar in extreme pier	75.9	1.12	0.55
893	Maximum displacement; Extensive cracking and crushing of masonry at north end of wall base and at center pier - wall base connection; buckling of reinforcement at base of column	77.0	1.80	0.86

Table 6.2: Specimen 1a test: significant events, southward loading

Load Point	Test Event	Base Shear Kips	Top Displ. in	Overall Drift Ratio %
83	Bed joint cracking at 1st story center pier and column	30.6	0.040	0.020
116	Flexural cracking of wall base	40.9	0.048	0.024
356	Diagonal cracking at the wall base under extreme pier; Yielding of longitudinal reinforcement in center pier and column	80.2	0.19	0.095
550	Diagonal cracking at extreme pier	96.5	0.49	0.24
596	Yielding of longitudinal reinforcement at south end of wall base Splitting cracking at south end of window sill	97.7	0.49	0.24
628	Maximum lateral load capacity	95.7	0.49	0.24
649	Crushing of masonry at south end of wall base; yielding of drag bar	104.5	0.79	0.39
753	1-inch out-of-plane displacement is imposed at top of specimen	100.6	1.20	0.59
834	Maximum displacement; Splitting and crushing of masonry at south end of wall base			
904		95.6	1.84	0.90

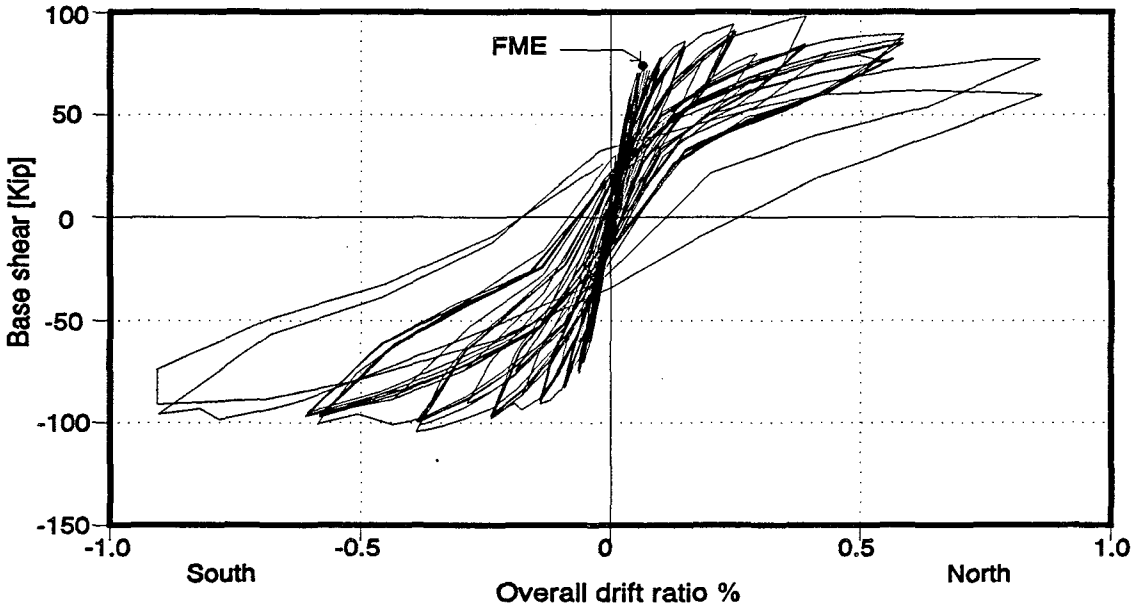

Figure 6.4: Specimen 1a: Base shear - Overall drift ratio history.

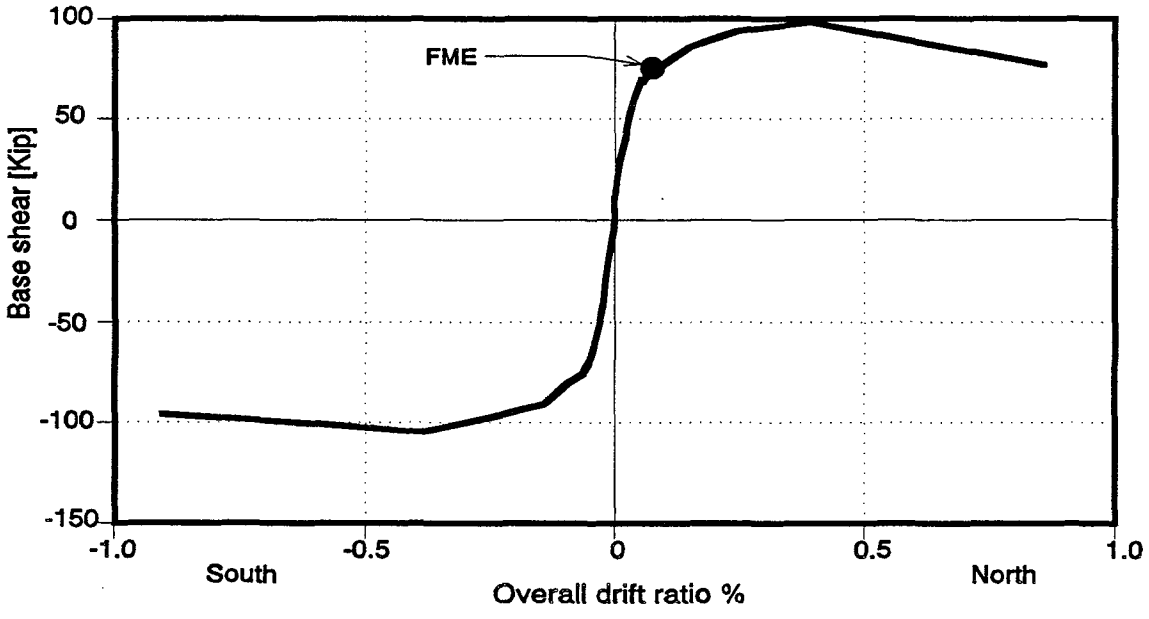

Figure 6.5: Specimen 1a: First peak envelope of the Base shear - Overall drift ratio history.

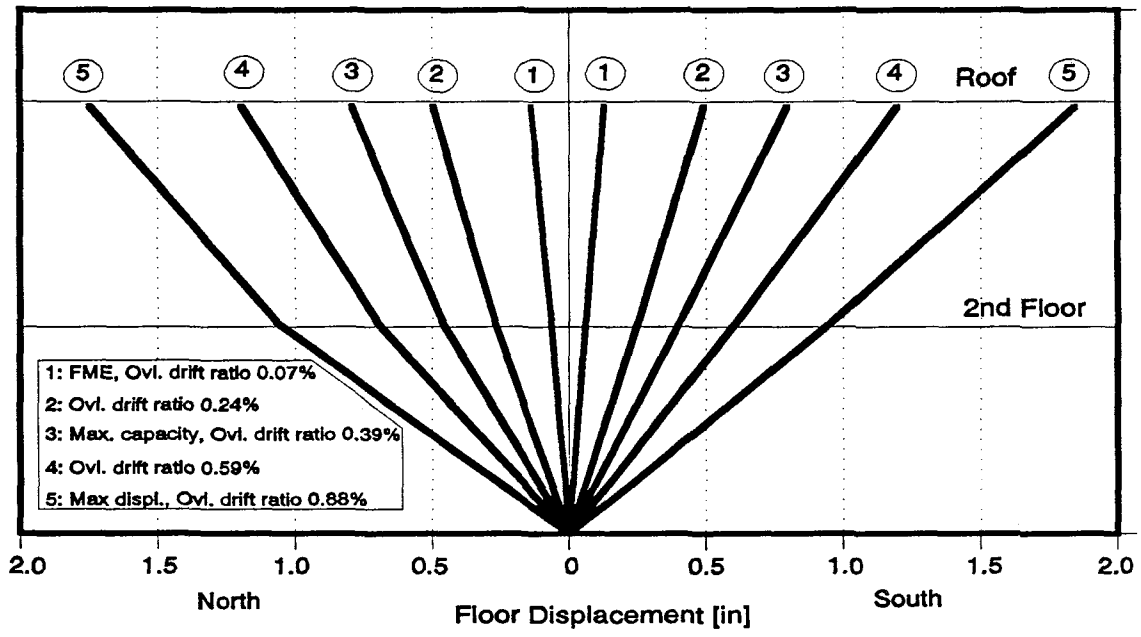

Figure 6.6: Specimen 1a: Displacement profiles for some first peak points.

Displacement profiles over the height of the specimen, for some selected first peak points, are shown in Fig. 6.6. Roof and 2nd floor displacements were obtained from displacement transducers 57 and 56 respectively.

Deformations and strains measured in the 1st story column are shown in Figs. 6.7 and 6.8. First peak values of readings from displacement transducers 2 and 6 are shown in Fig 6.6. DT 2 measured the total axial deformation of the 1st story at the north end of the specimen, and DT 6 measured the crack opening at the base of the column. Fig. 6.8 shows first peak values of readings from strain gauges (SG) 62 and 63, at the base and top sections of the 1st story column respectively. The rest of the strain gauges in this element did not work properly.

Displacements and deformations measured at the base of the wall are shown in Figs. 6.9 to 6.15. Slipping of the wall base on the foundation beam is shown in Figs. 6.9 and 6.10. The first plot shows first peak slip values versus overall drift ratio. The second figure shows slip as a fraction of the total roof displacement versus the overall drift ratio. Strain distributions in longitudinal reinforcement at the base of the wall, for some of the first peak points, are shown in Figs. 6.11 and 6.12, for northward and southward loading respectively. The readings were obtained from strain gauges 76, 77, 110, and 111, and the load points have been identified by the overall drift ratio. Strain values measured in the drag bars during the first peaks of the loading process, are shown in Figs. 6.13 to 6.15. In those plots, each curve contains the readings of one strain gauge.

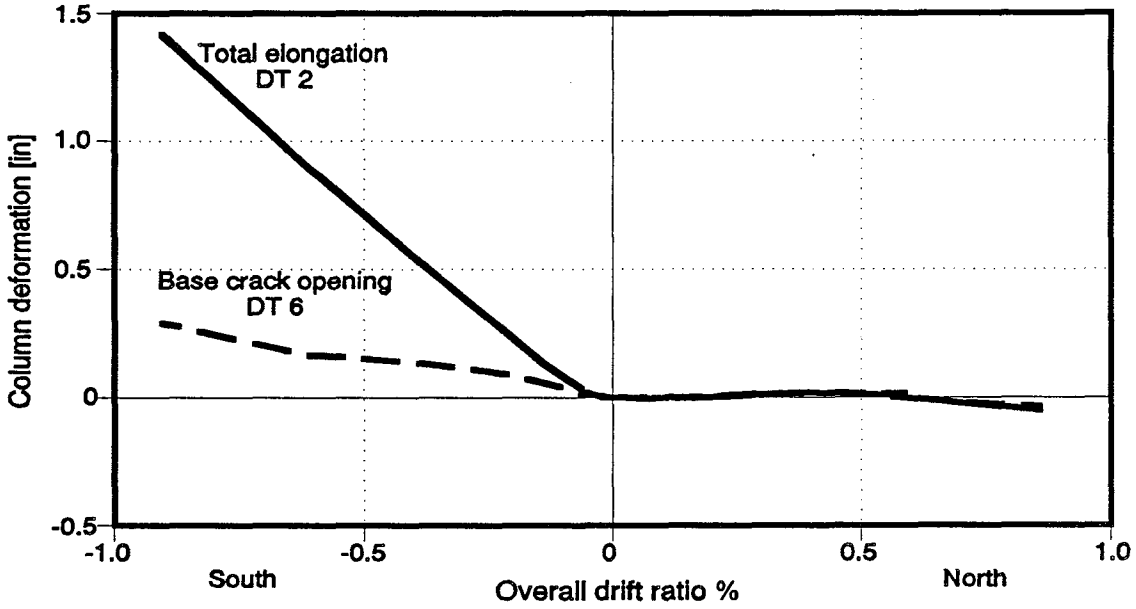

Figure 6.7: Specimen 1a: 1st story column deformations.

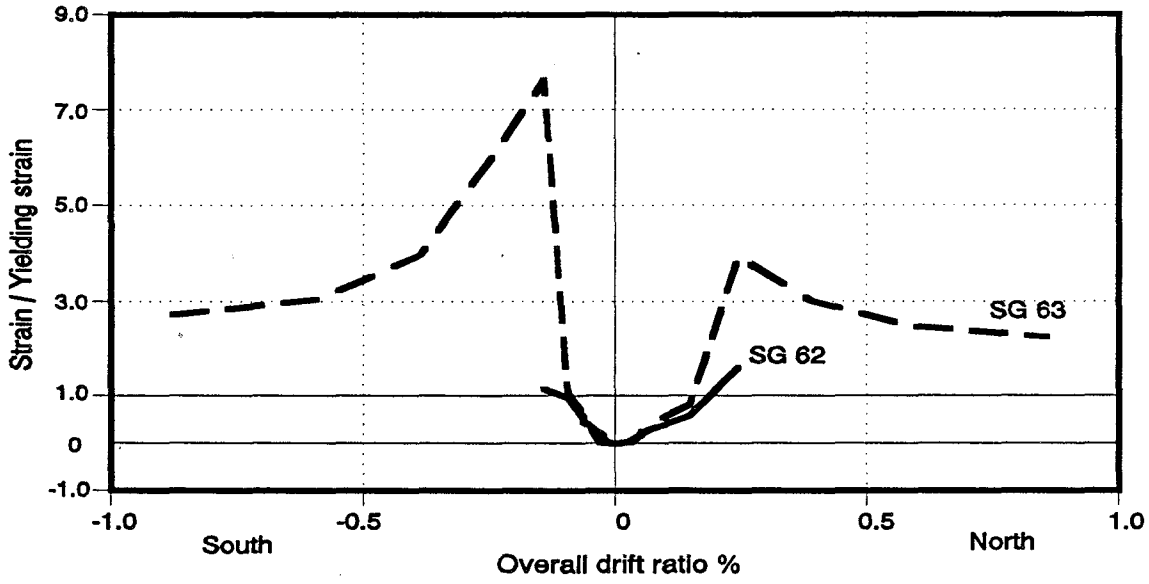

Figure 6.8: Specimen 1a: Strains in longitudinal reinforcement at end sections of 1st story column.

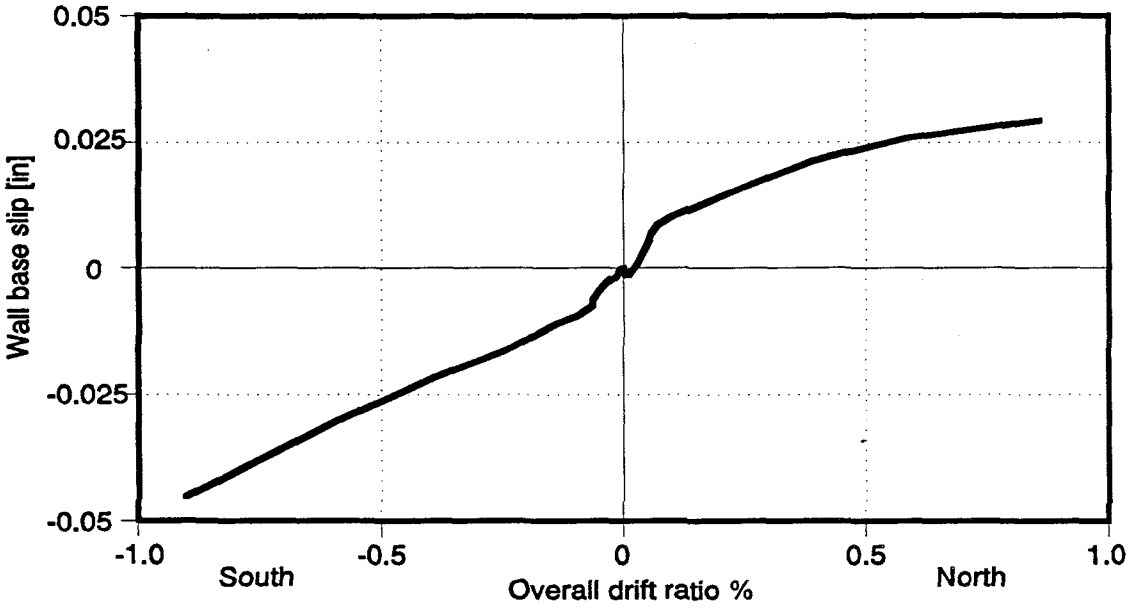

Figure 6.9: Specimen 1a: Slip of the wall base on the foundation beam.

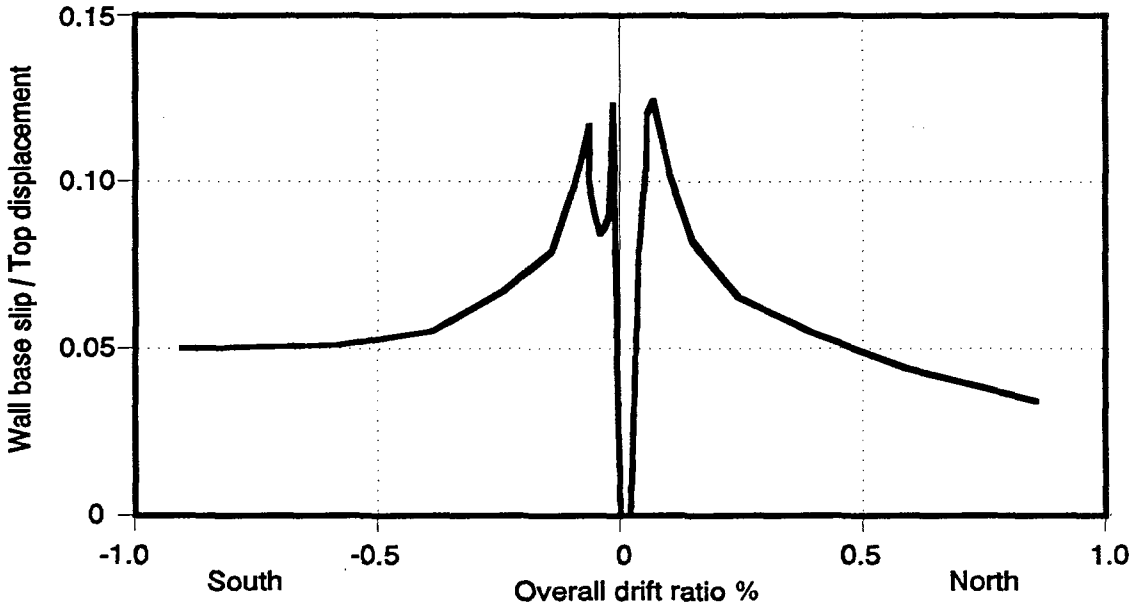

Figure 6.10: Specimen 1a: Slip of the wall base on the foundation beam.

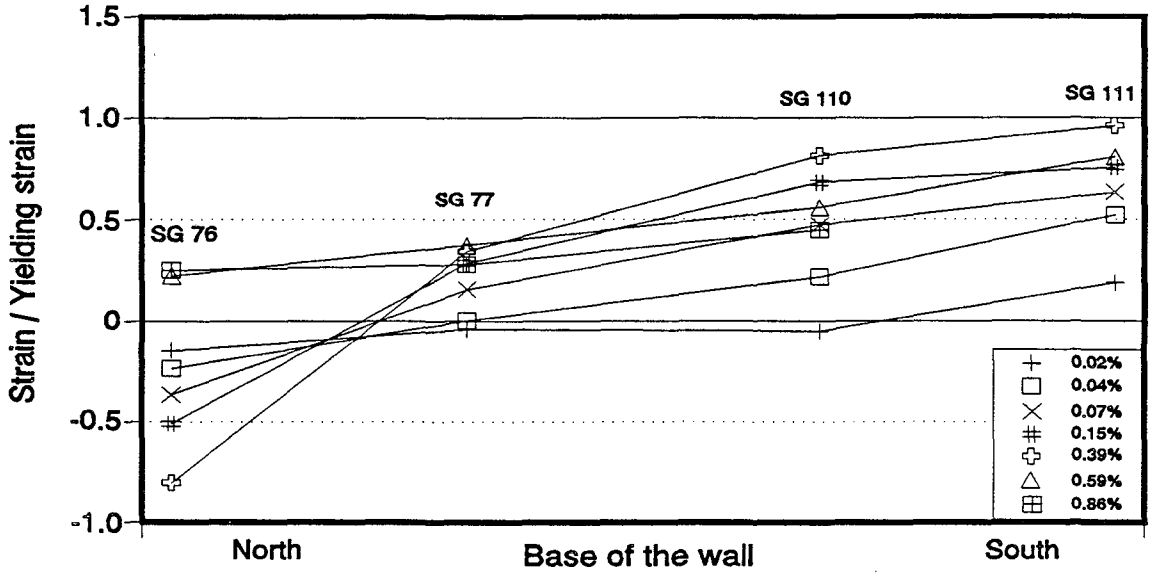

Figure 6.11: Specimen 1a: Strain in longitudinal reinforcement at the base of the wall, northward loading.

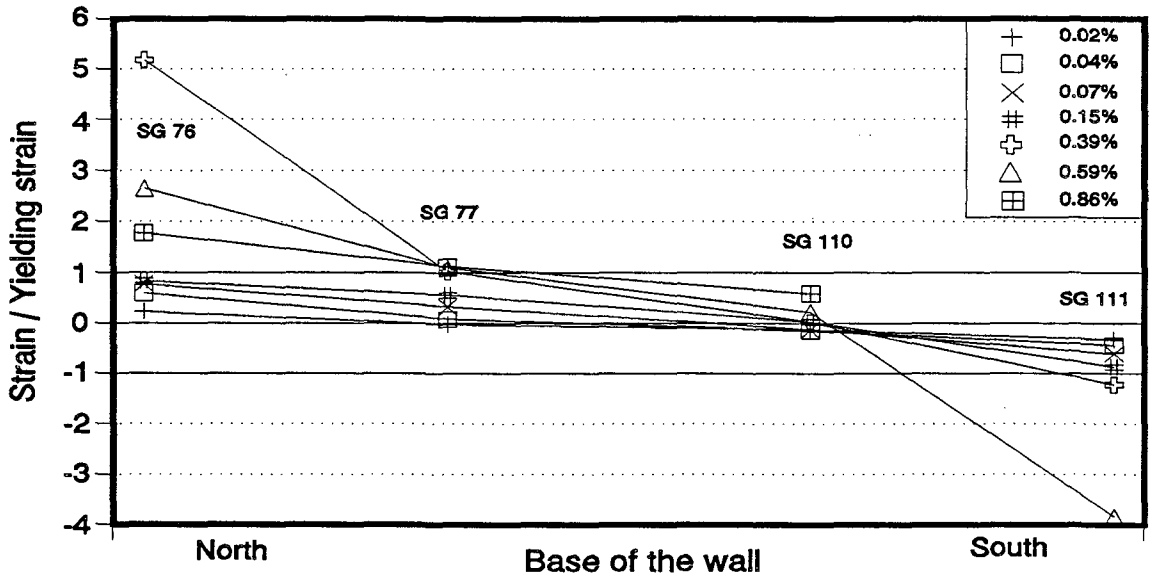

Figure 6.12: Specimen 1a: Strain in longitudinal reinforcement at the base of the wall, southward loading.

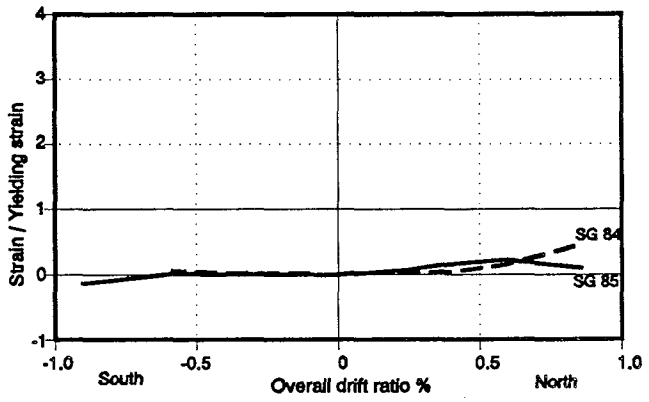

Figure 6.13: Specimen 1a: Strains in top drag bar at wall base under center pier.

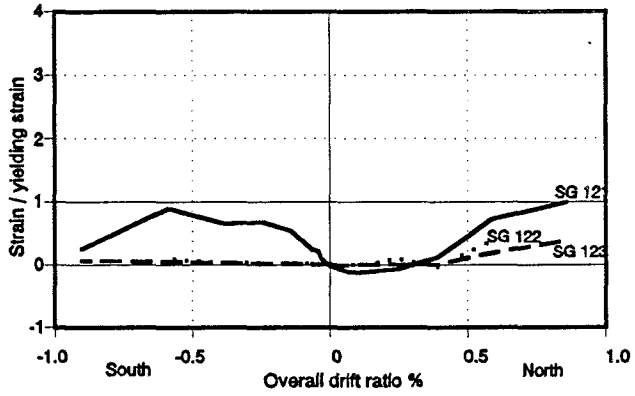

Figure 6.14: Specimen 1a: Strains in top drag bar at wall base under extreme pier.

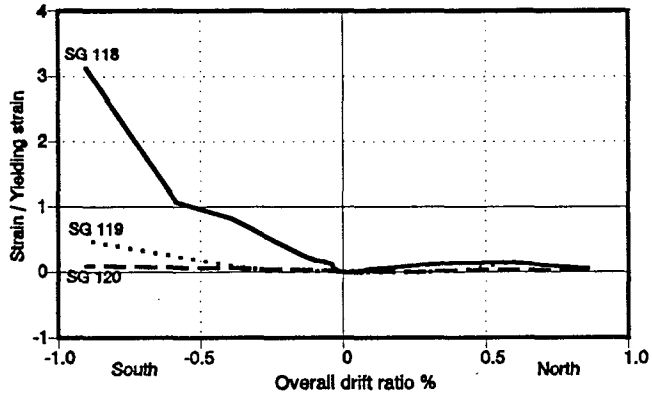

Figure 6.15: Specimen 1a: Strains in second top drag bar at wall base under extreme pier.

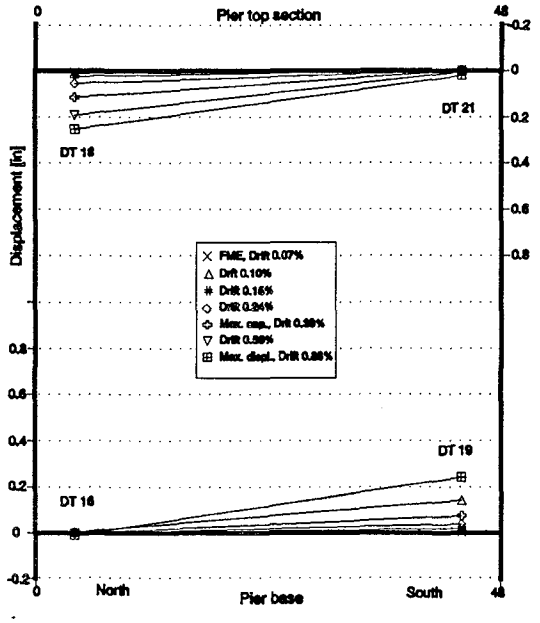

Figure 6.16: Specimen 1a: Flexural deformations at end sections of center pier, northward loading.

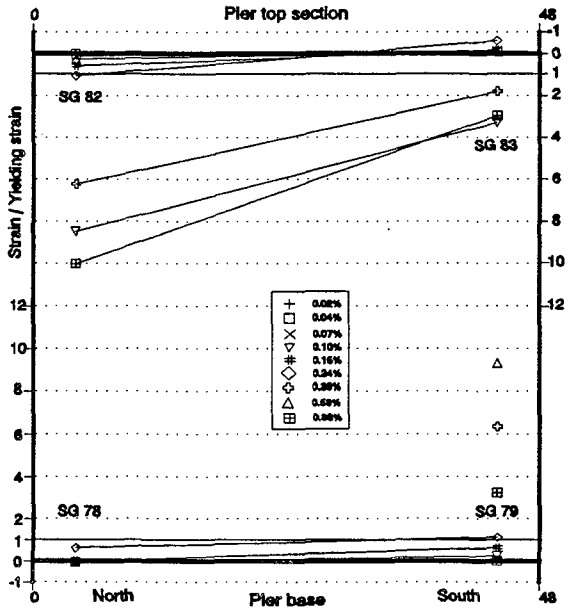

Figure 6.17: Specimen 1a: Strains in longitudinal reinforcement of center pier, northward loading.

Deformations measured at the end sections of the 1st story piers for some of the first peak points, are shown in Figs. 6.16 to 6.23. In each figure, the bottom and top horizontal axes define the position of the instruments on the pier base and top sections respectively. Deformations measured in the base section have been plotted on the bottom axis, and their values are indicated in the vertical scale at the left side. Deformations measured in the top section have been plotted on the top axis, and their values are indicated in the vertical scale at the right side. Displacement transducers were used to measure flexural deformations at the edges of the pier. Strains gauges were attached to the longitudinal reinforcing bars at the end sections. Each figures shows deformations measured at some selected first peak points, for a given loading direction. Load points and instrumentation channels are indicated in the figures.

Slip of the end sections of the 1st story extreme pier, measured at the first peak points, is shown in Fig. 6.24. Displacement transducer 46 measured the slip of the pier with respect to the wall base. Displacement transducer 49 measured the slip of the 2nd floor with respect to the pier top section. Readings of the DT 49 have been plotted with opposite sign in Fig. 6.24. Since a crack developed trough the support of displacement transducer 24 early during the test, no measures of slip were available for the center pier.

6.2.3 Cracking and Yielding Progression Maps. Maps of the cracking and reinforcement yielding progression, for some selected first peak points, are shown in Figs. 6.25 to 6.36. Cracks were identified and marked as the test was progressing. Shadowed areas in crack maps indicate masonry crushing or spalling off. Yielding points were detected from the readings of the instrumentation system. A diagonal line crossing the reinforcement indicates fracture of the bar. Only the events clearly and unmistakably identified were marked in the yielding maps.

6.2.4 Description of Test Events. A detailed description of the observations made during the test of Specimen 1a is given in this section.

The test was initiated under load control with cycles of 10-kip amplitude. No significant events occurred during this series, nor during the next, of 20-kip amplitude.

At Load Point 76, corresponding to a base shear of 29.8 kips and overall drift ratio of 0.009% (0.018 in. roof displacement) in north direction (the first north peak of the 30-kip series), cracks formed along bed joints in the extreme 1st story pier and the 1st story column. A flexural crack formed at the bottom bed joint in the south side of the wall base.

At Load Point 83, corresponding to a base shear of 30.6 kips and overall drift ratio of 0.020% (0.040 in. roof displacement) in south direction (the first south peak of the 30-kip series), cracks formed at bed joints in the center 1st story pier and at the extreme sections in the 1st story column. Some cracking developed at bed joints in the second story piers.

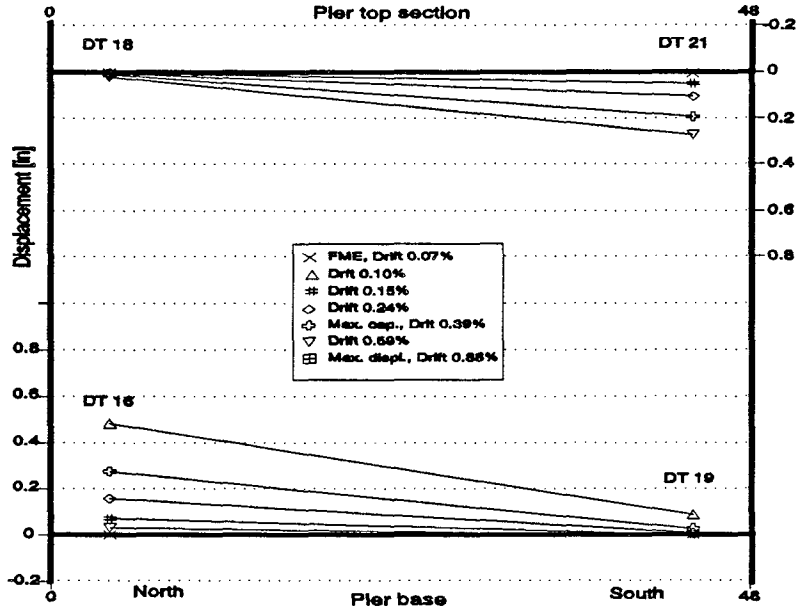

Figure 6.18: Specimen 1a: Flexural deformations at end sections of center pier, southward loading.

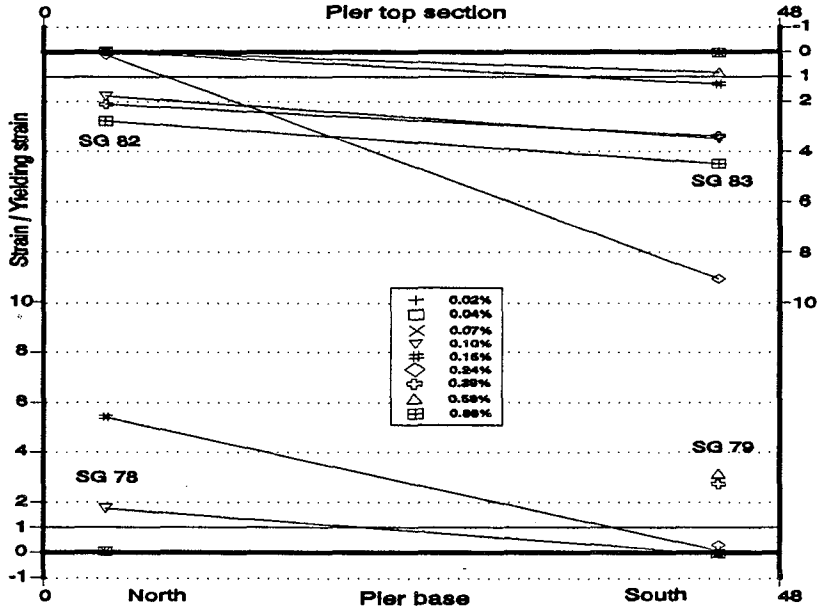

Figure 6.19: Specimen 1a: Strains in longitudinal reinforcement of center pier, southward loading.

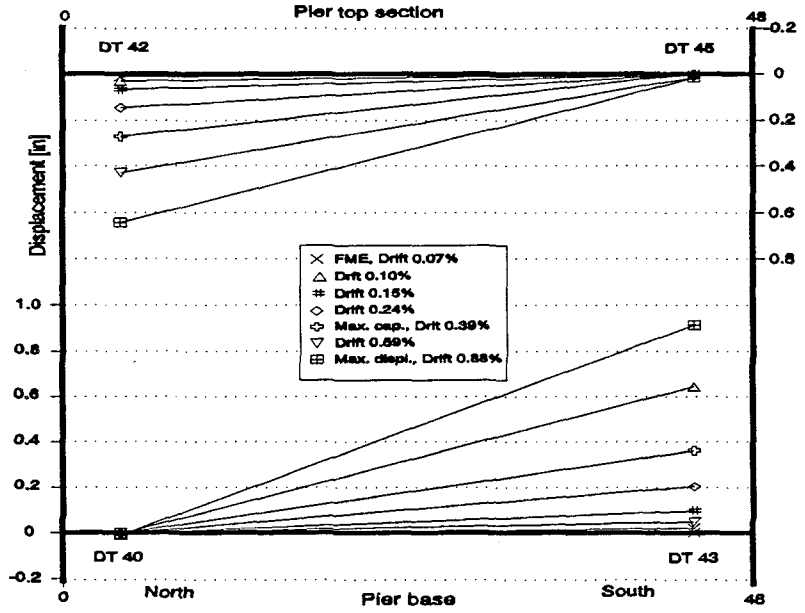

Figure 6.20: Specimen 1a: Flexural deformations at end sections of extreme pier, northward loading.

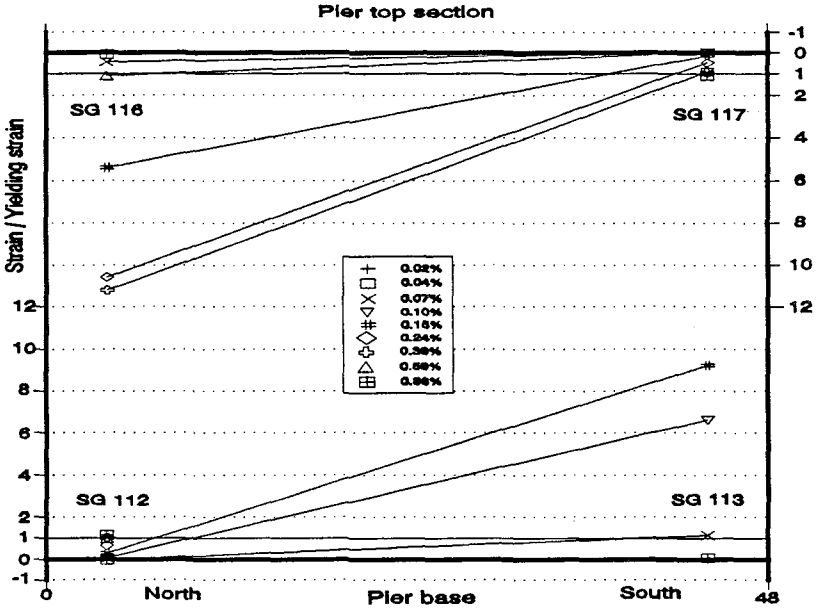

Figure 6.21: Specimen 1a: Strains in longitudinal reinforcement of extreme pier, northward loading.

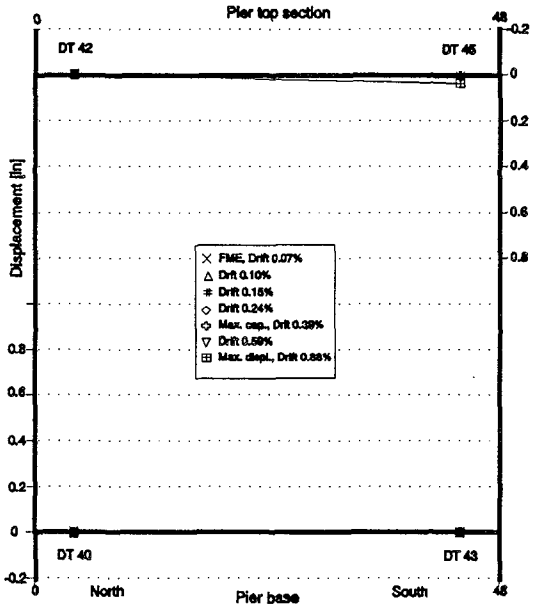

Figure 6.22: Specimen 1a: Flexural deformations at end sections of extreme pier, southward loading.

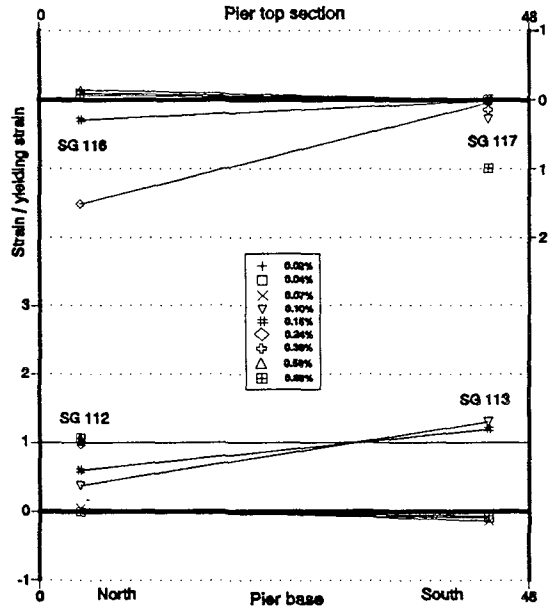

Figure 6.23: Specimen 1a: Strains in longitudinal reinforcement of extreme pier, southward loading.

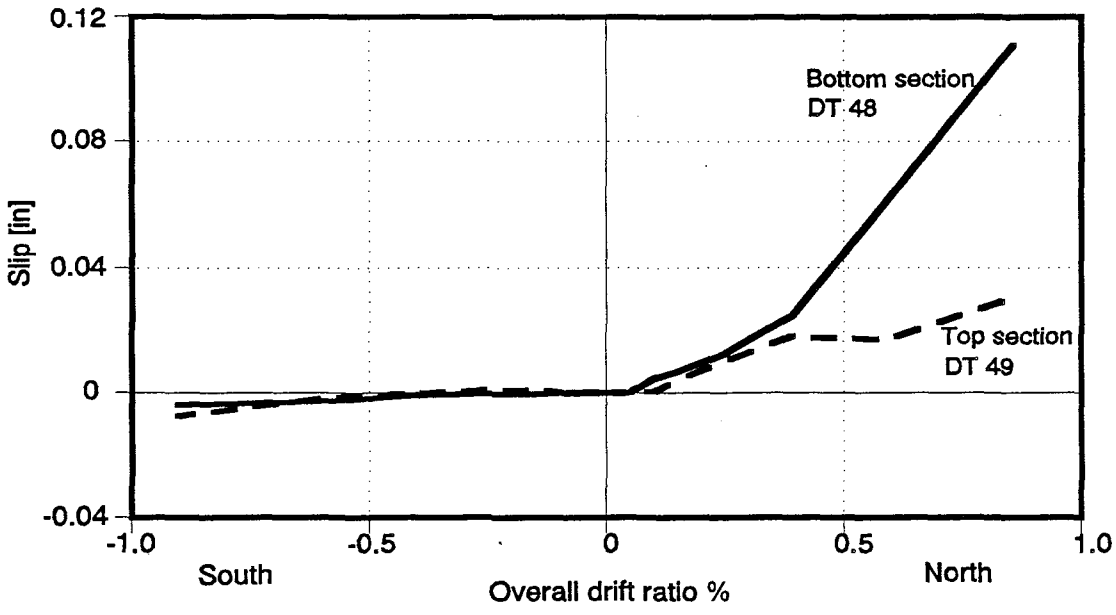

Figure 6.24: Specimen 1a: Slip at the end sections of the 1st story extreme pier.

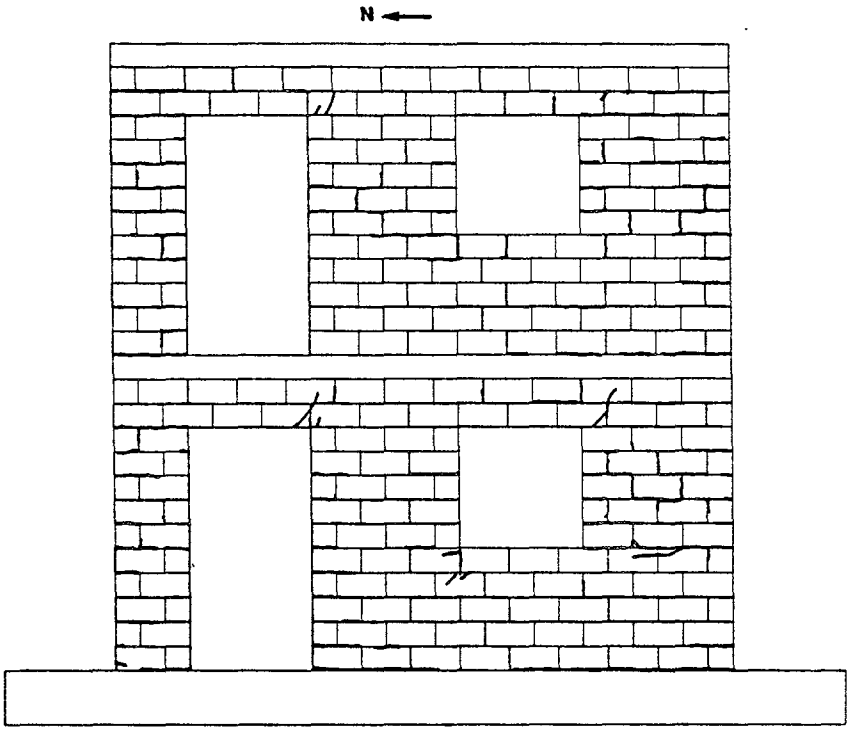

Figure 6.25: Specimen 1a: Cracking progression at FME, overall drift ratio 0.07%.

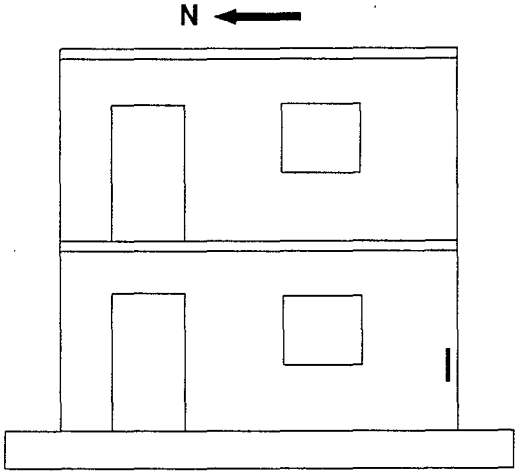

Figure 6.26: Specimen 1a: Yielding progression at FME, overall drift ratio 0.07%.

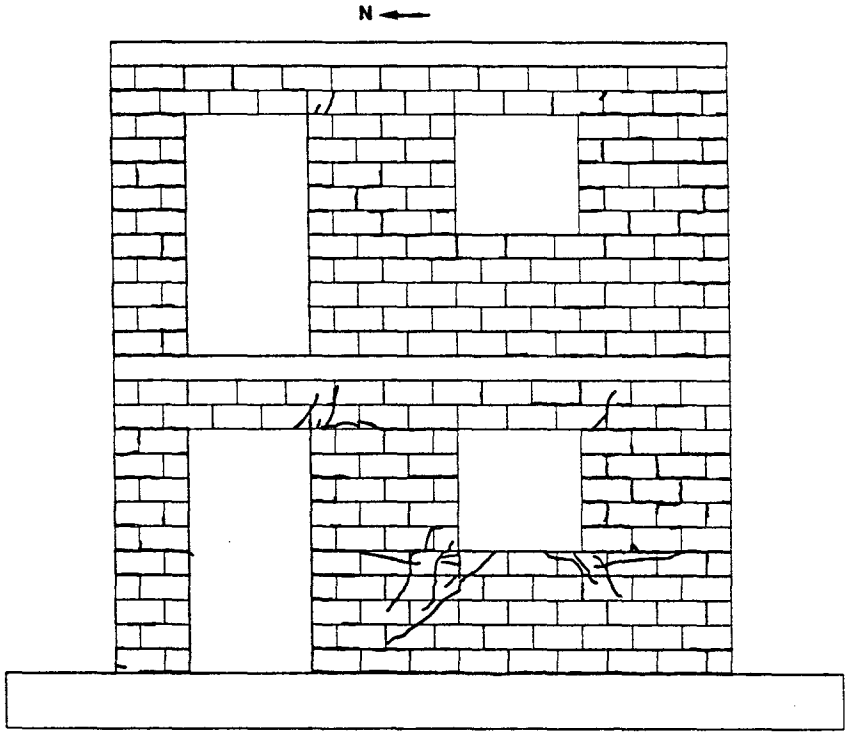

Figure 6.27: Specimen 1a: Cracking progression at overall drift ratio 0.15%.

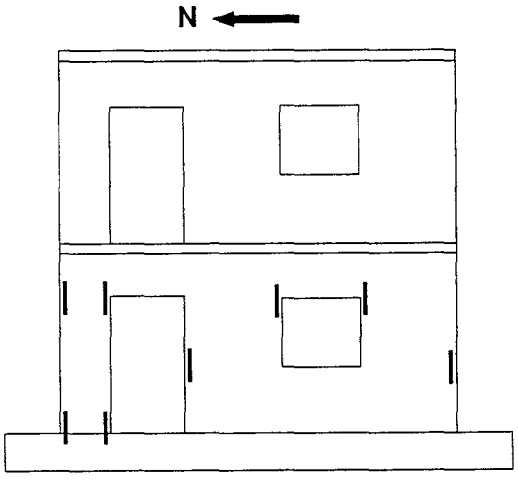

Figure 6.28: Specimen 1a: Yielding progression at overall drift ratio 0.15%.

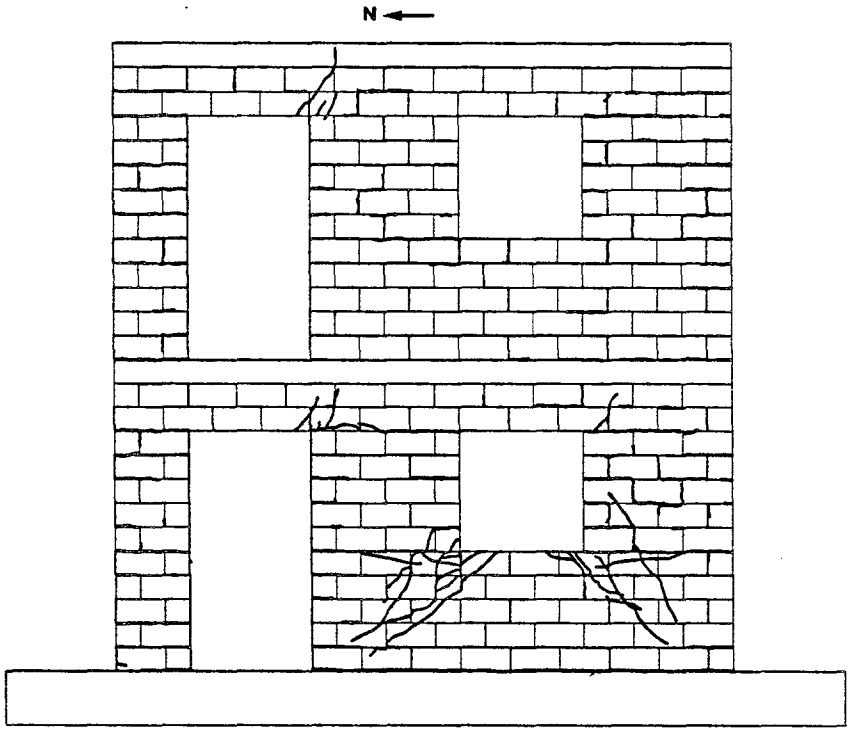

Figure 6.29: Specimen 1a: Cracking progression at overall drift ratio 0.24%.

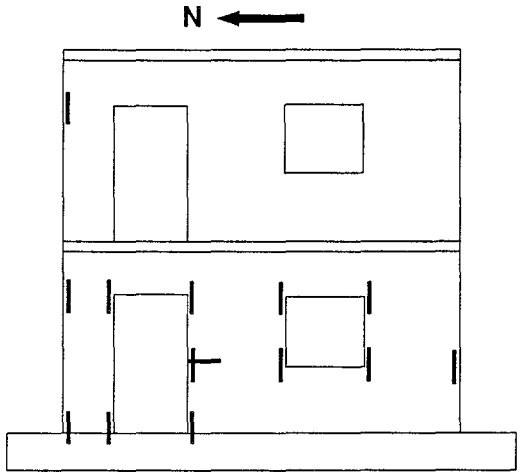

Figure 6.30: Specimen 1a: Yielding progression at overall drift ratio 0.24%.

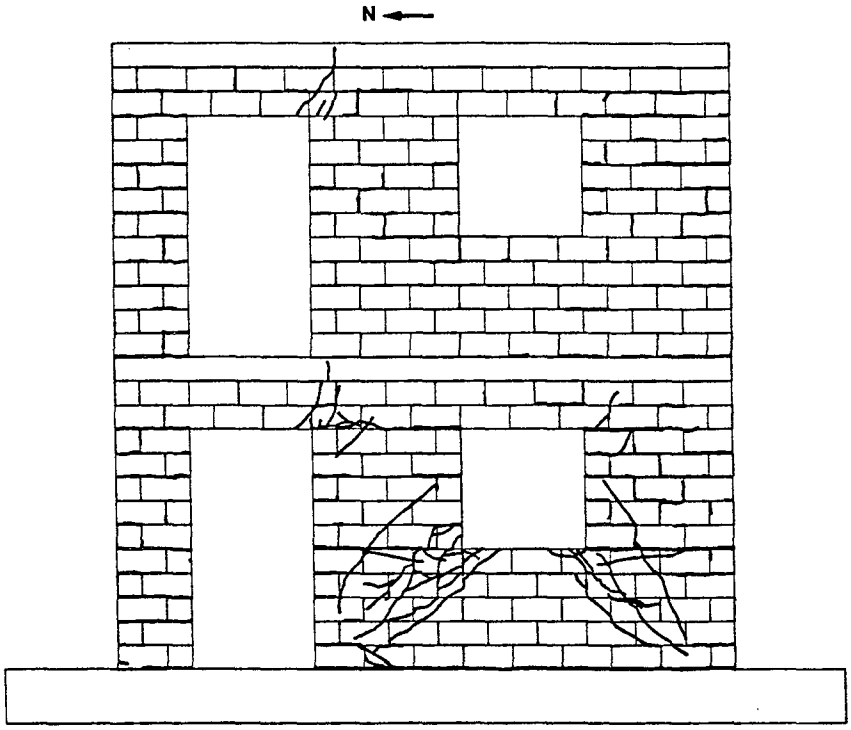

Figure 6.31: Specimen 1a: Cracking progression at overall drift ratio 0.39%.

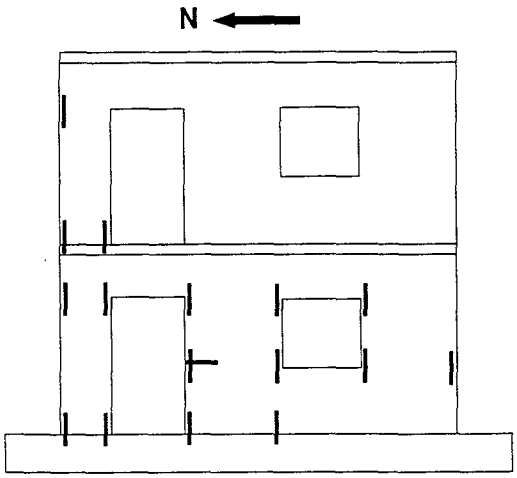

Figure 6.32: Specimen 1a: Yielding progression at overall drift ratio 0.39%.

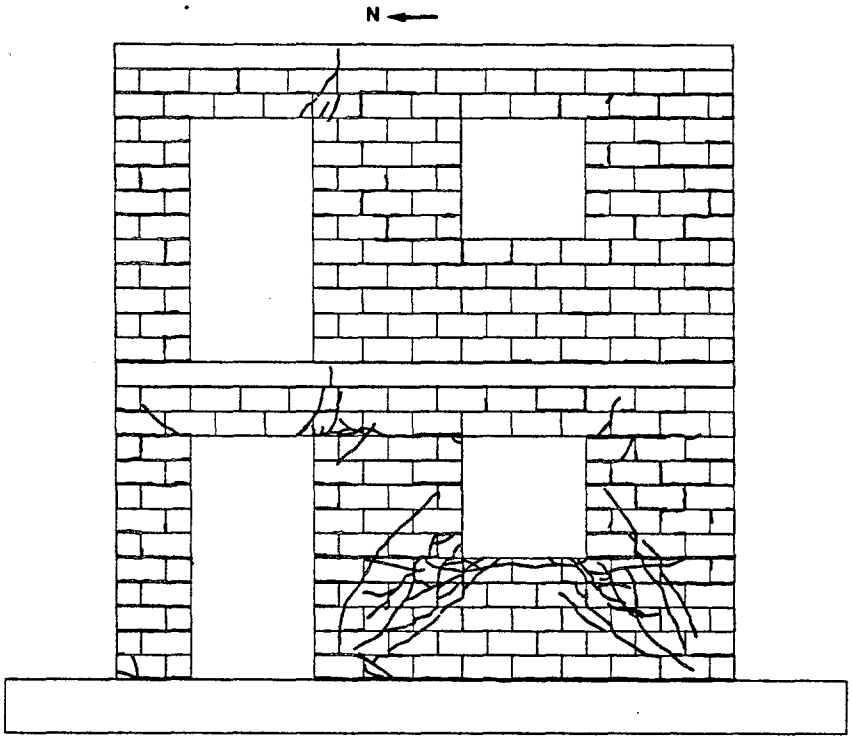

Figure 6.33: Specimen 1a: Cracking progression at overall drift ratio 0.59%.

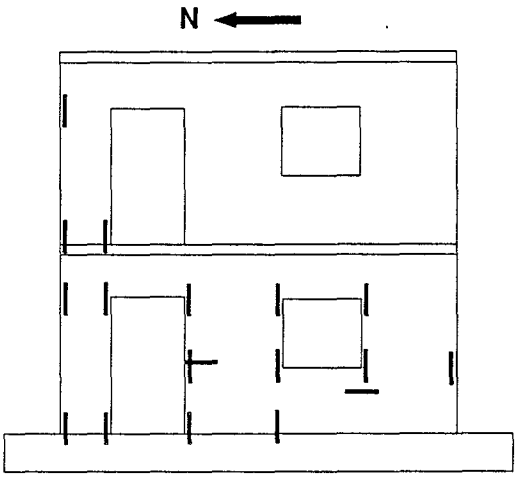

Figure 6.34: Specimen 1a: Yielding progression at overall drift ratio 0.59%.

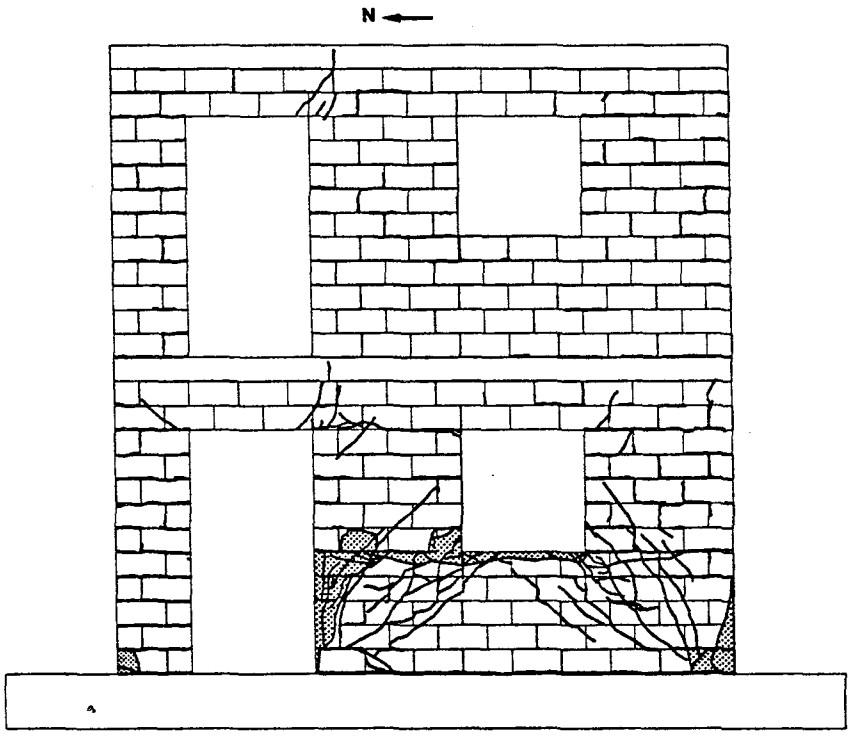

Figure 6.35: Specimen 1a: Cracking progression at end of the test, overall drift ratio 0.88%.

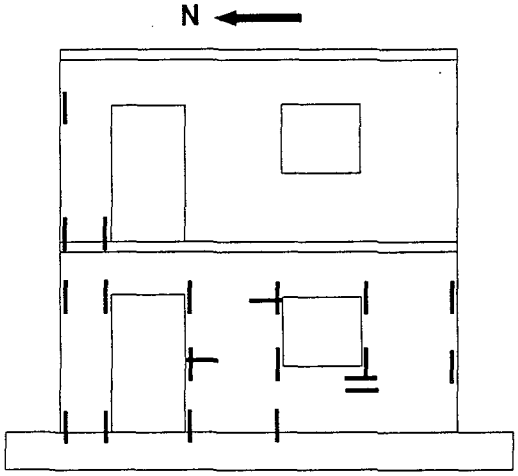

Figure 6.36: Specimen 1a: Yielding progression at end of the test, overall drift ratio 0.88%.

At Load Point 116, corresponding to a base shear of 40.9 kips and overall drift ratio of 0.024% (0.048 in. roof displacement) in south direction (the first south peak of the 40-kip series), a flexural crack formed at the bottom bed joint in the north side of the wall base. Bed joint cracking in the column progressed during the next two cycles in the south direction at 40 kips and 50 kips respectively. Some degradation of stiffness became noticed from the load-displacement plot.

Bed joint cracking in the 1st story column and extreme pier showed more progress after the series of 60-kip cycles. The flexural crack at the base of the wall continued extending.

At Load Point 218, corresponding to a base shear of 70.1 kips and overall drift ratio of 0.052% (0.11 in. roof displacement) in north direction (the first north peak of the 70-kip series), cracking initiated at the bottom north corner of the 1st story window and at the bottom face of the 1st story lintel-pier connection. The flexural crack at the base of the wall extended at both sides of the wall at the end of this loading series. Load-deformation curves showed some degree of stiffness degradation. The test was switched to displacement control mode after completing the 70-kip series.

At Load Point 258, corresponding to an overall drift ratio of 0.055% (0.11 in. roof displacement) and base shear of 68.5 kips in north direction (the first north peak of the 0.12-in series), cracking initiated at the south top corner of the 1st story window, and at the south top and north bottom corners of the 2nd story window. Horizontal cracking initiated at the first course of the wall base under the extreme pier.

The First Major Event (FME) occurred at Load Point 297, corresponding to an overall drift ratio of 0.069% (0.14 in. roof displacement) and base shear of 73.6 kips in north direction. At that point, the longitudinal bar in the south side of the extreme pier yielded at the pier bottom section. Cracking extended at the north lintel-pier connections at both stories.

Cracking and yielding progressions after completing the 0.14-in series are shown in Figs. 6.25 and 6.26 respectively.

At Load Point 348, corresponding to an overall drift ratio of 0.10% (0.20 in. roof displacement) and base shear of 77.9 kips in north direction (the first north peak of the 0.20-in series), a diagonal crack, starting close to the north bottom corner of the first story window, extended almost three courses through the base of the wall. Cracking extended under the base of the 1st story extreme pier. Longitudinal reinforcement in the north side of the 1st story extreme pier reached yielded at the pier top section.

At Load Point 356, corresponding to an overall drift ratio of 0.095% (0.19 in. roof displacement) and base shear of 80.2 kips in south direction (the first south peak of the 0.20-in series), diagonal cracking in the base of the wall initiated at the south bottom corner

of the 1st story window. Horizontal cracking initiated at the first course of the wall base under the center pier. Cracking extended under the base of the 1st story extreme pier. Longitudinal reinforcement yielded at the bottom section in the north side of the 1st story center pier, and at the top section in the north side of the 1st story column.

At Load Point 438, corresponding to an overall drift ratio of 0.15% (0.30 in. roof displacement) and base shear of 86.0 kips in north direction (the first north peak of the 0.30-in series), the 1st story extreme pier showed development of plastic hinging at both end sections. Diagonal cracking extended along the base of the wall under the center pier and in the vicinity of the bottom north corner of the window.

At Load Point 450, corresponding to an overall drift ratio of 0.14% (0.29 in. roof displacement) and base shear of 90.5 kips in south direction (the first south peak of the 0.30-in series), wide cracks opened at both end sections in the 1st story column and 1st story center pier. Diagonal cracking at the base of the wall extended under the extreme pier and in the vicinity of the south bottom corner of the window. Longitudinal reinforcement reached yielded at the south side of the column base and at the top section in the south side of the center pier.

Cracking and yielding progressions after completing the 0.30-in series are shown in Figs. 6.27 and 6.28 respectively.

At Load Point 537, corresponding to an overall drift ratio of 0.20% (0.40 in. roof displacement) and base shear of 89.9 kips in north direction (a point preceding the first north peak of the 0.50-in series), longitudinal reinforcement yielded at the top section in the north side of the 2nd story column.

At Load Point 538, corresponding to an overall drift ratio of 0.24% (0.50 in. roof displacement) and base shear of 94.0 kips in north direction (the first north peak of the 0.50-in series), a crack developed at the 2nd story north lintel-pier connection and penetrated through the bottom face of the slab. The crack extended all the way through the width of the slab. The flexural crack at the bottom section of the 1st story extreme pier was about 5 mm. maximum opening. Diagonal cracking in the base of the wall under the center pier continued extending. Longitudinal reinforcement reached yielded at the top section, north side, and bottom section, south side, in the center pier.

At Load Point 550, corresponding to an overall drift ratio of 0.24% (0.49 in. roof displacement) and base shear of 96.5 kips in south direction (the first south peak of the 0.50-in series), diagonal cracking in the base of the wall under the extreme pier continued extending. A diagonal crack occurred in the extreme 1st story pier. Longitudinal reinforcement yielded in compression at the bottom section in the south side of the wall base. Longitudinal reinforcement yielded at the bottom section in the north side of the extreme pier. The bottom transverse bar in the center pier yielded at the north side.

At Load Point 596, corresponding to an overall drift ratio of 0.24% (0.49 in. roof displacement) and base shear of 97.7 kips in south direction (the second south peak of the 0.50-in series), longitudinal reinforcement yielded at the bottom section in the north side of the wall base.

At Load Point 620, corresponding to an overall drift ratio of 0.25% (0.50 in. roof displacement) and base shear of 88.9 kips in north direction (the last north peak of the 0.50-in series), a splitting crack about 16-in. long developed at the north end of the 1st story window sill. A crack developed at the 1st story north lintel-pier connection and penetrated trough the bottom face of the slab. The crack extended all the way through the width of the slab. The flexural cracks at the bottom and top sections in the 1st story extreme pier opened about 5 mm and 3 mm respectively.

At Load Point 628, corresponding to an overall drift ratio of 0.24% (0.49 in. roof displacement) and base shear of 95.7 kips in south direction (the last south peak of the 0.50-in series), a splitting crack about 16-in. long developed at the south end of the 1st story window sill. The flexural crack at the bottom section in the 1st story center pier opened about 4 mm. Some crushing of the masonry occurred at the top bed joint in the center pier. Cracks at the three bottom bed joints in the 1st story column opened about 1.5 mm and the crack at the top bed joint opened about 2.5 mm.

Cracking and yielding progressions after completing the 0.50-in series are shown in Figs. 6.29 and 6.30 respectively.

At Load Point 636, corresponding to an overall drift ratio of 0.34% (0.70 in. roof displacement) and base shear of 95.6 kips in north direction (a point preceding the first north peak of the 0.80-in series), a diagonal crack initiated in the center pier and extended through the two top courses of the base of the wall.

At Load Point 637, corresponding to an overall drift ratio of 0.39% (0.80 in. roof displacement), the first north peak of the 0.80-in series, the specimen reached its maximum lateral load capacity of 98.2 kips in north direction. Longitudinal reinforcement yielded at the bottom section in the south side of the 2nd story column.

At Load Point 648, corresponding to an overall drift ratio of 0.34% (0.69 in. roof displacement) and base shear of 101.6 kips in south direction (a point preceding the first south peak of the 0.80-in series), longitudinal reinforcement yielded at the bottom section in the north side of the 2nd story column.

At Load Point 649, corresponding to an overall drift ratio of 0.39% (0.79 in. roof displacement), the first south peak of the 0.80-in series, the specimen reached its maximum lateral load capacity of 104.5 kips in south direction. Diagonal cracking under extreme pier continued extending. Yielding progressed through the longitudinal reinforcement at the bottom section in the north side of the wall base.

Cracking and yielding progressions after completing the 0.80-in series are shown in Figs. 6.31 and 6.32 respectively.

At Load Point 673, corresponding to an overall drift ratio of 0.20% (0.40 in. roof displacement) and base shear of 65.1 kips in north direction (a point of the 0.80-in series), vertical splitting of masonry occurred at the base of the column.

At Load Point 699, corresponding to an overall drift ratio of 0.39% (0.79 in. roof displacement) and base shear of 101.4 kips in south direction (the second south peak of the 0.80-in series), a horizontal crack developed at the top course of the wall base and extended all the way under the window.

At Load Point 739, corresponding to an overall drift ratio of 0.44% (0.90 in. roof displacement) and base shear of 86.5 kips in north direction (a point preceding the first north peak of the 1.20-in series), crushing of masonry occurred at the base of the column.

At Load Point 753, corresponding to an overall drift ratio of 0.59% (1.20 in. roof displacement) and base shear of 100.6 kips in south direction (the first south peak of the 1.20-in series), crushing of masonry initiated at the bottom course in the south side of the wall base. Diagonal cracking in the wall base continued extending under both piers. The drag bar in the second course under the extreme pier yielded.

After Load Point 833 (the last point of the 1.20-in series), the specimen was subjected to an out-of-plane displacement of 1.00 in. at the roof and 0.50 in. at the 2nd floor. At Load Point 840, corresponding to an overall drift ratio of 0.55% (1.12 in. roof displacement) and base shear of 75.9 kips in north direction (a point preceding the first north peak of the 1.20 in.-in-plane, 1.00 in.-out-of-plane series), a loud noise and a jump in the force-displacement curve seemed to indicate fracture of one of the longitudinal bars in the 1st story extreme pier. No additional damage was produced by the cycles including the out-of-plane displacement.

Cracking and yielding progressions after completing the 1.20-in series are shown in Figs. 6.33 and 6.34 respectively.

At Load Point 893, corresponding to an overall drift ratio of 0.86% (1.75 in. roof displacement) and base shear of 77.0 kips in north direction (the first north peak of the 1.80 in.-in-plane, 1.00 in.-out-of-plane series), extensive cracking and crushing of masonry occurred at the top courses in the north edge of the wall base and at the base of the center pier. The top drag bar in the base of the wall yielded under the extreme pier area. The top transverse bar in the center pier yielded at the south side.

At Load Point 904, corresponding to an overall drift ratio of 0.90% (1.84 in. roof displacement) and base shear of 95.6 kips in south direction (the first south peak of the 1.80

in.-in-plane 1.00 in.-out-of-plane series), splitting and crushing of masonry occurred at the south edge of the base of the wall.

At Load Point 918, corresponding to an overall drift ratio of 0.51% (1.04 in. roof displacement) and base shear of 79.2 kips in south direction (a point of the 1.80 in.-in-plane, 1.00-in.-out-of-plane series), longitudinal reinforcement yielded at the top section in the south side of the extreme pier.

At Load Point 920, corresponding to an overall drift ratio of 0.91% (1.85 in. roof displacement) and base shear of 90.8 kips in south direction (the second south peak of the 1.80in.-in-plane, 1.00 in.-out-of-plane series), a loud noise and a jump in the load-displacement plot seemed to indicate fracture of one of the longitudinal bars in the center pier. Base shear dropped to 73.6 kips. Because of the extensive damage on the specimen, confirmed from the high degradation in the load-displacement curves, the test was stopped after this cycle. Most of the damage occurred at the center pier-wall base connection and at the north edge of the wall base. Crushing of masonry also occurred at the south edge of the base of the wall and at the base of the column. Splitting of masonry occurred along the sill of the window opening.

Cracking and yielding conditions of the specimen after completing the test are shown in Figs. 6.35 and 6.36 respectively.

6.3 Test Results for Specimen 1b

6.3.1 Test Result Summary. Specimen 1b was subjected to the roof in-plane displacement history shown in Fig. 6.37.

Constant vertical loads of 40.8 kips were applied on the roof at the top of each 2nd story pier, making a total externally applied vertical load of 81.6 kips.

Because of the specimen's high initial stiffness, the test of Specimen 1b was initiated under load control. The test was switched to displacement control when the overall drift ratio was 0.059% (0.12 in. top displacement).

The First Major Event (FME) was defined as the first yielding of the longitudinal reinforcement in the wall base. It occurred when the wall was being loaded in the north direction, at an overall drift ratio of 0.053% (0.11 in. top displacement) and a base shear of 64.9 kips, as shown in Fig. 6.37. At that stage, the bar at the south edge of the wall base yielded.

Lateral load capacity of the specimen was 89.9 kips at an overall drift ratio of 0.38% (0.77 in. top displacement) when loaded to the north, and 145.0 kips at an overall drift ratio

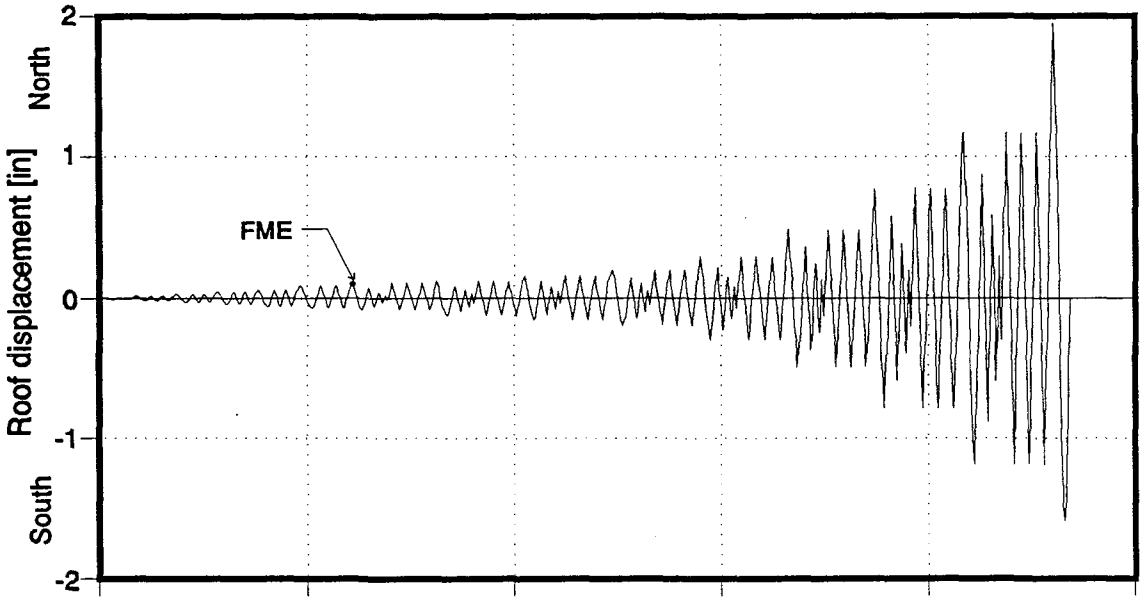

Figure 6.37: Specimen 1b: Roof displacement history.

of 0.39% (0.79 in. top displacement) in the south direction.

The test was stopped due to local damage of the roof slab in areas not restrained by reinforcement. Inelastic behavior and damage of this specimen was concentrated at the base of the wall and at the lintel-column and lintel-pier connections, as shown in Fig. 6.73. The maximum overall drift ratio was 0.96% (1.95 in. top displacement) when loaded in the north direction with 72.0 kips, and 0.78% (1.59 in. top displacement) when loaded in the south direction with 108.9 kips.

The most significant events that occurred during the test have been summarized in Tables 6.3 and 6.4 for northward and southward loading respectively.

6.3.2 Load-Displacement History and Deformations. The overall load-displacement history, and displacements and deformations measured in some critical areas of the specimen, are presented in this section. The description of results is concentrated on the behavior of the critical elements of the specimen.

The base shear-overall drift ratio history for the entire test is shown in Fig. 6.38. The envelope of the first peaks of the hysteresis loops is shown in Fig. 6.39. Lateral roof displacement was measured with displacement transducer (DT) 57.

Table 6.3: Specimen 1b test: significant events, northward loading

Load Point	Test Event	Base Shear Kips	Top Displ. in	Overall Drift Ratio %
38	Flexural cracking of wall base	20.0	0.016	0.008
80	Flexural crack in lintel-pier connection at both stories	30.2	0.029	0.014
211	Yielding of longitudinal reinforcement in the 1st story lintel	55.1	0.076	0.037
212	Yielding of longitudinal reinforcement in the 2nd story lintel	59.8	0.089	0.043
267	FME, yielding of longitudinal reinforcement in wall base	64.9	0.11	0.054
730	Yielding of longitudinal reinforcement at the base of the column	82.9	0.39	0.19
731	Damage initiated at the 2nd floor column-slab connection	86.0	0.49	0.24
823	Maximum lateral load capacity; Diagonal cracking in the lintel-column connection at the 2nd story	89.9	0.77	0.38
865	Fracture of extreme bar at south end of wall base	73.2	0.59	0.29
916	Crushing of masonry at the north end of wall base	82.1	1.07	0.52
963	Damage in the slab-wall connection at the roof north corner of the specimen	75.5	1.17	0.57
1013	Maximum displacement; Crushing of masonry at the base of the column	72.0	1.95	0.96

Displacement profiles over the height of the specimen, for some selected first peak points, are shown in Fig. 6.40. Roof and 2nd floor displacements were obtained from displacement transducers 57 and 56 respectively.

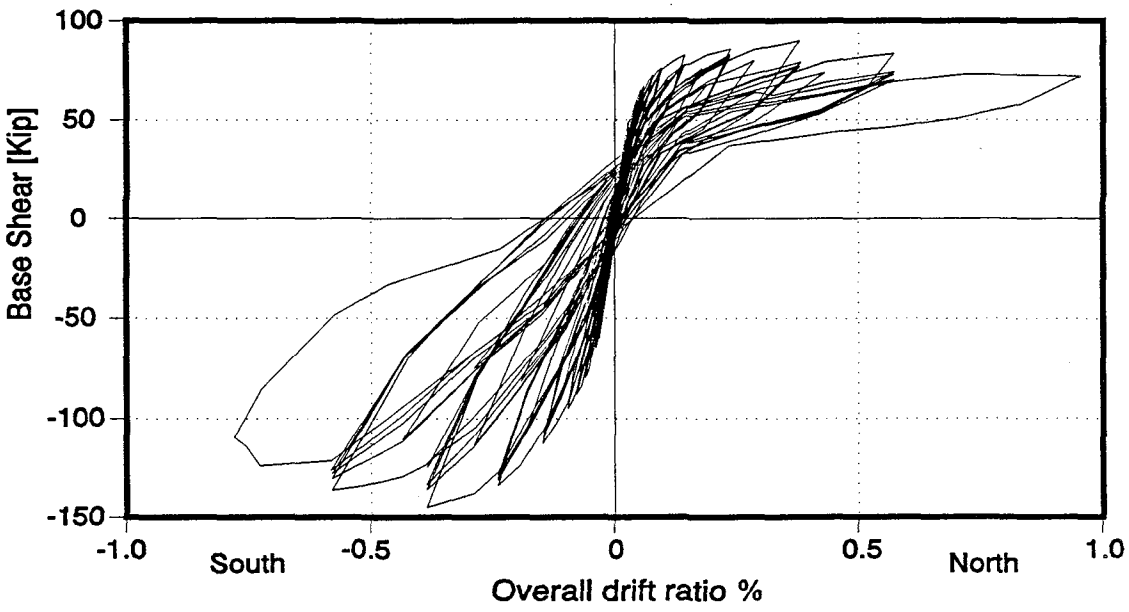

Figure 6.38: Specimen 1b: Base shear - Overall drift ratio history.

Deformations and strains measured in the column are shown in Figs. 6.41 to 6.46 for some selected first peak points. Distributions of flexural deformations at the base of the column, measured with displacement transducers 6 and 7, are shown in Figs. 6.41 and 6.43 for northward and southward loading respectively. Distributions of strains in the longitudinal reinforcement at the base of the column, measured with strain gauges 61 and 62, are shown in Figs. 6.42 and 6.44 for northward and southward loading respectively. Distributions of flexural deformations at the top section of the column, measured with displacement transducers 8 and 9, are shown in Figs. 6.45 and 6.46 for northward and southward loading respectively. The load points have been identified by the overall drift ratio in each figure.

Table 6.4: Specimen 1b test: significant events, southward loading

Load Point	Test Event	Base Shear Kips	Top Displ. in	Overall Drift Ratio %
47	Flexural cracking of wall base and column	19.6	0.016	0.008
277	Cracking in the top face of slab at the 2nd floor	64.8	0.077	0.038
461	Cracking in the top face of slab at the roof; Yielding of longitudinal reinforcement at north edge of wall base	87.6	0.16	0.077
647	Yielding of longitudinal reinforcement at base of 2nd story column	102.8	0.25	0.12
740	Crushing of masonry at the south end of wall base	122.8	0.39	0.19
833	Maximum lateral load capacity	145.0	0.79	0.39
906	Fracture of extreme bar at north end of wall base	119.7	0.76	0.37
1025	Maximum displacement; Extensive cracking and damage of masonry and concrete at the column-lintel-slab connections	108.9	1.59	0.78

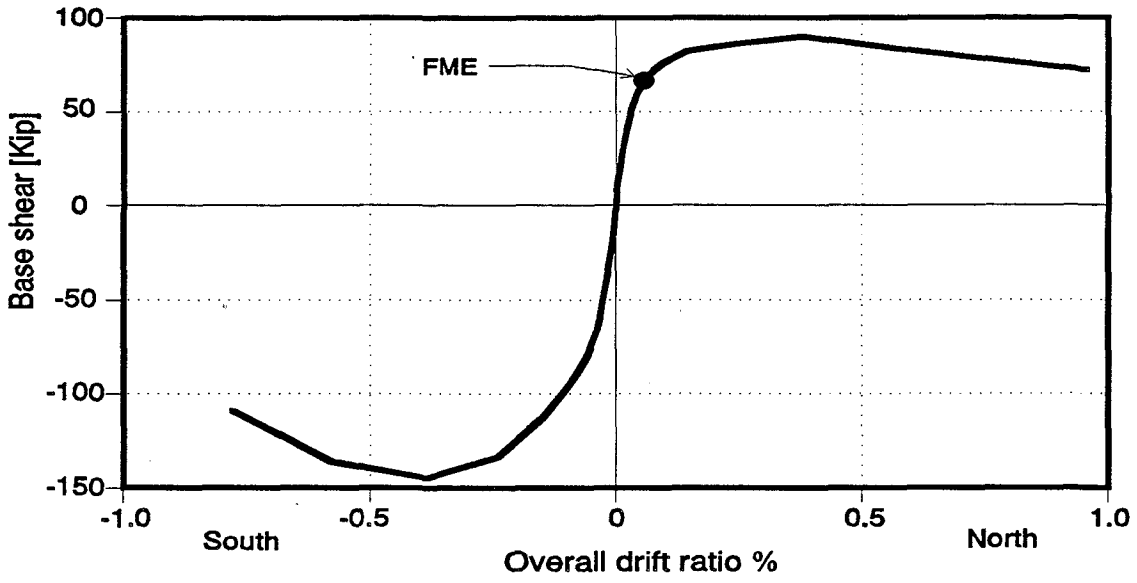

Figure 6.39: Specimen 1b: First peak envelope of the Base shear - Overall drift ratio history.

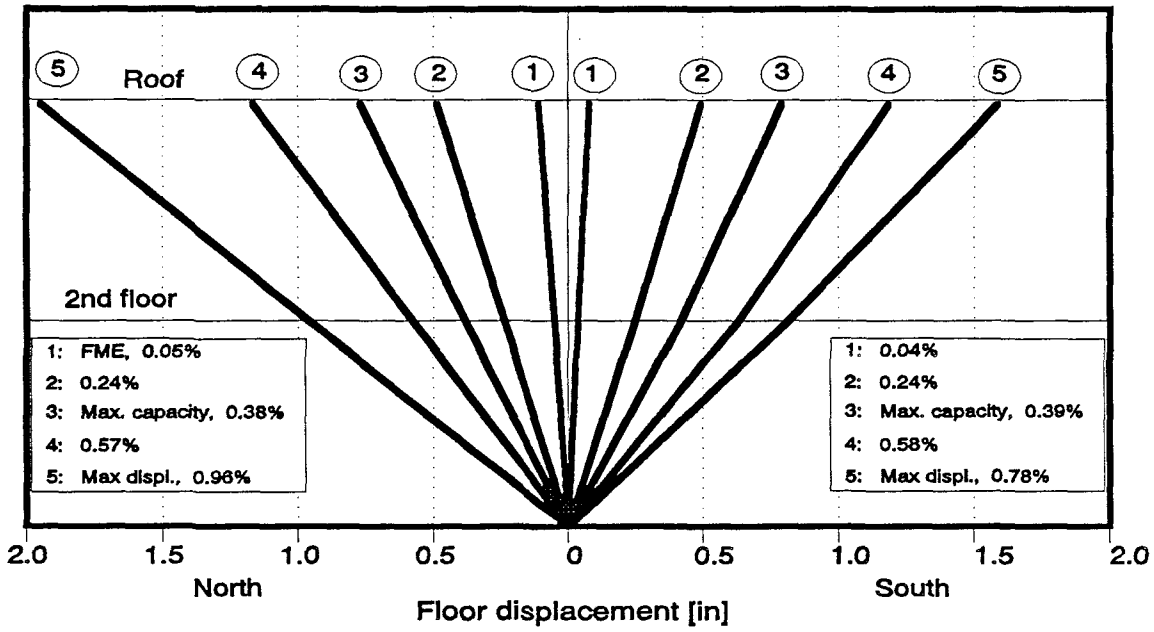

Figure 6.40: Specimen 1b: Displacement profiles for some first peak points.

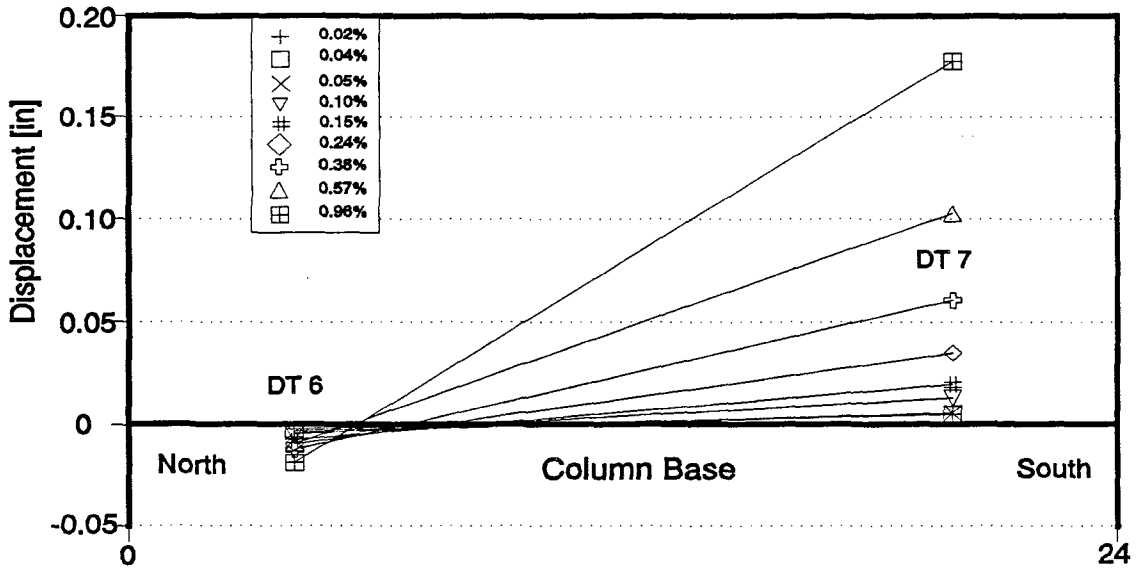

Figure 6.41: Specimen 1b: Flexural deformations at the base of the column, northward loading.

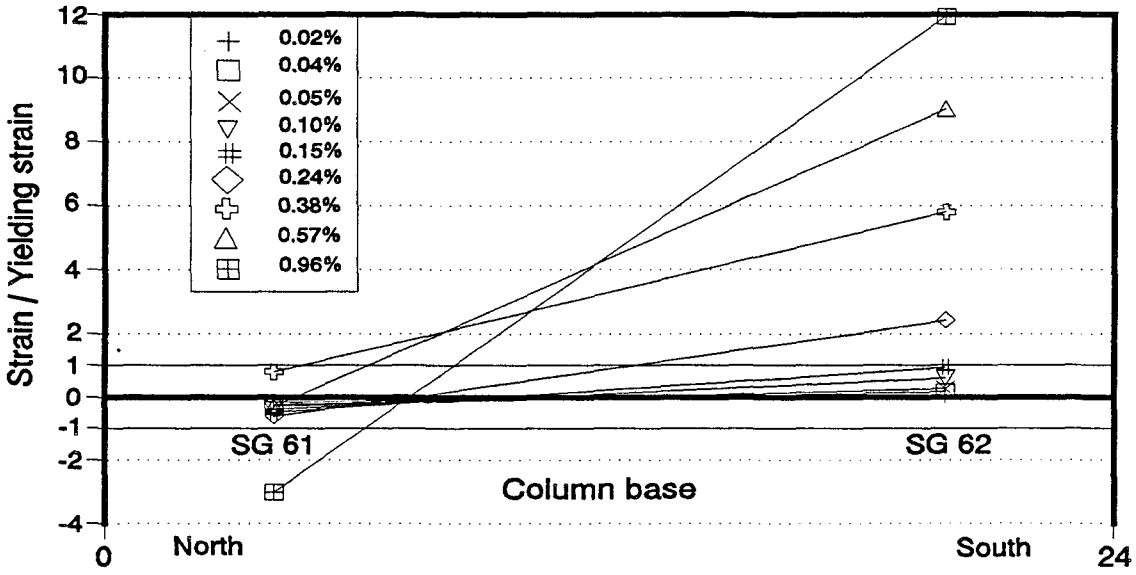

Figure 6.42: Specimen 1b: Strains in longitudinal reinforcement at the base of the column, northward loading.

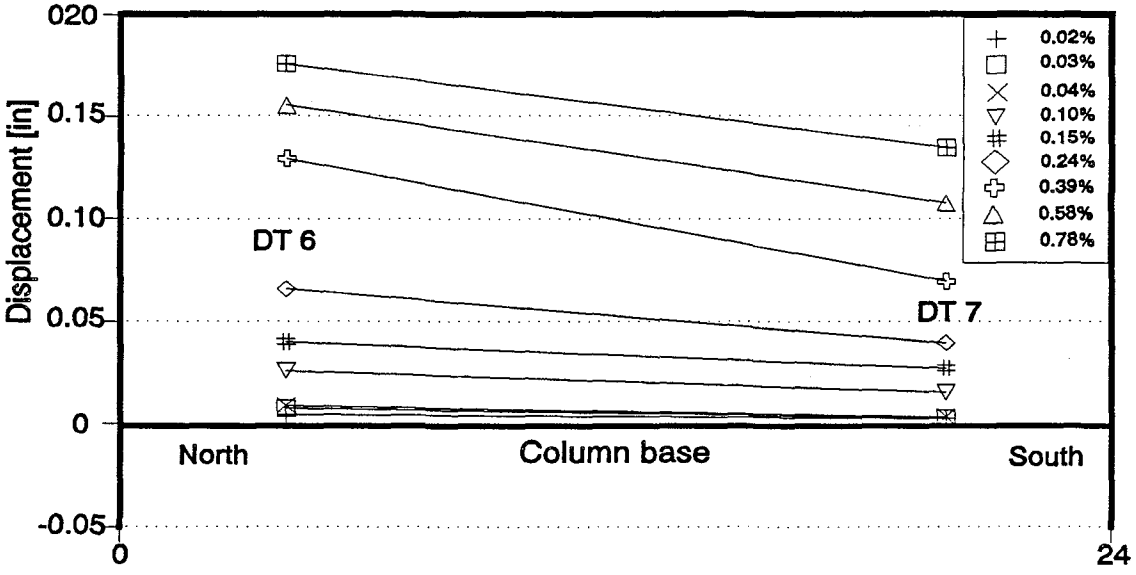

Figure 6.43: Specimen 1b: Flexural deformations at the base of the column, southward loading.

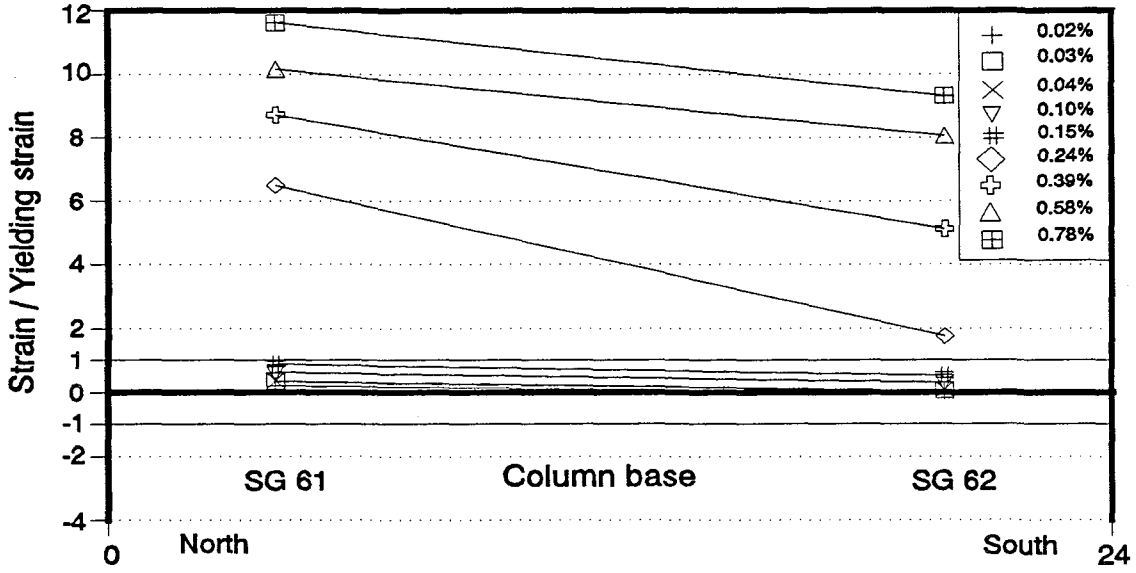

Figure 6.44: Specimen 1b: Strains in longitudinal reinforcement at the base of the column, southward loading.

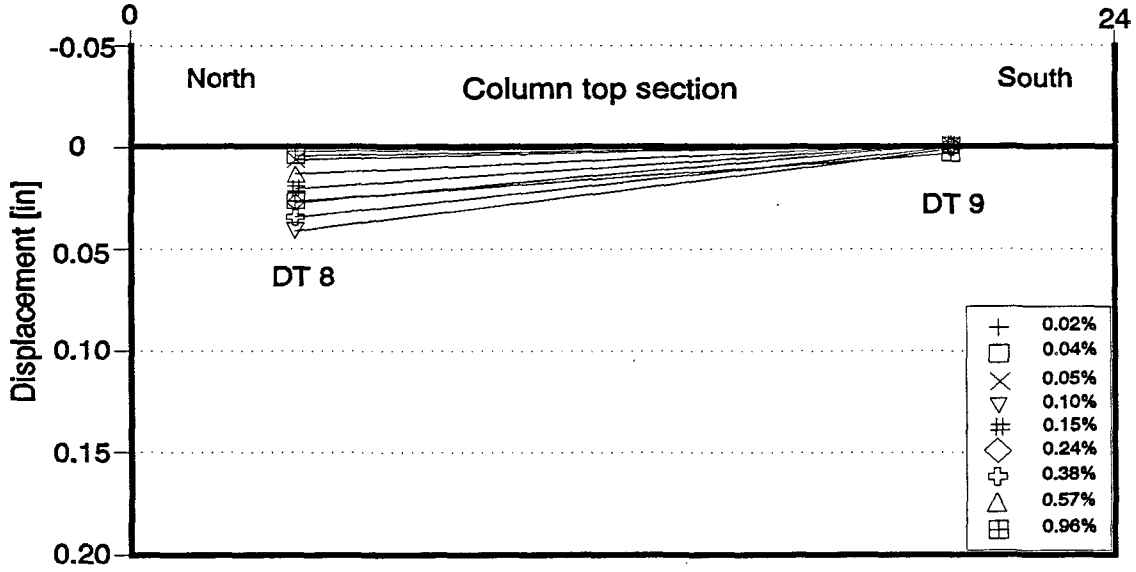

Figure 6.45: Specimen 1b: Flexural deformations at the top section of the column, northward loading.

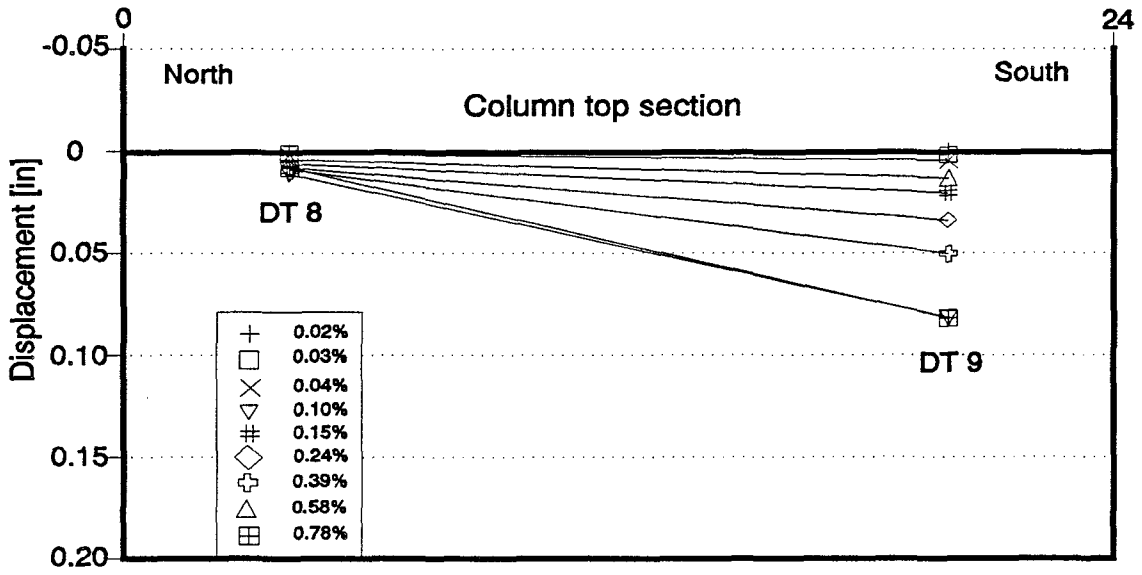

Figure 6.46: Specimen 1b: Flexural deformations at the top section of the column, southward loading.

Displacements and deformations measured at the base of the wall are shown in Figs. 6.47 to 6.50 for some selected first peak points. Flexural deformations at the ends of the base of the wall, measured with displacement transducers 18 and 43, are shown in Figs. 6.47 and 6.49 for northward and southward loading respectively. Distributions of strains in the longitudinal reinforcement at the base of the wall, measured with strain gauges 77, 78, 110 and 111, are shown in Figs. 6.48 and 6.50 for northward and southward loading respectively. The load points have been identified by the overall drift ratio in each figure.

Strains measured at the ends of the debonded portions of the longitudinal reinforcement at the base of the wall, are shown in Figs. 6.51 and 6.52. Each plot includes first peak readings of the two strain gauges on each bar: 77 and 79 for the bar at the north edge of the base wall; and 111 and 112 for the bar at the south edge.

Slipping of the wall base on the foundation beam is shown in Figs. 6.53 and 6.54. The first plot shows first peak slip values versus overall drift ratio. The second figure shows slip as a fraction of the total roof displacement versus the overall drift ratio.

Deformations and strains measured at the end sections of the lintels are shown in Figs. 6.55 to 6.62 for the first peak points. Figs. 6.55, 6.57, 6.59, and 6.61 show readings obtained with displacements transducers intended to measure the angular distortion between the end section of the lintel and the vertical element (pier or column). Figs. 6.56, 6.58, 6.60,

and 6.62 show strains in the top and bottom longitudinal reinforcement of the lintels, measured at the lintel end sections.

6.3.3 Cracking and Yielding Progression Maps. Maps of the cracking and reinforcement yielding progressions, for some selected first peak points, are shown in Figs. 6.63 to 6.74. Cracks were identified and marked as the test was progressing. Shadowed areas in crack maps indicate masonry crushing or spalling off. Yielding points were detected from the readings of the instrumentation system. A diagonal line crossing the reinforcement indicates fracture of the bar. Only the events clearly and unmistakably identified were marked in the yielding maps.

6.3.4 Description of Test Events. A detailed description of the observations made during the test of Specimen 1b is given in this section.

The test was initiated under load control with cycles of 10-kip amplitude. No significant events occurred during this series.

At Load Point 38, corresponding to a base shear of 20.0 kips and overall drift ratio of 0.008% (0.016 in. roof displacement) in north direction (the first north peak of the 20-kip series), flexural cracking initiated in the bottom section of the wall base at the south edge of the specimen.

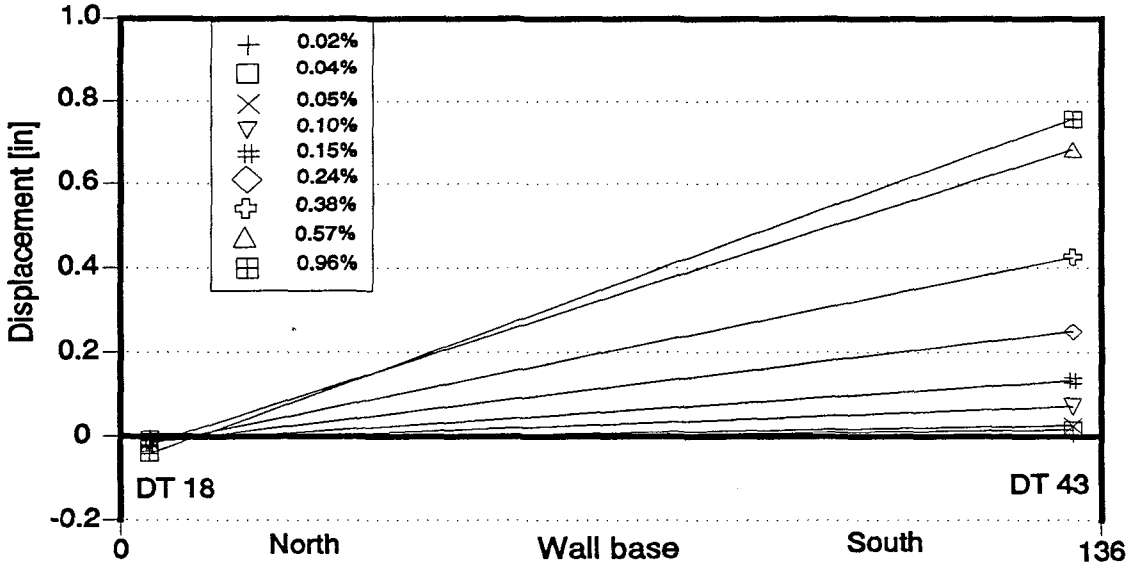

Figure 6.47: Specimen 1b: Flexural deformations at the base section of the wall, northward loading.

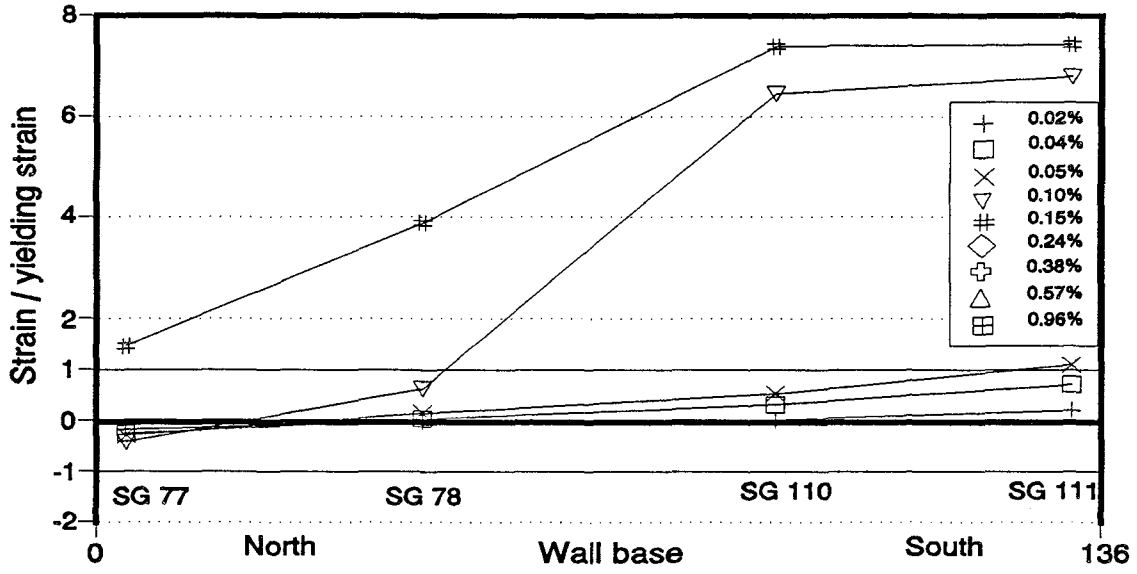

Figure 6.48: Specimen 1b: Strains in longitudinal reinforcement at the base section of the wall, northward loading.

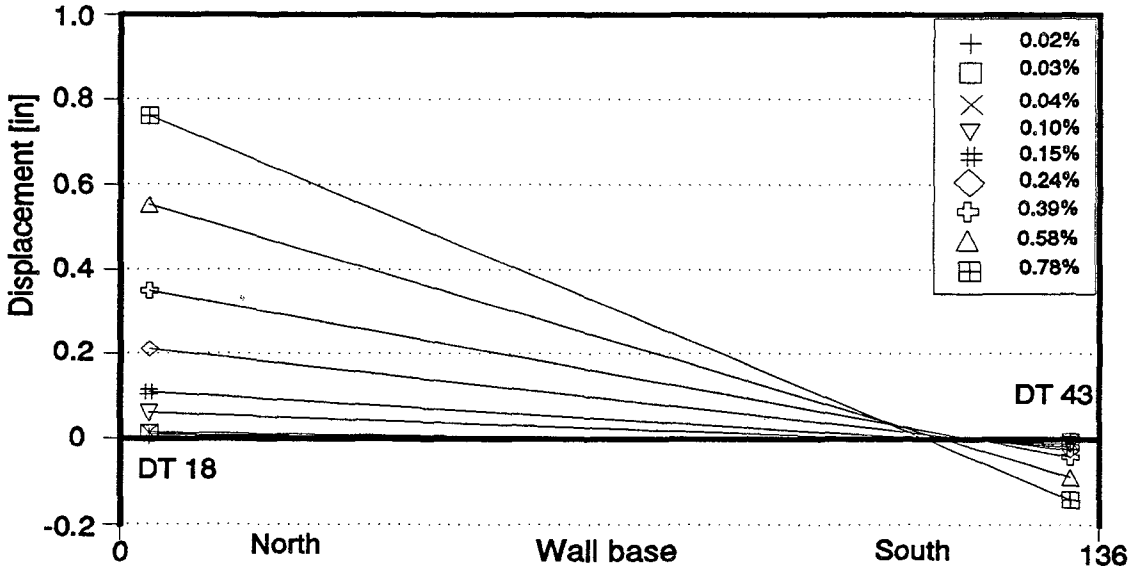

Figure 6.49: Specimen 1b: Flexural deformations at the base section of the wall, southward loading.

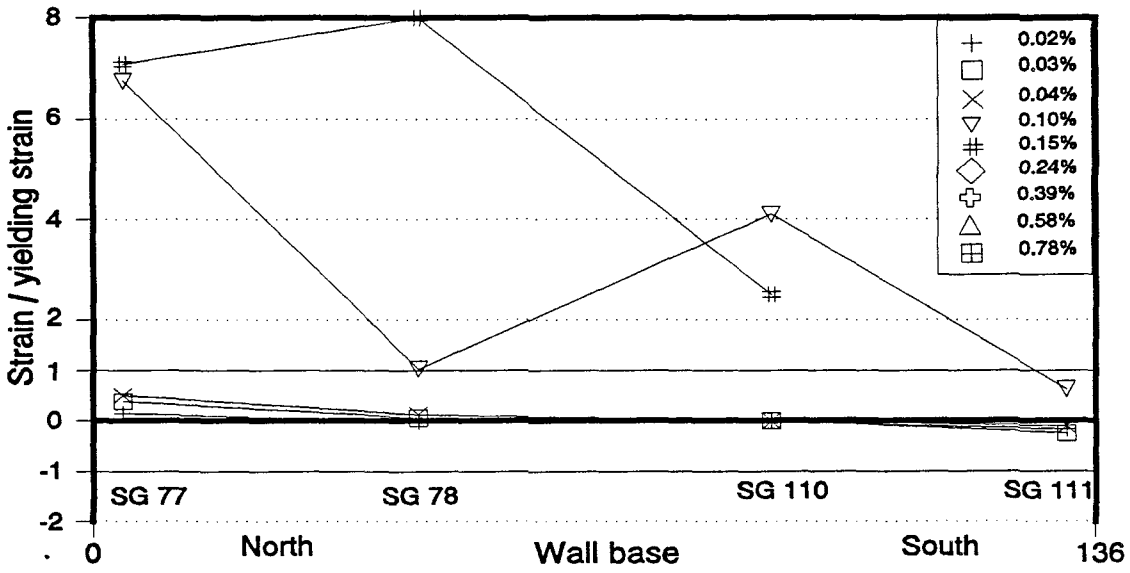

Figure 6.50: Specimen 1b: Strains in longitudinal reinforcement at the base section of the wall, southward loading.

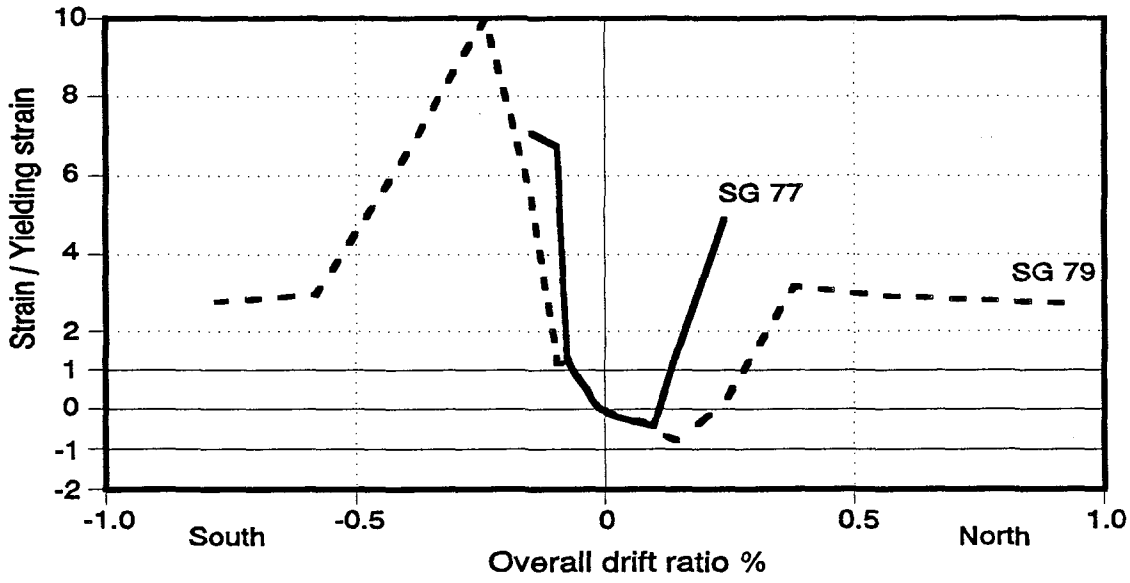

Figure 6.51: Specimen 1b: Strains measured at the end of the debonded portion of the reinforcing bar at the north edge of the wall base.

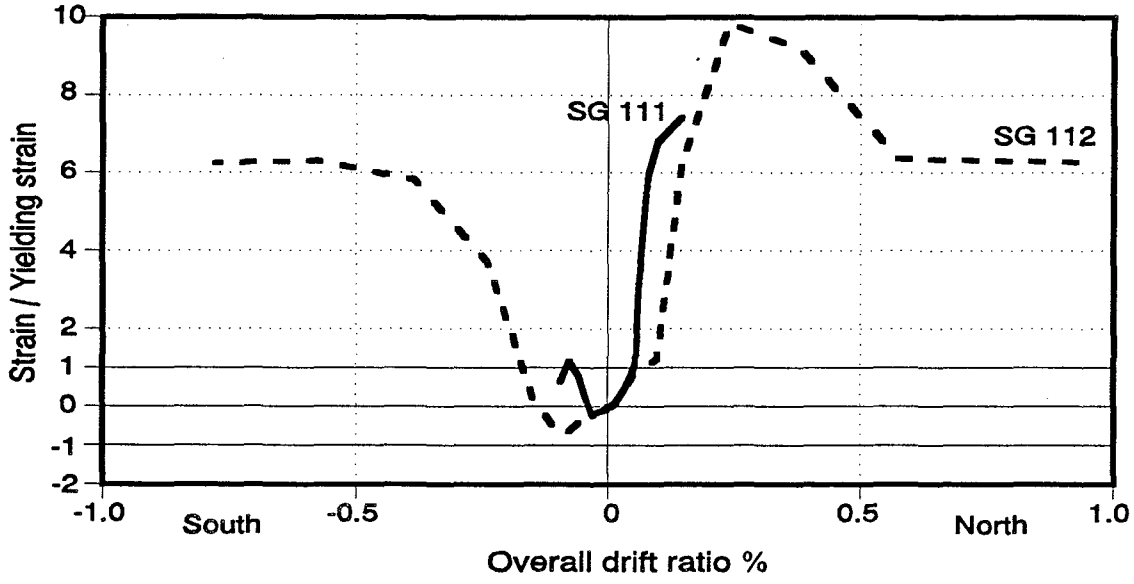

Figure 6.52: Specimen 1b: Strains measured at the end of the debonded portion of the reinforcing bar at the south edge of the wall base.

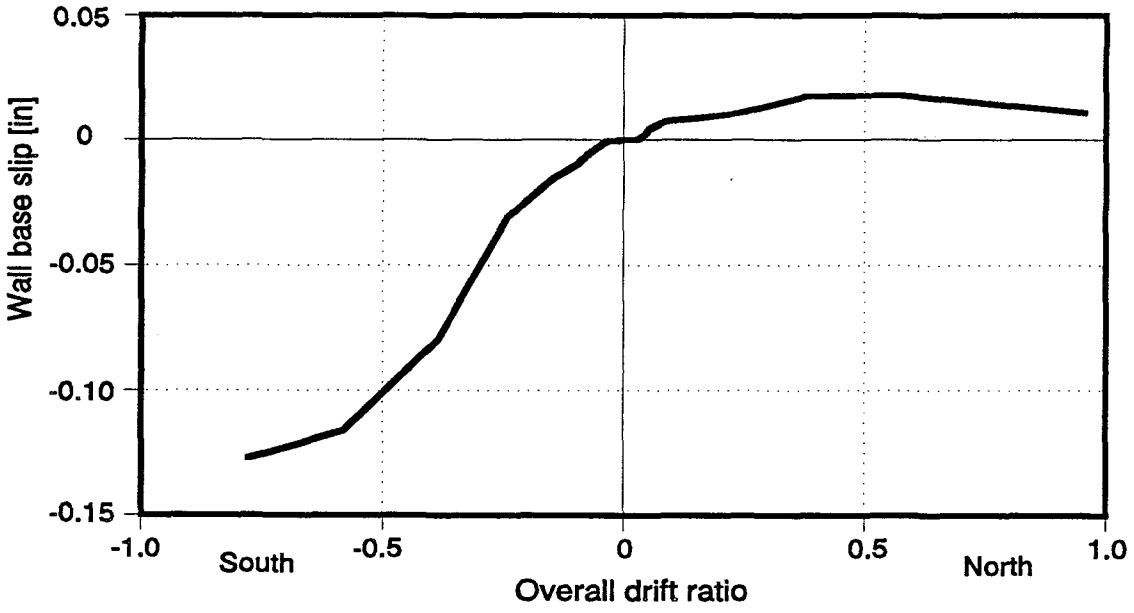

Figure 6.53: Specimen 1b: Slip of the wall base on the foundation beam.

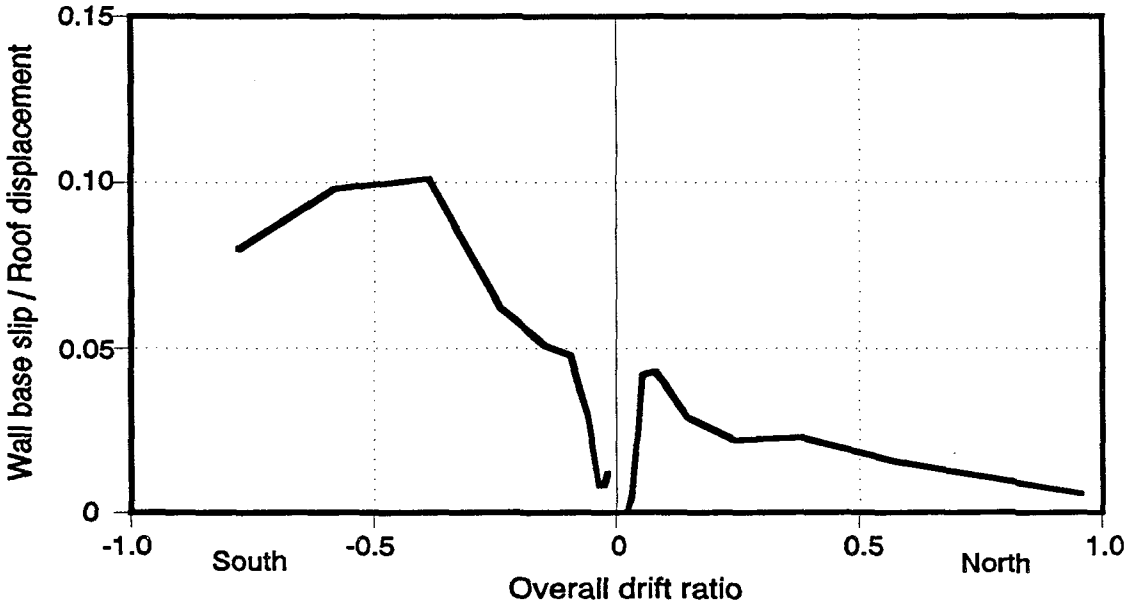

Figure 6.54: Specimen 1b: Slip of the wall base on the foundation beam.

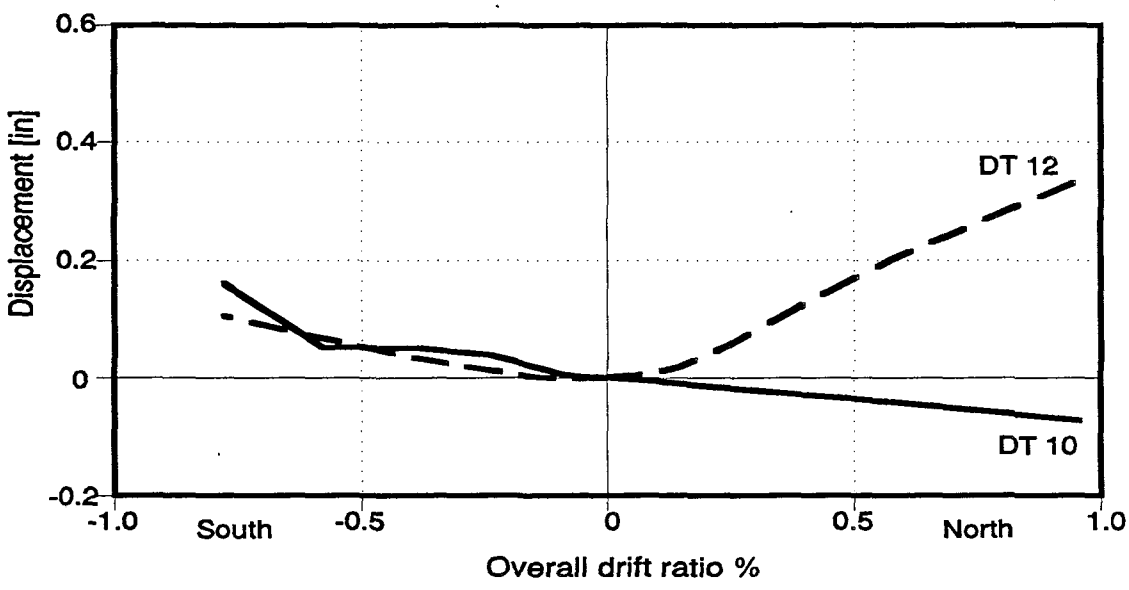

Figure 6.55: Specimen 1b: Deformations at the 1st story lintel-column connection, first peak values.

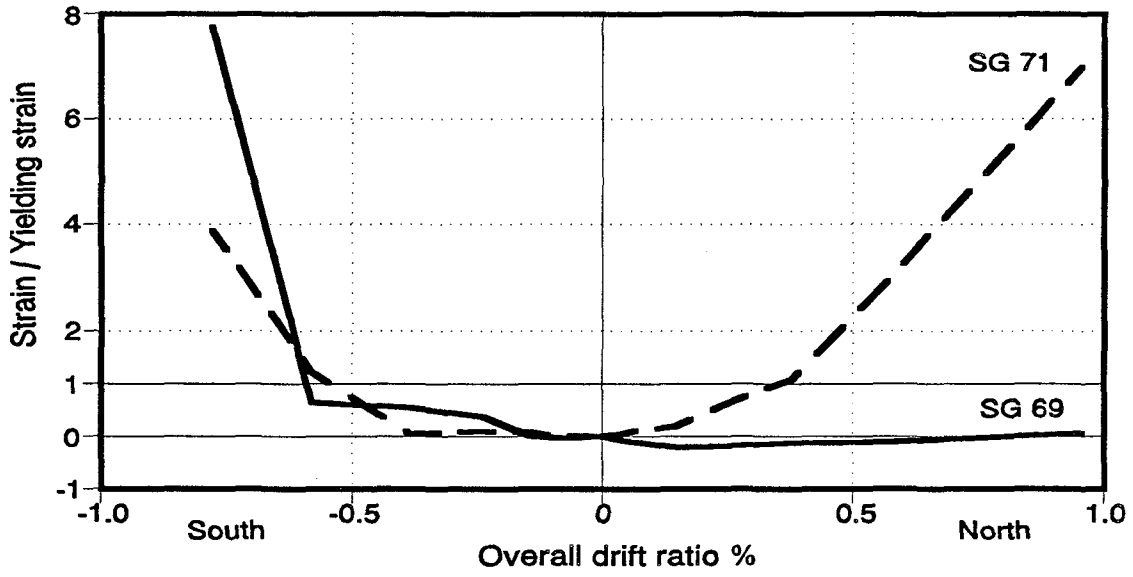

Figure 6.56: Specimen 1b: Strains in the longitudinal reinforcement of the 1st story lintel at the lintel-column connection, first peak values.

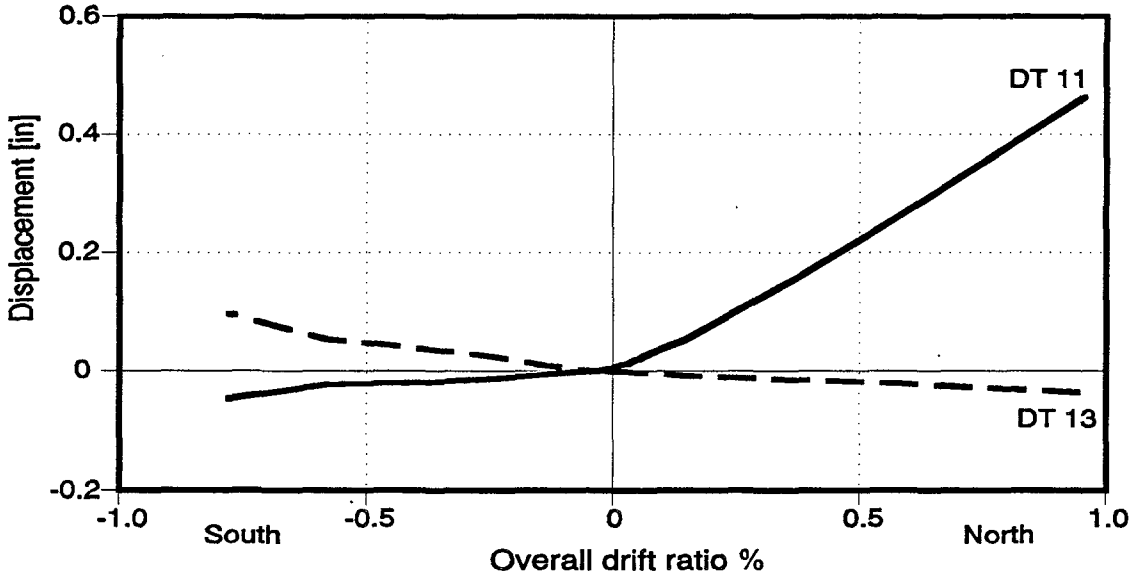

Figure 6.57: Specimen 1b: Deformations at the 1st story lintel-pier connection, first peak values.

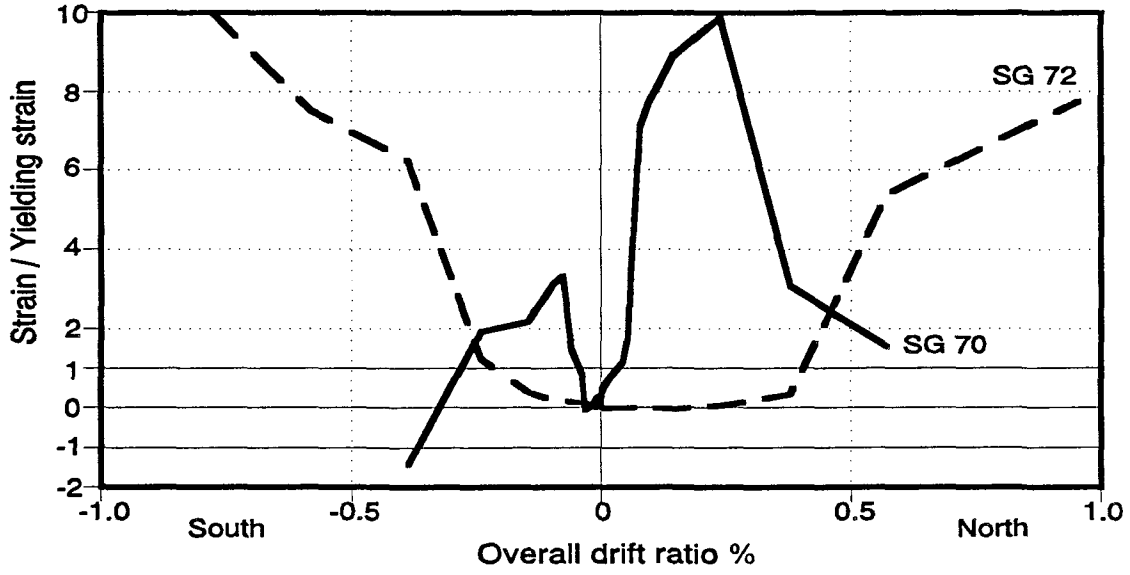

Figure 6.58: Specimen 1b: Strains in the longitudinal reinforcement of the 1st story lintel at the lintel-pier connection, first peak values.

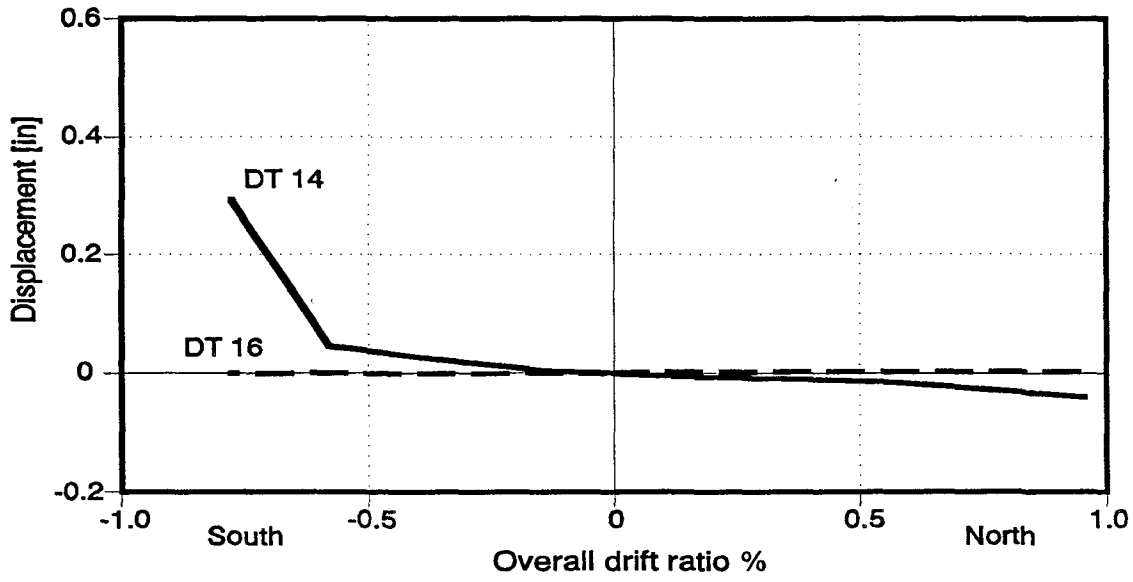

Figure 6.59: Specimen 1b: Deformations at the 2nd story lintel-column connection, first peak values.

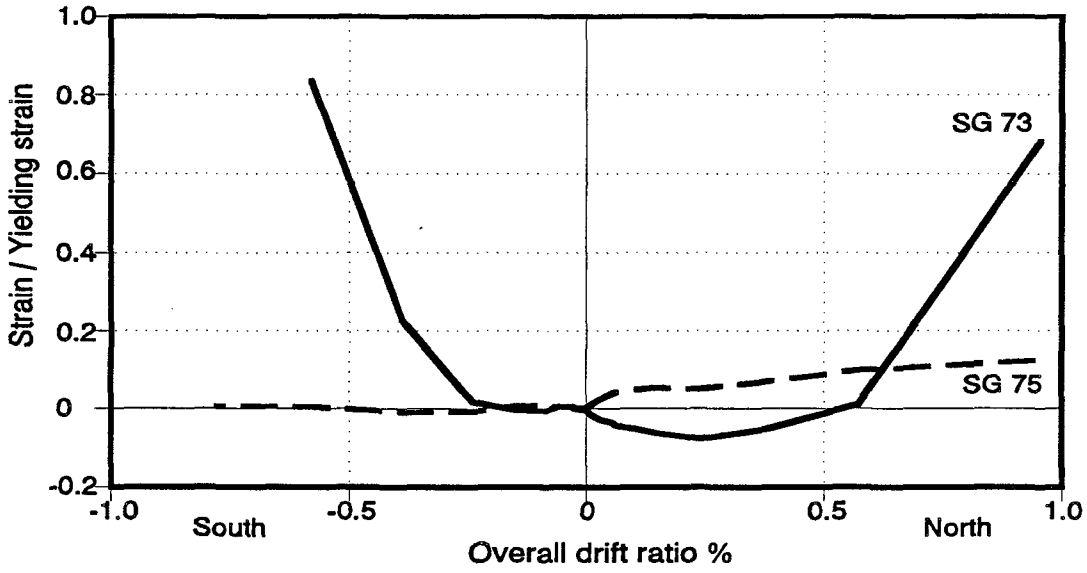

Figure 6.60: Specimen 1b: Strains in the longitudinal reinforcement of the 2nd story lintel at the lintel-column connection, first peak values.

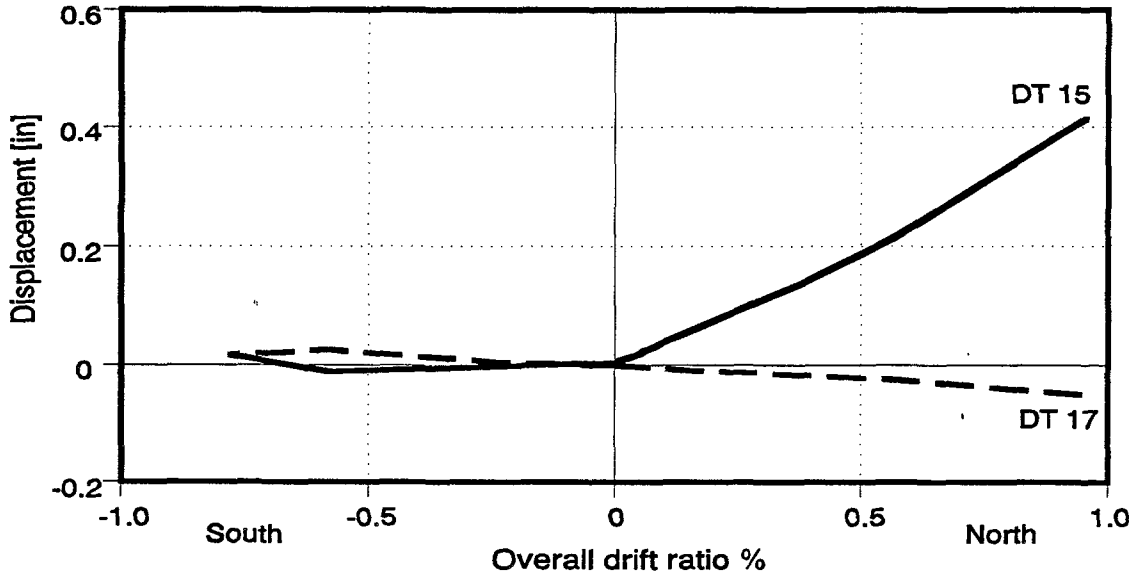

Figure 6.61: Specimen 1b: Deformations at the 2nd story lintel-pier connection, first peak values.

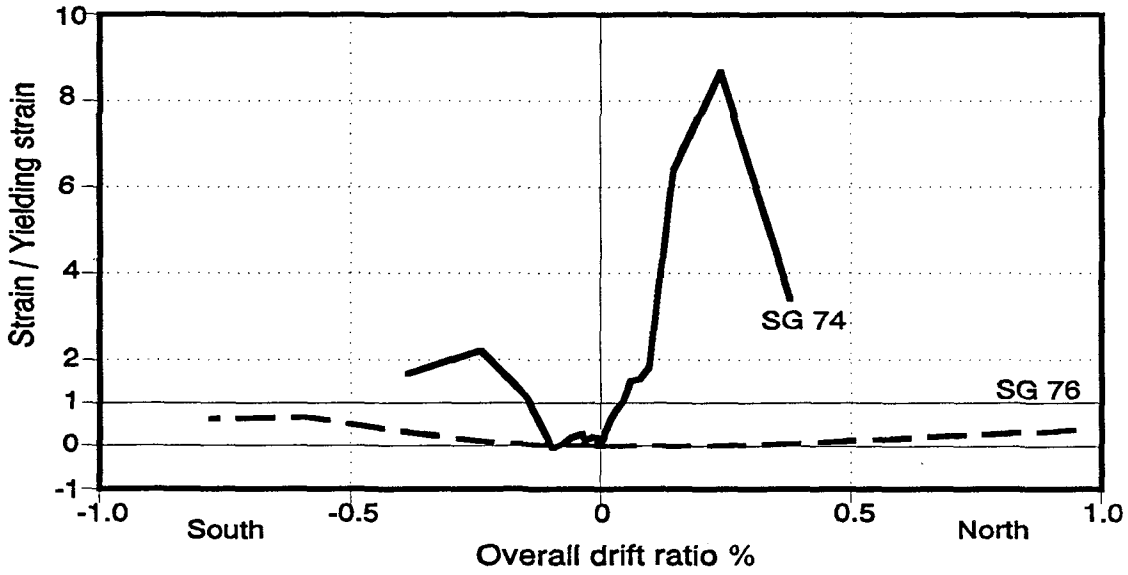

Figure 6.62: Specimen 1b: Strains in the longitudinal reinforcement of the 2nd story lintel at the lintel-pier connection, first peak values.

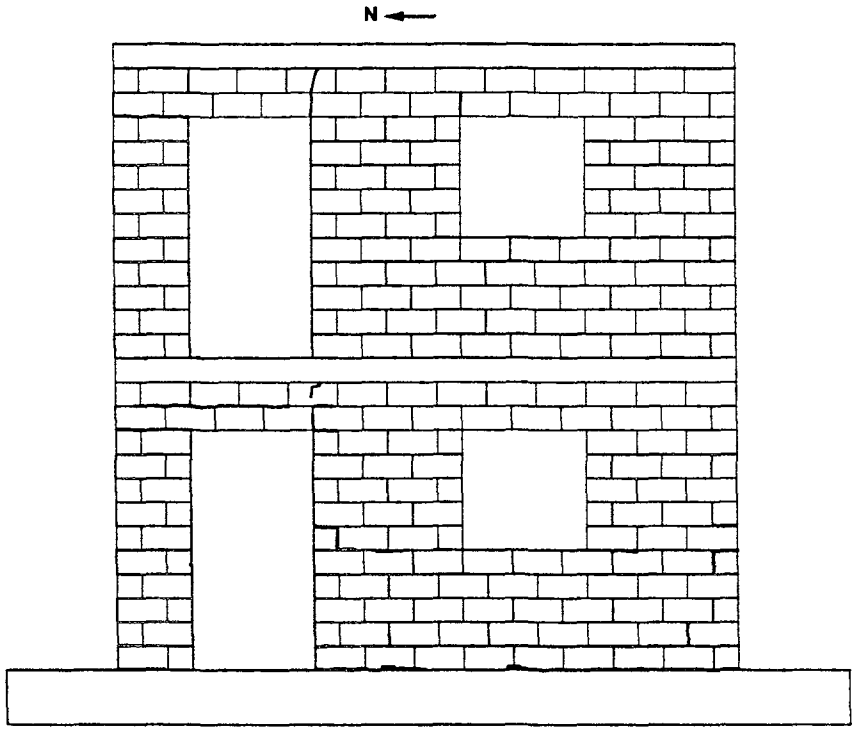

Figure 6.63: Specimen 1b: Cracking progression at FME, overall drift ratio 0.05% north and 0.04% south.

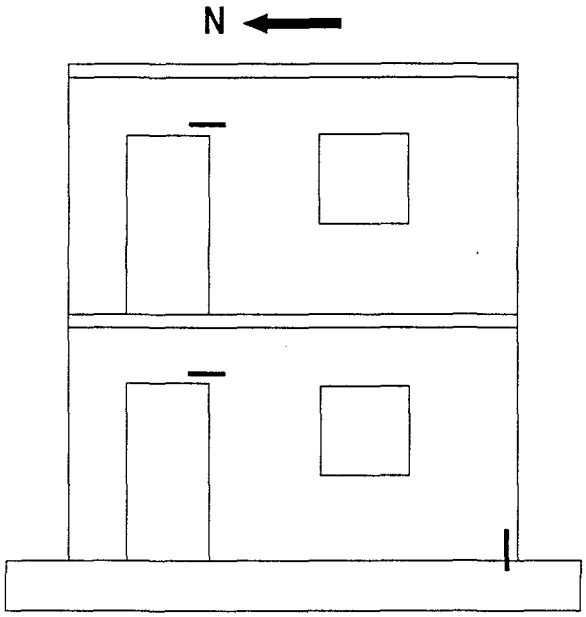

Figure 6.64: Specimen 1b: Yielding progression at FME, overall drift ratio 0.05% north and 0.04% south.

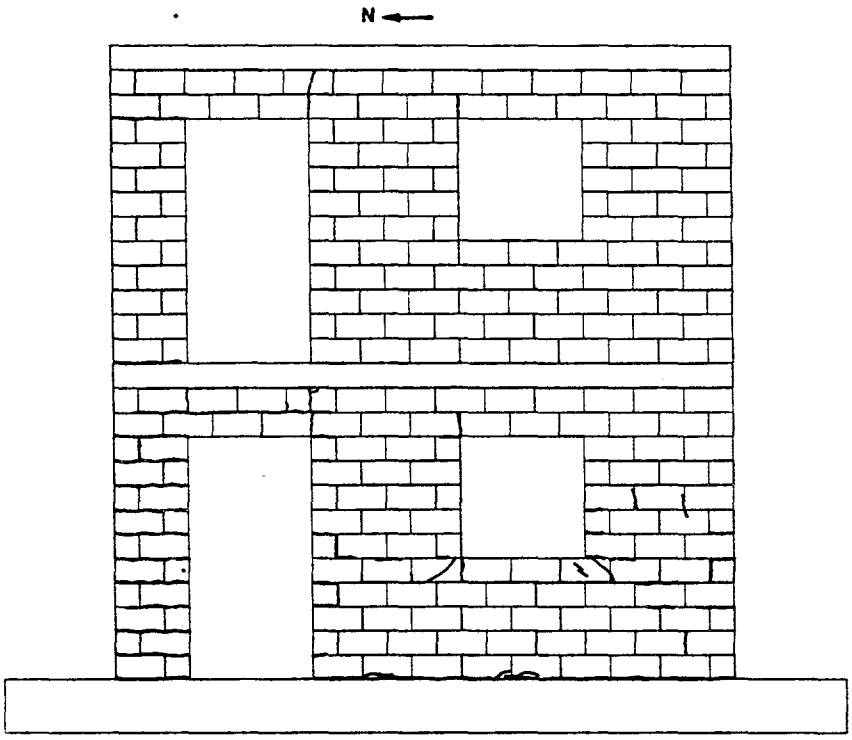

Figure 6.65: Specimen 1b: Cracking progression at overall drift ratio 0.15%.

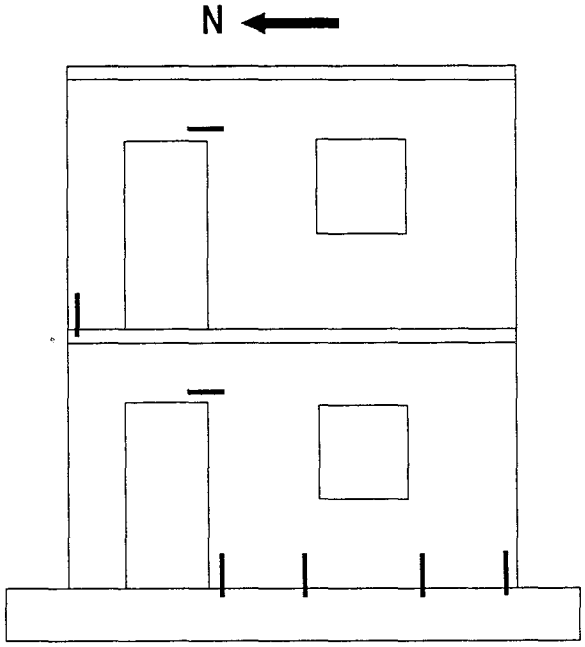

Figure 6.66: Specimen 1b: Yielding progression at overall drift ratio 0.15%.

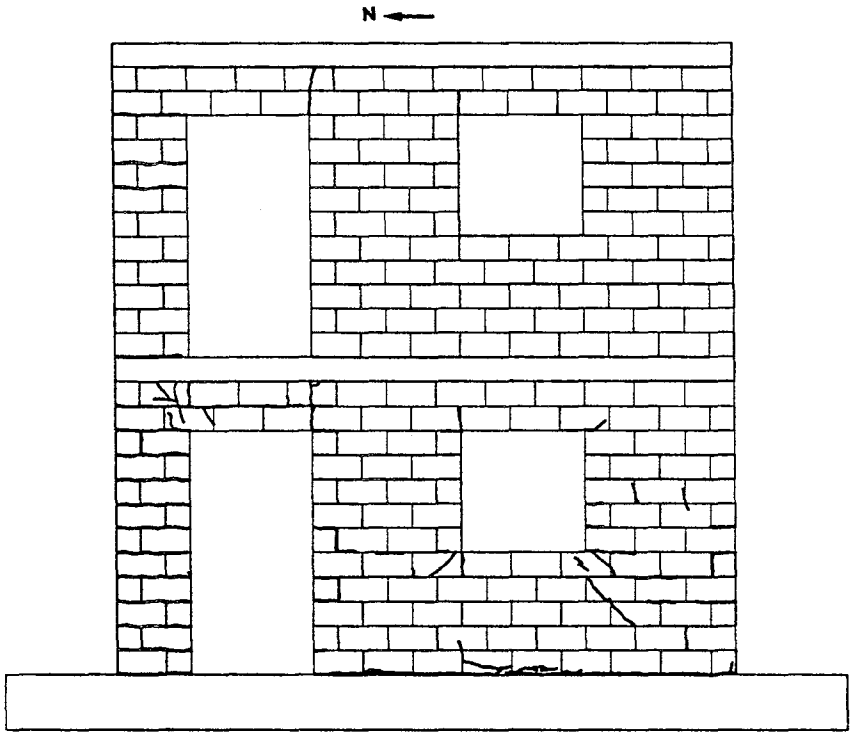

Figure 6.67: Specimen 1b: Cracking progression at overall drift ratio 0.24%.

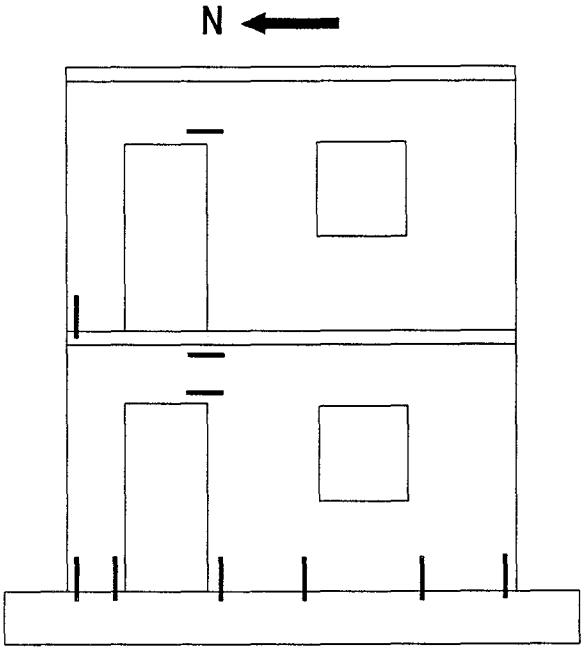

Figure 6.68: Specimen 1b: Yielding progression at overall drift ratio 0.24%.

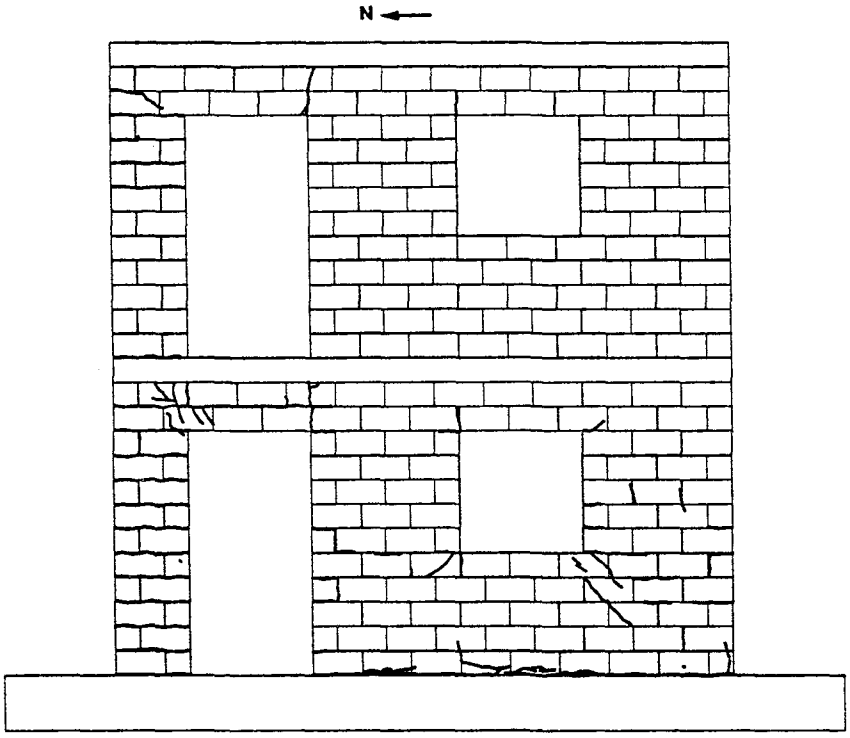

Figure 6.69: Specimen 1b: Cracking progression at overall drift ratio 0.39%.

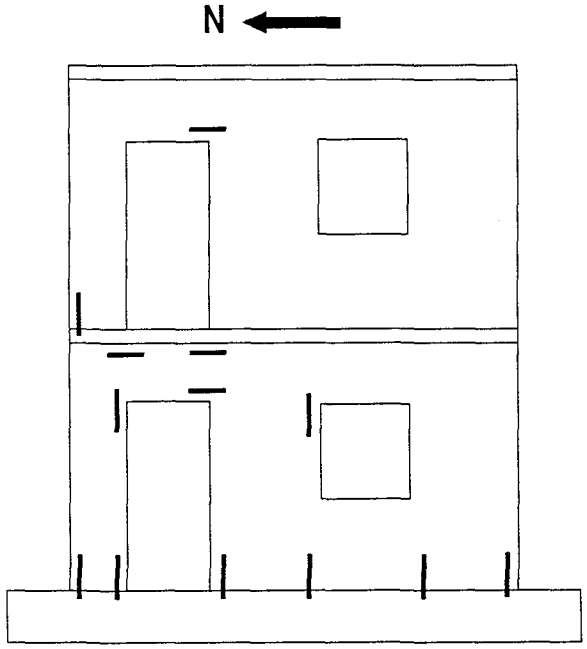

Figure 6.70: Specimen 1b: Yielding progression at overall drift ratio 0.39%.

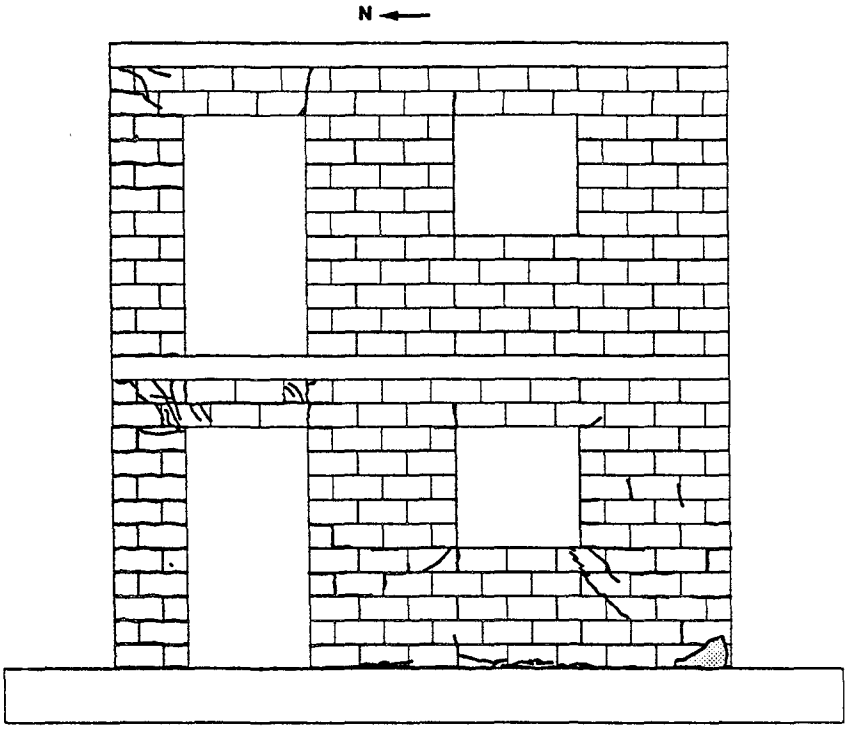

Figure 6.71: Specimen 1b: Cracking progression at overall drift ratio 0.59%.

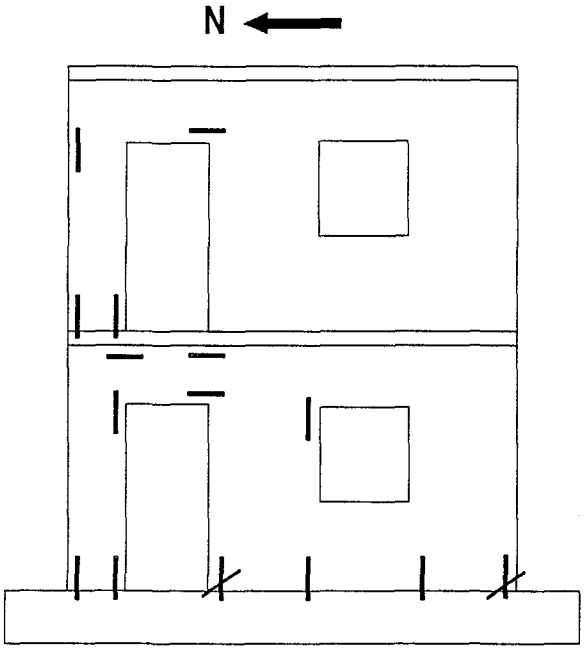

Figure 6.72: Specimen 1b: Yielding progression at overall drift ratio 0.59%.

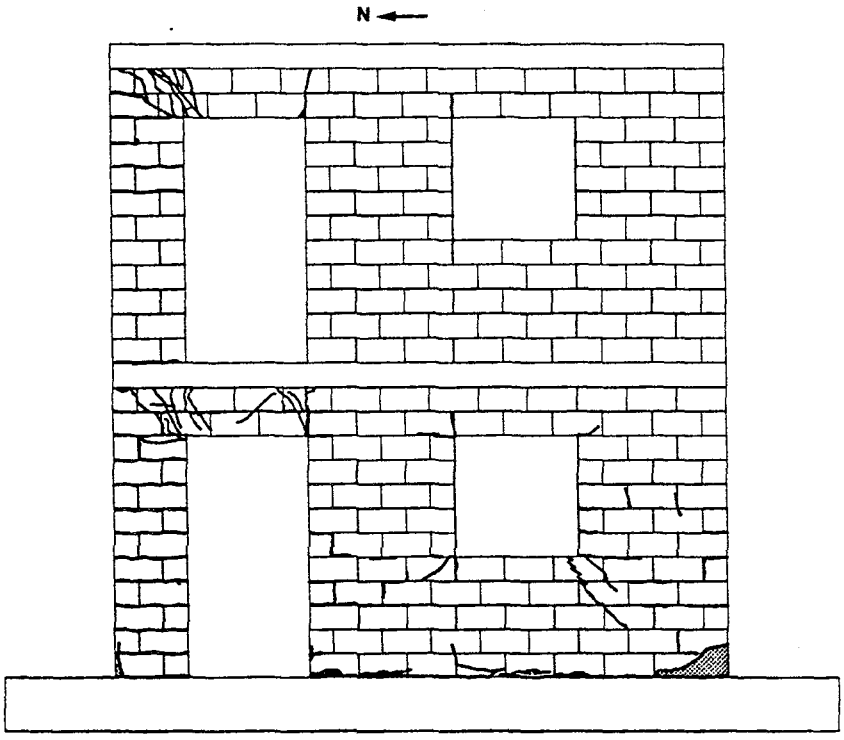

Figure 6.73: Specimen 1b: Cracking progression at end of the test, overall drift ratio 0.96% north and 0.78% south.

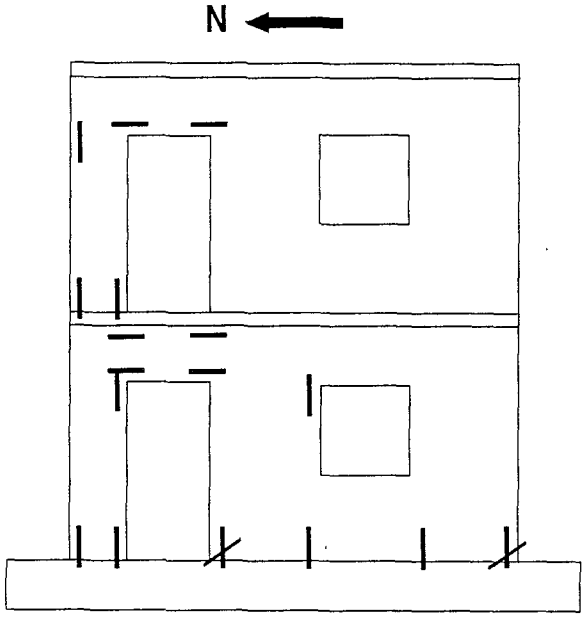

Figure 6.74: Specimen 1b: Yielding progression at end of the test, overall drift ratio 0.96% north and 0.78% south.

At Load Point 47, corresponding to a base shear of 19.6 kips and overall drift ratio of 0.008% (0.016 in. roof displacement) in south direction (the first south peak of the 20-kip series), flexural cracking initiated in the bottom section at the north edge of the wall base and in the north side at the base of the column.

At Load Point 80, corresponding to a base shear of 30.2 kips and overall drift ratio of 0.014% (0.029 in. roof displacement) in north direction (the first north peak of the 30-kip series), a flexural crack formed in the bottom face of the north lintel-pier connection at both stories.

At Load Point 124, corresponding to a base shear of 40.0 kips and overall drift ratio of 0.021% (0.043 in. roof displacement) in north direction (the first north peak of the 40-kip series), the flexural crack in the north lintel-pier connection at the 2nd story progressed toward the slab.

At Load Point 177, corresponding to a base shear of 49.9 kips and overall drift ratio of 0.027% (0.055 in. roof displacement) in south direction (the first south peak of the 50-kip series), a horizontal crack developed in the top section at the 2nd story column. A crack formed in the bottom face of the 2nd story south lintel at the connection of the lintel with the extreme pier.

At Load Point 211, corresponding to a base shear of 55.1 kips and overall drift ratio of 0.037% (0.076 in. roof displacement) in north direction (a point preceding the first north peak of the 60-kip series), the bottom longitudinal reinforcement in the 1st story lintel yielded at the lintel-pier connection.

At Load Point 212, corresponding to a base shear of 59.8 kips and overall drift ratio of 0.043% (0.089 in. roof displacement) in north direction (the first north peak of the 60-kip series), cracks formed in some bed joints at both 1st story piers and at the 1st story lintel. Some non-linearity became evident in the load-displacement plot. The bottom longitudinal reinforcement in the 2nd story lintel yielded at the lintel-pier connection.

The First Major Event (FME) occurred at Load Point 267, corresponding to an overall drift ratio of 0.054% (0.11 in. roof displacement) and base shear of 64.9 kips in north direction. At that point, the longitudinal bar in the south edge of the wall base yielded at the bottom section. The crack at the 2nd story north lintel-pier connection penetrated through the bottom face of the slab.

At Load Point 277, corresponding to a base shear of 64.8 kips and overall drift ratio of 0.038% (0.077 in. roof displacement) in south direction (the first south peak of the 65-kip series), cracking initiated in the top face of the slab at the second floor. The specimen showed larger stiffness when loaded to the south. Test was switched to displacement control mode after completing the 65-kip series.

Cracking and yielding progressions after completing the 65-kip series are shown in Figs. 6.63 and 6.64 respectively.

At Load Point 369, corresponding to an overall drift ratio of 0.060% (0.12 in. roof displacement) and base shear of 79.5 kips in south direction (the first south peak of the 0.12-in series), extensive horizontal cracking occurred in the bed joints at the 1st story column. A horizontal crack developed in the bottom bed joint at the 2nd story column.

At Load Point 450, corresponding to an overall drift ratio of 0.07% (0.14 in. roof displacement) and base shear of 69.5 kips in north direction (a point preceding the first north peak of the 0.16-in series), a diagonal crack developed in the wall base in the vicinity of the bottom north corner of the window opening.

At Load Point 451, corresponding to an overall drift ratio of 0.078% (0.16 in. roof displacement) and base shear of 72.6 kips in north direction (the first north peak of the 0.16-in series), cracking in the bottom face of the roof slab progressed to the edge of the slab. The second longitudinal bar in the south side of the wall base yielded at the bottom section.

At Load Point 461, corresponding to an overall drift ratio of 0.077% (0.16 in. roof displacement) and base shear of 87.6 kips in south direction (the first south peak of the 0.16-in series), cracking occurred in the top face of the roof slab at the lintel-pier connection. Diagonal cracking initiated in the wall base in the vicinity of the bottom south corner of the window opening. Horizontal cracking in the base of the wall extended along the length of the bottom section. The longitudinal reinforcement in the north edge of the wall base yielded at the bottom section.

At Load Point 544, corresponding to an overall drift ratio of 0.097% (0.20 in. roof displacement) and base shear of 76.2 kips in north direction (the first north peak of the 0.20-in series), cracking initiated in the bottom face of the 2nd floor slab at the lintel-pier connection.

At Load Point 555, corresponding to an overall drift ratio of 0.096% (0.20 in. roof displacement) and base shear of 95.1 kips in south direction (the first south peak of the 0.20-in series), horizontal cracking progressed in the bed joints at the 1st story column. The second longitudinal bar in the north side of the wall base yielded at the bottom section.

At Load Point 647, corresponding to an overall drift ratio of 0.12% (0.25 in. roof displacement) and base shear of 102.8 kips in south direction (a point preceding the first south peak of the 0.30-in series), the longitudinal reinforcement in the north edge of the column yielded at the 2nd story base section.

Cracking and yielding progressions after completing the 0.30-in series are shown in Figs. 6.65 and 6.66 respectively.

At Load Point 730, corresponding to an overall drift ratio of 0.19% (0.39 in. roof displacement) and base shear of 82.9 kips in north direction (a point preceding the first north peak of the 0.50-in series), the longitudinal reinforcement in the north edge of the column yielded at the base section.

At Load Point 731, corresponding to an overall drift ratio of 0.24% (0.49 in. roof displacement) and base shear of 86.0 kips in north direction (the first north peak of the 0.50-in series), diagonal cracking initiated in the lintel-column connection at the 1st story and propagated through the 2nd floor slab. Damage initiated in the column-slab connection at the 2nd floor.

At Load Point 740, corresponding to an overall drift ratio of 0.19% (0.39 in. roof displacement) and base shear of 122.8 kips in south direction (a point preceding the first south peak of the 0.50-in series), diagonal cracking in the lintel-column connection at the 1st story progressed. Horizontal cracking occurred in the top bed joints at the 2nd story column. Crushing of masonry initiated at the south end of the wall base. The longitudinal reinforcement in the south edge of the column yielded at the base section.

At Load Point 741, corresponding to an overall drift ratio of 0.24% (0.49 in. roof displacement) and base shear of 133.7 kips in south direction (the first south peak of the 0.50-in series), diagonal cracking in the wall base progressed under the extreme pier. The top longitudinal reinforcement in the 1st story lintel yielded at the lintel-pier connection.

Cracking and yielding progressions after completing the 0.50-in series are shown in Figs. 6.67 and 6.68 respectively.

At Load Point 823, corresponding to an overall drift ratio of 0.38% (0.77 in. roof displacement), the first north peak of the 0.80-in series, the specimen reached its maximum lateral load capacity of 89.9 kips in north direction. Damage progressed in the column-slab connection at the 2nd floor, and diagonal cracking initiated in the lintel-column connection at the 2nd story. The top longitudinal reinforcement in the 1st story lintel yielded at the lintel-column connection.

At Load Point 831, corresponding to an overall drift ratio of 0.24% (0.49 in. roof displacement) and base shear of 126.9 kips in south direction (a point preceding the first south peak of the 0.80-in series), the longitudinal reinforcement in the south edge of the column yielded at the 1st story top section.

At Load Point 833, corresponding to an overall drift ratio of 0.39% (0.79 in. roof displacement), the first south peak of the 0.80-in series, the specimen reached its maximum lateral load capacity of 145.0 kips in south direction. Vertical splitting and crushing of masonry progressed at the south end of the wall base. The longitudinal reinforcement in the south edge of the column yielded at the 2nd story base section. The longitudinal reinforcement in the south edge of the 1st story center pier yielded at the top section.

Cracking and yielding progressions after the specimen reached its maximum lateral capacity in both directions are shown in Figs. 6.69 and 6.70 respectively.

At Load Point 865, corresponding to an overall drift ratio of 0.29% (0.59 in. roof displacement) and base shear of 73.2 kips in north direction (a point preceding the second north peak of the 0.80-in series), the bar at the south edge of the wall base fractured at the bottom section.

At Load Point 906, corresponding to an overall drift ratio of 0.37% (0.76 in. roof displacement) and base shear of 119.7 kips in south direction (a point preceding the last south peak of the 0.80-in series), the bar at the north edge of the wall base fractured at the bottom section.

At Load Point 916, corresponding to an overall drift ratio of 0.52% (1.07 in. roof displacement) and base shear of 82.1 kips in north direction (a point preceding the first north peak of the 1.20-in series), diagonal cracking progressed in the lintel-column connection at the 1st story. Crushing of masonry initiated at the north end of the wall base.

At Load Point 917, corresponding to an overall drift ratio of 0.57% (1.17 in. roof displacement) and base shear of 83.3 kips in north direction (the first north peak of the 1.20-in series), the longitudinal reinforcement in the north edge of the column yielded at the 2nd story top section.

Cracking and yielding progressions after completing the 1.20-in series are shown in Figs. 6.71 and 6.72 respectively.

At Load Point 961, corresponding to an overall drift ratio of 0.33% (0.67 in. roof displacement) and base shear of 62.7 kips in north direction (a point preceding the second north peak of the 1.20-in series), a loud noise and a jump in the force-displacement curve seemed to indicate fracture of a steel bar.

At Load Point 963, corresponding to an overall drift ratio of 0.57% (1.17 in. roof displacement) and base shear of 74.5 kips in north direction (the second north peak of the 1.20-in series), damage initiated in the slab-wall connection at the roof north corner of the specimen.

At Load Point 971, corresponding to an overall drift ratio of 0.58% (1.18 in. roof displacement) and base shear of 130.1 kips in south direction (the second south peak of the 1.20-in series), the bottom longitudinal reinforcement in the 2nd story lintel yielded at the lintel-column connection.

At Load Point 1013, corresponding to an overall drift ratio of 0.96% (1.95 in. roof displacement) and base shear of 72.0 kips in north direction (the first north peak of the

2.00-in series), crushing initiated in the base of the column. Damage continued progressing in the column-slab connections.

At Load Point 1020, corresponding to an overall drift ratio of 0.23% (0.48 in. roof displacement) and base shear of 57.4 kips in south direction (a point preceding the first south peak of the 2.00-in series), the bottom longitudinal reinforcement in the 1st story lintel yielded at the lintel-column connection.

At Load Point 1025, corresponding to an overall drift ratio of 0.78% (1.59 in. roof displacement) and base shear of 108.9 kips in south direction (a point preceding the first south peak of the 2.00-in series), extensive cracking and damage occurred at the lintel-column connection at the 2nd story. Wide diagonal cracks and crushing of masonry initiated in the lintel. Concrete in the slab-wall connection at the roof north corner of the specimen started to suffer crushing. While the damage was localized in a small portion of the specimen, it was occurring in areas no restrained by reinforcement. The test was stopped after this cycle.

Cracking and yielding conditions of the specimen after completing the test are shown in Figs. 6.73 and 6.74 respectively.

7. DISCUSSION OF TEST RESULTS FOR PERFORATED WALL SPECIMENS

In this chapter, test results of the perforated wall Type 1 specimens are discussed. The results are reviewed in terms of the failure mechanism and the load-displacement response of the specimens.

This discussion is based on the description of the results given in Chapter 6. Visual observations, load-displacement curves obtained directly during each test, and readings from the data acquisition system are used to describe the results. Instrumentation channels are designated as described in Section 4.3. The elements of the specimens are designated as shown in Fig. 6.1. Within each load-displacement series, the cycles and peaks are denominated as defined in Section 6.1 and as shown in Fig. 6.2.

7.1 Lateral Load Capacity and Failure Mode

The expected mode of failure and predicted monotonic lateral load capacity for each Type 1 specimen have been described in Chapter 5. Experimental lateral load capacity of each specimen has been defined as the maximum base shear obtained from the load-displacement history, for each direction of the loading process. Predicted values of lateral load capacity were calculated in advance of each test and used to design the specimens. Predicted and experimental values of the specimens' lateral load capacity are summarized in Table 7.1. Differences between the expected behavior and the test results are discussed in this section.

Table 7.1: Lateral load capacity of Type 1 specimens

Specimen	North		South	
	Predicted [kips]	Experimental [kips]	Predicted [kips]	Experimental [kips]
1a	98.3	98.2	122.1	104.5
1b	88.0	89.9	130.0	145.0

7.1.1 Lateral Load Capacity and Failure Mode of Specimen 1a. The lateral load capacity of Specimen 1a was 98.2 kips at an overall drift ratio of 0.39% (0.80 in. roof displacement) when loaded to the north, and 104.5 kips at an overall drift ratio of 0.39% (0.79 in. roof displacement) when loaded to the south.

The spread of cracking in Specimen 1a before reaching the specimen's lateral load capacity is shown in Fig. 6.29: diagonal cracks had initiated in both piers; extensive diagonal cracking had occurred in the wall base under both piers; cracking had occurred in the lintel-pier connections at both stories and in the column bed joints; and horizontal splitting of the masonry had occurred in the window sill. As shown in Fig. 6.30, the longitudinal reinforcement had yielded in both end sections of all 1st story vertical elements.

Collapse Mechanism and Lateral Load Capacity of Specimen 1a for Northward Loading

At the time the specimen reached its north lateral load capacity, wide bed-joint cracks had opened at top and bottom of both piers, and strains in the longitudinal reinforcement were larger than yielding strain at those locations, as shown in Figs. 6.16 and 6.17, and 6.20 and 6.21 for the center and extreme pier respectively. A wide crack extended from the south end of the base of the extreme pier into the first course of the base wall, out of the reach of the instrumentation, as shown in Fig. 6.31. As shown in Figs. 6.8 and 6.32, longitudinal reinforcement yielded at top and bottom of the column. Longitudinal reinforcement at the base of the wall did not yield, as shown in Figs. 6.11 and 6.32.

The large opening of the bed-joint crack under the extreme pier suggested that this element was subjected to almost pure tensile axial force at its base at the time the specimen developed its lateral load capacity. At the same time, it was evident that plastic flexural hinges developed at the end sections of the center pier and column. The resultant mechanism is shown in Fig. 7.1. These results were in good agreement with the assumed collapse mechanism for Specimen 1a, as described in Section 5.4. As shown in Table 7.1, the calculated lateral load capacity was a very good prediction of the specimen's ultimate capacity.

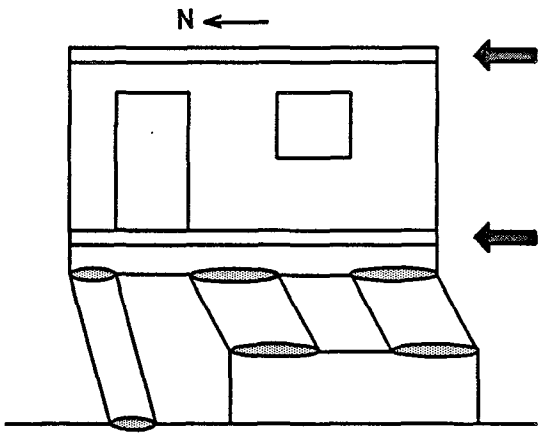

Figure 7.1: Observed collapse mechanism for Specimen 1a; Northward loading.

Collapse Mechanism and Lateral Load Capacity of Specimen 1a for Southward Loading

At the time the specimen reached its south lateral load capacity, wide cracks had opened at the bed joints in the column, specially at the base section, as shown in Fig. 6.7. As shown in Figs. 6.18 and 6.19, wide cracks had opened at the top and bottom of the center pier, and strains in the longitudinal reinforcement at those sections were larger than yielding strain. Most of the deformations in the extreme pier were due to rotation about the section defined by the crack on the top course of the base beam, as previously described. However, the instruments were not able to measure those deformations, as shown in Figs.

6.22 and 6.23. Diagonal cracks under the extreme pier extended and opened significantly. As shown in Figs. 6.12 and 6.32, longitudinal reinforcement in the north side of the base of the wall yielded.

The large opening and distribution of cracks in the column and center pier suggested that these elements were subjected to almost pure tensile axial force at the time the specimen developed its lateral load capacity. However, each element showed a different pattern of behavior. Horizontal cracks formed in most of the bed joints of the column, indicating that the axial deformations were distributed over the entire height of this element. The wide cracks at the top and bottom of the center pier indicated that most of the axial deformations were concentrated in those sections.

Deformations and damage conditions of the column and center pier agreed with the conditions of the expected collapse mechanism, as described in Section 5.4. As expected, a plastic hinge clearly formed at the bottom of the extreme pier. However, as shown in Figs. 6.12, 6.23, 6.32, and 7.2, the evidence indicated that the last plastic hinge needed to define the collapse mechanism formed at the base of the wall instead of at the top of the pier as expected. Thus, the observed collapse mechanism that defined the lateral load capacity for Specimen 1a, when loaded to the south, was basically a cantilever wall connected through the lintels to a strut, as shown in Fig. 7.3.

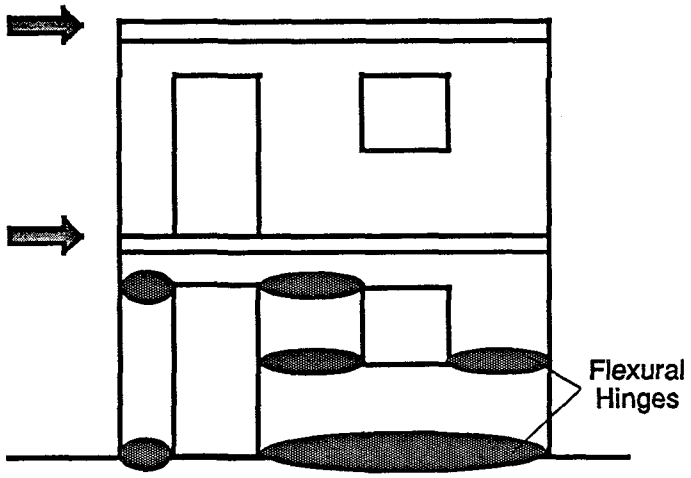

Figure 7.2: Observed plastic hinging regions at the time Specimen 1a reached its southward lateral capacity.

The predicted south lateral load capacity of 122.1 kips for the assumed collapse mechanism, as described in Section 5.4, was larger than the specimen's ultimate load of 104.5 kips, as shown in Table 7.1. To maintain consistency with the calculations made before the test, the south lateral load capacity of the specimen was recalculated for the mechanism shown in Fig. 7.3 using the same material properties as in the original calculations, and following the process outlined in Section 5.5.2. Assuming that the column had developed its expected axial yielding capacity of 15.8 kips with zero flexural capacity, the axial force transmitted through the lintels would have been 26.1 kips, the total axial compressive force on the wall base 125.8 kips, and the wall flexural capacity 12,993 kip-in. The ultimate load for that mechanism, calculated using Eq. (5.16), would have been **106.1 kips**. This value showed a better agreement with the specimen's lateral load capacity of 104.5 kips.

As expected, the lateral load capacity calculated for the observed mechanism, 106.1 kips, was lower than that originally calculated in Section 5.4.2 of 122.1 kips. The collapse mechanism did not develop as expected because the wall base showed a flexural capacity lower than anticipated. In addition to that, the column was not able to develop its full axial tensile capacity, as discussed later in this Section.

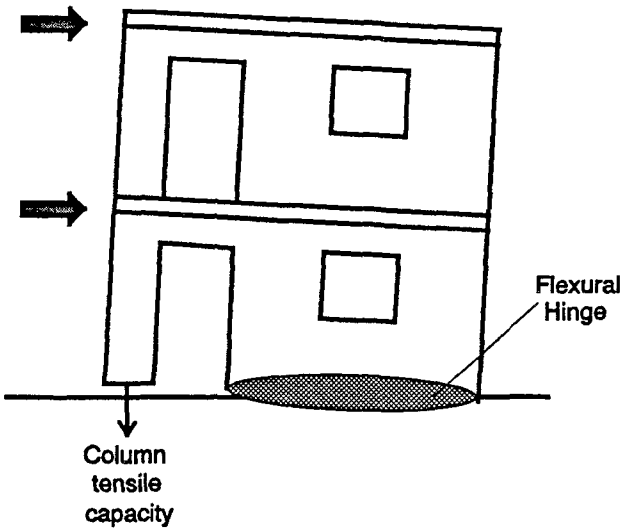

Figure 7.3: Observed collapse mechanism for Specimen 1a; Southward loading.

The analysis of the distribution of displacements on the height of the specimen confirmed the occurrence of a different collapse mechanism in each loading direction. As shown in Fig. 6.6, when loaded to the north, the inter-story relative displacement was larger at the 1st story than at the second story. This result, as discussed in Section 2.2.2, is typical of pierced walls that develop a column sidesway type of mechanism, in which most of the inelastic deformations tend to concentrate in a single story. When loaded to the south, the distribution of displacements was almost uniform, which is typical of walls that rotate about a single plastic hinge at the base, as described in Section 2.2.1.

Failure Mode of Specimen 1a

As previously described, Specimen 1a developed different collapse mechanisms on each direction of the loading process. However, damage and deformation capacity were governed by the same mechanisms: shear transfer between the piers and the wall base; and fracture of longitudinal reinforcement in the piers.

When the specimen was loaded to the north at high levels of lateral displacement, the extreme pier was practically under pure tensile force. This pier suffered the apparent fracture of one of its longitudinal bars close to the end of the test. The column was taking most of the overturning compressive force, which produced crushing of the masonry and buckling of the longitudinal reinforcement at the column base. Under these conditions, the center pier was subjected to relatively low levels of compressive force and was carrying most of the lateral force. Because of the low amount of longitudinal reinforcement in the pier, this shear force was transferred to the wall base mainly through a small zone in the compression toe of the center pier, as discussed in Section 2.3.3. This concentration of stresses would have caused the extensive damage which occurred at the north end of the wall base under the center pier, as shown in Fig. 6.35.

When the specimen was loaded to the south at high levels of lateral displacement, the column was practically under pure tensile force, as shown in Fig 7.3. Axial deformations were distributed over the height of the column, as evident from Fig. 6.7. The distribution and opening of cracks in practically every bed joint, as shown in Fig. 6.35, suggested that the reinforcement yielded not only at the top and bottom, but spread along the column height. This distributed yielding may have limited the strain in the reinforcement to values well below the strain hardening level, keeping the column from reaching its axial tensile capacity as assumed in design. The center pier was also subjected to practically pure tensile force. This pier also suffered the apparent fracture of one of its longitudinal bars close to the end of the test. Under these conditions, the extreme pier was subjected to high levels of compressive force and was carrying practically all the lateral force. Because of the high compressive force, the mechanism for transferring shear from the pier to the wall base was more efficient than the previous case, and the damage in the extreme pier-wall base connection was limited, as shown in Fig. 6.35. When the test was stopped, the wall base reached its flexural capacity, and simultaneously began to crush at the compression toe, as shown in Fig 6.35.

As anticipated in design, the drag bars in the wall base were particularly important in transferring shear from the piers to the wall base. Figs. 6.13 to 6.15 show measured strains in those bars for the first peak points. It is evident from those plots how the shear force was transferred from the top drag bars to the lowest ones as the horizontal splitting cracking progressed along the top course of the wall base, and bond of the reinforcement was deteriorating there.

Diagonal cracking occurred in the piers, but it did not progress after the specimen reached its lateral load capacity. This shows that the shear capacity provided to the piers was adequate.

The progression of cracking in the lintels was consistent with the specimen's behavior as previously described. Cracks only occurred at the lintel-pier connection when the specimen was loaded to the north, and the presence of the column restrained the rotation of the lintels. Due to its relatively low tensile axial capacity and stiffness, the column did not significantly restrain the rotation of the lintels when the specimen was loaded to the south, and no cracking occurred under these circumstances. Strain gauges in the lintel reinforcement showed no yielding at those locations.

No evidence of instability or additional damage was observed due to the out-of-plane displacement.

7.1.2 Lateral Load Capacity and Failure Mode of Specimen 1b. The lateral load capacity of Specimen 1b was 89.9 kips at an overall drift ratio of 0.38% (0.77 in. roof displacement) when loaded to the north, and 145.0 kips at an overall drift ratio of 0.39% (0.79 in. roof displacement) when loaded to the south.

The progression of cracking in Specimen 1b before reaching its lateral load capacity is shown in Fig. 6.67: extensive horizontal cracking had occurred in the bed joints at the column; a flexural crack extended along the base of the wall and crushing of masonry had initiated at the south edge of that section; diagonal cracking had began in the wall base at the corners of the window opening; extensive cracking had occurred in the lintel-column connection at the 1st story; and cracks had initiated in the lintel-pier connections at both stories. As shown in Fig. 6.68, the longitudinal reinforcement had yielded at the base sections of the wall and column, at the base section of the 2nd story column, and at the lintel-pier connections at both stories.

Collapse Mechanism and Lateral Load Capacity of Specimen 1b for Northward Loading

At the time the specimen reached its north lateral load capacity, flexural hinges had formed at the bases of the column and the wall, as evident from deformation and strain distributions shown in Figs. 6.41, 6.42, 6.47, 6.48, and 6.52. The crack at the base of the wall opened almost 0.5 in. at the south edge of the section. As evident from Figs. 6.55 to 6.58 and 6.70, the lintel at the 1st story was in double curvature and developed flexural hinges at both end sections. The 2nd story lintel developed a flexural hinge only at the connection with the pier, as evident from Figs. 6.59 to 6.52 and 6.70. A flexural hinge was expected to develop at the top section in the 2nd story column at the time the specimen had reached its lateral load capacity, as described in Section 5.5.2. However, strain gauges in the reinforcement at that location showed values close to but still under the yielding strain. The initiation of diagonal cracks at the lintel-column joint seemed to indicate that the inelastic deformations were occurring mainly due to distortion of the joint instead of flexural rotations at the end of the column. Thus, the observed collapse mechanism for Specimen 1b, when loaded to the north, is shown in Fig. 7.4.

These results were in good agreement with the expected behavior of Specimen 1b when loaded to the north, and predicted and observed values of the lateral load capacity were very close, as shown in Table 7.1.

Collapse Mechanism and Lateral Load Capacity of Specimen 1b for Southward Loading

At the time the specimen reached its south lateral load capacity, a flexural hinge had formed at the base of the wall, as evident from deformation and strain distributions shown in Figs. 6.49 and 6.51. The crack at the base of the wall opened almost 3/8 in. at the north edge of the section. Wide cracks opened at the bed joints in the column, specially at the base

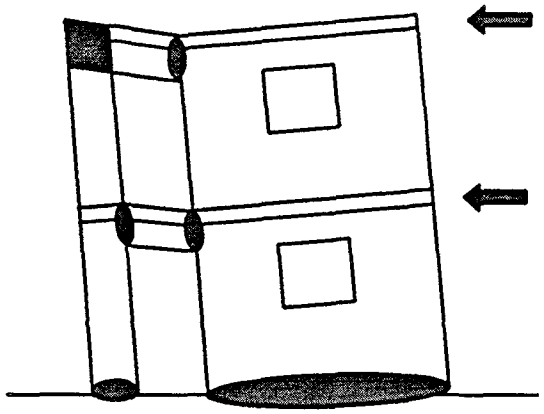

Figure 7.4: Observed collapse mechanism for Specimen 1b; Northward loading.

section, as shown in Figs. 6.43, and all the longitudinal reinforcement had yielded at that location, as shown in Fig. 6.44. As evident from Figs. 6.55 to 6.58, both lintels were practically in single curvature and a plastic hinge developed only at the 1st story lintel-pier connection.

The large opening and distribution of the cracks in the column suggested that this element was subjected to almost pure tensile axial force at the time the specimen developed its lateral load capacity. It was evident that a plastic flexural hinge developed at the base of the wall. Thus, the observed collapse mechanism for Specimen 1b, when loaded to the south, was similar to the one developed by specimen 1a: a cantilever wall connected through the lintels to a strut, as shown in Fig. 7.3. This result did not completely agree with the expected collapse mechanism, as described in Section 5.4.

The predicted south lateral load capacity of 130 kips for the assumed collapse mechanism as described in Section 5.4, was lower than the specimen's ultimate load of 145 kips, as shown in Table 7.1. To be consistent with the calculations made before the test, the south lateral load capacity of the specimen was recalculated for the mechanism shown in Fig. 7.3 using the same material properties as in the original calculations, and following the process outlined in Section 5.5.2. Assuming that the column had developed its expected axial yielding capacity of 67.0 kips with zero flexural capacity, the axial force transmitted through the lintels would have been 77.3 kips, the total axial compressive force on the wall base 177.0 kips, and the wall flexural capacity 12,442 kip-in. The ultimate load for that mechanism, calculated using Eq. (5.16), would have been **142.9 kips**. This value showed a better agreement with the specimen's lateral load capacity of 145.0 kips.

The lateral load capacity calculated for the observed mechanism, 142.9 kips, was higher than that calculated in Section 5.4.2 for the mechanism originally assumed as the correct one, 130.0 kips. This apparent contradiction was due to an increased effectiveness of the coupling system caused by lintels with flexural capacities larger than expected. This overstrength of the lintels was mainly due to a material strength larger than expected. The predicted flexural capacities at the end sections of the 40-in. span lintels, as described in Section 5.5.2, were 267 kip-in and 991 kip-in. The maximum shear force that the coupling system would be able to transmit, would occur when the lintels, bending in double curvature, reached their flexural capacities at each end. This shear force was calculated as 62.9 kips. However, the experimental evidence indicated that the coupling system transmitted a force of 69.6 kips, corresponding to the axial yielding capacity of the column, and that only one of the lintels developed its flexural capacity at both end sections. This results indicated that the lintels were stronger than originally assumed, and that the contribution of the overturning forces to the lateral load capacity of the specimen was larger than expected.

The distribution of displacements over the height of the specimen, shown in Fig. 6.40, was typical of a system developing a mechanism in which most of the inelastic action is concentrated in inelastic rotations at the base of the elements.

Failure Mode of Specimen 1b

Damage and deformation capacity of Specimen 1b were governed by fracture of longitudinal reinforcement in the wall base, and by extensive damage in the lintel-column connections.

When the specimen was loaded to the north at high levels of lateral displacement, the mechanism previously described continued governing the behavior of the system. Fracture of the extreme bar occurred at the base of the wall, and crushing of masonry began at the compression toe of the wall and column. Extensive diagonal cracking occurred at the lintel-column joints, showing a behavior typical of joints with insufficient transverse reinforcement to resist the unbalanced forces. At the same time, the slab-column joint suffered some damage, apparently due to punching shear.

When the specimen was loaded to the south at high levels of lateral displacement, the same mechanism, with the column acting like an strut, continued governing the behavior of the system. Fracture of the extreme bar occurred at the base of the wall, and crushing of masonry progressed at the compression toe of the wall. Diagonal cracking continued progressing in the lintel-column joints, due to the high shear forces transferred from the column to the lintels. As the lateral displacement of the specimen was increasing, the imposed rotations on the lintel end sections became larger, and eventually, a flexural hinge developed at the lintel-column connections at the 2nd story. The joint was not able to resist those forces, and extensive damage and crushing of masonry and concrete occurred at that area.

As anticipated in design, the piers suffered only minor cracking, and yielding occurred only in one of the longitudinal bars. The high amount of longitudinal reinforcement limited the crack opening at the end sections, providing sufficient shear sliding capacity.

7.2 Load - Displacement Histories

The load-displacement history for each test, in terms of the base shear-overall drift ratio hysteresis loops, have been shown in Figs. 6.4 and 6.38 for Specimens 1a and 1b respectively. The same plots, in terms of the roof displacement, are shown in Figs. 7.5 and 7.6. The base shear versus roof displacement and base shear versus second floor displacement histories for the first cycle of each series, are shown in Figs. 7.7 and 7.8 for Specimen 1a, and Figs. 7.9 and 7.10 for Specimen 1b. Since enough readings with the data acquisition system were taken during the test, those curves can be considered a very good representation of the loading and unloading process.

As observed in those figures, the hysteresis loops remained very stable throughout both tests, typical of basically flexural behavior. Most of the strength degradation occurred after the first cycle of each series. Sudden losses of strength due to the occurrence of some

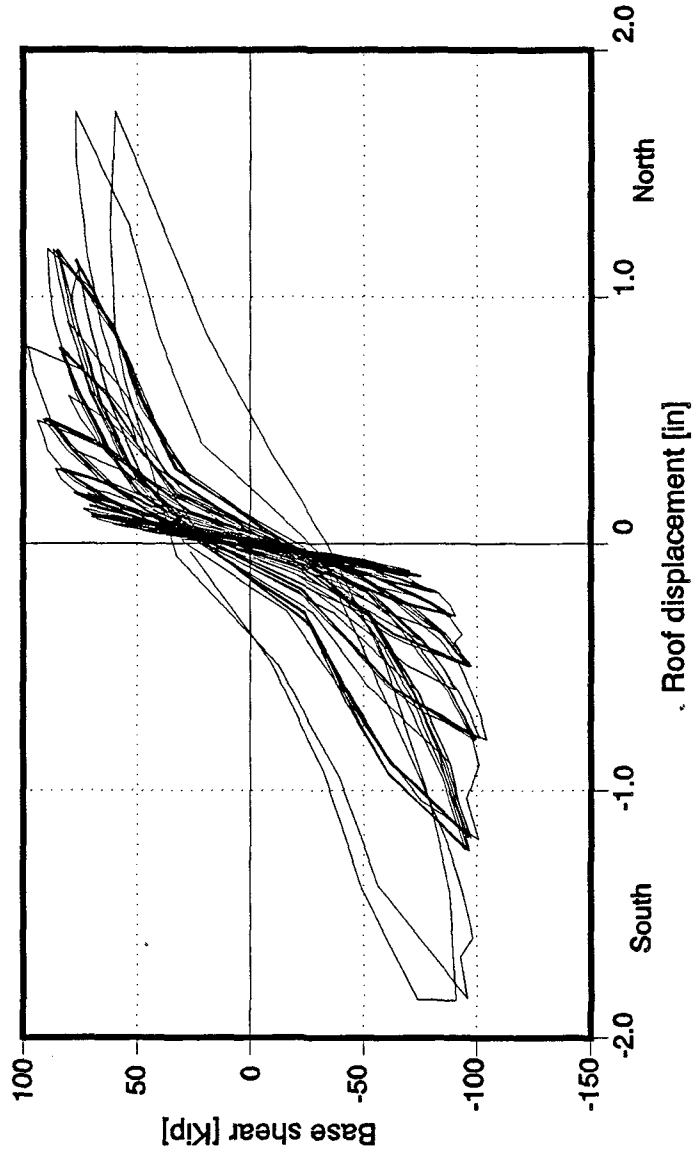

Figure 7.5: Specimen 1a: Base shear - Roof displacement history.

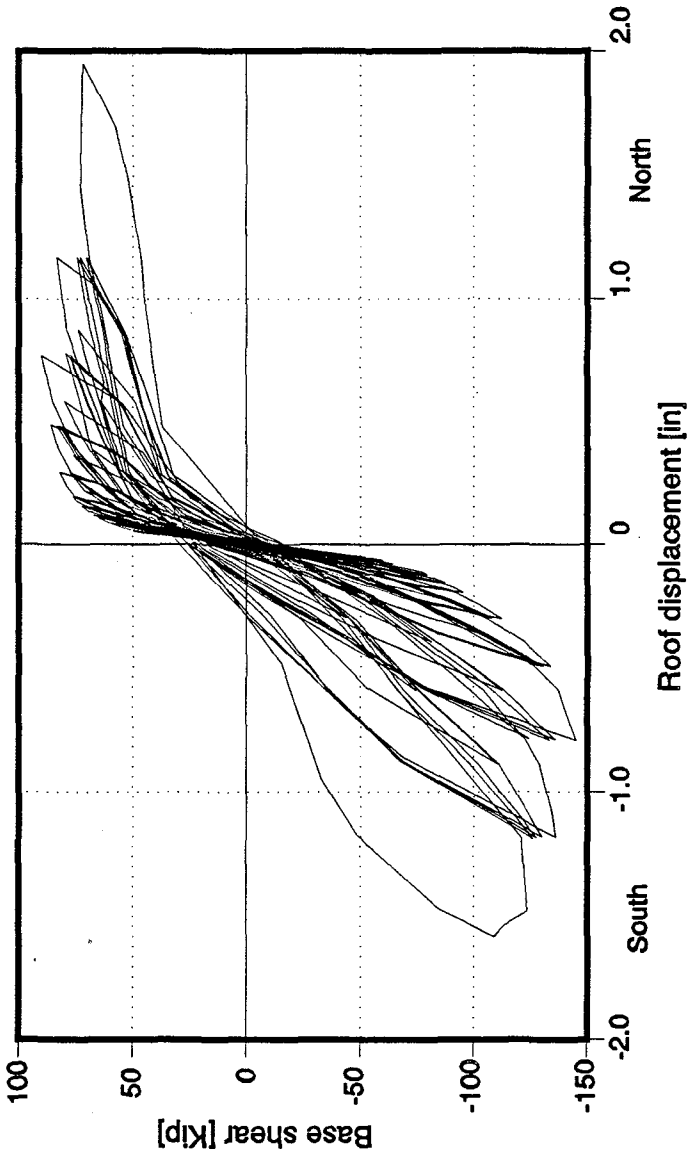

Figure 7.6: Specimen 1b: Base shear - Roof displacement history.

major events, like fracture of reinforcement or crushing of masonry, are clearly observed in some of the loops.

As shown in Figs. 7.7 to 7.10, the load-displacement history was very similar for both floor levels in both tests.

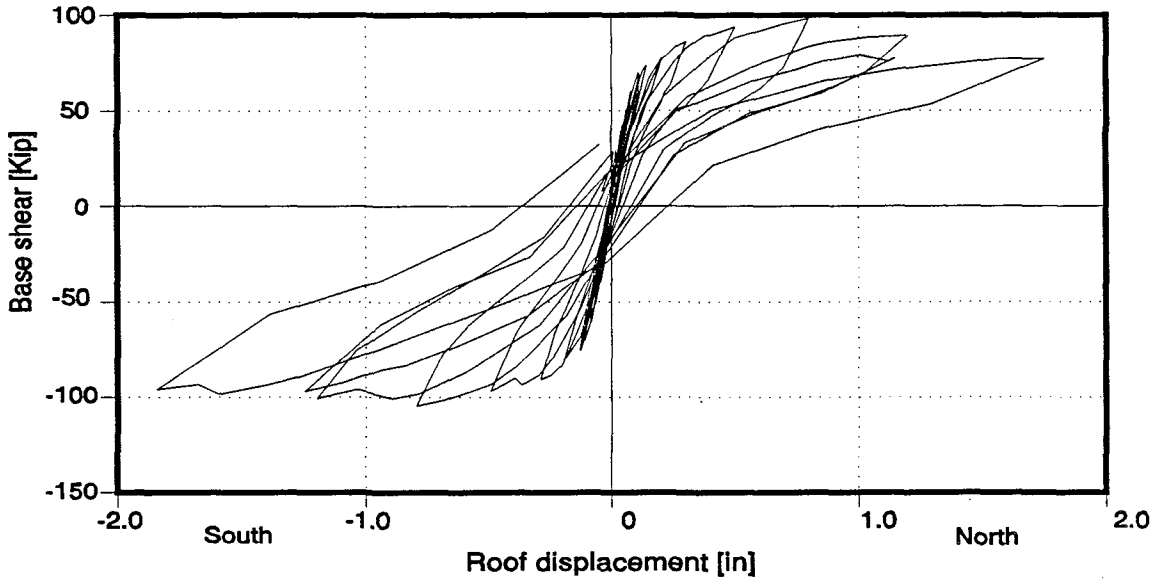

Figure 7.7: Specimen 1a: Base shear - roof displacement history for first cycle of each series.

No evidence of pinching was observed in the hysteresis loops, indicating that deformations by shear, sliding shear, and reinforcement bond deterioration were not important. Fig. 7.11 shows the first cycle history of the base shear versus total slip for the extreme (south) pier of Specimen 1a. The total slip (summation of the slip measured at the top and bottom of the pier), was important only when the specimen was loaded to the north, and the pier was practically under pure tensile force. When the specimen was loaded to the south, and the pier was subjected to high levels of compressive forces, and was carrying most of the specimen's lateral load, slip was insignificant. Fig. 7.12 shows the first cycle history of base shear versus slip measured at the base of the wall of Specimen 1b. Slip was important only when the wall was being loaded to the south at loading levels close to the ultimate load in that direction. In both cases, slip hysteresis loops did not show the typical stiffening spring behavior that causes pinching in the response hysteresis loops of the structure.

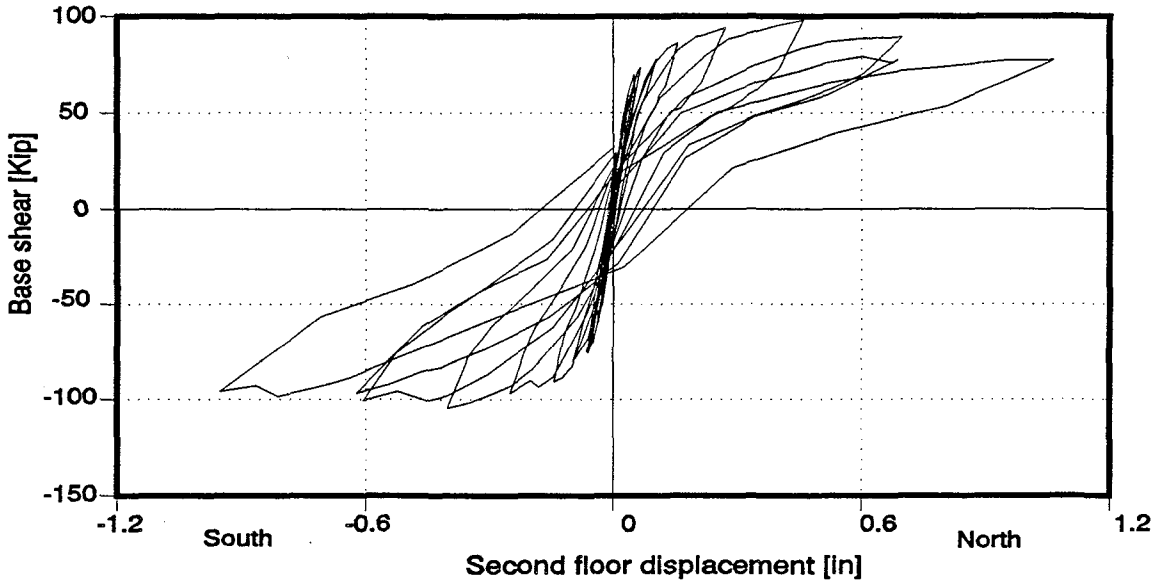

Figure 7.8: Specimen 1a: Base shear - second floor displacement history for first cycle of each series.

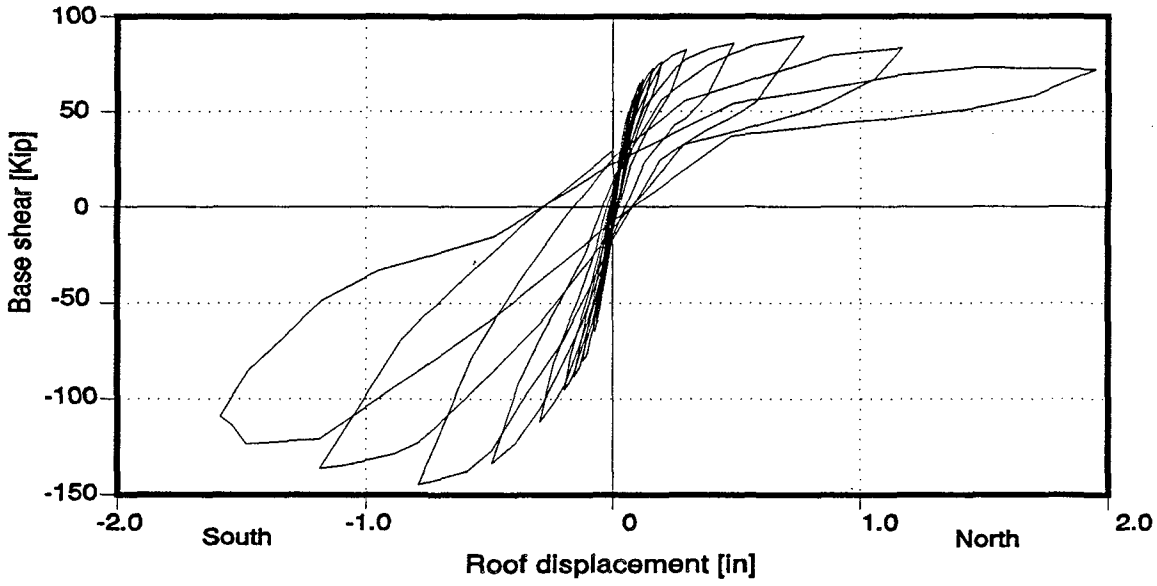

Figure 7.9: Specimen 1b: Base shear - roof displacement history for first cycle of each series.

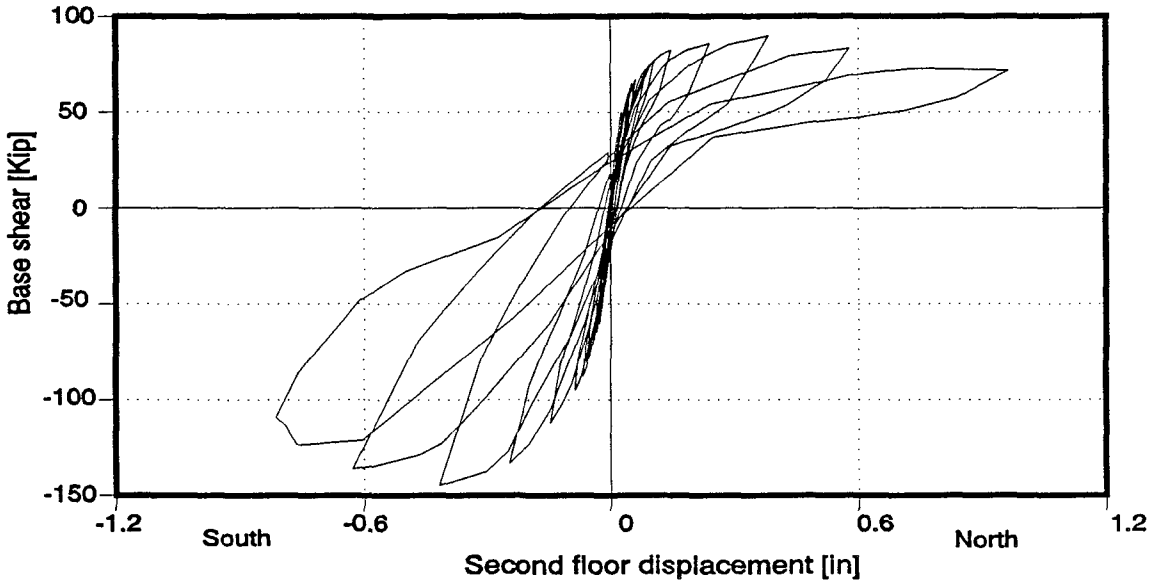

Figure 7.10: Specimen 1b: Base shear - second floor displacement history for first cycle of each series.

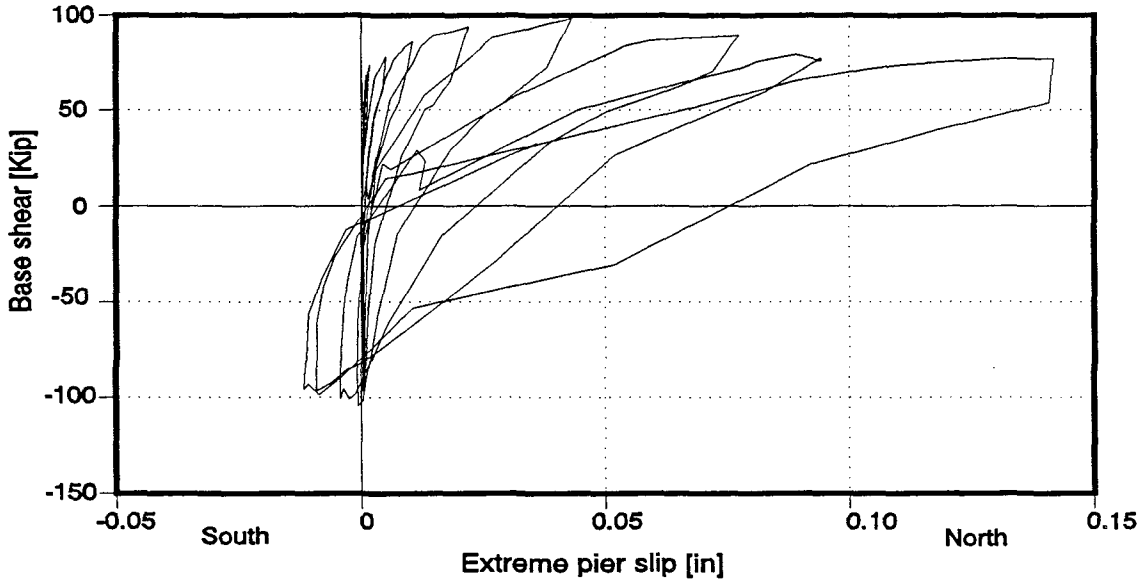

Figure 7.11: Specimen 1a: History of total slip measured at top and bottom of extreme (south) pier for first cycles.

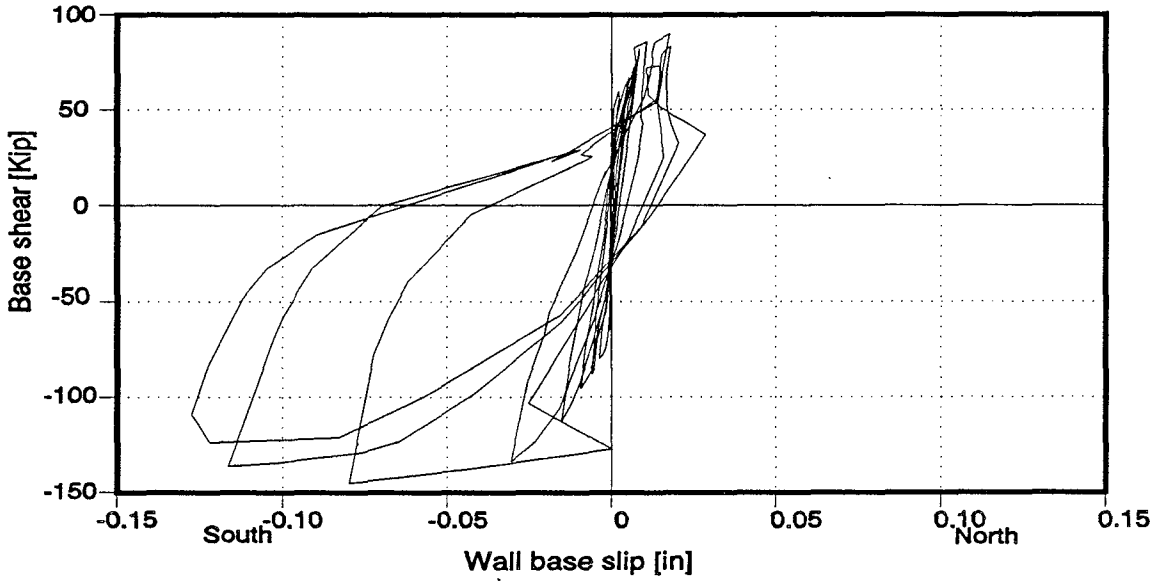

Figure 7.12: Specimen 1b: History of wall base slip on foundation beam for first cycles.

Table 7.2: Specimen 1a: Energy dissipation

Loading series	Energy / Average peak displacement [Kip-in/in]		
	1st Cycle	2nd Cycle	Last Cycle
0.12 in.	15.4	9.7	10.0
0.14 in.	13.4	5.3	10.3
0.20 in.	16.8	12.6	15.9
0.30 in.	30.6	21.3	18.7
0.50 in.	41.3	29.9	28.5
0.80 in.	48.6	32.0	28.8
1.20 in.	47.4	35.3	34.6
1.20 in.	35.4	32.6	30.8
1.80 in.	48.0	65.8	—

Even though the structural response was very stable and typically flexural in both tests, the specimens showed a relatively low energy dissipation capacity. The hysteresis loops were narrow for the most of the test, as shown in Figs. 7.5 to 7.10. The energy dissipated per cycle was calculated and normalized by the average peak displacement for that cycle. Results are summarized in Tables 7.2 and 7.3 and shown in Figs. 7.13 and 7.14. Both specimens showed similar energy dissipation capacity when loaded to the north. However, as evident from the wider hysteresis loops of its response, when loaded to the south, Specimen 1b showed better energy dissipation capacity than Specimen 1a. In general, as shown in Figs. 7.13 and 7.14, the largest loss in energy dissipation capacity occurred after the 1st cycle of each series. During the next cycles within the series, the response was very stable, as evident from the hysteresis loops, and the reduction in dissipated energy per cycle was smaller.

Table 7.3: Specimen 1b: Energy dissipation

Loading series	Energy / Average peak displacement [Kip-in/in]		
	1st Cycle	2nd Cycle	Last Cycle
0.12 in.	16.3	14.3	13.6
0.16 in.	21.9	14.4	14.5
0.20 in.	22.7	15.7	16.4
0.30 in.	30.8	21.3	19.7
0.50 in.	41.2	28.6	27.0
0.80 in.	61.9	41.0	33.7
1.20 in.	57.4	39.7	30.4
1.80 in.	49.5	—	—

To examine the influence of the out-of-plane displacement on the response of Specimen 1a, the hysteresis loops of the complete 1.2-in series have been plotted in Fig. 7.15. First, the specimen was subjected to a complete series of cycles with a peak roof displacement of 1.2 in. Then, out-of-plane displacements of 1.0 in. at the roof and 0.5 in. at the second floor were imposed on the specimen. Finally, as shown in Fig. 6.3, the out-of-plane displacements were maintained constant as the specimen was subjected to three complete cycles at 1.2 in. peak roof displacement. As shown in Fig. 7.15, no significant events occurred during the first series of cycles in the north direction. Crushing of masonry occurred during the first south cycle before imposing the out-of-plane displacements. No significant degradation was observed during the rest of the south loading cycles. After imposing the out-of-plane displacements, one of the longitudinal bars of the extreme pier

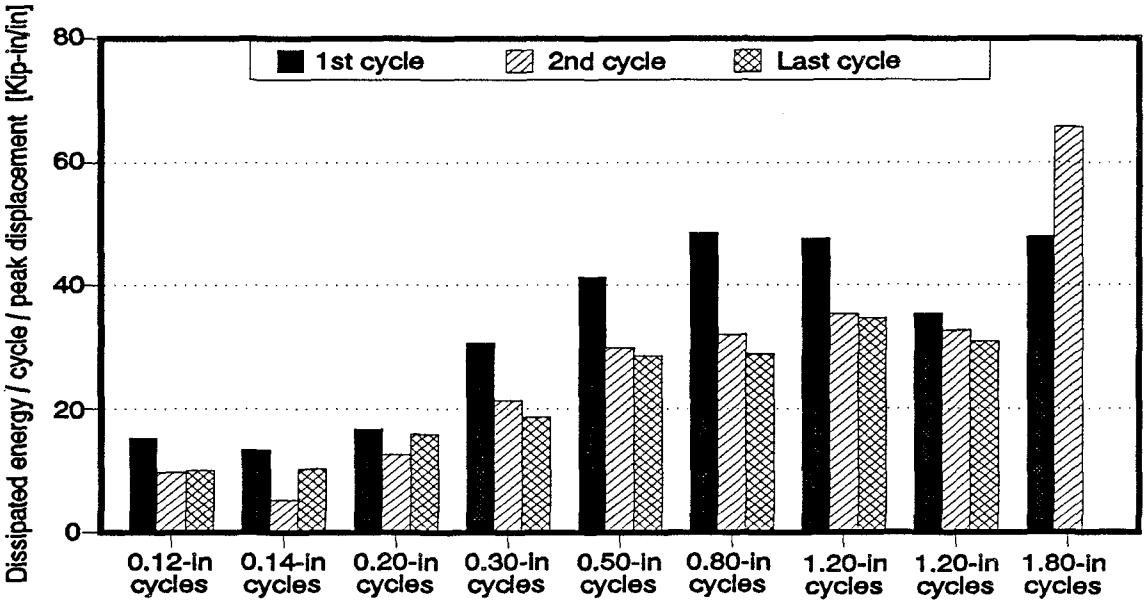

Figure 7.13: Specimen 1a: Normalized energy dissipated during cyclic loading.

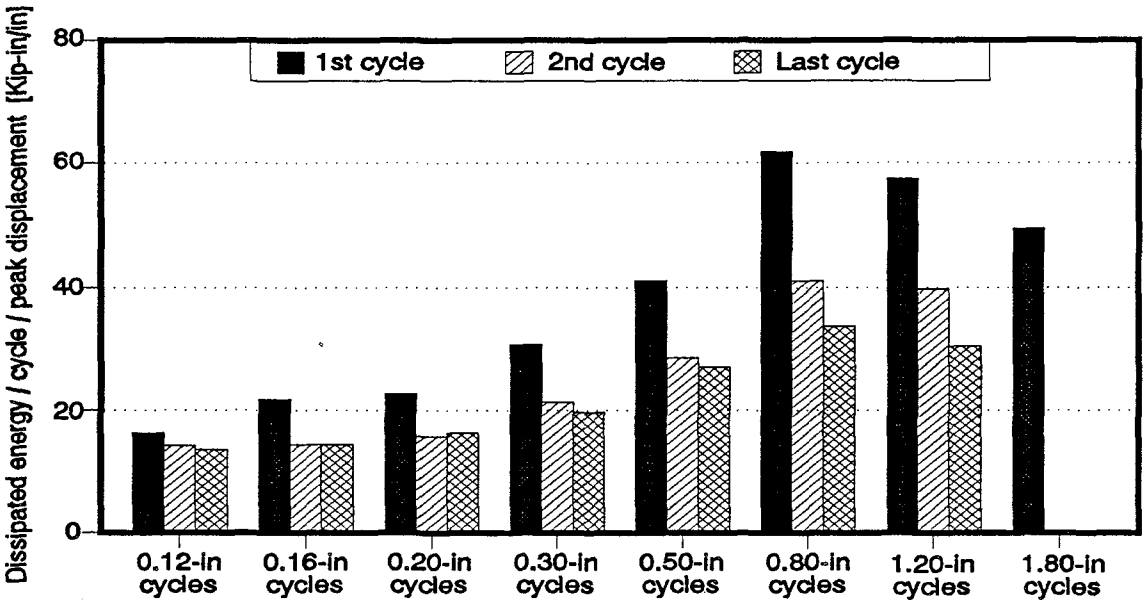

Figure 7.14: Specimen 1b: Normalized energy dissipated during cyclic loading.

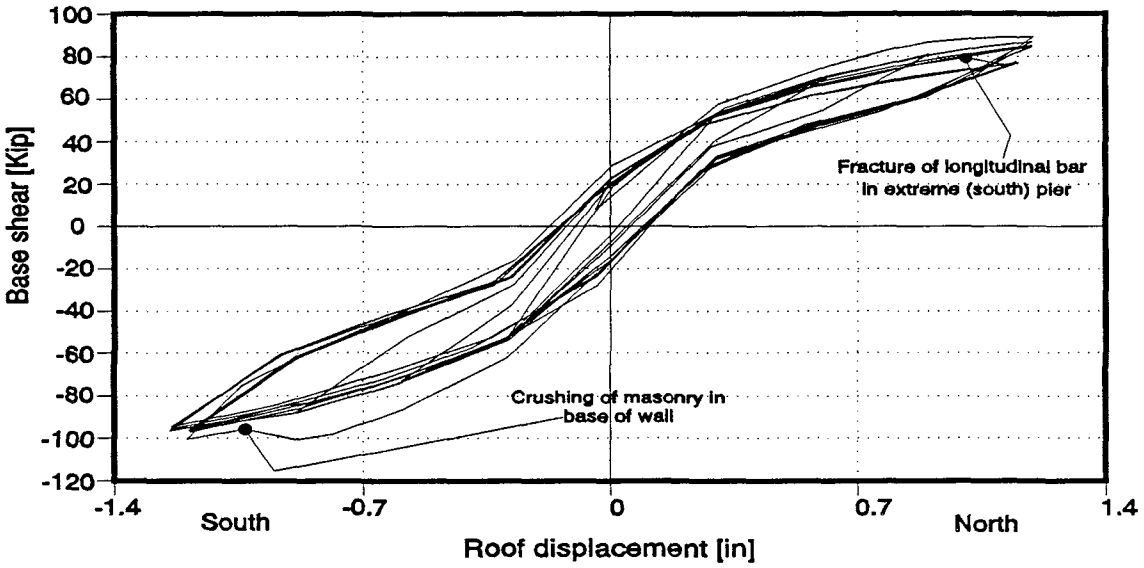

Figure 7.15: Specimen 1a: Load - Roof displacement history for series of 1.2 in. cycles.

was fractured when the specimen was being subjected to a roof lateral displacement slightly lower than the 1.2 in. peak. No significant events and degradation were observed during the rest of the loading cycles. As seen in Fig. 7.13, dissipation energy capacity of the specimen showed little reduction during the second series of cycles at 1.2 in. roof displacement. Since the fracture of the pier reinforcement could hardly be attributed to the out-of-plane displacement effects, it was concluded that the out-of-plane displacements had little if any influence on the response of the specimen.

7.3 Load - Displacement Envelopes

Envelopes of the first peaks of the load-displacement response have been shown in Figs. 6.5 and 6.39 for Specimens 1a and 1b respectively. The same plots, in terms of the roof displacement, are shown in Figs. 7.16 and 7.18. Those curves permitted comparison of the north and south loading behavior of each specimen, and provided useful information about their general behavior.

As shown in Figs. 7.16 and 7.18, the behavior of the specimens became markedly nonlinear after reaching the first major event, at 0.14 in. and 0.11 in. of roof displacement respectively.

The envelopes of the first peaks of the response before reaching the first major event are shown in Figs. 7.17 and 7.19, for Specimens 1a and 1b respectively. Both specimens showed the highest stiffness during the first north cycle of 10-kip amplitude of the loading

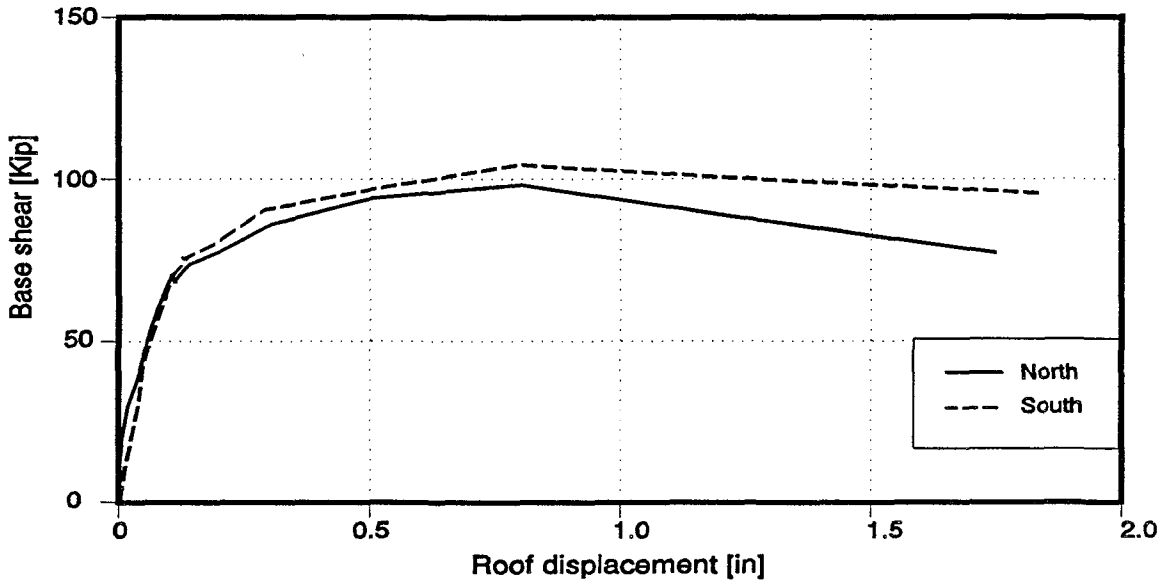

Figure 7.16: Specimen 1a: First peak envelopes of the load-displacement response.

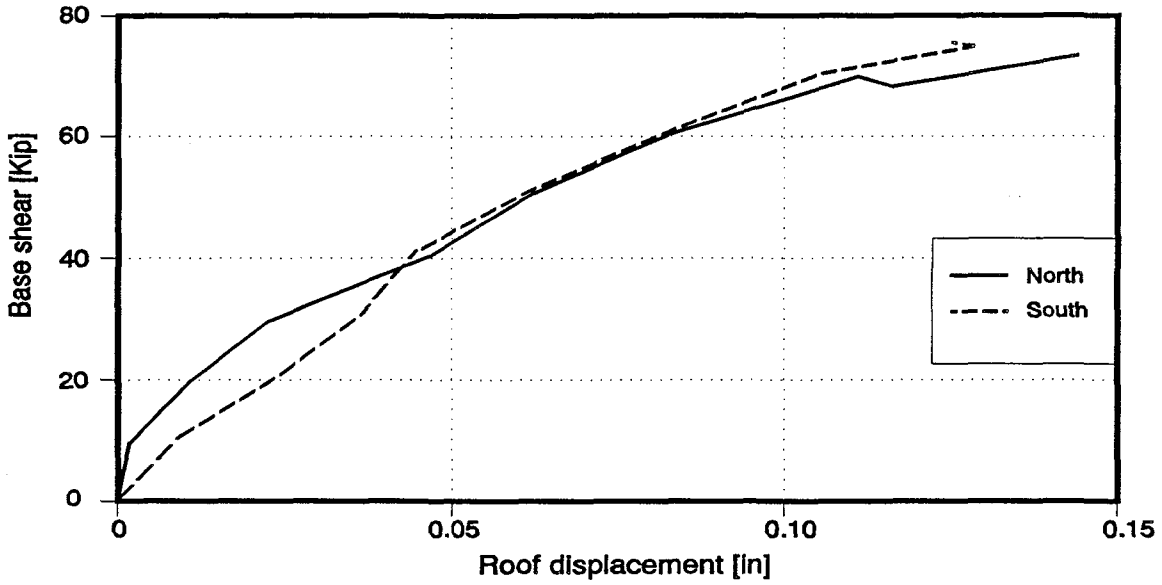

Figure 7.17: Specimen 1a: First peak envelopes of the load-displacement response, initial cycles.

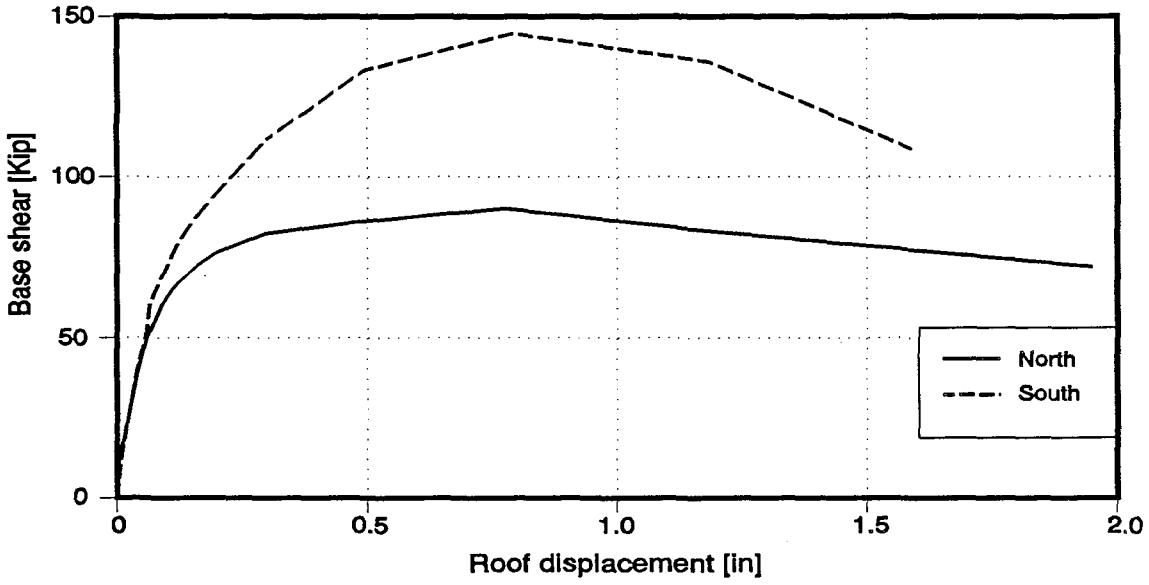

Figure 7.18: Specimen 1b: First peak envelopes of the load-displacement response.

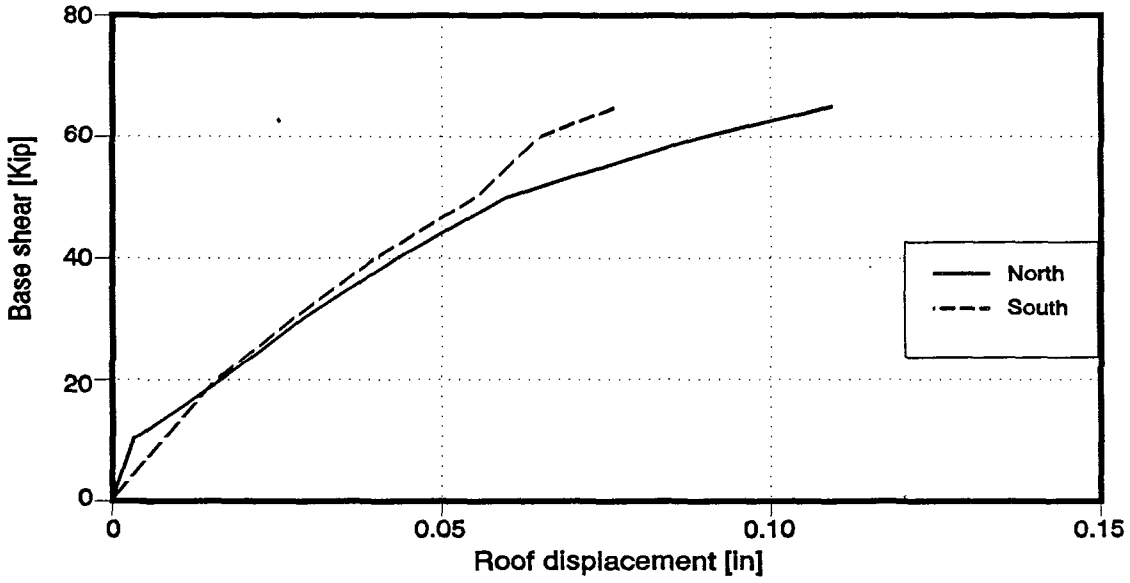

Figure 7.19: Specimen 1b: First peak envelopes of the load-displacement response, initial cycles.

process: 5722 kip/in Specimen 1a; and 3094 kip/in Specimen 1b. As the amplitude of the cycles was increased, the stiffness became comparable in both directions.

As shown in Fig. 7.20, the specimens reached their maximum lateral load capacities at the same roof displacement of about 0.8 in. In both cases, the south ultimate load was the largest: 6% and 61% larger than the north capacity for Specimens 1a and 1b respectively.

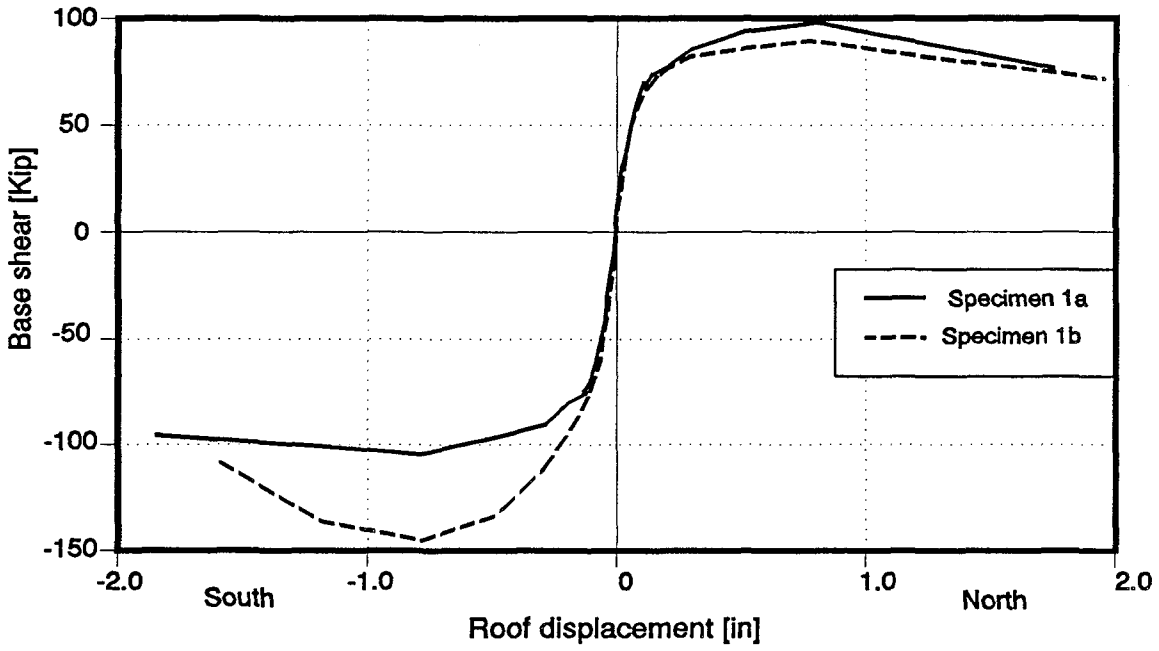

Figure 7.20: First peak envelopes of the load-displacement response of Specimens 1a and 1b.

In the case of Specimen 1a, the descending branch of the load-displacement envelope was practically a straight line in both directions. While Specimen 1b showed the same behavior when loaded to the north, the specimen was rapidly degradating when subjected to roof displacements in excess of the displacement corresponding to its south ultimate capacity. As previously discussed, the displacement capacity of this specimen was limited by extensive damage of the lintel-column connection when loaded to the south.

To examine the strength degradation that occurred during the tests, the first, last, and next peak envelopes of the load displacement response have been plotted in a single chart for each specimen, as shown in Figs. 7.21 and 7.22 for Specimens 1a and 1b respectively. In both cases, strength reduction became noticeable with the appearance of nonlinearity in

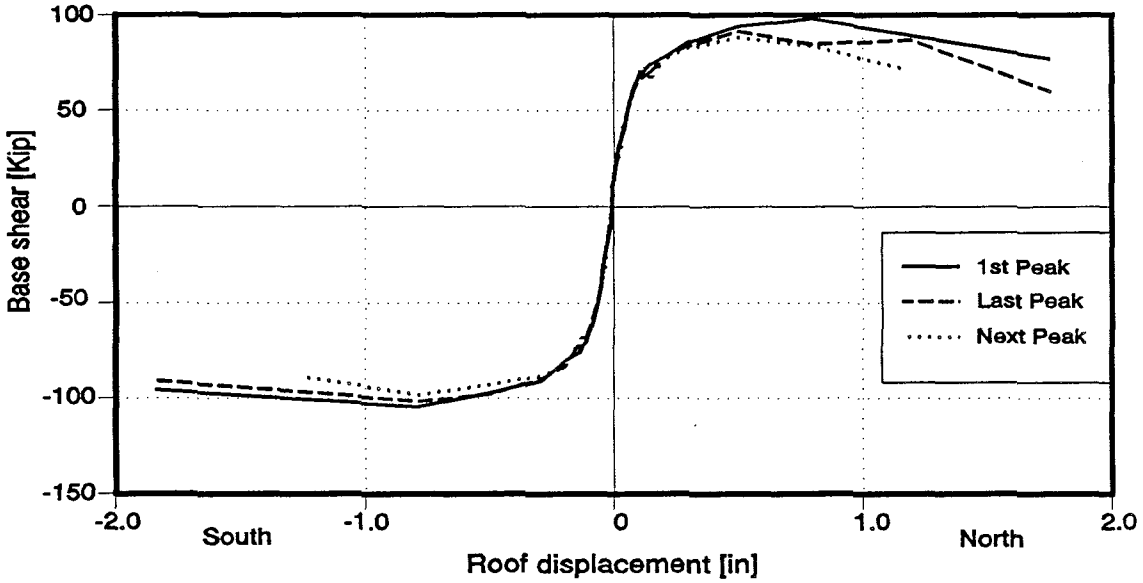

Figure 7.21: Specimen 1a: First, last, and next peak envelopes of the load-displacement response.

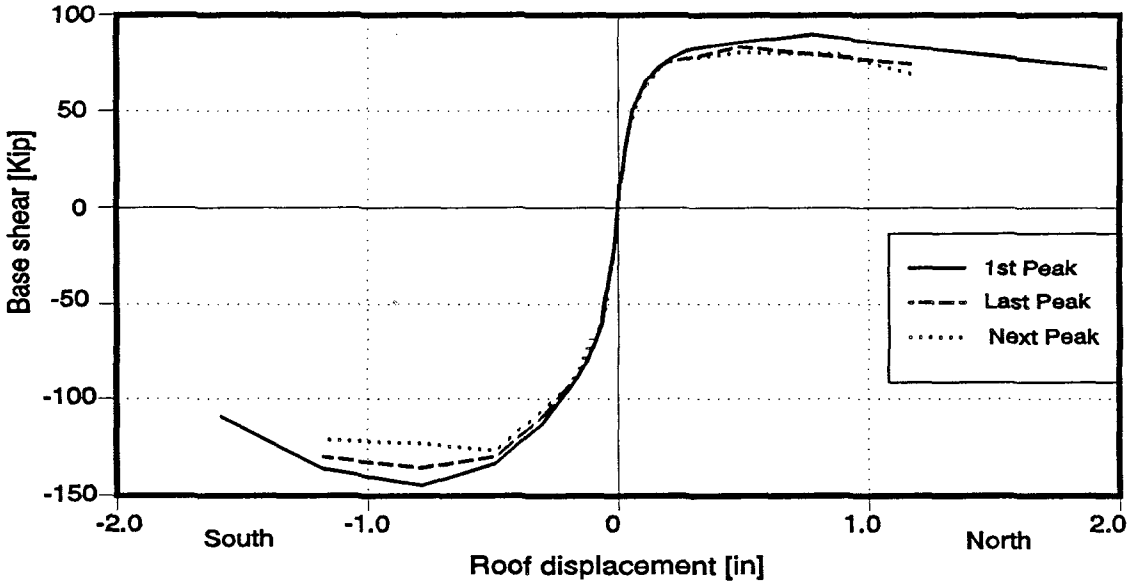

Figure 7.22: Specimen 1b: First, last, and next peak envelopes of the load-displacement response.

the envelopes. As previously mentioned, strength reduction was maintained within acceptable limits, and the response of the specimen was stable until reaching the maximum displacement.

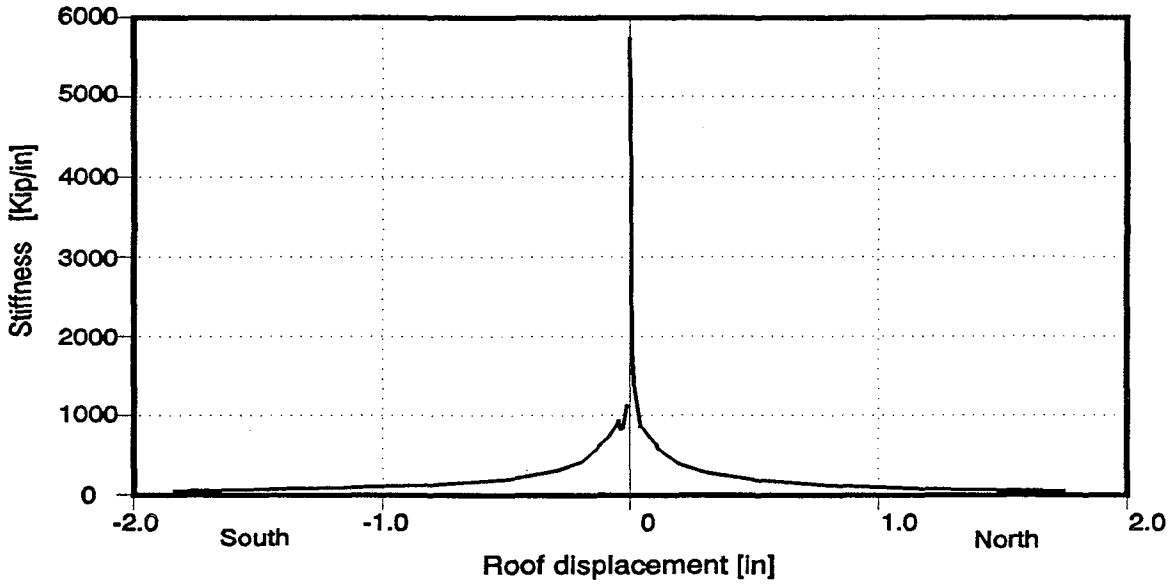

Figure 7.23: Specimen 1a: First peak envelopes of the stiffness versus roof displacement.

7.4 Stiffness Envelopes

The stiffness was defined as the ratio between the peak values of base shear and roof displacement in a particular cycle. As shown in Figs. 7.23 and 7.24, stiffness calculated for first peak points decreased rapidly as the roof displacement increased, especially at the beginning of the tests.

As shown in Figs. 7.17 and 7.19 and as previously discussed, the specimens showed the highest stiffness during the first north cycle of the loading process. The stiffness was sharply reduced after the first load peak, even before any crack was visible in the specimens. As the specimens reached their first major event and nonlinear behavior became evident, the degradation of stiffness became more stable.

As shown in Figs. 7.25 and 7.26, the degradation of stiffness that occurred between cycles of the same displacement amplitude was practically negligible.

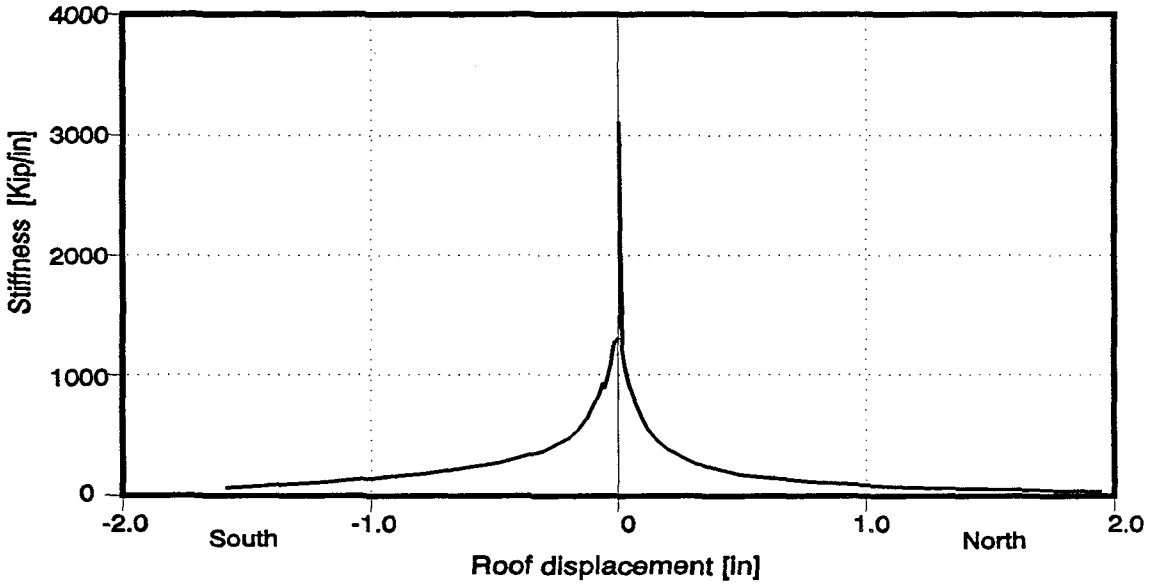

Figure 7.24: Specimen 1b: First peak envelopes of the stiffness versus roof displacement.

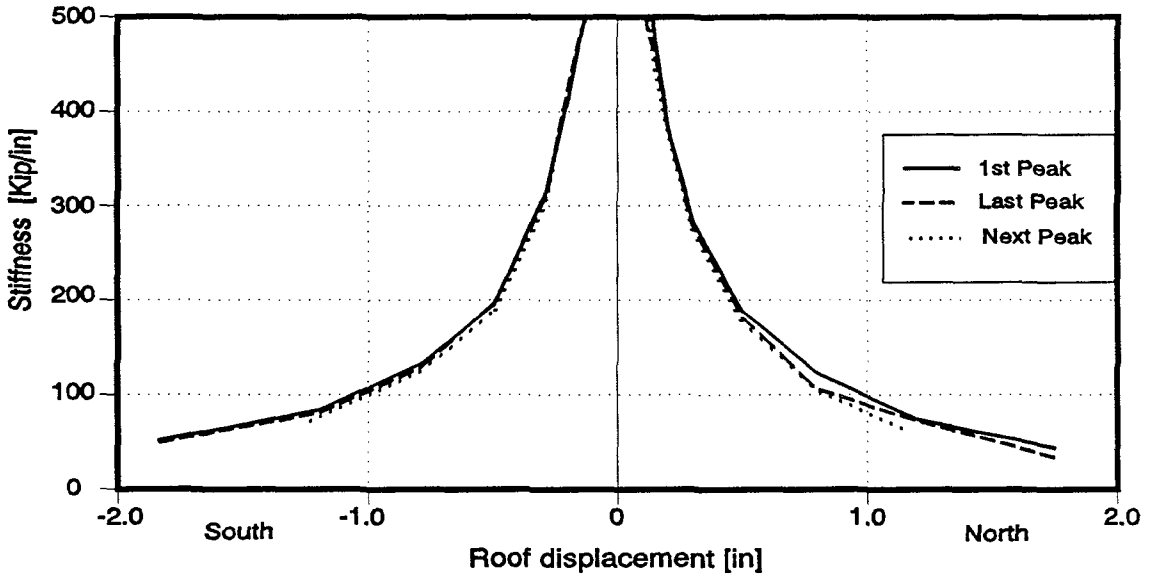

Figure 7.25: Specimen 1a: First, last, and next peak envelopes of the stiffness versus roof displacement.

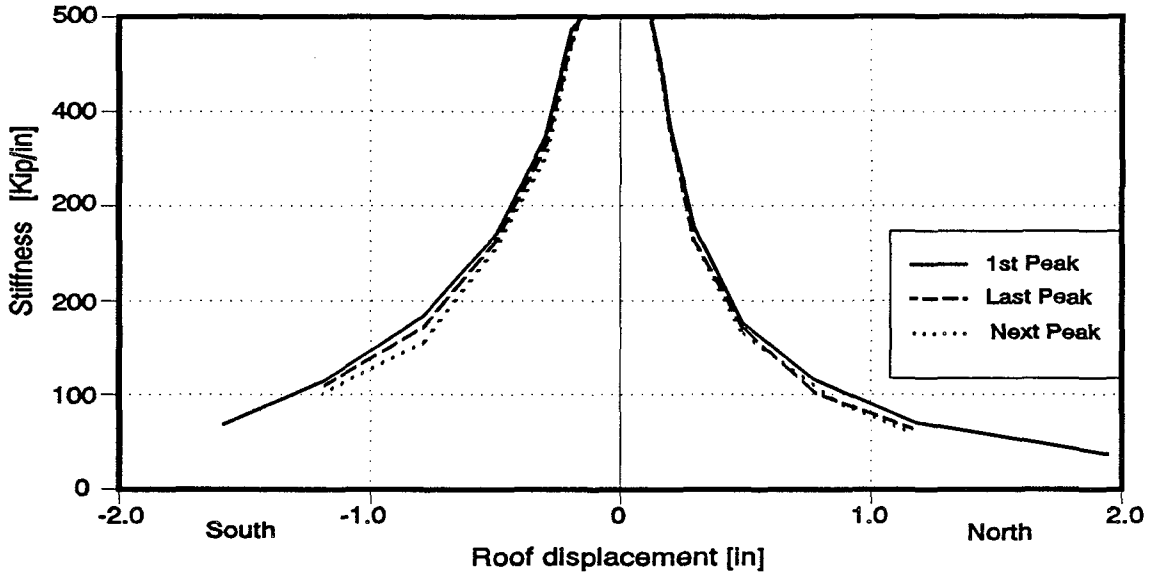

Figure 7.26: Specimen 1b: First, last, and next peak envelopes of the stiffness versus roof displacement.

7.5 Design and Construction Details

In this Section, design and construction details are discussed based on their performance during the tests.

7.5.1 Walls and Piers. Shear keys proved to be an effective way to increase the sliding shear capacity between the base of the walls and the foundation beam. The wall-foundation beam connection had been shown to be highly susceptible to sliding by shear in previous tests [13]. To improve sliding shear capacity of that connection, smooth shear keys in the form of truncated cones were drilled in the base beam as described in Section 3.2.2. As previously discussed, sliding by shear showed little if any influence in the results of the test of Specimens 1a and 1b.

The necessity of a minimum ratio of longitudinal reinforcement for walls and piers was evident from the results of the tests. It was observed that walls and piers with small reinforcement ratios are highly susceptible to fracture of the extreme longitudinal reinforcement, especially in the case of long walls. This limits the deformation capacity of such walls. A minimum ratio of distributed longitudinal reinforcement is needed to control inelastic rotations at the base of the walls, and to enhance the sliding shear resistance, especially at the wall-foundation connection. Some research is needed to relate the requirement for a minimum longitudinal reinforcement with the requirements to limit the wall's flexural capacity in order to insure ductile behavior.

The transverse reinforcement, as designed, proved to be adequate for both specimens. Transverse bars anchored using 180-degree hooks around the extreme longitudinal bars showed excellent characteristics: anchorage was adequate; the hooks restrained against lateral buckling of the longitudinal reinforcement; and the hooks provided some degree of confinement to the grout.

Anchorage and lap splices of the longitudinal reinforcement were adequate as designed. No evidence of deterioration of the bond between reinforcement and grout was observed in the anchorage and splice zones during the tests.

7.5.2 Lintels. As described in Section 3.2.2, to reduce the bottom shell cover, the bottom course of the lintels was constructed with bond beam units placed in an inverted position. This detail proved to be effective in reducing masonry spalling in zones subjected to high levels of inelastic deformations. Such spalling is potentially dangerous to building occupants.

Transverse reinforcement in the lintels proved to be adequate as designed. "U" shaped ties, as shown in Fig. 3.6, were used as transverse reinforcement in the lintels. Test results showed that the slabs contributed to the shear capacity of the lintels. The extent of this contribution is a matter for further research.

The need for adequate reinforcement in the lintel-column connections was evident, especially after the test of Specimen 1b. Enough transverse reinforcement must be provided at the lintel-column connection to resist the unbalanced forces associated with the development of the flexural capacities of the elements connected by the joint.

7.5.3 Floor System. The design and construction details of the floor system proved to be adequate to maintain the required strength and integrity. No evidence of deterioration of the bond between the different elements forming the floor system was observed during the tests.

The welded wire fabric reinforcement added to the topping on the wall areas, as described in Section 3.2.3, provided adequate punching shear resistance to the slab. No deterioration of the wall-slab connection was observed during the tests.

The bond between the precast planks and the cast-in-place concrete of the topping was adequate to resist the shear stresses associated with the development of the flexural capacities of the coupling elements. Apart from deep cleaning using a steel brush and removal of the dust, no special provisions were taken to improve the bond between the planks and the topping.

8. EXPECTED BEHAVIOR OF COUPLED WALL SPECIMENS

In this chapter, expected behavior and lateral load capacity calculations of the four coupled wall Type 2 specimens (Fig. 3.10 to 3.13) are described, and the results obtained are discussed. Essentially, the same process outlined in Chapter 5 for Type 1 specimens has been followed for Type 2 specimens: lateral load-resisting elements were provided with enough flexural and shear strength to satisfy UBC requirements; the lateral load capacity of each specimen was predicted; and all wall elements were then re-designed to satisfy the requirements consistent with the development of the expected collapse mechanism. Two approaches were considered in analyzing the specimens: a simple plastic analysis for the collapse mechanism; and a step-by-step nonlinear analysis of the walls under monotonically increasing lateral loads.

Since most of the assumptions and steps of the process have already been described in Chapter 5, no further details will be given here except when necessary. A detailed description of the analysis of Specimens 2a and 2b is given in Ref. [13].

8.1 Design Criteria

Type 2 Specimens were designed for gravity and lateral loads as specified in the 1985 UBC [34], acting on the wall as part of the prototype building [35]. A wall density of 121 pcf was used. The floor dead and live loads were 113 and 43 psf respectively. The tributary width of the wall in the prototype building was taken as 20 ft. The resulting base shear acting on the wall was 16.3 kips. When needed, the actual specimens were loaded vertically by constant loads representing the gravity loads on the wall's tributary area.

Because the analyses were intended to be predictions rather than post-test verifications, actual material properties were usually not known in advance. As explained below, representative material properties were estimated.

Reinforcement Actual properties of the reinforcement, as given in Chapter 3, were used. Typical behavior curves given in the *PCI Design Handbook* [40] were used for prestressing steel.

Masonry A masonry compressive strength f'_m = 3000 psi was used in analyzing Specimen 1a. Based on the results of Specimen 2a material tests, f'_m = 2200 psi was used for Specimen 2b. Based on the results of previous material tests, f'_m = 2500 psi was used for Specimens 2c and 2d.

Concrete Based on a 7-day compressive strength of 4250 psi, concrete compressive strength was estimated as f_c' = 5700 psi for Specimen 2a. Specified f_c' = 4000 psi and 5000 psi were considered for cast-in-place topping and precast planks respectively for Specimens 2b, 2c, and 2d.

Code Design The code-type design was the same for all specimens. Essentially, an allowable stress design was performed on the lateral load-resisting elements under service loads. Required longitudinal reinforcement in each wall was 5 #4 bars. One #3 bar every other course was required as transverse reinforcement in these elements. A detailed description of the code design is given in Appendix A of Ref. [13].

8. Expected Behavior of Type 2 Specimens

The specimens were designed to behave in a basically flexural mode, in which most of the inelastic action is due to inelastic flexural deformations at the end sections of critical elements. Essentially, Type 2 specimens were expected to behave in the same general way previously described in Section 5.3 for Type 1 specimens. In a coupled wall system, inelastic deformation occurs in a beam-type sidesway mechanism in which flexural hinges form at the base of the coupled walls and at the ends of coupling elements, as shown schematically in Fig. 8.1 for Type 2 specimens. The elements are intended to be constrained to ductile flexural failure modes by the use of a capacity design approach for shear. Energy dissipation is provided by large inelastic deformations, first of the horizontal elements (lintels), and later, of the vertical load bearing elements. This behavior permits a great part of the inelastic action to take place before the vertical load bearing elements start to suffer damage.

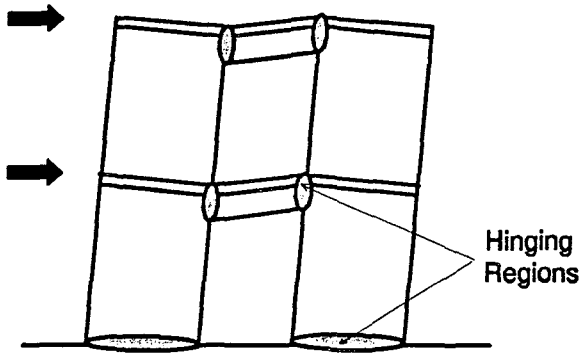

Figure 8.1: Collapse mechanism for coupled wall.

The shear distribution between the two walls depends on the stage of the loading process. Before cracking, one half of the base shear would be taken by each wall. After cracking, the relative lateral stiffness of the walls depends on their axial load levels, which in turn depend on their gravity load and overturning force. It was expected that at higher levels of lateral load, most of the base shear would be taken by the wall under higher compressive forces. This assumption is particularly valid for those specimens with a strong coupling system.

Because of their low shear span to depth ratio, high shear forces are associated with the development of the flexural capacity of the lintels. Because of the physical limitations

produced by the size and location of the masonry cells, it is usually not possible to provide all the required transverse reinforcement in those elements. As a result, even when the minimum flexural reinforcement is used, some shear damage can be expected to occur in the lintels.

Behavior of the elements' sections was modeled using the same assumptions described in Section 5.3. However, shear strength of all elements was evaluated using provisions of ACI 318-86 [34].

8.3 Plastic Analysis of Collapse Mechanism

A plastic analysis was performed on the flexural collapse mechanism shown in Fig. 8.1 for each specimen. The walls are assumed to rotate about their compression toes, and all deformations were assumed to be concentrated at the plastic hinges. In performing the plastic collapse analysis, all elements were assumed to have enough deformation capacity to develop the collapse mechanism with no strength deterioration. By either applying the principle of virtual displacements, or by imposing equilibrium conditions to the collapse mechanism when the same lateral load is applied on each floor (Fig. 8.2), the following expression is derived for the lateral load capacity V_b of the specimen [13]:

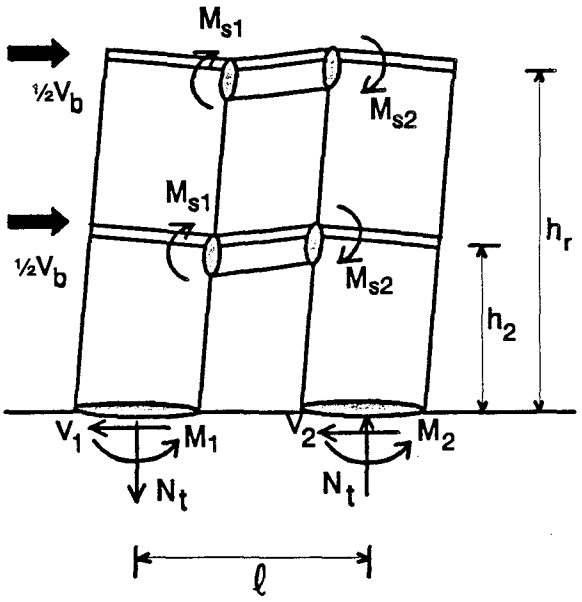

Figure 8.2: Forces acting on the collapse mechanism of the "coupled wall-based" Specimen 1b.

$$V_b = \frac{2}{h_2 + h_r}[M_1 + M_2 + N_t \ell] \qquad (8.1)$$

Where

M_1, M_2	=	Flexural capacities at the base of the tensioned and compressed wall respectively
M_{s1}, M_{s2}	=	Flexural capacity of end sections of coupling elements
N_t	=	Total shear force transmitted through the coupling elements
	=	$2(M_{s1} + M_{s2})$/(Lintel span = 56 in)
ℓ	=	Distance between plastic centroids of vertical elements = 128 in

h_2 = 2nd floor height = 100 in
h_r = Roof height = 204 in

Note that the expression for the lateral load capacity of the specimen is valid for load acting in both directions. Flexural capacities at wall bases depend on the axial load acting on each element, which in turn depends on the gravity load level and overturning forces in the wall. The total axial force transmitted between the walls depends on the flexural capacity of the end sections of the coupling elements.

As determined from equilibrium, the shear force taken by each wall at the time the collapse mechanism has developed is:

$$V_1 = \frac{2}{h_2 + h_r}[M_1 + \tfrac{1}{2}N_t\ell] \tag{8.2}$$

$$V_2 = \frac{2}{h_2 + h_r}[M_2 + \tfrac{1}{2}N_t\ell] \tag{8.3}$$

Where

V_1, V_2 = Shearing forces at the base of the tensioned and compressed wall respectively

Flexural capacities of the end sections of the coupling elements for all Type 2 specimens, as shown in Fig. 3.16, are given in Table 8.1.

Table 8.1
Flexural Capacity of Coupling Element End Sections

Specimen	M_{s1} (kip-in)	M_{s2} (kip-in)	N_t (kip)
2a	760	760	54.2
2b	1343	478	65.2
2c	1586	2506	146.1
2d	698	1506	78.7

Under lateral loads, overturning axial force N_t acting on the walls must be combined with gravity forces, resulting in net axial forces N_1 and N_2 on the tension and compression wall respectively. Because they were intended to represent bearing walls in the prototype building, Specimens 2a and 2d were vertically loaded at the top of the walls to simulate floor load actions. Specimens 2b and 2c, representing non-bearing walls, were subjected only to their own weight, as described in Section 3.3. At collapse, the total axial forces on the walls

and the associated flexural capacities M_1 and M_2 for each Type 2 specimen are given in Table 8.2.

Because of its strong coupling system and the absence of externally applied vertical loads, the net axial force acting on the tensioned wall of Specimen 2c was larger than the tensile axial capacity of the wall. For this reason, as shown in Table 8.2, it was assumed that failure would occur when the tensioned wall reached its tensile axial capacity N_1 = 106.4 kips, which defines the axial force in the compressed wall.

Table 8.2
Axial Loads and Flexural Capacities of Walls at Collapse

Specimen	Tensioned Wall		Compressed Wall	
	N_1 (kip)	M_1 (kip-in)	N_2 (kip)	M_2 (kip-in)
2a	17.0 (Tens)	3319	91.4 (Comp)	5510
2b	52.5 (Tens)	2209	77.9 (Comp)	4764
2c	106.4 (Tens)	0	132.4 (Comp)	5784
2d	41.3 (Tens)	1596	116.2 (Comp)	5279

Substituting values of Table 8.2 in Eq. 8.1, the lateral load capacity V_b of each Type 2 specimen were calculated as shown in Table 8.3:

These values are upper bounds to the actual lateral load capacity of the specimens.

Table 8.3
Collapse Lateral Load Capacity of Type 2 Specimens

Specimen	Lateral Load Capacity V_b (kip)
2a	101
2b	102
3c	141
2d	112

8.4 Nonlinear Step-by-Step Analysis

A planar frame model of the coupled walls was subjected to an incremental collapse analysis under monotonically increasing lateral loads. Each increment in load was defined by the occurrence of a major event in one or more elements. A major event could be first flexural cracking of an element, yielding of the extreme flexural reinforcement of an element, or attainment of flexural capacity in an element. Each load increment was determined by performing an elastic analysis using the member properties calculated for that increment. The modulus of elasticity of each element was assumed to remain constant during the loading process. Equivalent flexural and shear stiffness were calculated using the moment-curvature relationship for each critical section. Since this method works by using load increments, it is not possible to analyze the specimen beyond the point of maximum lateral load capacity. A more detailed description of this analysis is given in Section 6.4 of Ref. [13].

Results of these analyses for Specimens 2a, 2b, and 2c, presented in the form of base shear versus lateral displacement at the top of the specimen, are given in Tables 8.4 to 8.6,

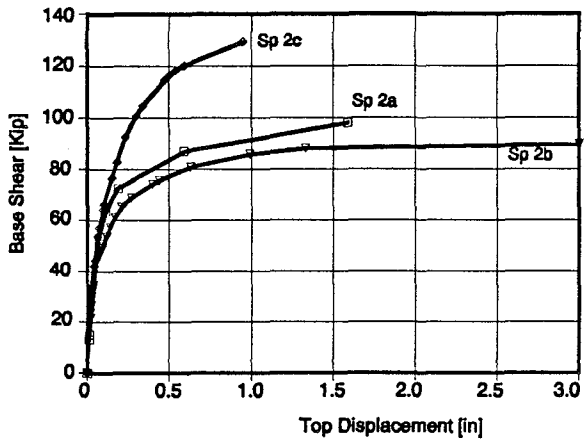

Figure 8.3: Predicted base shear versus displacement envelope for Type 2 specimens

Table 8.4
Predicted Base Shear
Displacement History for Specimen 2

Base Shear (kip)	Top Displ. (in.)	Event
13.0	0.012	Flexural crack at base of tension wall
15.0	0.014	Flexural crack at base of compression wall
50.9	0.070	Yielding of reinforcement at base of tension wall
53.3	0.074	Yielding of reinforcement at 2nd floor slab
63.3	0.11	Yielding of reinforcement at roof slab
72.7	0.19	Yielding of reinforcement at base of compression wall
87.2	0.59	Flexural capacity of compressed wall
98.0	1.59	Flexural capacity of tensioned wall; collapse mechanism

and Fig. 8.3. These calculations, made in advance to each test, were intended to predict the behavior of the specimens. Because of time constraints before testing Specimen 2d, no analysis was performed at that time for this specimen.

It can be observed that the predicted values of the lateral load capacities obtained from the plastic analysis of the collapse mechanism (Table 8.3), are consistently larger than those obtained from the nonlinear step-by-step analysis. As previously mentioned, in performing the plastic analysis, it was assumed that the considered mechanism was the actual one, and that all the elements were capable of reaching and maintaining simultaneously their maximum flexural capacities. The lateral load capacity so obtained is an upper bound to the actual capacity. Because the specimens were relatively simple structures, it was not a difficult task to identify the correct kinematically admissible mechanism. However, due to their different load-deformation characteristics, it was expected that some elements of the specimen failed before the other were able to develop their full capacities. For this reason, the second assumption was not completely valid, and the actual lateral load capacity of the specimen was expected to be lower than that predicted using the collapse mechanism. Because the non-linear step-by-step analysis was able to model this behavior, predictions so obtained were considered to be more reliable.

Table 8.5 Predicted Base Shear - Displacement History for Specimen 2b

Base Shear (Kip)	Top Displ. (in)	Event
21.6	0.020	Flexural crack at base of tensioned wall
26.3	0.026	Flexural crack at base of compressed wall
34.5	0.041	Yielding of reinforcement at base of tensioned wall; Flexural crack at 2nd floor slab top face
43.4	0.055	Flexural crack at top of 1st story tensioned wall; Flexural crack at top of 2nd story tensioned wall
49.3	0.095	Yielding of reinforcement at top of 1st story tensioned wall; Yielding of reinforcement at roof slab top face
53.8	0.12	Yielding of reinforcement at top of 2nd story tensioned wall
57.6	0.14	Flexural crack at base of 2nd story tensioned wall
61.4	0.17	Flexural crack at 2nd floor slab bottom face
65.2	0.21	Yielding of reinforcement at base of compressed wall
68.8	0.27	Yielding of reinforcement at base of 2nd story tensioned wall
74.2	0.40	Flexural crack at top of 1st story compressed wall; Flexural crack at top of 2nd story compressed wall
75.8	0.44	Flexural crack at roof slab bottom face
81.0	0.63	Flexural capacity of 2nd floor slab (top face)
85.9	0.99	Flexural capacity of roof slab (top face)
88.2	1.33	Flexural capacity of compressed wall base
91.0	4.26	Flexural capacity of tensioned wall base; Collapse mechanism

Table 8.6 Predicted Base Shear - Displacement History for Specimen 2c

Base Shear (Kip)	Top Displ. (in)	Event
22.9	0.016	Flexural crack at 2nd floor lintel bottom face
24.8	0.018	Flexural crack at base of tensioned wall
31.5	0.025	Flexural crack at base of compressed wall
33.6	0.028	Flexural crack at roof lintel bottom face
42.0	0.043	Yielding of reinforcement at base of tensioned wall
44.2	0.047	Flexural crack at top of 1st story tensioned wall
53.8	0.065	Flexural crack at top of 2nd story tensioned wall; Yielding of reinforcement at top of 1st story tensioned wall
57.2	0.074	Flexural crack at top of 1st story compressed wall
64.3	0.096	Flexural crack at 2nd floor slab top face
66.0	0.10	Flexural crack at base of 2nd story tensioned wall
66.4	0.10	Flexural crack at top of 2nd story compressed wall
76.6	0.15	Yielding of reinforcement at top of 2nd story tensioned wall
82.9	0.18	Yielding of reinforcement at base of 2nd story tensioned wall
92.6	0.23	Yielding of reinforcement at base of compressed wall
100.6	0.30	Flexural capacity of tensioned wall base
104.3	0.34	Flexural crack at roof slab top face
114.4	0.47	Yielding of reinforcement at top of 1st story compressed wall
116.4	0.50	Flexural capacity of top section 1st story tensioned wall
118.3	0.54	Yielding of reinforcement and flexural capacity of 2nd floor lintel top face
120.1	0.59	Yielding of reinforcement at top of 2nd story compressed wall
129.2	0.95	Flexural capacity of compressed wall base; Collapse mechanism

8.5 Capacity Design

Because all Type 2 specimens were analyzed and tested in advance to Type 1 specimens, there are some differences in methods and criteria of analysis. This is the case of the shear strength calculations. As previously described, shear capacities of all the elements of the Type 2 specimens were calculated using the provisions of the 1983 edition of the ACI-318 code [41]. More appropriate formulas were later used to calculate shear strength of masonry piers of Type 1 specimens.

Each wall was provided with enough shear capacity to resist the shearing forces associated with the development of the collapse mechanism. Sections in which plastic hinges were expected to develop, were checked for sufficient interface shear transfer capacity. The resulting reinforcement and detailing for Type 2 specimens is completely described in Section 3.

8.6 Comparison among Expected Behavior of Each Specimen

All specimens were intended to develop their lateral load capacity in a predominantly flexural mode. The elements were assumed to have enough deformation capacity to develop a collapse mechanism with no strength deterioration.

Because all Type 2 specimens had identical wall reinforcement, their behavior was expected to be differentiated by the characteristics of their floor systems. Those specimens with stiffer and stronger coupling system were expected to develop higher axial loads on the walls due to overturning. In the absence of externally applied vertical forces on the walls, the lateral load capacity of the specimen was expected to be controlled by the tensile axial capacity of the tensioned wall, as in the case of Specimen 2c. High levels of tensile axial loads were expected to reduce the shear and sliding-shear capacity of the tensioned walls, and, consequently, to increase the shear demand on compressed walls.

High rotation demands were expected to develop at the end sections of the coupling elements. In the case of Specimen 2b (planks parallel to the wall with no lintel) there was a strong potential for explosive failure of the prestressed plank. Shear damage was expected to develop in the lintels of Specimens 2c and 2d.

9. TEST RESULTS FOR COUPLED WALL SPECIMENS

9.1 General

Test results for coupled wall Type 2 specimens are presented and discussed in this Chapter. Since most of these results have already been published [13,32,45], only a general description and discussion of the results concerning the overall behavior of the specimens is included here.

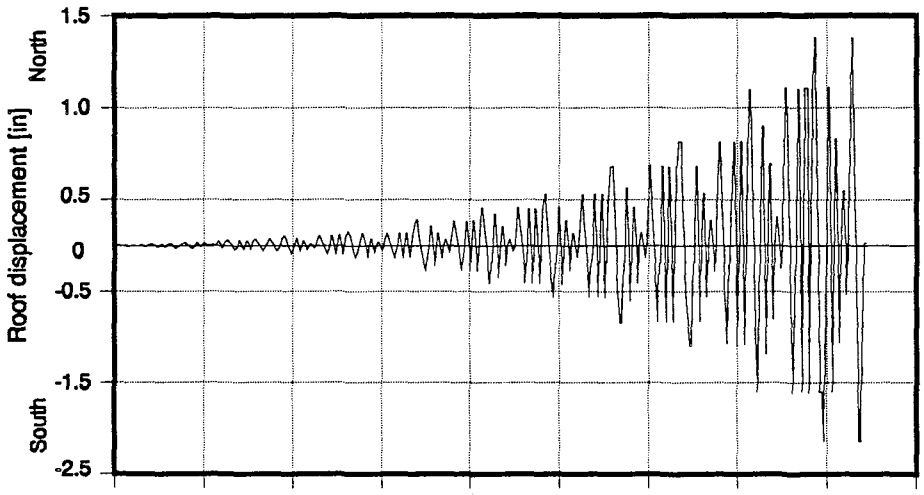

Figure 9.1: Specimen 2a: Roof displacement history

9.2 Test Results for Specimen 2a

Specimen 2a was subjected to the roof displacement history shown in Fig 9.1. Significant events for northward and southward loading are summarized in Tables 9.1 and 9.2 respectively. Progression of cracking and damage of walls is shown in Figs. 9.2 through 9.5. The observed history of base shear versus roof displacement is shown in Fig. 9.6. The envelopes of base shear versus roof displacement are shown in Figs. 9.7 and 9.8. In Fig. 9.7, the envelope of base shear versus overall drift ratio is compared with analytical predictions made before the test using a sequential collapse analysis. The variation of lateral backbone stiffness (defined as the ratio between the peak values of load and displacement in a particular cycle) during the test is shown in Fig. 9.9.

Table 9.1: Specimen 2a test: significant events, northward loading

Load Point	Test Event	Base Shear Kips	Top Displ. in	Overall Drift Ratio %
39	FME: Flexural cracking of tension wall	24.2	0.036	0.018
58	Flexural cracking of compression wall	24.2	0.045	0.022
95	Yield of longitudinal reinforcement in tension wall	48.3	0.11	0.054
131	Cracking and yield of both slabs; Yield of compression wall	58.5	0.16	0.078
169	Cracking of bottom of both slabs	62.4	0.24	0.12
170	Flexural cracking above lap splices	66.8	0.28	0.14
207	Diagonal cracks in tension wall	73.2	0.41	0.20
279	Diagonal cracks in compression wall	86.7	0.86	0.42
317	Toes of both walls start to crush; Wide flexural crack at wall bases and splices	89.4	1.13	0.55
357	Maximum lateral load capacity	95.9	1.69	0.83
384	Face shell spall at toe of compression wall	77.9	1.67	0.82
414	Maximum lateral displacement; Extreme compression bar buckles in compression wall; Walls slide on base	80.5	2.23	1.09

Table 9.2: Specimen 2a test: significant events, southward loading

Load Point	Test Event	Base Shear Kips	Top Displ. in	Overall Drift Ratio %
43	Flexural cracking of tension wall	24.3	0.037	0.018
99	Yield of longitudinal reinforcement in tension wall	48.6	0.10	0.049
135	Cracking and yield of both slabs; Yield of compression wall	45.5	0.14	0.069
247	Diagonal cracks in tension wall	71.2	0.57	0.28
284	Diagonal cracks in compression wall; Toes of both walls start to crush	77.7	0.84	0.42
361	Maximum lateral load capacity	84.7	1.64	0.80
386	Face shell split at toe of compression wall	72.6	1.63	0.80
397	Fracture of extreme tension bar of tension wall	45.9	1.63	0.80
418	Maximum lateral displacement; Longitudinal and lateral sliding of walls	63.5	2.17	1.06

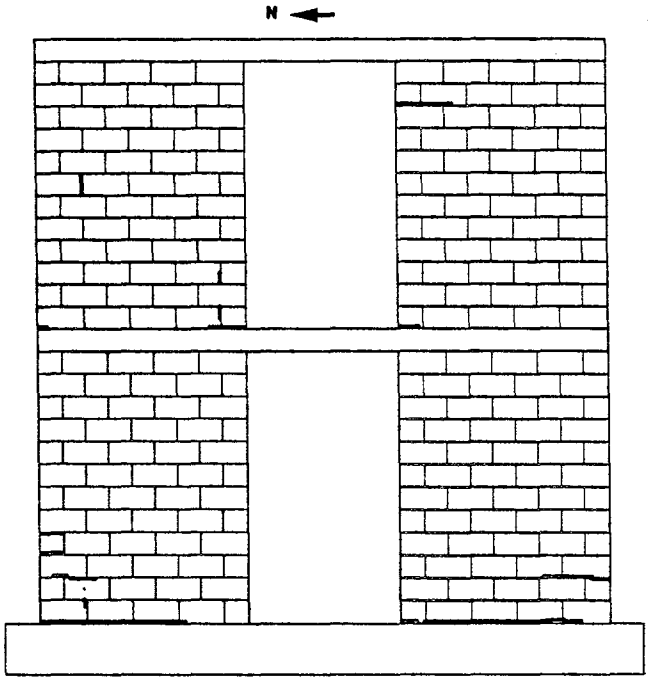

Figure 9.2: Specimen 2a: Cracking progression at overall drift ratio 0.42%.

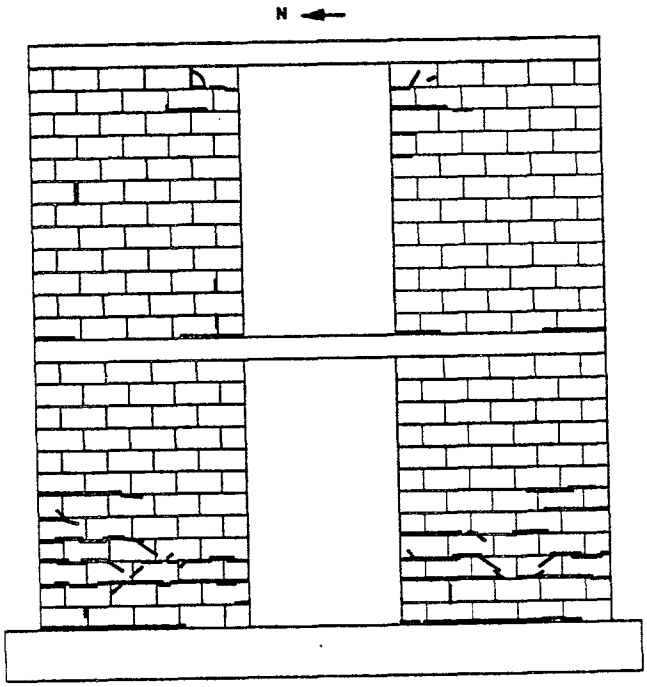

Figure 9.3: Specimen 2a: Cracking progression at overall drift ratio 0.07%.

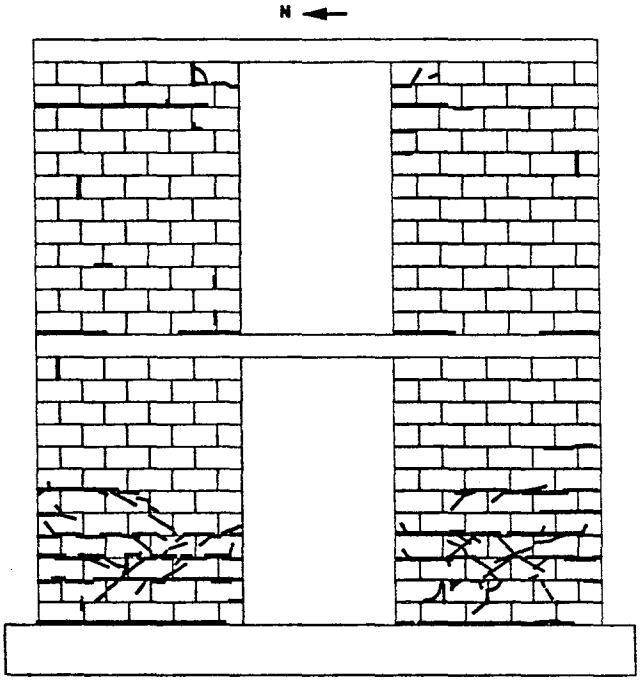

Figure 9.4: Specimen 2a: Cracking progression at overall drift ratio 0.82%.

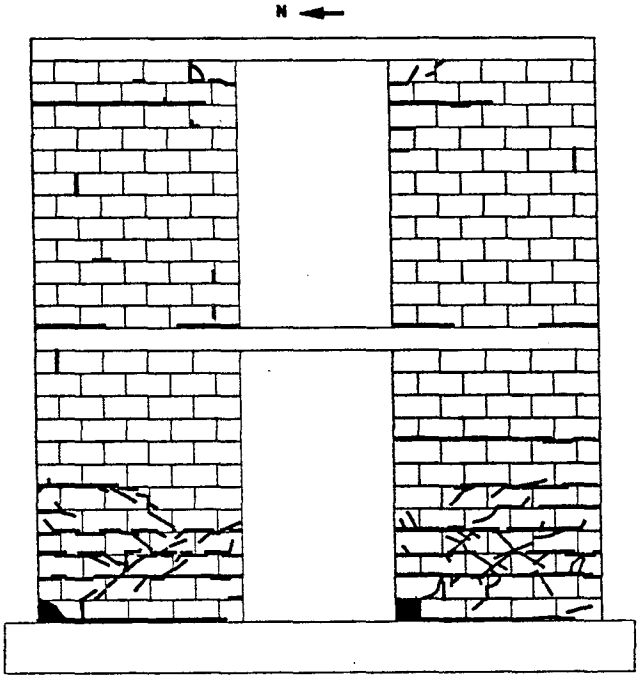

Figure 9.5: Specimen 2a: Cracking progression at end of the test, overall drift ratio 1.08%.

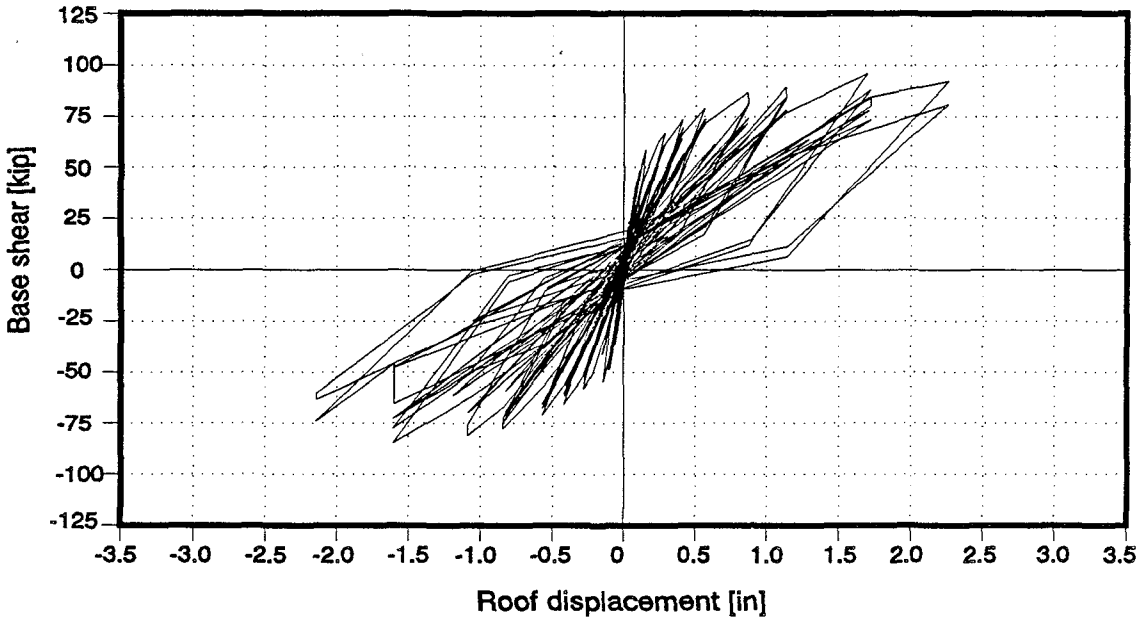

Figure 9.6: Specimen 2a: Base shear - Roof displacement history

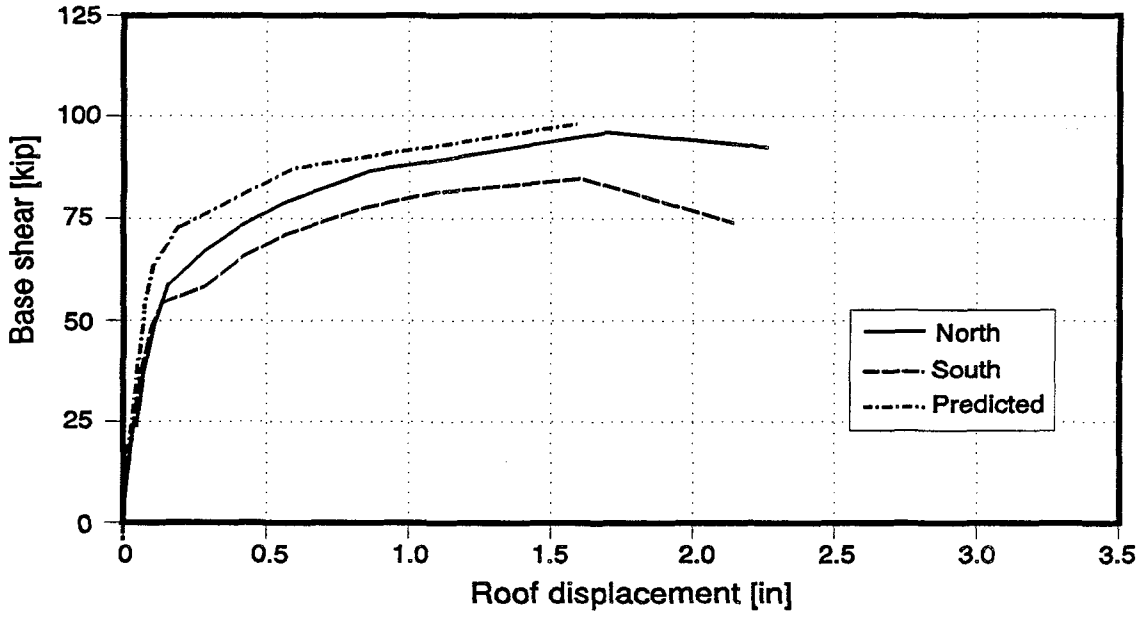

Figure 9.7: Specimen 2a: First peak envelopes and predicted response

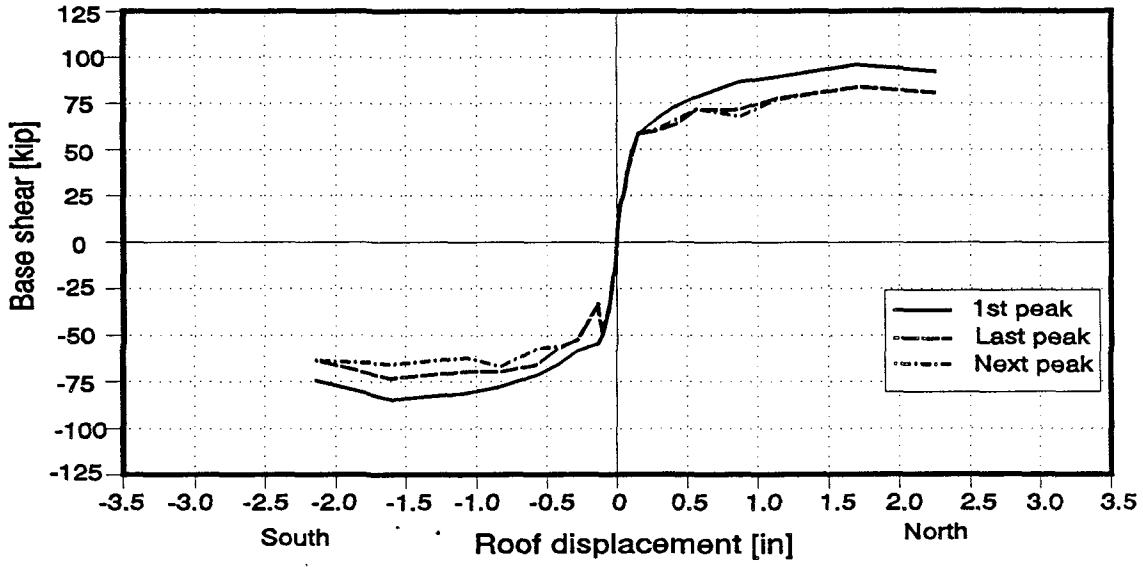

Figure 9.8: Specimen 2a: First, last, and next peak envelopes of the load displacement response.

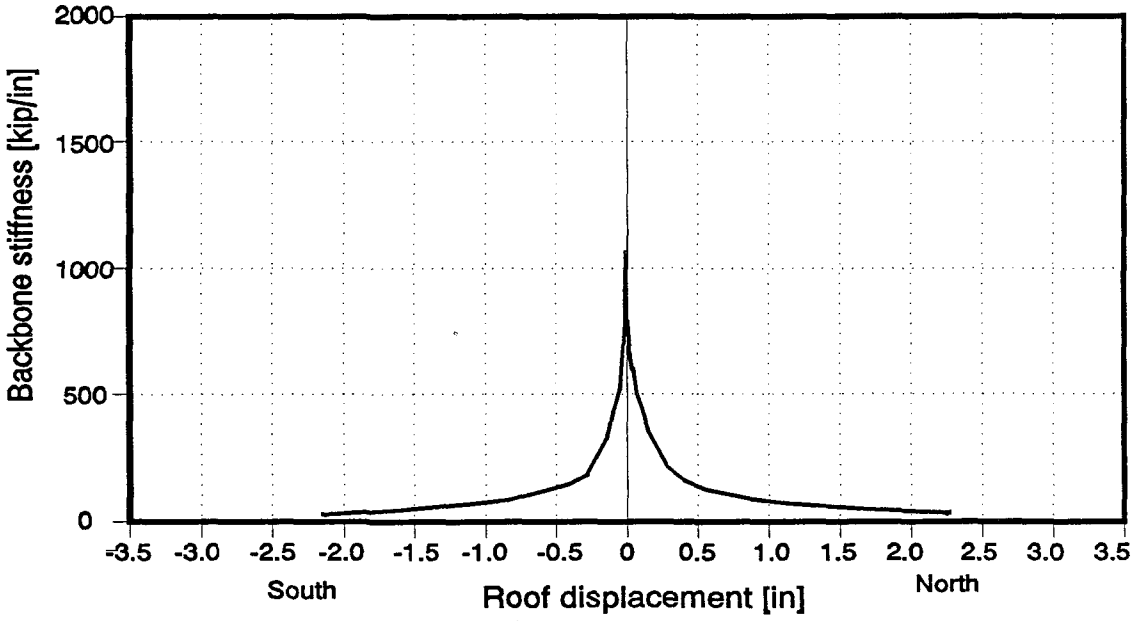

Figure 9.9: Specimen 2a: First peak backbone stiffness

When testing Specimen 2a, vertical load was to be maintained at 19.4 kips per wall (92.2 psi at the wall base). Due to a problem with the calibration of the load cell, the vertical load was kept at only 12 kips per wall until Load Point 137. The calibration problem was then detected and corrected, and the load was increased to the proper level. This occurred at the same time the lateral loading system was switched from load to displacement control.

As shown in Figs. 9.6 and 9.7, Specimen 2a reached a maximum base shear of 95.9 kips, at an overall drift ratio of 0.83% (1.69 in. roof displacement) when loaded to the North direction, and a maximum base shear of 84.7 kips, at an overall drift ratio of 0.80% (1.64 in. roof displacement) when loaded to the South direction. Ultimate capacity was determined by formation of a flexural mechanism: after plastic hinges developed in the coupling elements, flexural failure occurred at the bases of the walls. Displacement capacity was limited by crushing of the compression toes, tensile fracture of a longitudinal bar at the first-story of the north wall, and sliding movement of the walls' bases both in-plane and out-of-plane.

As shown in Fig. 9.6, the hysteresis loops remained very stable throughout the test. The longitudinal reinforcement eventually fractured at the north end of the first story of the north wall; the subsequent loss of strength is shown in Figure 9.6 by the decrease of base shear in the largest loop while loading to the south. The specimen's hysteretic behavior was basically flexural, consistent with the observed failure modes.

Pinching of the hysteretic loops was observed at high levels of lateral displacement. This pinching is due to sliding of the coupled wall at the base of the first story. Plots of earlier load series, before the onset of substantial base sliding, exhibit little pinching.

Wide flexural cracks developed at the bases of both walls, and crushing of masonry occurred at the toes of the walls. From visual observations at the end of the test, the tension walls uplifted across their entire length. Large sliding shear displacements occurred due to the deterioration of shear transfer capacity between the walls and the foundation beam. The north wall had a final in-plane displacement at the base of 0.25 inches to the north. The south wall in-plane displacement at the base was 0.5 inches. The out-of-plane displacement for the north wall varied from 1/2 to 9/16 inches. The south wall displacement varied from zero to 3/4 inches.

Shearing cracks formed in both 1st story walls, especially near their bases, but did not widen. As shown by the strain gauge readings, transverse reinforcement did not yield.

Specimen 2a had a cast-in-place concrete slab. Throughout the test, the slab and wall remained monolithic, and the slab-wall joint showed no signs of deterioration. Slab cracks formed in a regular, flexural pattern across the full width of both slabs near the slab-wall intersection at the openings. As evident from the observed yielding of the longitudinal reinforcement across the full width of both slabs, plastic hinges formed in each slab at both

sides of the opening, and the full widths of both slabs were effective in transferring shear and moment between the walls.

The cast-in-place concrete slabs used a reinforcing detail which in effect created an embedded beam centered over the walls and spanning the full length of Specimen 2a (Section 3.3.3). This reinforcing beam detail was used to ensure sufficient slab coupling. Visual observations showed that both the second-floor and roof slabs cracked and yielded across their entire widths. This suggests that the beam reinforcement detail of Specimen 2a was unnecessary.

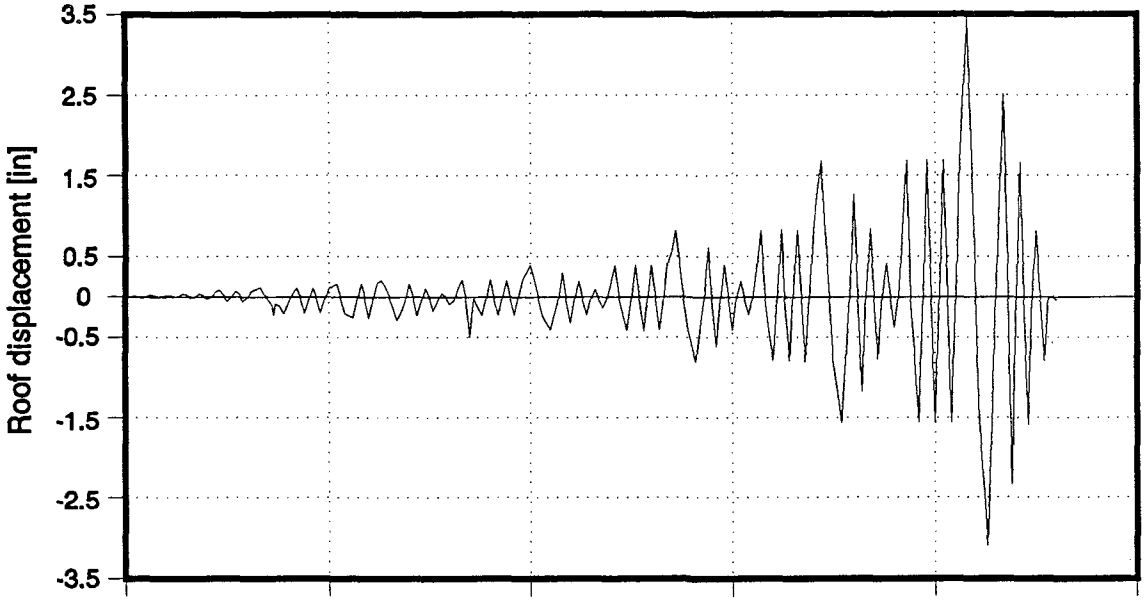

Figure 9.10: Specimen 2b: Roof displacement history

9.3 Test Results for Specimen 2b

Specimen 2b was subjected to the roof displacement history shown in Fig.9.10. Significant events for northward and southward loading are summarized in Tables 9.3 and 9.4 respectively. Progression of cracking and damage of walls is shown in Figs. 9.11 to 9.14. The observed history of base shear versus overall drift ratio is shown in Fig. 9.15. The envelopes of base shear versus overall drift ratio are shown in Figs. 9.16 and 9.17. In Fig. 9.16 the envelope of base shear versus overall drift ratio is compared with analytical predictions made before the test using a sequential collapse analysis. The variation of lateral stiffness during the test is shown in Fig. 9.18.

Table 9.3: Specimen 2b test: significant events, northward loading

Load Point	Test Event	Base Shear Kips	Top Displ. in	Overall Drift Ratio %
52	Flexural cracking of 2nd story tension wall; Yield of 1st story tension wall	34.9	0.112	0.055
63	Flexural cracking of 2nd story compression wall; Yield of 2nd story compression wall; Cracking of 2nd floor slab top face	43.9	0.202	0.099
	Yield of 2nd story north wall joint opening			
85		67.9	0.59	0.29
	Cracking of roof slab top face			
100		59.1	0.40	0.19
	Diagonal shear cracking of both 1st story walls; Yield of 2nd story			
135	south wall joint opening; Cracking of 2nd story slab bottom face	65.5	0.56	0.27
	Yield of 2nd story tension wall base			
171	Cracking of roof slab bottom face; Yield of 2nd story south wall joint opening; Longitudinal shear cracking of roof slab top face	80.8	1.25	0.61
172		88.0	1.69	0.82
	Cracking of compression toe of both walls; Face shell spall at toe of compression wall; Longitudinal shear cracking of 2nd floor slab top face			
207		86.6	2.55	1.25
	Maximum lateral load capacity and maximum roof displacement; Longitudinal shear cracking of bottom face of both slabs			
208	Fracture of extreme tension bar of compression wall	88.1	3.46	1.69
	Loss of compression toe			
217	Extreme compression bar of compression wall buckles in	46.0	2.51	1.23
219		-55.4 (south)	-2.34 (south)	-1.15
220		6.9	2.23	1.09

Table 9.4: Specimen 2b test: significant events, southward loading

Load Point	Test Event	Base Shear Kips	Top Displ. in	Overall Drift Ratio %
16	Flexural cracking of tension wall and compression wall	10.3	0.017	0.008
36	After load jump: Yield of longitudinal reinforcement of 1ast story tension and compression walls	53.8	0.40.	0.20
56	Flexural cracking of 2nd story walls; Cracking of both slabs' top faces; Diagonal shear cracking of tension wall	42.3	0.27	0.13
85	After load jump: Yield of 2nd story north wall joint opening	67.9	0.59	0.29
105	Longitudinal shear cracking of 2nd floor slab bottom face	46.1	0.41	0.20
140	Cracking of 2nd story slab bottom face	60.3	0.62	0.30
176	Longitudinal shear cracking of roof slab bottom face	69.1	1.18	0.58
177	Yield of 1st story north wall joint opening	74.8	1.57	0.77
212	Yield of 2nd story tension wall; Cracking of roof slab bottom face	72.4	2.32	1.14
213	Maximum lateral load capacity and maximum roof displacement; vertical cracking of compression wall toe	78.3	3.10	1.52

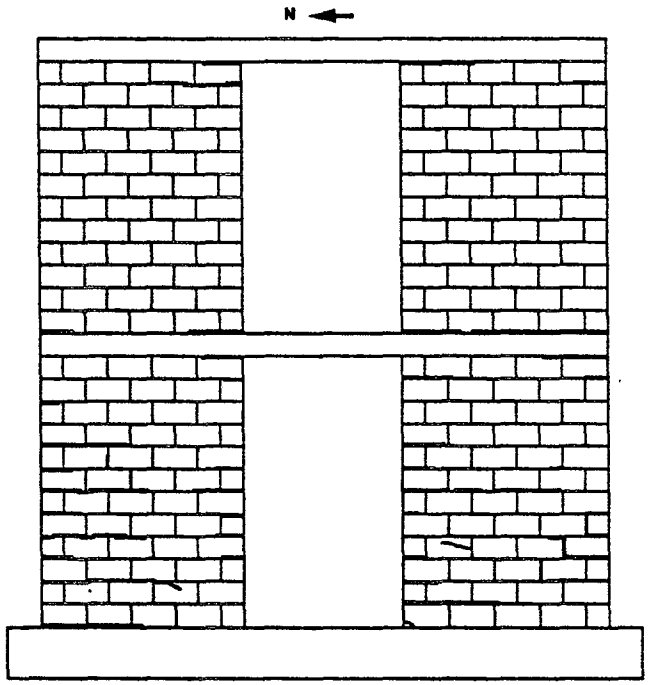

Figure 9.11: Specimen 2b: Cracking progression at overall drift ratio 0.29%.

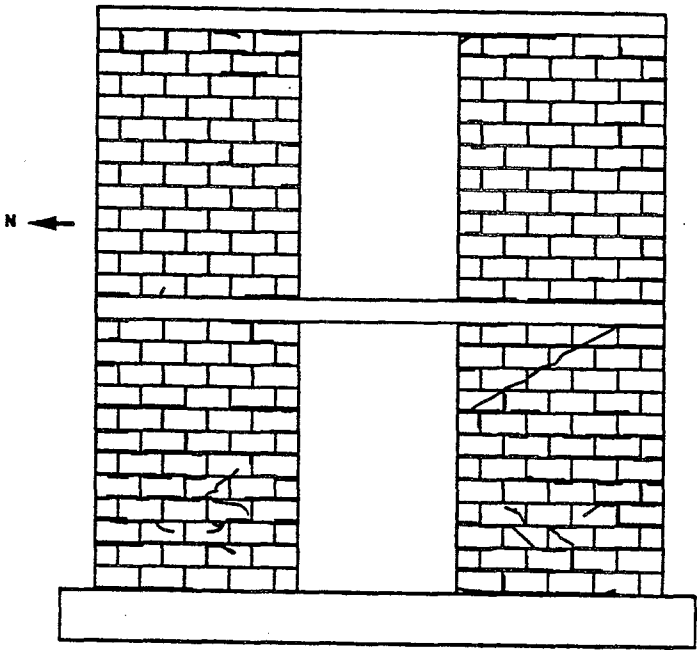

Figure 9.12: Specimen 2b: Cracking progression at overall drift ratio 0.10%.

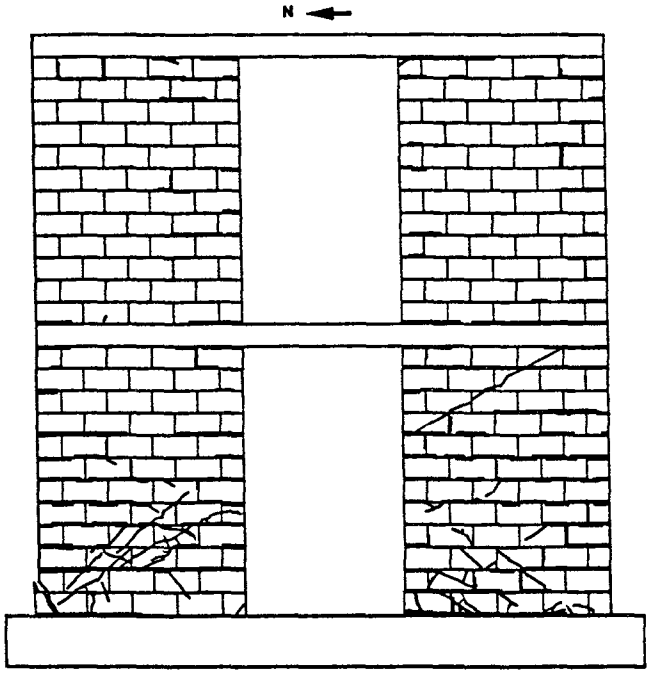

Figure 9.13: Specimen 2b: Cracking progression at overall drift ratio 1.61%.

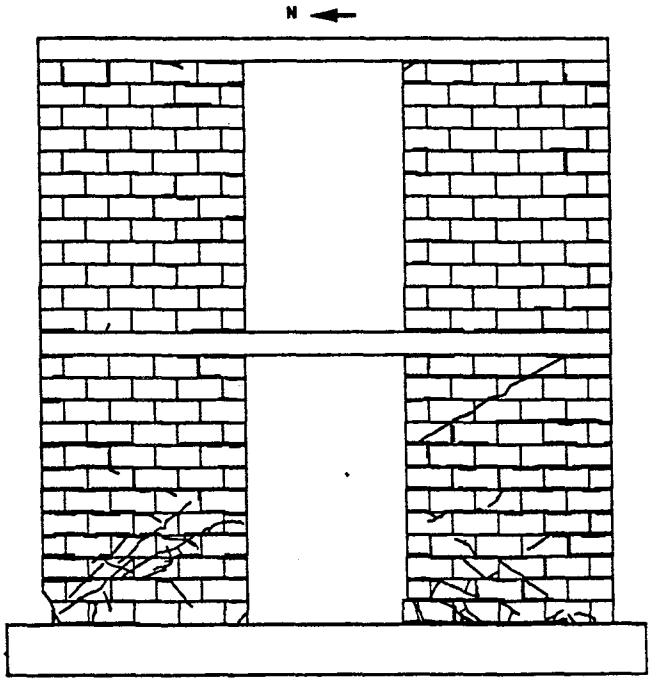

Figure 9.14: Specimen 2b: Cracking progression at end of the test, overall drift ratio 1.61%.

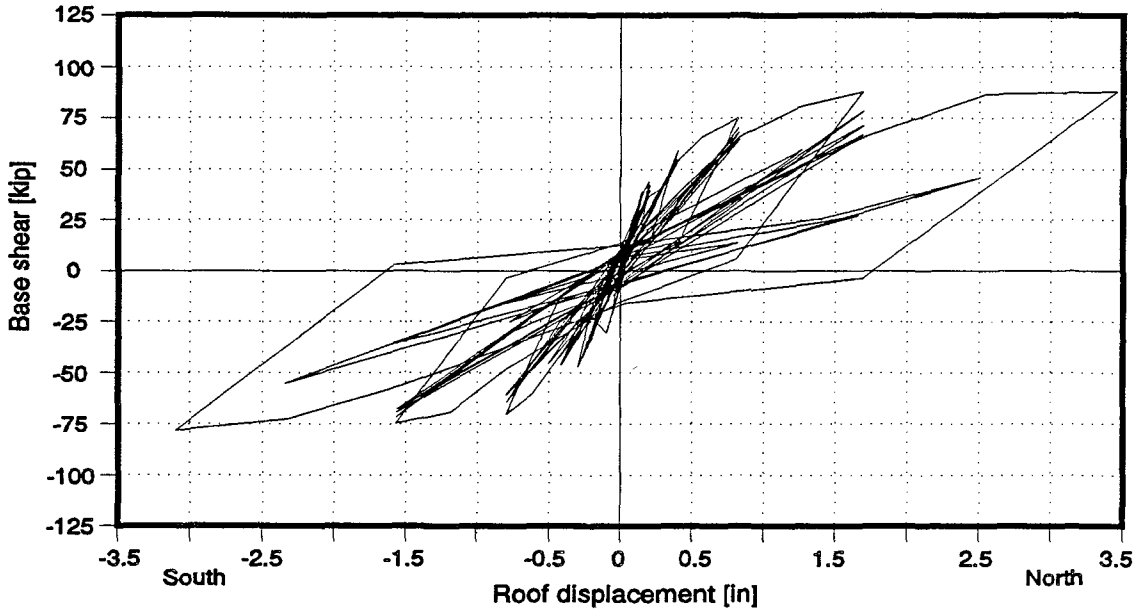

Figure 9.15: Specimen 2b: Base shear - Roof displacement history

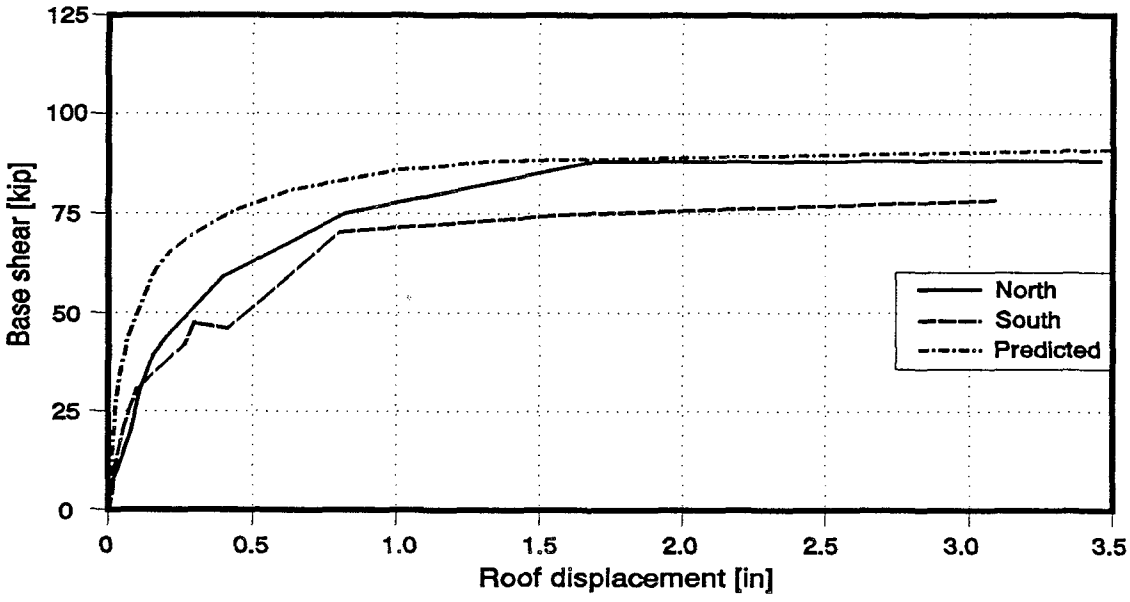

Figure 9.16: Specimen 2b: First peak envelopes and predicted response

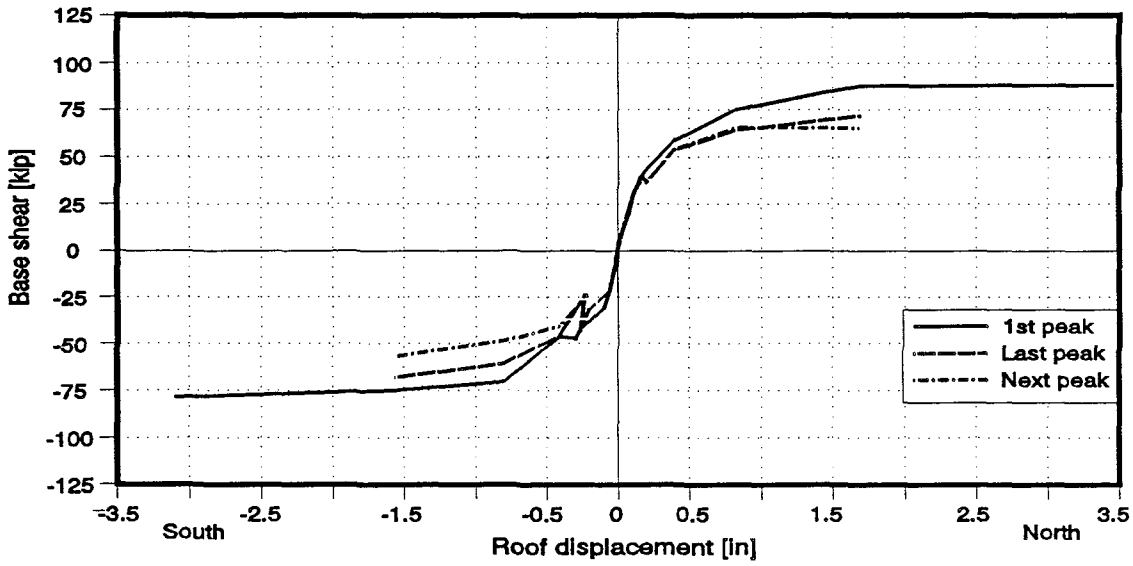

Figure 9.17: Specimen 2b: First, last, and next peak envelopes of the load displacement response.

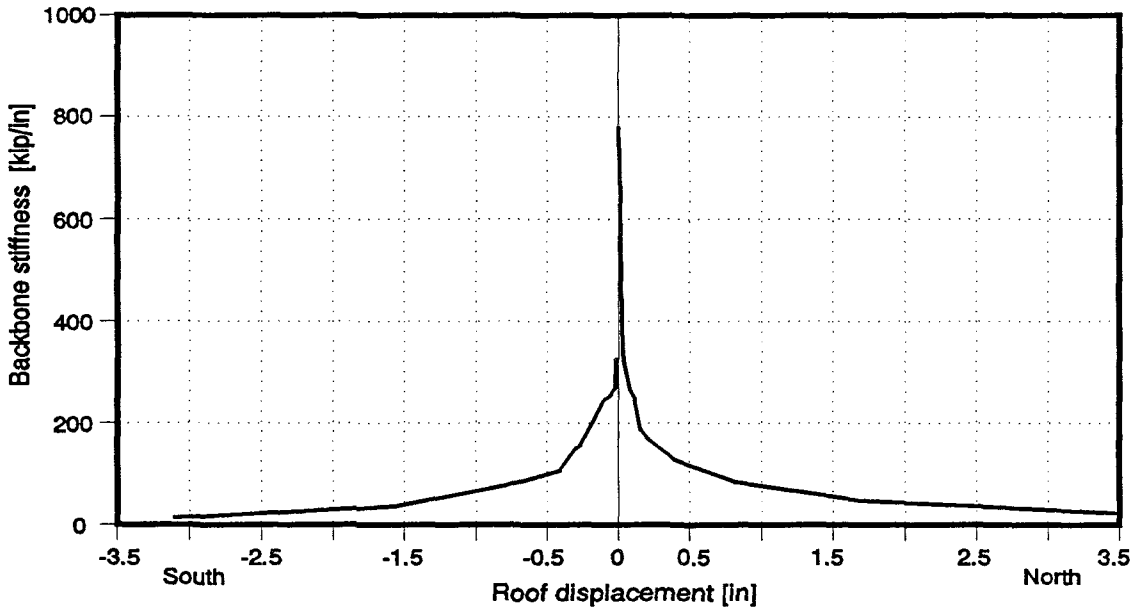

Figure 9.18: Specimen 2b: First peak backbone stiffness

Since the floor system of Specimen 2b spanned parallel to the walls, no additional vertical load was applied to the specimen.

Before the testing began, due to a malfunction of the closed loop servocontroller system, the specimen was accidentally loaded when the first-story ram on the east side began to extend after being connected to the load transfer beam. Hairline diagonal cracks formed in each wall. The bed joint on the concrete base beam was cracked at the south end of the south wall. Local cracking also occurred in the roof slab near the south sway brace plate. The only noticed effect of this damage on the response of the specimen was a decrease of the expected initial stiffness.

As shown in Figs. 9.15 and 9.16, Specimen 2b reached a maximum base shear of 88.1 kips, at an overall drift ratio of 1.70% (3.46 in. roof displacement) when loaded to the North direction, and a maximum base shear of 78.3 kips, at an overall drift ratio of 1.52% (3.10 in. roof displacement) when loaded to the South direction. Ultimate capacity was determined by formation of a flexural mechanism: after some degradation occurred at the coupling elements, flexural failure occurred at the bases of the walls. Displacement capacity was limited by the loss of the compression toes for both walls when loading to the north and by crushing of the south wall compression toe when loading to the south; by tensile fracture of a longitudinal bar at the first-story of the north wall; by buckling of the longitudinal reinforcement at the compression toes; and by sliding movement of the walls' bases, both in- and out-of-plane.

As shown in Fig. 9.15, the hysteresis loops remained very stable throughout the tests. The specimens' hysteretic behavior was basically flexural, consistent with the observed failure mode.

Similar to the previous case, large shear sliding displacements were observed between the walls and the foundation beam. This sliding caused pinching in the hysteresis loops at high levels of lateral displacement. When the test ended, the residual out-of-plane displacements due to sliding were 7/8 inches for the north wall, and 1-3/8 inches for the south wall. The north wall had a final in-plane residual displacement of 0.13 inches to the south, and the south wall had a final in-plane residual displacement of 0.19 inches to the north.

Due to malfunctions of the servo-controller system, sudden increases in load were applied towards the south twice during the testing. Even though the load peak values were not recorded by the data acquisition system, their values were obtained from the plotter used to monitor the test. The first jump in the applied load produced some flexural cracking at the 1st story walls and at the wall-slab connections. The second jump produced yielding of the longitudinal reinforcement of the coupling system at the roof level. However, the actual damage produced on the specimen was less than expected for those levels of loads. It is believed that because of inertial forces, the base shear was less than the applied load.

The floor system of Specimen 2b suffered a high degree of deterioration during the test: 1) shear cracks formed at the vertical faces of the plank-wall connections; 2) punching shear cracks developed at the slab-wall intersection near the openings; 3) the horizontal joint between slab and walls deteriorated at the top of wall openings in both stories; 4) flexural cracking, while present, was limited to a couple of cracks across the full width of the slab at the wall openings; and 5) local cracking was produced by load transfer from the testing apparatus to the second-floor and roof slabs.

The effectiveness of the coupling system was reduced due to two principal factors: shear cracking at portions of the slab-wall intersections; and deterioration of the horizontal joint at the coupled wall openings between second-floor and roof slabs and walls. These factors caused reduced continuity between the walls and the slabs, allowing the slabs to rotate less than the walls at each story level. Smaller rotations of the slabs result in lower slab moments, which in turn reduce the amount of shear transferred by the slabs between the walls. This produced a decrease in the strength and stiffness of the specimen. Evidence of this effect was observed during testing of Specimen 2b: 1) while double-curvature flexural cracking was observed in the walls during the early stages of the test, single-curvature flexural cracking governed the response of the walls as the load cycles increased during the test; and 2) due to their smaller rotations, the slabs did not develop their flexural capacities, and the flexural cracks that developed in the planks were totally closed at the end of testing, indicating that the planks remained essentially elastic throughout the test.

An eccentric shear stress transfer model has been used to evaluate the reduction of shear transfer from slabs to walls in Specimen 2b [13]. Results of those analysis showed that high shear stresses would develop at the wall-slab connections, indicating possible problems in shear transfer from the slabs to the walls, which was in fact observed for Specimen 2b.

The problems encountered with eccentric shear stress transfer for Specimen 2b are not likely to be encountered often in the field, because that specimen represents a worst case. In the prototype building, restraint against the longitudinal shear cracking and subsequent movement of the planks is provided by the adjoining floor system; while for Specimen 2b, restraint is not provided to inhibit plank movement away from the coupled walls.

9.4 Test Results for Specimen 2c

Specimen 2c was subjected to the roof displacement history shown in Fig. 9.19. Significant events for northward and southward loading are summarized in Tables 9.5 and 9.6 respectively. Progression of cracking and damage of walls is shown in Figs. 9.20 to 9.23. The observed history of base shear versus roof displacement is shown in Fig. 9.24. The envelopes of base shear versus overall drift ratio are shown in Figs. 9.25 and 9.26. In Fig. 9.25 the envelope of base shear versus overall drift ratio is compared with analytical

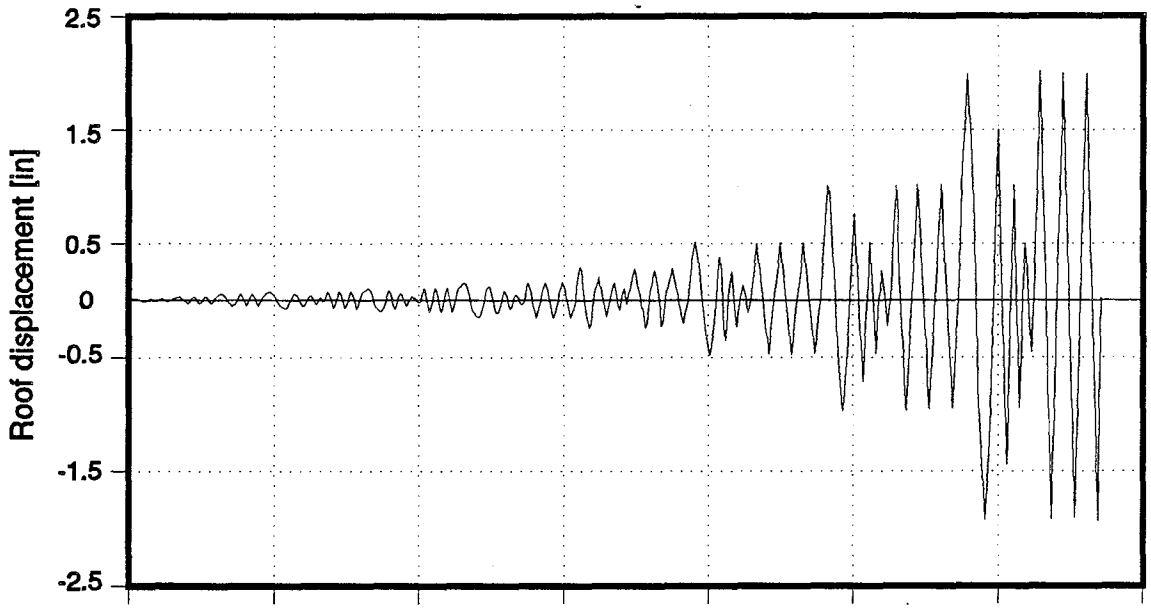

Figure 9.19: Specimen 2c: Roof displacement history

Table 9.5: Specimen 2c test: significant events, northward loading

Load Point	Test Event	Base Shear Kips	Top Displ. in	Overall Drift Ratio %
32	Flexural cracking of tension wall	12.8	0.014	0.007
35	Flexural cracking of compression wall	20.2	0.029	0.014
63	Flexural crack bottom face roof lintel	30.3	0.058	0.028
96	FME: Yield of longitudinal reinforcement in tension wall	40.2	0.074	0.036
230	Cracking at the tension wall-2nd floor lintel connection	60.1	0.15	0.074
311	Cracking at the top face of 2nd floor slab	81.3	0.29	0.14
390	Diagonal cracks in tension and compression walls; Cracking at top face of roof slab	94.6	0.45	0.22
483	Wide flexural cracks at bases of both walls	113.1	1.01	0.50
579	Maximum lateral load capacity; Compression wall toe starts to crush; Both walls slide on foundation beam; Extensive diagonal cracking of compression wall; Horizontal crack at tension wall just below the 2nd floor slab; Diagonal cracks in web of 2nd floor lintel; Compression zone of 2nd floor lintel starts to crush	122.1	1.99	0.98
629	Crushing of both wall toes; Crushing of compression zone of 2nd floor lintel	102.9	2.01	0.99
645	Complete crushing of wall toes; Both walls slide on foundation beam; Strong pinching effect in hysteresis loops	96.0	2.00	0.98
661	Last peak in north direction; Extreme compression bar buckles in compression wall; Walls slide on base	92.4	2.00	0.98

Table 9.6 Specimen 2c test: significant events, southward loading

Load Point	Test Event	Base Shear Kips	Top Displ. in	Overall Drift Ratio %
41	Flexural cracking of tension wall; Flexural crack bottom face roof lintel	19.7	0.032	0.016
70	Flexural cracking of compression wall; Flexural crack bottom face 2nd floor lintel	24.7	0.036	0.018
107	FME: Yield of longitudinal reinforcement in tension wall	39.5	0.071	0.035
240	Cracking at the tension wall-2nd floor lintel connection	59.5	0.14	0.069
318	Cracking at the top face of 2nd floor and roof slabs	71.3	0.24	0.12
401	Diagonal cracks in tension and compression walls; Cracking at the wall-lintel connection at both floor levels	92.0	0.48	0.24
493	Wide flexural cracks at bases of both walls; Splitting crack in compression toe, masonry starts to crush	104.3	0.98	0.48
591	Maximum lateral load capacity; Both wall toes show vertical splitting and crushing; Wide flexural cracks in both walls; Both walls slide on foundation beam; Diagonal cracking of both walls; Diagonal cracks in web of 2nd floor lintel; Extensive damage of 2nd floor lintel	107.0	1.92	0.94
637	Crushing of both wall toes; Crushing of compression zone of 2nd floor lintel	94.7	1.92	0.94
653	Complete crushing of wall toes; Both walls slide on foundation beam; Strong pinching effect in hysteresis loops	86.6	1.90	0.93
669	Last peak in south direction; Extreme compression bar buckles in compression wall; Walls slide on base; Fracture of extreme bar of tension wall	70.3	1.93	0.95

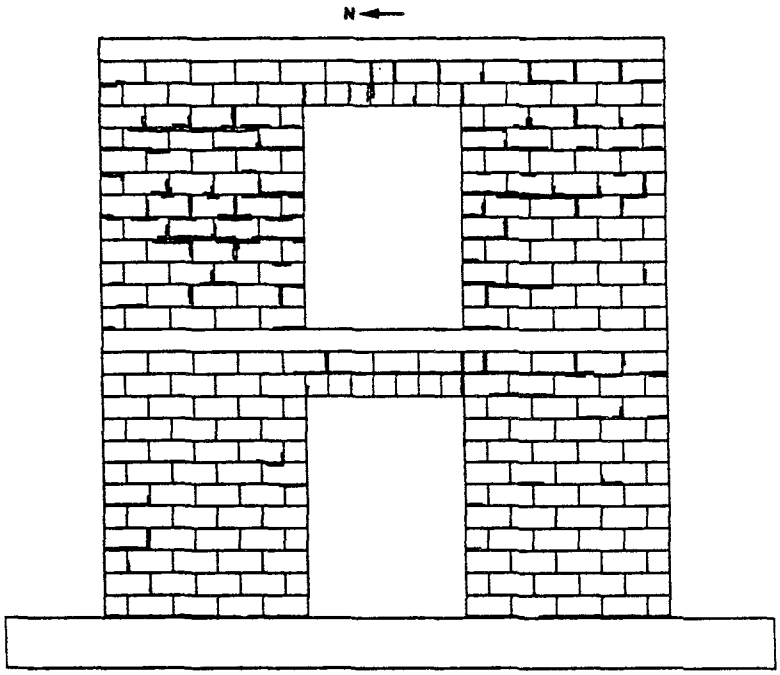

Figure 9.20: Specimen 2c: Cracking progression at overall drift ratio 0.14%.

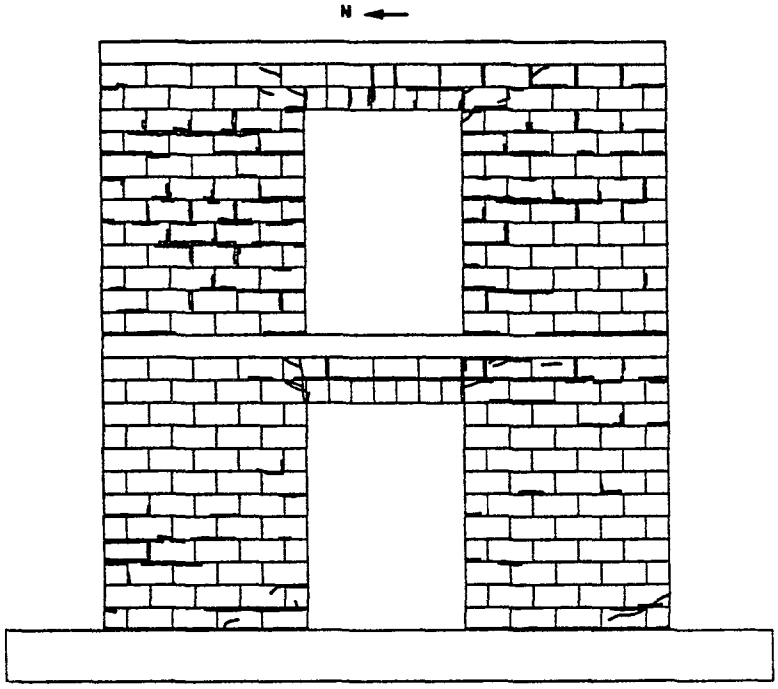

Figure 9.21: Specimen 2c: Cracking progression at FME, overall drift ratio 0.036%.

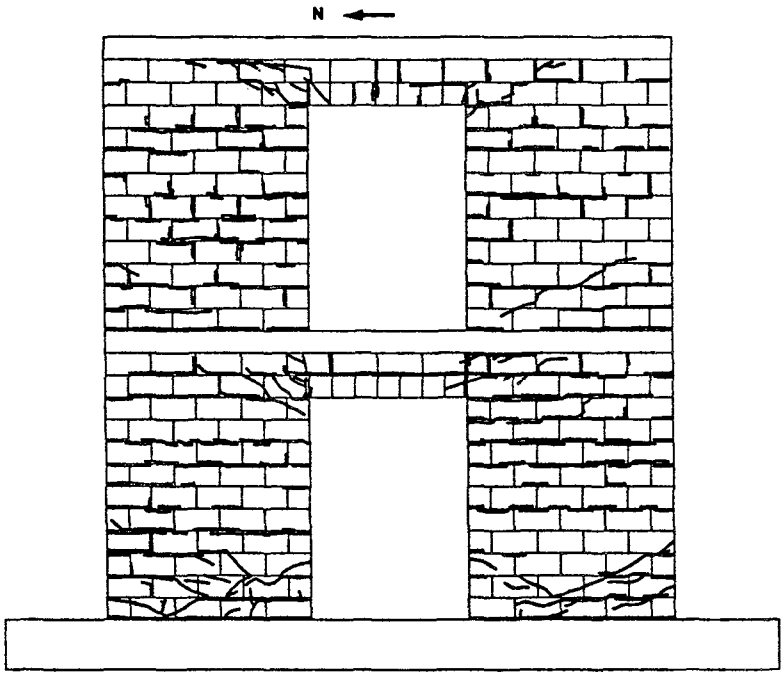

Figure 9.22: Specimen 2c: Cracking progression at overall drift ratio 0.50%.

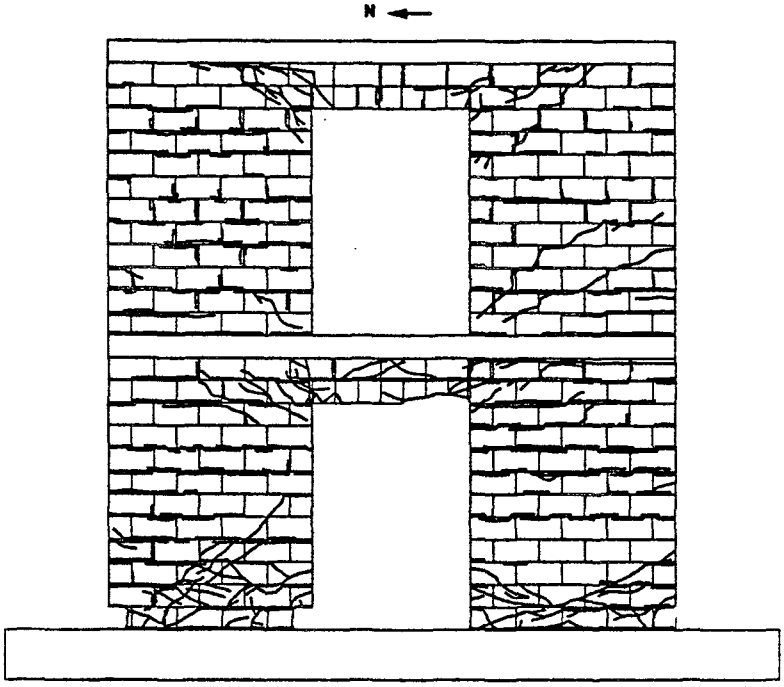

Figure 9.23: Specimen 2c: Cracking progression at overall drift ratio 0.98%.

predictions made before the test using a sequential collapse analysis. The variation of lateral stiffness during the test is shown in Fig. 9.27.

As shown in Figs. 9.24 and 9.25, Specimen 2c reached a maximum base shear of 122.1 kips, at an overall drift ratio of 0.98% (1.99 in.) when loaded to the North direction, and a maximum base shear of 107.0 kips, at an overall drift ratio of 0.94% (1.92 in.) when loaded to the South direction. Ultimate capacity was determined by formation of a flexural mechanism: after plastic hinges developed at the coupling elements, flexural failure occurred at the bases of the walls. Displacement capacity was limited by the loss of the compression toes in both walls, by buckling of some longitudinal bars at the bases of the walls, and by slip of the bases of the walls with respect to the base beam.

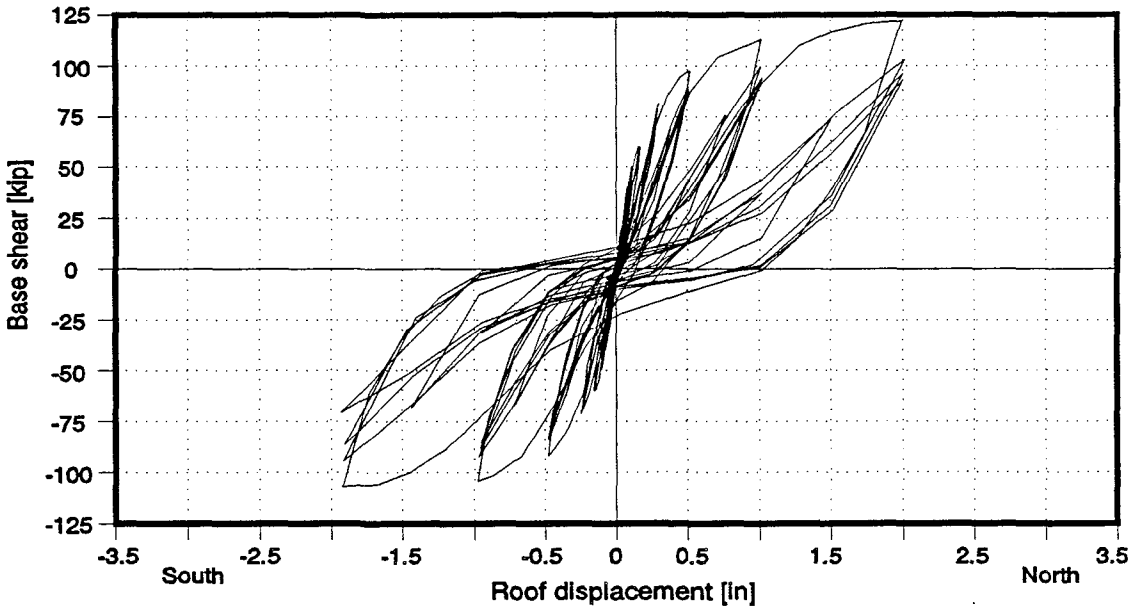

Figure 9.24: Specimen 2c: Base shear - Roof displacement history

Wide flexural cracks developed at the wall bases. Extensive crushing of masonry occurred at the compression toes of both walls. After spalling of the masonry shell cover at the toes, extreme longitudinal reinforcement of the walls showed buckling in the clear span defined between the bottom transverse bar and the base beam. However, transverse reinforcement with 180 degree hooks at the ends proved to offer a good confinement for longitudinal reinforcement. During the last cycles, slip of the bases of the walls with respect to the base beam became more significant. This effect is clearly seen in the flattening of the hysteresis loops. Simultaneously, the crack pattern at the wall bases showed that some interior longitudinal bars started to buckle.

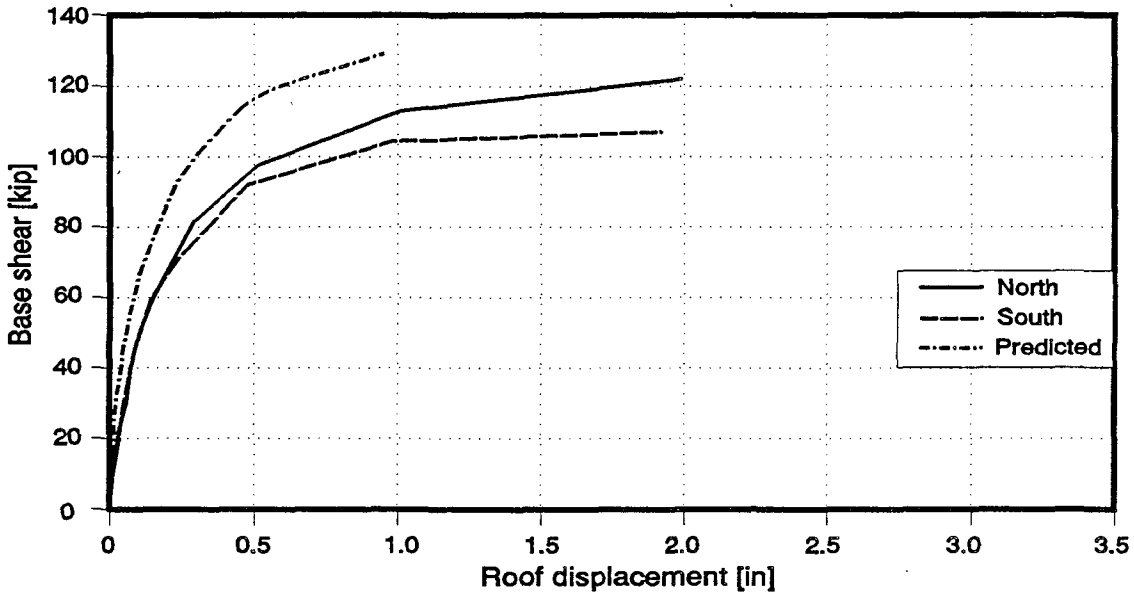

Figure 9.25: Specimen 2c: First peak envelopes and predicted response

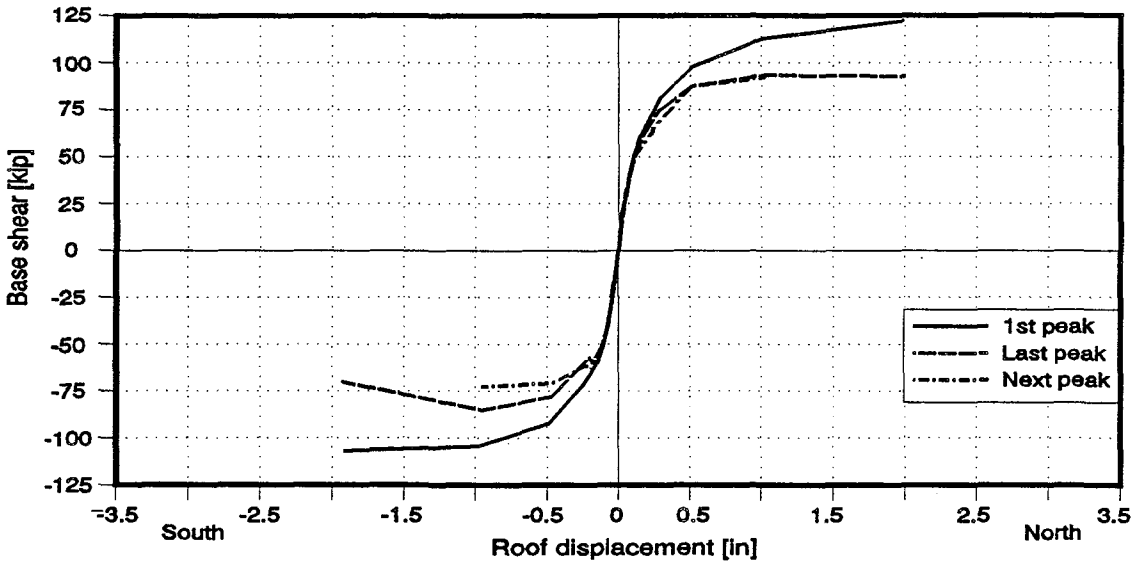

Figure 9.26: Specimen 2c: First, last, and next peak envelopes of the load displacement response.

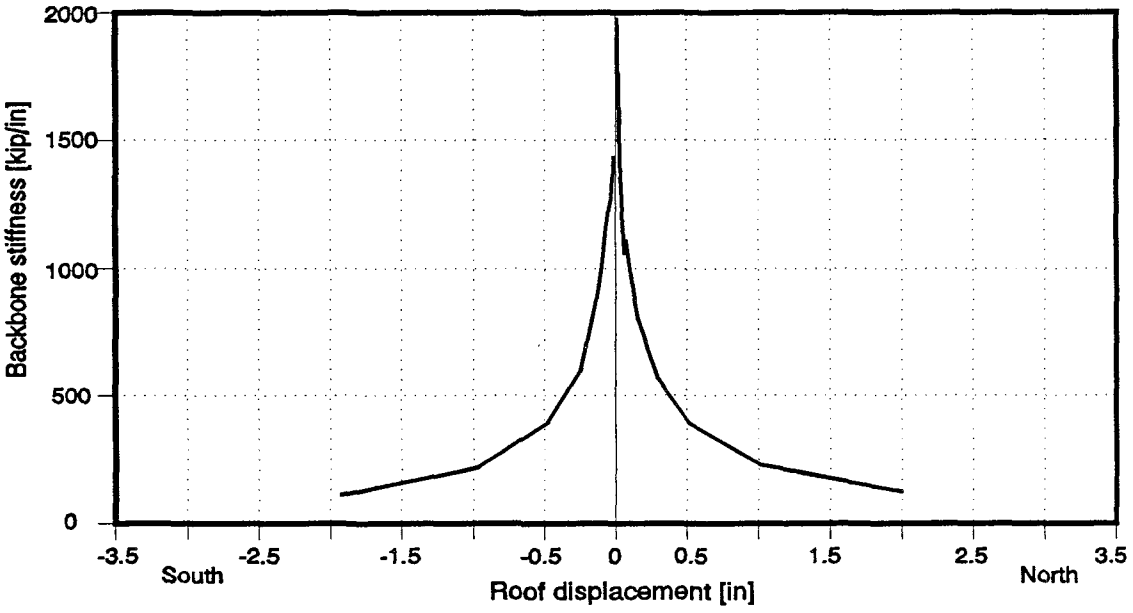

Figure 9.27: Specimen 2c: First peak backbone stiffness

At this point it was not clear if the buckling of those bars produced the out-of-plane slipping of the walls, or if the lateral movement of the walls caused the bars to buckle. During the last cycle, the extreme bar of the North wall fractured when the specimen was loaded in the South direction.

Shearing cracks formed in all the walls, especially near the bases of both first-story walls, but did not widen. Transverse reinforcement did not yield. Shear keys proved to be effective in preventing early significant slipping. After the test, it was found that the sliding shear plane passed through the shear keys. The shear capacity of the keys exceeded that of the bond between the grout and the base beam.

The coupling system showed progressive deterioration under the action of cyclic loads. Flexural cracks developed at the bottom face of the lintels and at the slab topping. After the test, it was found that the cracks from the topping penetrated into the top flange of the precast planks, but there was evidence that the planks remained elastic during the test. Crushing of the compression zone occurred at the second-floor lintel during the last cycles of the test. Strain gauges placed on the longitudinal reinforcement of the lintels, near to the edge of the North wall, showed no yielding. Shearing cracks developed at the web of the second floor lintel. Extensive cracking occurred at the walls near the connection with the lintels, especially at the second floor. There was no evidence of deterioration of the joint between the walls and the planks, nor of the horizontal joint between walls and slabs.

Extensive cracking occurred at the walls near to their connection with the lintels, especially at the second floor. Even though the strain gauges in the longitudinal reinforcement of the lintels showed no yielding, there was cracking in the anchorage zone of part of this reinforcement and wide flexural cracks in the lintels, indicating that strains probably exceeding yield occurred over an extended length of this reinforcement. The cracking pattern in the walls near the lintel ends suggests the existence of strong tensile forces in the anchored bars.

Owing to the characteristics of the coupling system, it was not possible to provide the lintels with a shear capacity larger than their theoretical flexural capacity. Consequently, a shear type of failure was expected for these elements. However, only the lintel in the second floor showed some shear cracking at the web and lintel behavior was typically flexural. In all probability, the coupling system was unable to develop its expected flexural capacity due to early damage in the masonry and slip of some lintel longitudinal reinforcement, and its shear capacity was larger that expected due to the contribution of the slabs.

In summary, Specimen 2c showed satisfactory maintenance of strength, stiffness, and energy dissipation up to story drifts of about 1%. The specimen behavior was basically flexural, as intended in design. Predicted base shears corresponding to significant events agreed well with observed values, even though predicted displacements in the final stages of the test were only about one-half of the observed values. The behavior of the coupling system was better than expected, with no deterioration of the slab-wall connections, and with a flexural failure.

9.5 Test Results for Specimen 2d

Specimen 2d was subjected to the roof displacement history shown in Fig.9.28. Significant events for northward and southward loading are summarized in Tables 9.7 and 9.8 respectively. Progression of cracking and damage of walls is shown in Figs. 9.29 to 9.32. The observed history of base shear versus roof displacement is shown in Fig. 9.33. The envelopes of base shear versus overall drift ratio are shown in Figs. 9.34 and 9.35. The variation of lateral stiffness during the test is shown in Fig. 9.36.

As shown in Figs. 9.33 and 9.34, Specimen 2d reached a maximum base shear of 111.4 kips, at an overall drift ratio of 0.48% (0.98 in. roof displacement) when load ed to the North direction, and a maximum base shear of 110.6 kips, at an overall drift ratio of 0.46% (0.95 in. roof displacement) when loaded to the South direction. Ultimate capacity was determined by formation of a flexural mechanism: after plastic hinges developed at the coupling elements, flexural failure occurred at the bases of the walls. Displacement capacity was limited by the loss of the compression toes in both walls, and by buckling and fracture of some longitudinal bars at the bases of the walls.

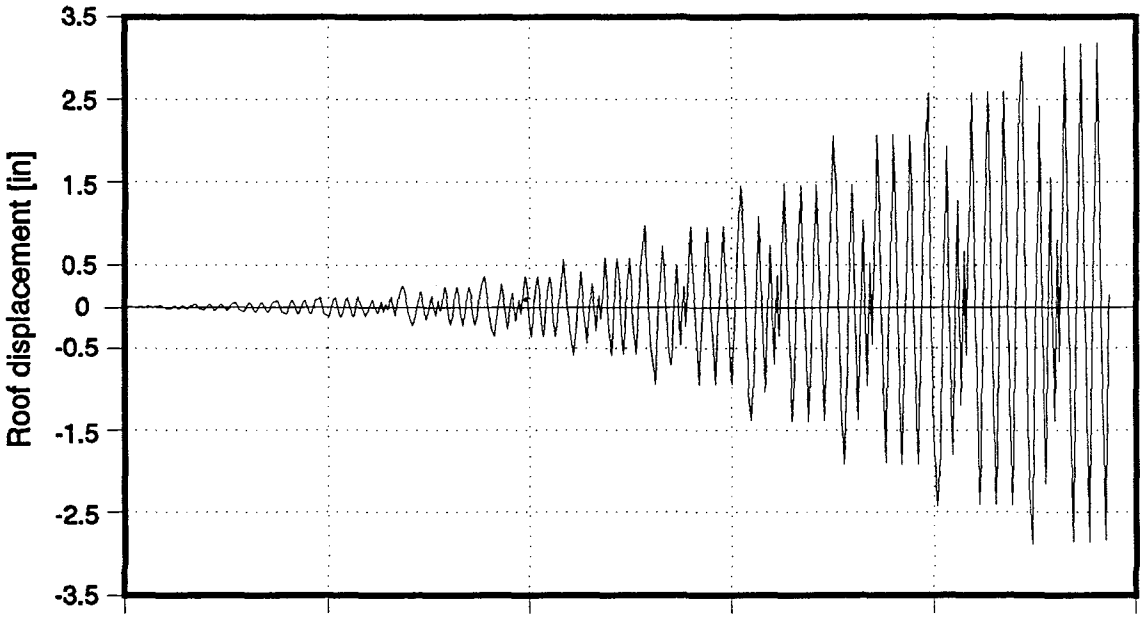

Figure 9.28: Specimen 2d: Roof displacement history

Table 9.7: Specimen 2d test: significant events, northward loading

Load Point	Test Event	Base Shear Kips	Top Displ. in	Overall Drift Ratio %
35	Flexural cracking of both walls	20.7	0.022	0.011
69	Cracks in mortar joints of 2nd floor lintel	31.1	0.036	0.018
150	Flexural cracking at the top face of the roof slab	50.3	0.078	0.038
191	FME: Yield of longitudinal reinforcement in tension wall	58.3	0.103	0.051
274	Diagonal cracks in compression wall; Cracking at the tension wall-lintel connections in both floor levels	87.4	0.25	0.12
434	Diagonal cracking progressed in both walls	101.7	0.58	0.29
514	Maximum lateral load capacity; Splitting crack in compression toe, masonry starts to crush; Diagonal cracks in web of 2nd floor lintel	111.4	0.98	0.48
684	Loss of compression toe of south wall; Longitudinal splitting crack at the compression zone of the 2nd floor lintel; Wide diagonal cracks in the 2nd story wall at the lintel-wall connection; Diagonal crack in 2nd story wall	96.1	1.48	0.72
701	Crushing of masonry in the compression toe progressed along the section; Crushing of compression zone of 2nd floor lintel	110.1	2.05	1.00
744	Complete crushing of wall toes; Extreme compression bar buckles in compression wall	93.1	2.08	1.01
792	Fracture of extreme bar of tension wall	73.1	2.04	1.00
887	Longitudinal bar buckles in compression zone of 2nd floor lintel	82.6	3.08	1.51
929	Maximum displacement; Fracture of welded wire fabric reinforcement in topping at roof	61.1	3.13	1.53

Table 9.8 Specimen 2d test: significant events, southward loading

Load Point	Test Event	Base Shear Kips	Top Displ. in	Overall Drift Ratio %
44	Flexural cracking of both walls	20.9	0.028	0.014
115	Yielding of bottom longitudinal reinforcement in 2nd floor lintel	35.2	0.052	0.026
159	Flexural cracking at the top face of the roof slabs	49.5	0.085	0.042
201	FME: Yield of longitudinal reinforcement in tension wall	59.4	0.122	0.060
284	Cracking at the tension wall-lintel connections in both floor levels	79.2	0.20	0.097
444	Diagonal cracking progressed in both walls	102.5	0.59	0.29
524	Maximum lateral load capacity; Splitting crack in compression toe, masonry starts to crush	110.6	0.95	0.46
692	Loss of compression toe of south wall; Longitudinal splitting crack at the compression zone of the 2nd floor lintel; Wide diagonal cracks in the 2nd story wall at the lintel-wall connection	102.2	1.39	0.68
711	Crushing of masonry in the compression toe progressed along the section; Crushing of compression zone of 2nd floor lintel	107.7	1.92	0.94
897	Maximum displacement; Fracture of extreme bar of tension wall	59.2	2.89	1.42

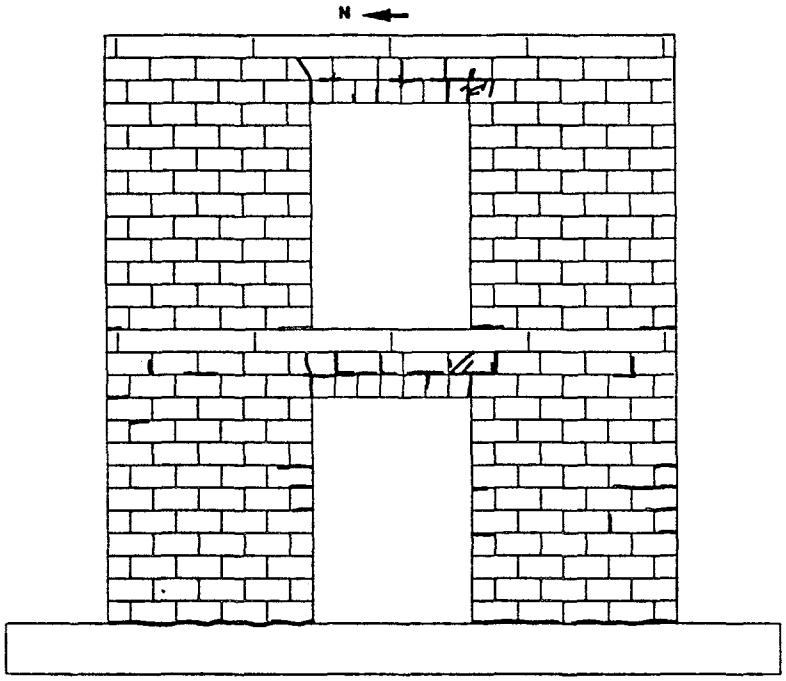

Figure 9.29: Specimen 2d: Cracking progression at overall drift ratio 0.47%.

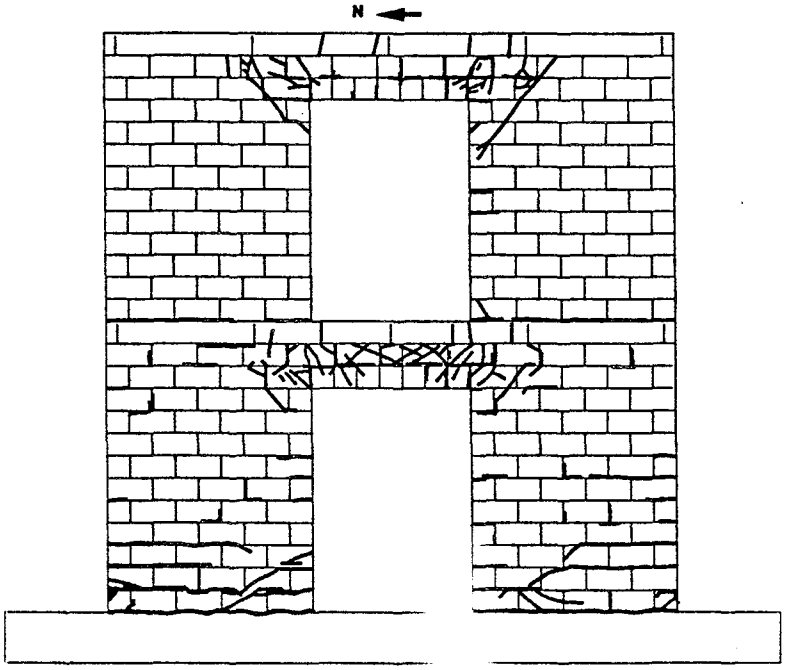

Figure 9.30: Specimen 2d: Cracking progression at FME, overall drift ratio 0.06%.

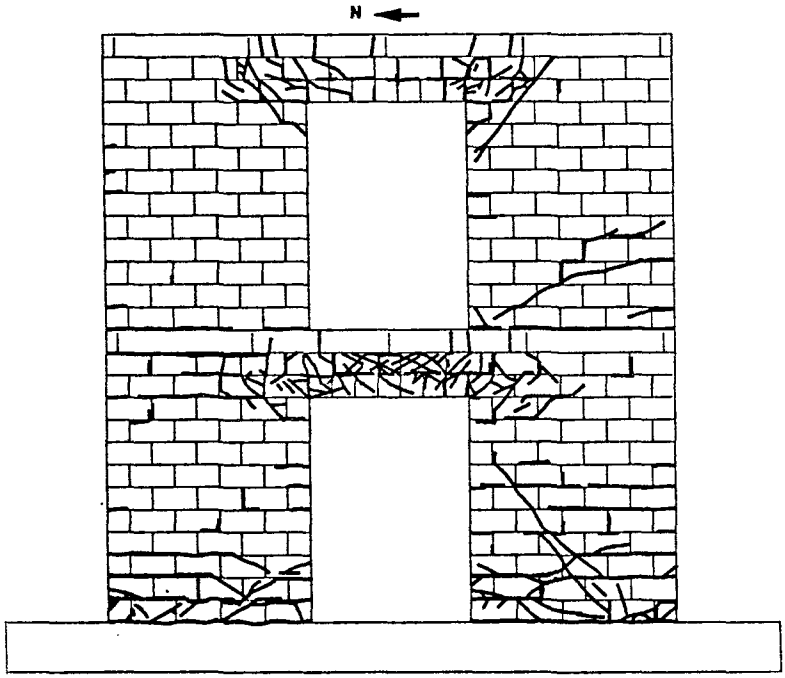

Figure 9.31: Specimen 2d: Cracking progression at overall drift ratio 0.97%.

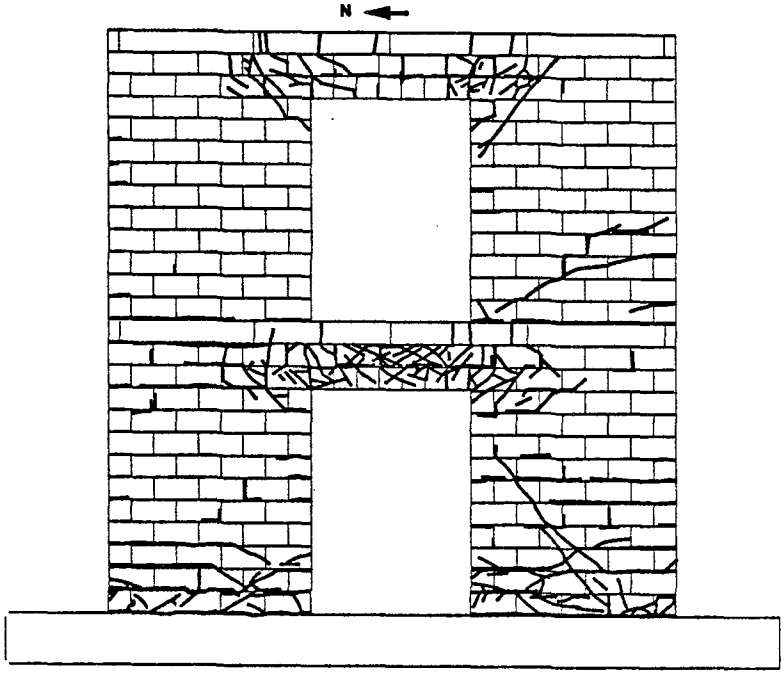

Figure 9.32: Specimen 2d: Cracking progression at end of the test, overall drift ratio 1.48%.

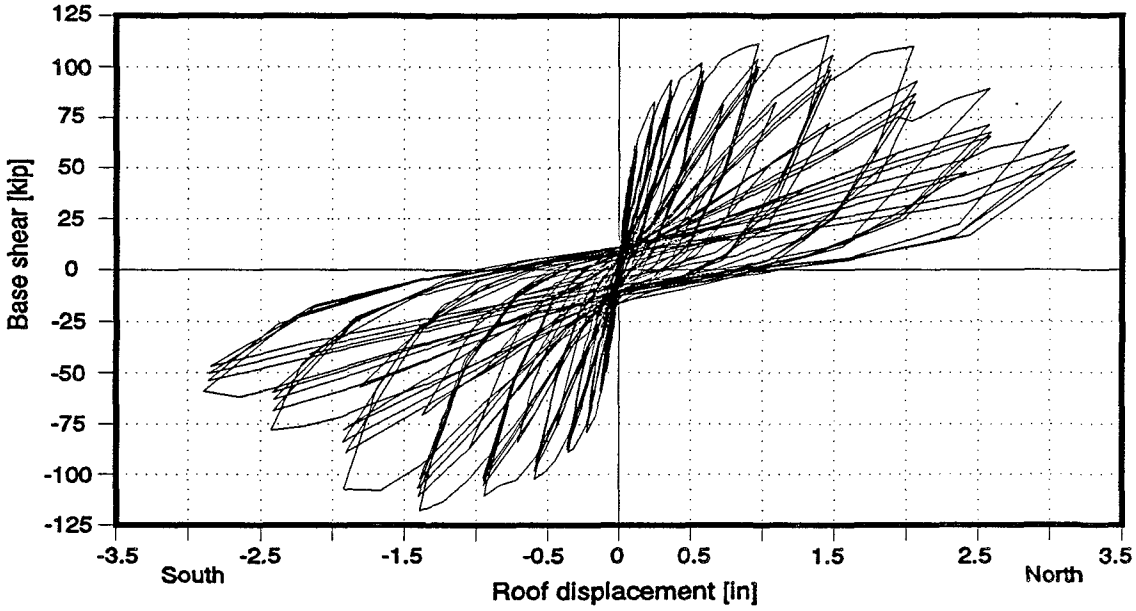

Figure 9.33: Specimen 2d: Base shear - Roof displacement history

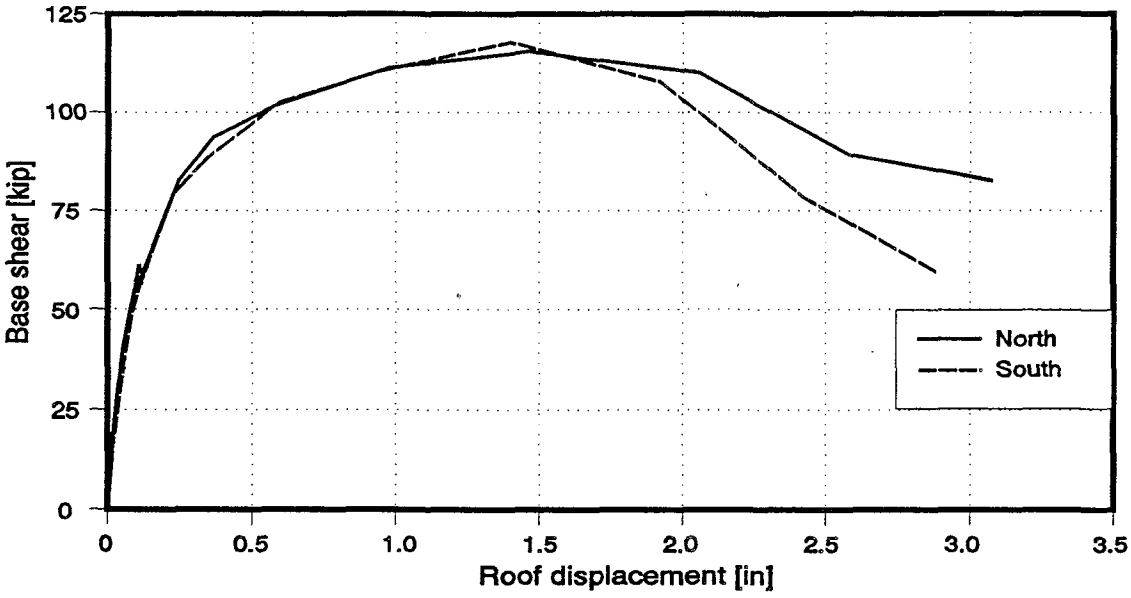

Figure 9.34: Specimen 2d: First peak envelopes and predicted response

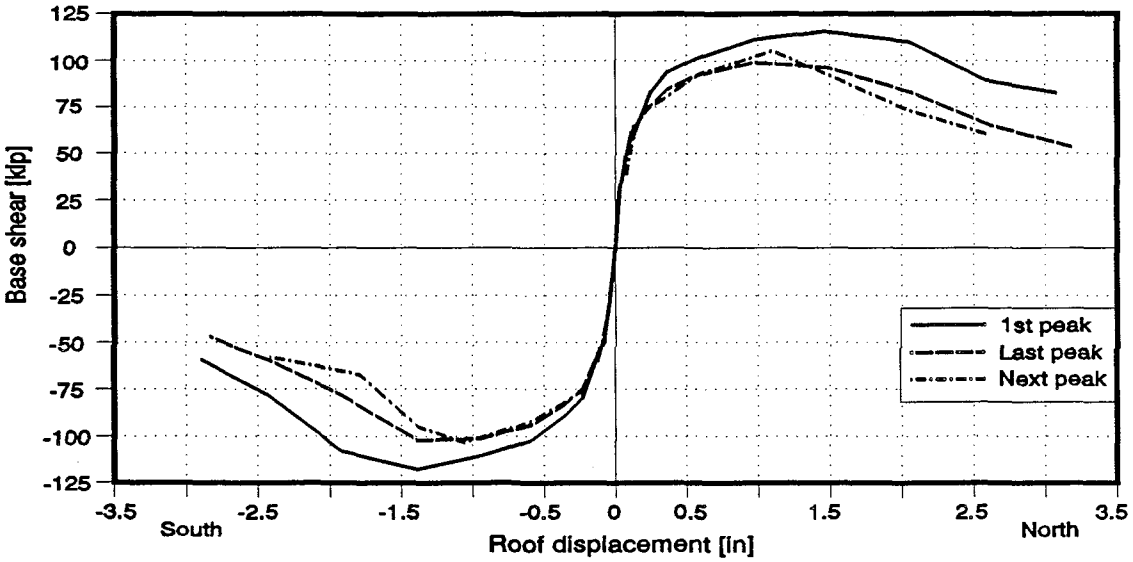

Figure 9.35: Specimen 2d: First, last, and next peak envelopes of the load displacement response.

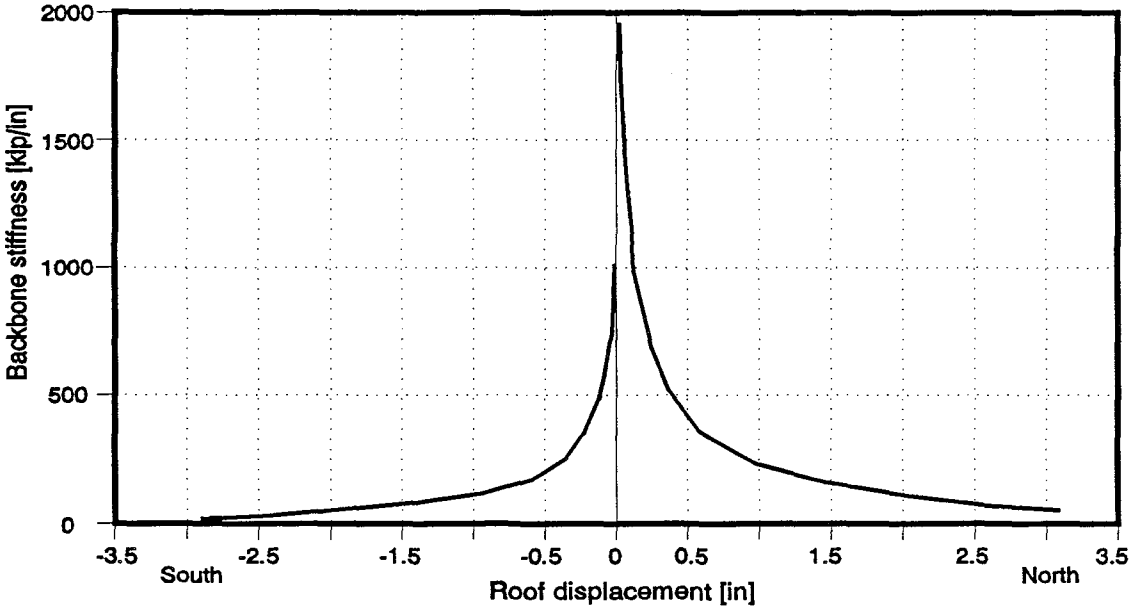

Figure 9.36: Specimen 2c: First peak backbone stiffness

Extensive crushing of masonry occurred at the compression toes of both walls. After spalling of the masonry shell cover at the toes, extreme longitudinal reinforcement of the walls showed buckling in the clear span defined between the bottom transverse bar and the base beam. As the specimen was being subjected to larger displacements, crushing of masonry was progressing inside the base sections. During the last cycles, all extreme longitudinal bars of the walls fractured.

The high degree of deterioration of the bases of the walls is evident from the flattening and degradation observed in the hysteresis loops during the final loading cycles. At that stage, most of the shear transfer resistance between the walls and the foundation beam was provided by shear friction due to the vertical loads applied on top of the walls.

Shearing cracks formed in all the walls, especially near the bases of both first-story walls, but did not widen. Transverse reinforcement did not yield. As with Specimen 2c, shear keys proved to be effective in preventing early significant slipping.

The coupling system showed a progressive deterioration under the action of cyclic loads. Flexural cracks developed at the bottom face of the lintels and at the slab topping. Extensive shear cracking in the span, and crushing of the masonry in the end sections, occurred in the 2nd floor lintel. Extensive damage, characterized by diagonal cracks in the walls, occurred in the lintel-wall connections in the roof lintel.

The cracking and damage pattern of the lintels and of the lintel-wall connections suggested that each lintel responded in a different way. Diagonal cracks in the web and crushing of masonry at the end sections of the 2nd floor lintel indicated that high moments and shears developed in that element. The extensive damage of the walls in the lintel-wall connections at the roof level limited the moment and shear transfer between those elements. Wide cracks, extending completely along the width and depth of the slab and lintel, indicated that the behavior of the roof lintel was dominated by axial forces.

There was no evidence of deterioration of the joint between the walls and the planks, nor of the horizontal joint between walls and slabs.

9.6 Discussion of Tests Results for Coupled Wall Specimens

9.6.1 Overall Response. As expected, each Type 2 specimen developed its lateral load capacity in a predominantly flexural mode: after plastic hinges developed at the coupling elements, flexural failure occurred at the bases of the walls. Displacement capacity was limited by crushing of masonry at the compression toes, tensile fracture of the walls' longitudinal reinforcement, and sliding movements of the walls' bases, both in- and out-of-plane.

As shown in Figs. 9.6, 9.15, 9.24, and 9.33, the hysteresis loops remained very stable throughout the tests up to overall drift ratio levels of the order of 1%. Most strength degradation occurred after the first cycle of each series. Due to the loss of the compression toes, to fracture of reinforcement, and to base sliding, important degradation of strength and stiffness occurred during the later cycles of each test. Pinching was observed in the hysteresis loops corresponding to high levels of lateral displacement. This pinching was primarily due to sliding of the coupled walls on the base of the first story. Plots of earlier load series, before substantial base sliding, exhibit little pinching.

As observed during the tests, shear was not a critical factor in the response of the specimens. Transverse steel did not come close to yielding during testing, and visual observations during the tests also showed that diagonal shear cracks formed but did not increase in width. Calculations of the contributing deformations for each wall showed that flexural deformations dominate the total lateral displacements of the walls [13].

Because all Type 2 specimens had identical wall reinforcement, their response was differentiated by the characteristics of their floor systems. Results of the tests have been summarized in Table 9.9, and are shown in Figs. 9.37 to 9.39. As seen from those results, the specimens subjected to vertical loads simulating floor gravity loads on the top of the walls, (Specimens 2a and 2d), were able to sustain deformations in excess of the ultimate deformation (corresponding to the lateral load capacity). The externally applied vertical load tends to balance the overturning axial tensile forces in the walls, and enhances the shear transfer capacity between the bases of the walls and the foundation beam.

Specimens 2c and 2d, with lintels spanning between the walls, showed the largest lateral load capacities. Specimen 2b, which suffered important degradation of the coupling system due to deterioration of the slab-wall connection, showed the smallest lateral load capacity and was the most flexible.

Large tensile axial forces transmitted to the walls through the lintels can overcome gravity loads in the tension wall, producing net tensile axial force. This is especially important in cases like Specimen 2c, which represented a non-bearing wall with little externally applied gravity load. The presence of this net tensile force can explain the extensive cracking of the bed joints, especially at the first-story walls, and the long crack at the top course of the first-story South wall just below the slab in the case of specimen 2d.

9.6.2 Floor Systems. The design and construction details of the floor system of Specimen 2a proved to be adequate to maintain the required strength and integrity. No evidence of deterioration of the bond between the different elements forming the floor system was observed during the tests.

Table 9.9: Type 2 specimen tests: Summary of results

Event	Specimen							
	2a		2b		2c		2d	
	Drift %	Base Shear [kips]	Drift %	Base Shear [kips]	Drift %	Base Shear [kips]	Drift %	Base Shear [kips]
Yielding of wall longitudinal reinforcement	0.054	48.3	0.055	34.9	0.036	40.2	0.054	60.8
Wall diagonal cracking	0.20	73.2	0.27	65.5	0.22	94.6	0.12	82.4
Lateral load capacity	0.83	95.9	1.70	88.1	0.98	122.1	0.72	115.5
Maximum displacement	1.09	80.5	1.70	88.1	0.98	92.4	1.56	53.7
Initial stiffness [kip/in]	1525		777		1973		1823	

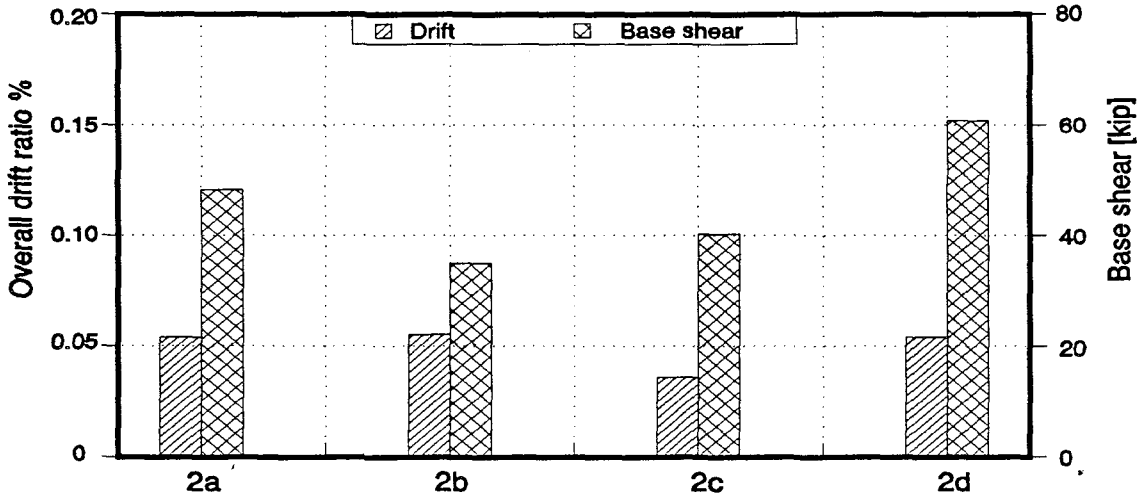

Figure 9.37: Type 2 specimens: Yielding of the longitudinal reinforcement of the walls.

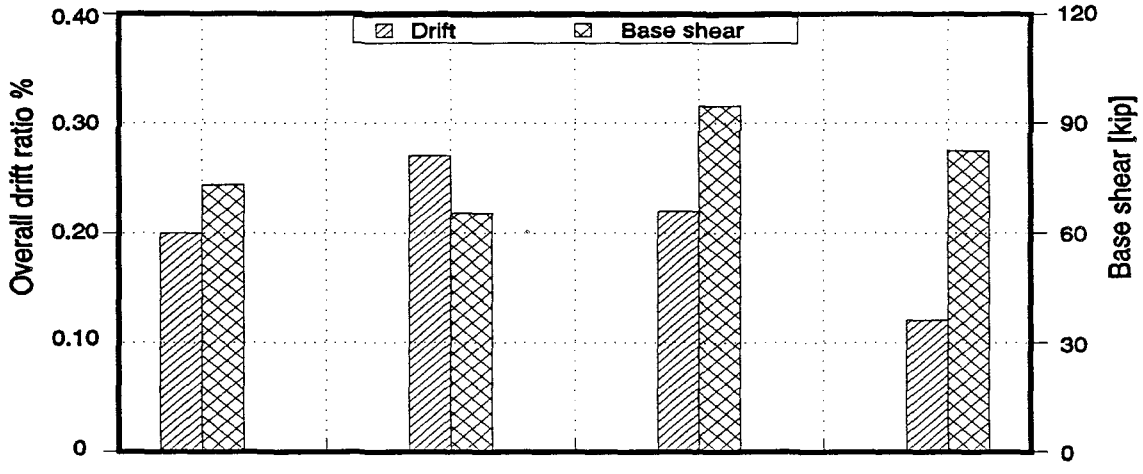

Figure 9.38: Type 2 specimens: Diagonal cracking of the walls.

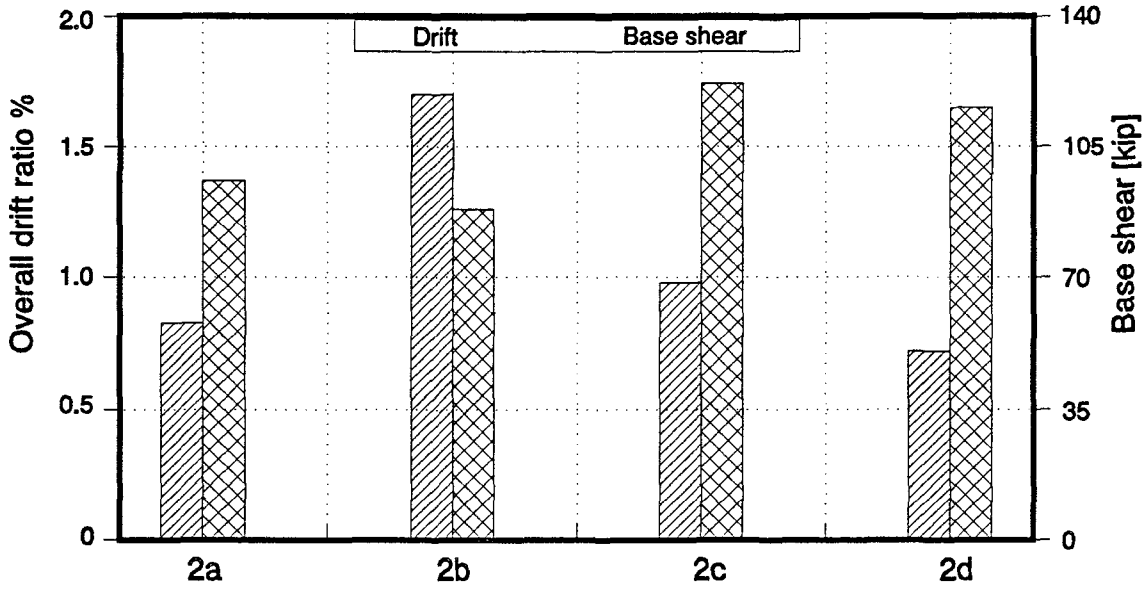

Figure 9.39: Type 2 specimens: Lateral load capacity.

As previously described, the floor system of specimen 2b suffered extensive deterioration of the slab-wall connections. As a result, it was decided to increase the welded wire reinforcement in the topping of Specimens 2c and 2d in the wall areas, as described in Section 3.3.3. This additional reinforcement provided adequate punching shear resistance to the slabs, and no deterioration of the wall-slab connection was observed during the tests for Specimens 2c and 2d.

9.6.3 Coupling Systems. As previously discussed, the coupling slab of Specimen 2a remained monolithic and showed no signs of deterioration. Yielding lines developed across the full width of the slabs, defining plastic hinges at both ends of the coupling elements.

Due to the damage of the slab-wall connections, the coupling system of Specimen 2b showed the lowest effectiveness of all Type 2 specimens. The planks remained essentially elastic throughout the test, and the shear transfer between the walls was reduced.

The lintels of Specimens 2c and 2d showed a common behavior: the degradation of the lintel-wall connection did not permit the lintels to develop their full flexural capacity. In some cases, like the roof lintel of Specimen 2d, the behavior of the coupling system was completely dominated by the action of the tensile axial forces transmitted between the walls.

9.6.4 Predicted Behavior. Figures 9.7, 9.16, and 9.25 compare the predicted monotonic response of each specimen with the envelopes of the base shear-roof

displacement history at first peaks. As discussed in Section 5.4, no prediction for Specimen 2d was available at the time of the test.

As observed for all the specimens, base shear for the south envelope is always less than for the north envelope at the same roof displacement. For each load cycle, specimens were first loaded towards the north, and the resulting loss in stiffness of the walls when loading to the north causes a reduced strength for the same displacement towards the south. Therefore, comparisons between the predicted and observed envelopes will be based on the observed envelope for northward loading. Results of the tests and predictions have been summarized in Table 9.10. In the same table, the ratios between the predicted values and the test results are indicated in parenthesis.

Table 9.10: Type 2 specimen tests: Predicted and observed results for ultimate capacity

Specimen	Test results		Sequential collapse analysis		Collapse mechanism analysis
	Base shear [kip]	Roof displacement [in]	Base shear [kip]	Roof displacement [in]	Base shear [kip]
2a	95.9	1.69	98.0 (1.02)	1.59 (0.94)	101 (1.05)
2b	88.1	3.46	91.0 (1.03)	4.26 (1.23)	102 (1.16)
2c	122.1	1.99	129.2 (1.06)	0.95 (0.48)	141 (1.15)
2d	111.4	0.98	—	—	112 (1.01)

The predicted envelopes are based on monotonic loading, while both specimens were tested cyclically. As shown in the figures, the north envelope model the predicted envelope fairly well. The difference between the predicted envelope and the north envelope can be accounted for by the fact that predicted analysis did not include slip at the base of the first-story walls (which actually occurred during the tests).

As expected from upper bound methods, the predicted values are consistently larger than the test results.

10. ANALYTICAL RESULTS

In Chapter 5, dealing with the design of perforated wall specimens, it was made clear how difficult it can be to determine the critical collapse mechanism for a complex perforated wall. To automate that process, it was decided to develop a computer program which would apply a fixed pattern of loads to a structure, stepping that structure through monotonically increasing displacements until a collapse mechanism would form.

This was the motivation for the development of the program SCAM (Sequential Collapse Analysis of Masonry). In this chapter, the basic operation of the program is described. This is supplemented by material in Appendix B. Also, the program is checked by using it as an analysis tool to calculate the load-deflection behavior of one perforated wall and one coupled wall specimen.

As another part of the analysis, a model was developed for computing the ultimate shear strength of reinforced concrete masonry walls. In this chapter, that model is also discussed.

10.1 Computer Program SCAM (Sequential Collapse Analysis of Masonry Walls)

SCAM is a computer program developed to analyze the nonlinear response of a masonry wall structure subjected to monotonically increasing displacements. The program idealizes the wall as an assemblage of line elements connected by rigid joints. The program performs an inelastic step-by-step analysis using the tangent stiffness properties of the structure. Tangent stiffnesses are calculated during each step using the force-deformation curves of the elements. The solution algorithm is based on a displacement-controlled scheme, making the solution process stable even when tangent stiffnesses are zero or negative. Output information includes the force-displacement curve for the specified degree of freedom used to control the process, force-deformation curves for the end sections of each element, and the values of the force and displacement vectors at each step of the process. The computer program SCAM and its solution algorithms are completely described in Appendix B of this work.

The prescribed displacement history of an arbitrarily specified degree of freedom is used to control the process. The incremental displacement of this specified degree of freedom, defined as part of the prescribed displacement history, must be small enough to permit the convergence of the solution algorithm.

Any arbitrary distribution of nodal forces that includes the force corresponding to the specified degree of freedom can be used. However, the pattern of the distribution cannot be modified during the process; that is, the ratio between each force and the force on the specified degree of freedom must remain constant.

The solution algorithm can be summarized in the following steps:

1) Given the tangent stiffness matrix calculated at the end of the previous step, find an incremental displacement vector such that:

   a) The vector component corresponding to the specified degree of freedom is equal to the prescribed value, and

   b) The associated incremental force vector contains non-zero components only in some specified degrees of freedom.

   For a given starting value of the incremental displacement vector, the problem is solved by successive iterations.

2) Element deformations are calculated using the cumulative nodal displacements.

3) Using the element deformations and the force-deformation relationships, internal forces and tangent stiffness properties are calculated for each element.

4) The structure tangent stiffness matrix is calculated using the tangent stiffness properties of each element.

5) The nodal force vector is calculated using the internal forces for each element. This vector contains unbalanced forces corresponding to degrees of freedom other than the specified ones. The unbalanced forces are carried on to the next iteration and are eliminated in step (1.b).

Element force-deformation behavior, described further in Appendix B, involved the non-linear relationships between axial forces and axial deformations, and between moments and curvatures. The latter relationship was evaluated assuming a maximum masonry compressive strain of 0.003. Masonry strength was arbitrarily decreased to zero for strains exceeding that value.

The program was written in Microsoft Fortran version 5.0, and was run in an IBM-compatible 386/25 MHz with an 80387 math co-processor.

10.2 Analysis of Specimen 1a using Computer Program SCAM

10.2.1 General. Specimen 1a was analyzed assuming that its behavior would be governed by a flexural mechanism. This assumption implies that the elements and connections have been provided with sufficient reinforcement, and that the reinforcement

has been detailed adequately, so that the elements will develop the required strength and deformation capacity, and shear and shear transfer failures will be avoided.

Constant vertical loads, as defined in Section 5.4.2, included 3.55 kips on the top of the column at each floor level, 47.9 kips on the top of the center pier at the roof level, 7.1 kips on the top of the center pier at the 2nd floor level, 44.35 kips on the top of the extreme pier at the roof level, and 3.55 kips on the top of the extreme pier at the 2nd floor level. The lateral movement of the roof at the top of the center pier was used as the specified degree of freedom. Constant increments of 0.01 in. were used to define the displacement history of this specified degree of freedom. The specimen was analyzed for a distribution of equal lateral loads applied at the top of each pier at both floor levels.

10.2.2 Model of the Structure. As shown in Fig. 10.1, Specimen 1a was modeled using line elements passing through the centroids of the actual element sections. Elements with rigid end portions were used to model the connections. The model was assumed rigidly connected to the floor through the foundation beam. A larger number of elements were used to model the members expected to suffer large inelastic deformations, such as the 1st story piers, the column, and the base of the wall.

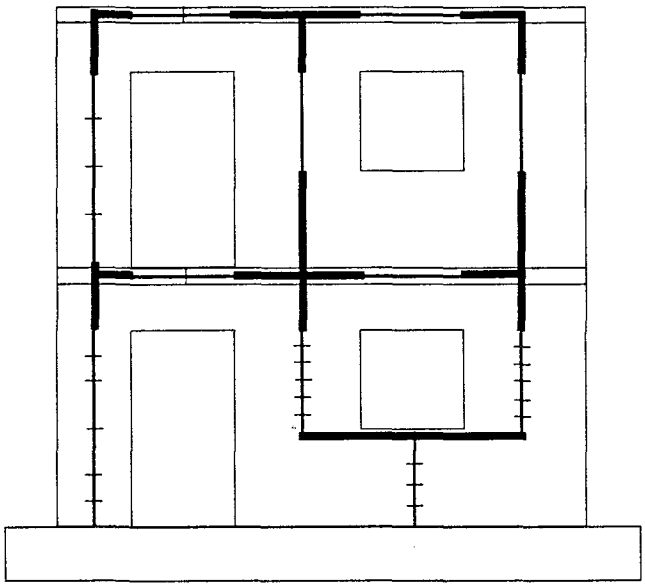

Figure 10.1: Model for Specimen 1a

10.2.3 Materials and Force-Deformation Relationships. Measured strengths of the materials used to built the specimen, as described in Chapter 3, were used in the analysis. The properties of the Grade 60 reinforcing steel used in these calculation are described in

Table 3.7. A masonry compressive strength = 2800 psi was used, and concrete compressive strength was f'_c = 4600 psi. A modulus of elasticity for the masonry E_m = 750 f_m' was used. A modulus of elasticity for the concrete E_c = 57,000 $\sqrt{f_c'}$ was used. Moduli of rupture for masonry and concrete equal to 4 $\sqrt{f_m'}$ and 4 $\sqrt{f_c'}$ respectively were used. The stress-strain behavior of the masonry and concrete was modeled using the curve given by Kent and Park for unconfined concrete [33].

Moment-curvature relationships for the cracked sections were calculated using the RCCOLA computer program [39]. The sections were assumed initially uncracked. Cracking moments and curvatures were calculated with the initial elastic properties for the gross section and the modulus of rupture of the material. A smooth transition was used between the cracking point and the curve obtained with RCCOLA. Fig. 10.2 shows a typical moment-curvature curve for the piers of Specimen 1a, for a given level of axial load. The moment-curvature curves were terminated at a masonry compressive strain of 0.003.

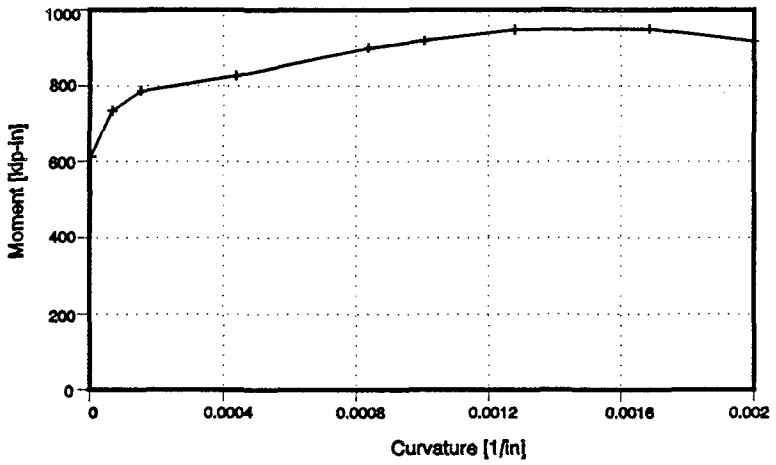

Figure 10.2: Typical moment-curvature relationship for the piers of Specimen 1a

The axial force-axial strain relationship shown in Fig. 10.3 was used to model the behavior of reinforced concrete and masonry elements under axial loads. Under compressive forces, the behavior is approximately linear up to stress of about 70% of f'_c or f'_m. Since it is not usual to find such high stresses in real elements under pure axial loads, it seems reasonable to use that point as (N_1,ϵ_1). Under tensile forces, it can be assumed the behavior is governed fully by the reinforcement. Thus, ϵ_2 corresponds to ϵ_y, ϵ_3 to ϵ_{sh}, and ϵ_4 to ϵ_u, and the N values are those associated with the yielding and ultimate capacity of the reinforcement respectively.

Fig. 10.4 shows a typical axial force-axial strain curve for the column of Specimen 1a, obtained as previously described.

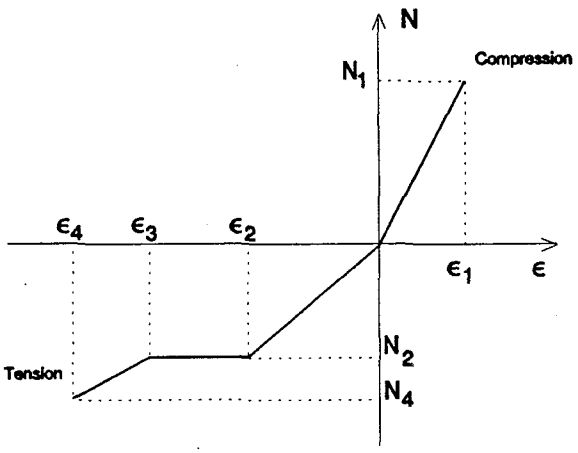

Figure 10.3: Axial force-axial deformation curve used in SCAM analysis

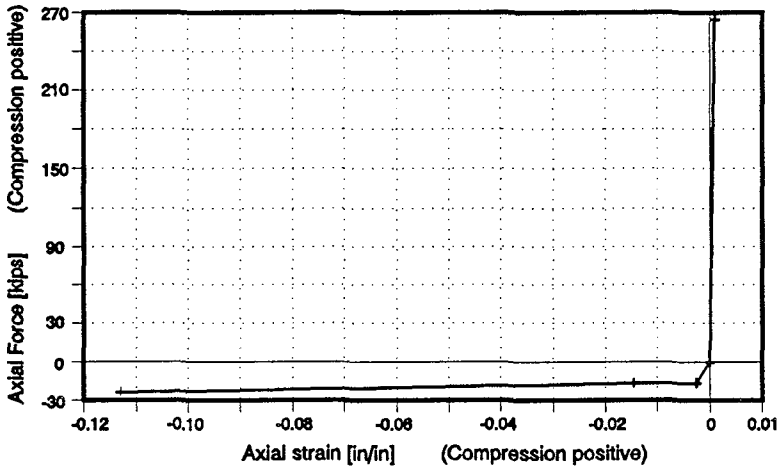

Figure 10.4: Typical axial force-axial strain relationship for the column of Specimen 1a

The effects of inelastic response on the shear force-shear deformation relationship were included by using an equivalent effective shear area A_v in the usual elastic expression for the shear force-shear deformation relationship. This effective area was assumed to be proportional to the neutral axis depth c of the section:

$$\Delta_v = \frac{V L}{G A_v} \tag{10.1}$$

$$A_v = c\ t_w \tag{10.2}$$

Where:

Δ_v	:	Relative shear deflection between the ends of an element of length L (Appendix B)
V	:	Shear force acting on the element
A_v	:	Effective shear area
G	:	Shear modulus of the material
t_w	:	Web thickness
c	:	Neutral axis depth

The neutral axis depth c is obtained from the RCCOLA analysis of the sections.

10.2.4 Results of the Analysis for Northward Load. The predicted history of base shear versus roof displacement for Specimen 1a when loaded to the North, obtained using SCAM, is shown in Fig. 10.5. Fig. 10.6 shows the comparison between the predicted response and experimental results for the envelope of the 1st peaks of the response for Specimen 1a. Run time for this case, in the 386/25 machine, was about 30 minutes.

As shown in Fig. 10.5, the predicted lateral load capacity was 102.7 kips at a roof displacement of 0.36 in. As shown in Fig. 10.6, this predicted maximum strength agreed well with the experimental value of 98.2 kips. However, the corresponding predicted displacement, 0.36 in., was far from the measured value of 0.80 in. In addition, the predicted load-displacement response ends at a maximum displacement of about 0.4 in., far less than the experimentally observed value. Reasons for these discrepancies are discussed in Section 10.4.

To examine the predicted response of the critical elements of the specimen, their internal force histories have been plotted in Figs. 10.7 through 10.10 in terms of the moment-axial load in the element ends. Portions of the ultimate capacity and yielding strength (point of first yielding of the longitudinal reinforcement) interaction diagrams calculated for those sections have been included in the same plots. Compressive axial force is positive in those plots.

Fig. 10.7 shows the moment-axial load history for the section at the base of the wall. The sections started with a small moment and axial load of 98.0 kips due to the initially applied vertical loads. As the loading process progressed, the axial load decreased due to overturning. The moment at the section increased until eventually reaching the yielding capacity. However, this section did not reach its flexural capacity at the time the specimen developed its lateral strength.

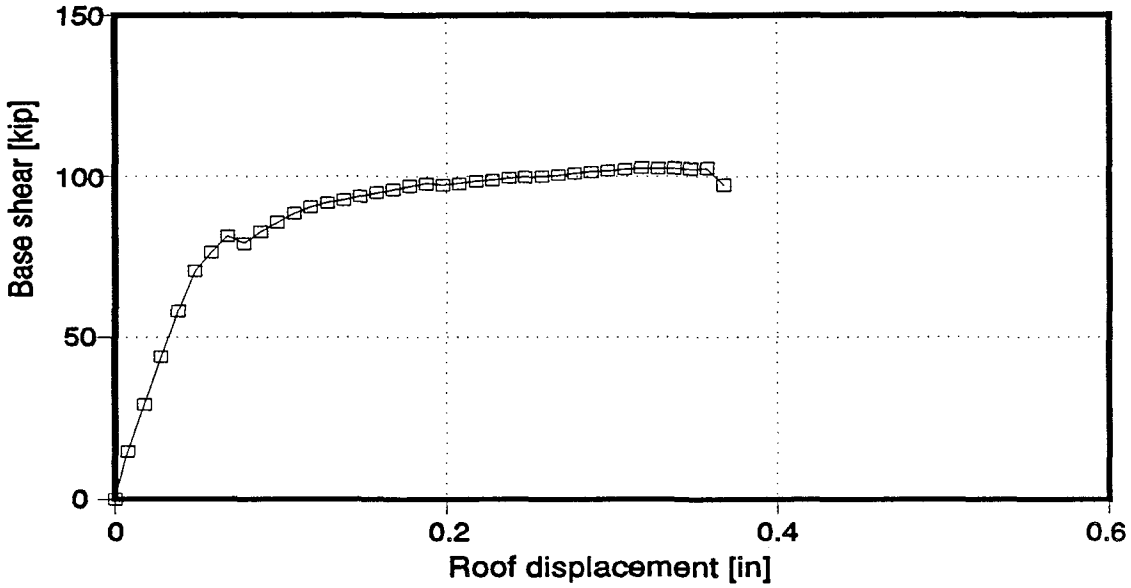

Figure 10.5: Specimen 1a: Predicted base shear-roof displacement history for northward loading, obtained using SCAM

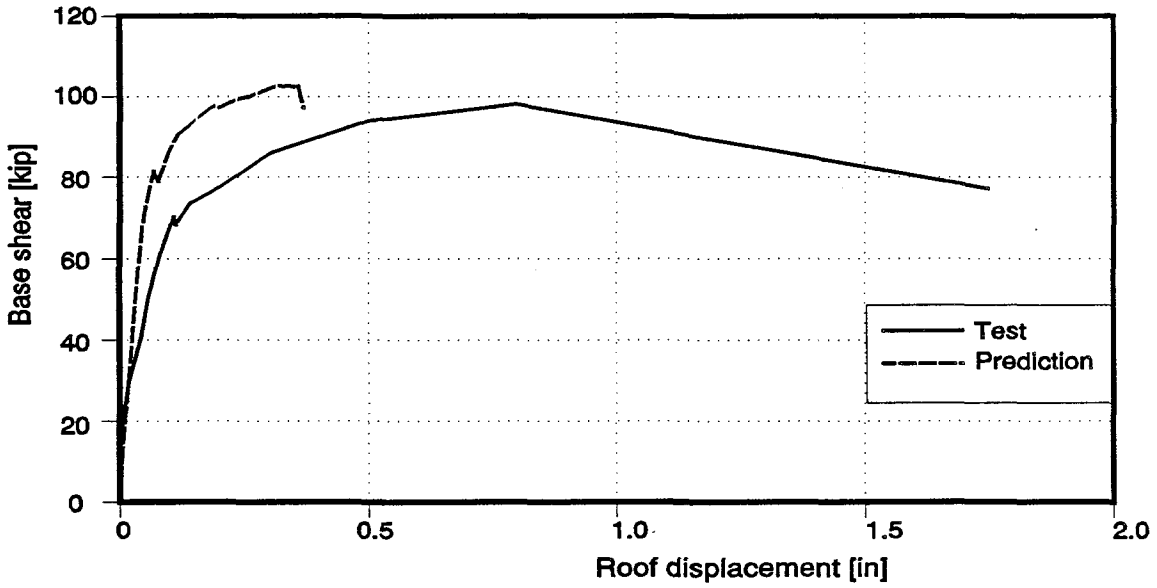

Figure 10.6: Specimen 1a: Comparison between the predicted response and experimental results for the envelope of the 1st peaks of the response, northward loading

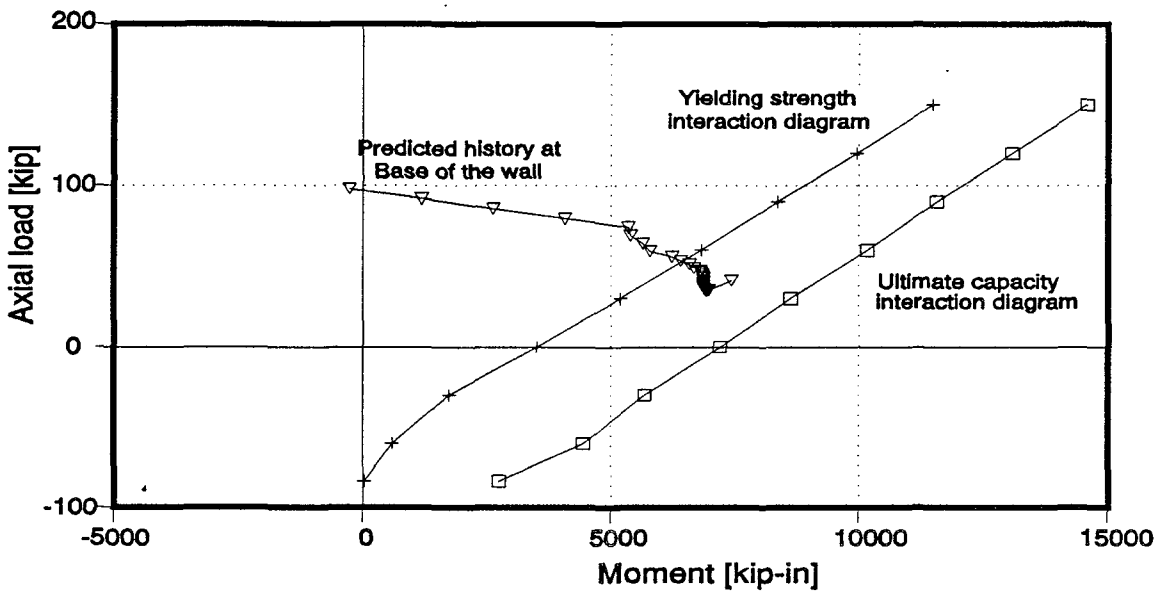

Figure 10.7: Specimen 1a: Predicted moment-axial force history for the section at the base of the wall, northward loading

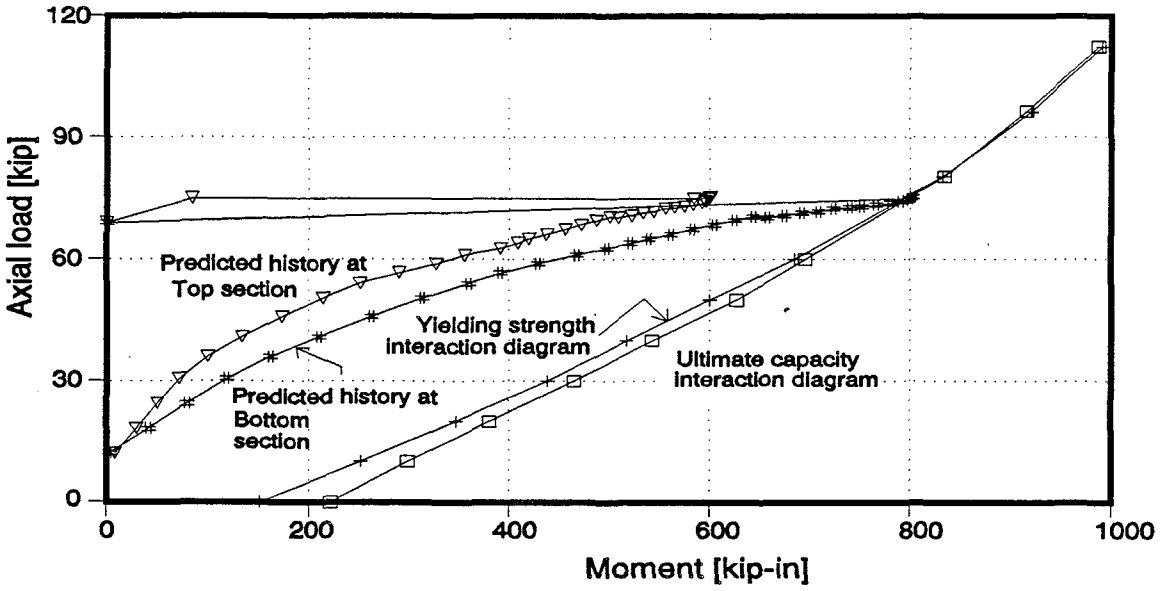

Figure 10.8: Specimen 1a: Predicted moment-axial force history for the sections at the end of the 1st story column, northward loading

Fig. 10.8 shows the moment-axial load history for the ends of the 1st story column. Both sections started with a small moment and with an axial load of 12 kips due to the initially applied vertical loads. As the loading process progressed, axial load increased due to overturning. The moment at both ends also increased, until the moment at the bottom section eventually reached the ultimate capacity.

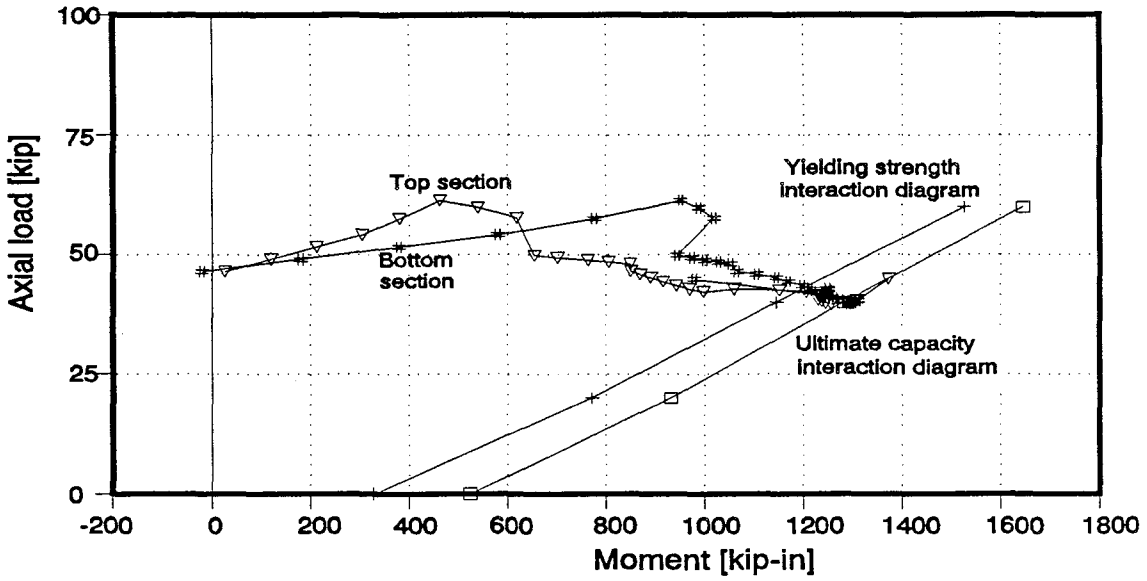

Figure 10.9: Specimen 1a: Predicted moment-axial force history for the end sections of the 1st story center pier, northward loading

Figs. 10.9 and 10.10 show the moment-axial load history for the ends of the 1st story center and extreme pier respectively. Both piers started at about the same level of axial load due to the vertically applied loads. As the loading process progressed, axial load decreased in the extreme pier and remained more or less constant in the center one. The moments at both ends in both piers increased, until they eventually reached their flexural capacities.

In summary, the SCAM analysis indicated that the northward lateral load capacity of Specimen 1a would be governed by a mechanism in which both piers develop their flexural capacities, and the column develops its flexural capacity at its bottom section. These results are in very good agreement with the expected mechanism for Specimen 1a as described in Section 4.4.2, and with the experimental results, as described in Section 7.1.1 and shown in Fig. 7.1.

10.2.5 Results of the Analysis for Southward Load. The predicted base shear-roof displacement history of Specimen 1a when loaded to the South, obtained using SCAM, is shown in Fig. 10.11. Fig. 10.12 shows the comparison between the predicted response and

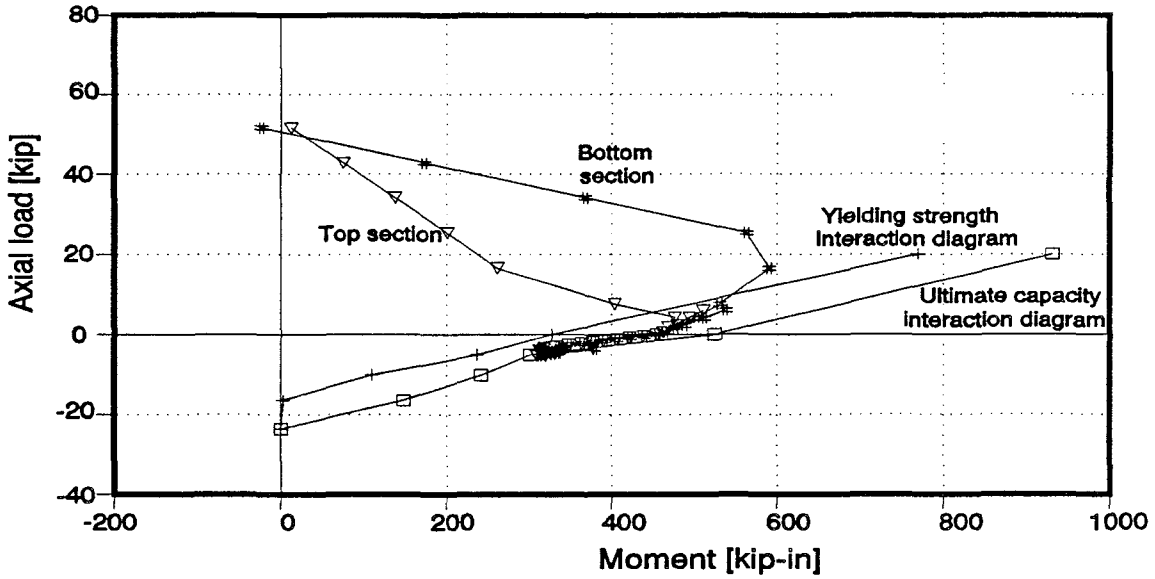

Figure 10.10: Specimen 1a: Predicted moment-axial force history for the end sections of the 1st story extreme pier, northward loading

experimental results for the envelope of the 1st peaks of the response for Specimen 1a. Run time, in the same 386/25 machine, was again about 30 minutes.

As shown in Fig. 10.11, the predicted lateral load capacity was 109.5 kips at a roof displacement of 0.66 in. As shown in Fig. 10.12, these results agreed fairly well with the experimental results of 104.5 kips and 0.79 in. respectively. However, as the previous case, the predicted load-displacement response ends at a maximum displacement of about 0.7 in., far less than the experimentally observed value. Reasons for these discrepancies are discussed in Section 10.4.

Fig. 10.13 shows the moment-axial load history for the section at the base of the wall. The sections started with a small moment and axial load of 98.0 kips due to the initially applied vertical loads. As the loading process progressed, the axial load increased very slowly. The moment at the section increased, until eventually reaching the yielding capacity, and later, the ultimate capacity at the time the specimen developed its lateral strength.

Fig. 10.14 shows the moment-axial load history for the ends of the 1st story column. Both sections started with a small moment and axial load of 12 kips due to the initially applied vertical loads. As the loading process progressed, axial load rapidly decreased due to overturning. Eventually, at the time the specimen reached its lateral load capacity, both end sections developed their tensile yielding capacity with a practically non-existent flexural capacity.

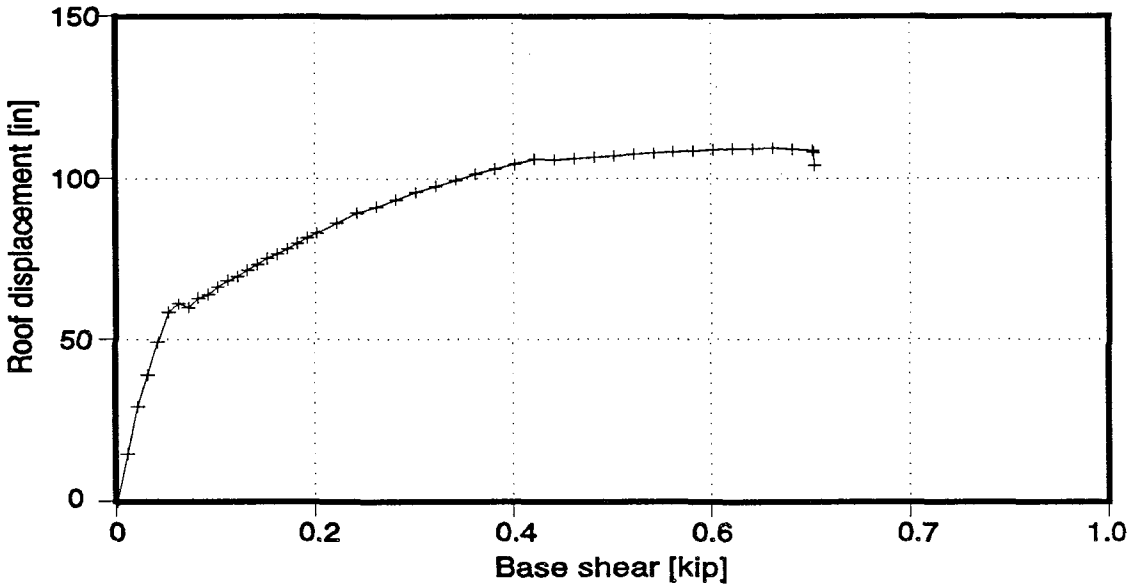

Figure 10.11: Specimen 1a: Predicted base shear-roof displacement history for southward loading, obtained using SCAM

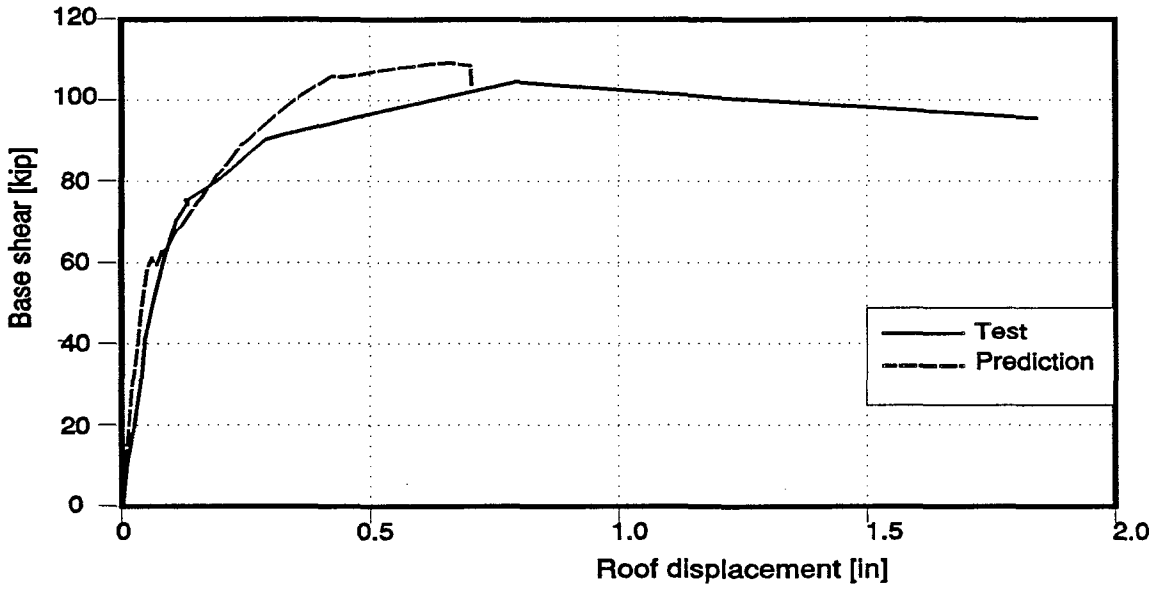

Figure 10.12: Specimen 1a: Comparison between the predicted response and experimental results for the envelope of the 1st peaks of the response, southward loading

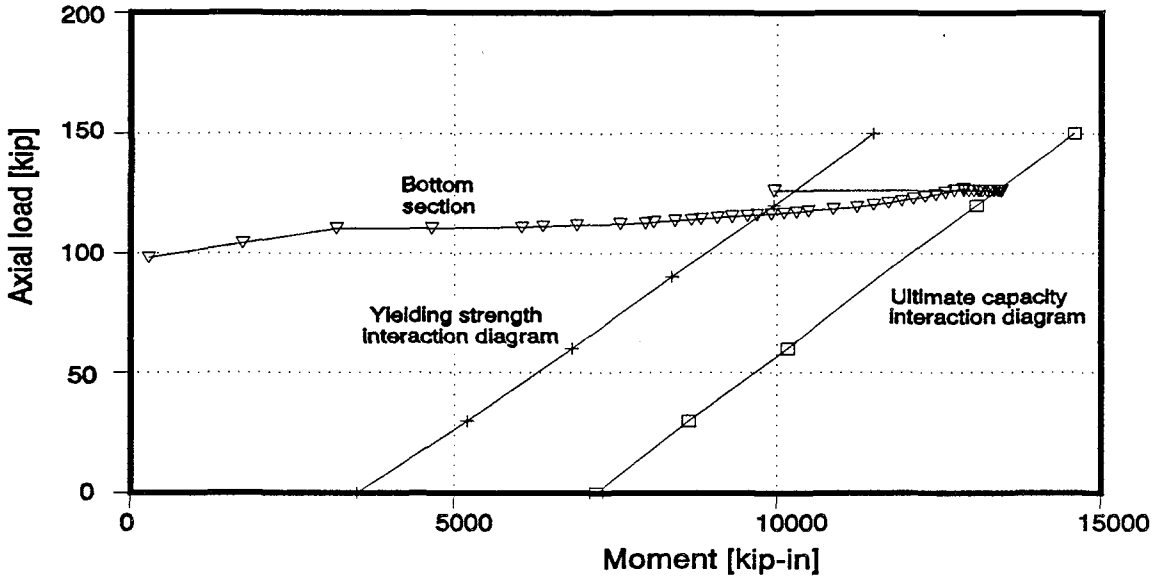

Figure 10.13: Specimen 1a: Predicted moment-axial force history for the section at the base of the wall, southward loading

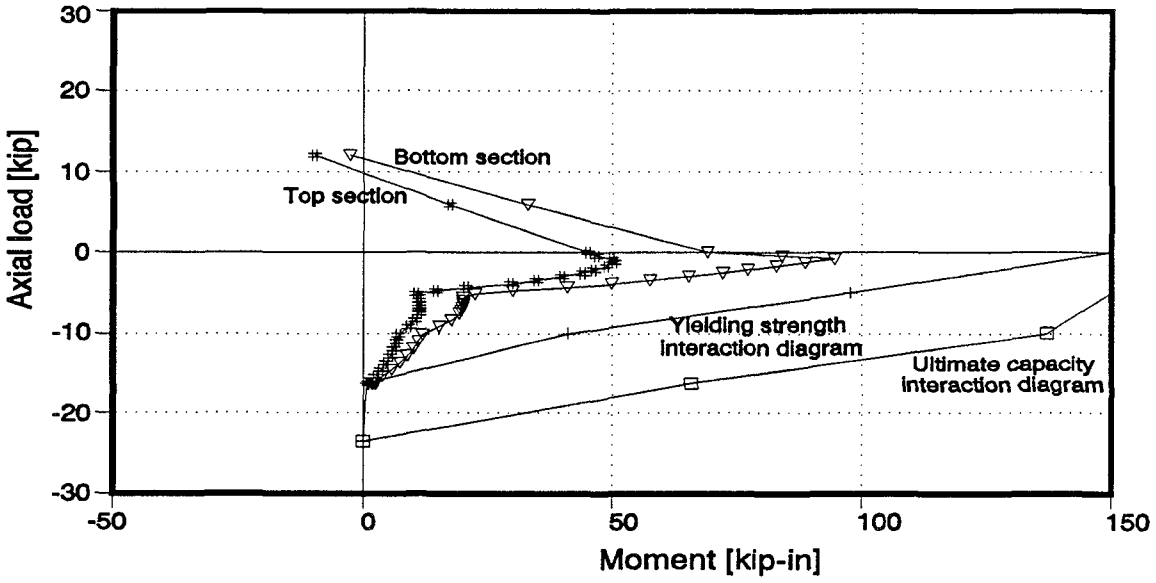

Figure 10.14: Specimen 1a: Predicted moment-axial force history for the end sections of the 1st story column, southward loading

Figs. 10.15 and 10.16 show the moment-axial load history for the ends of the 1st story center and extreme pier respectively. Both piers started at about the same level of axial load due to the vertically applied loads. As the loading process progressed, axial load decreased in the extreme pier, and both ends eventually reached their flexural capacity. Axial load and moments increased in the extreme pier, until the bottom end reached its flexural capacity, at the time the specimen developed its lateral strength. As shown in Fig. 10.16, the moment at the top end of the extreme pier was far from the ultimate capacity of that section at the time the specimen reached its lateral strength.

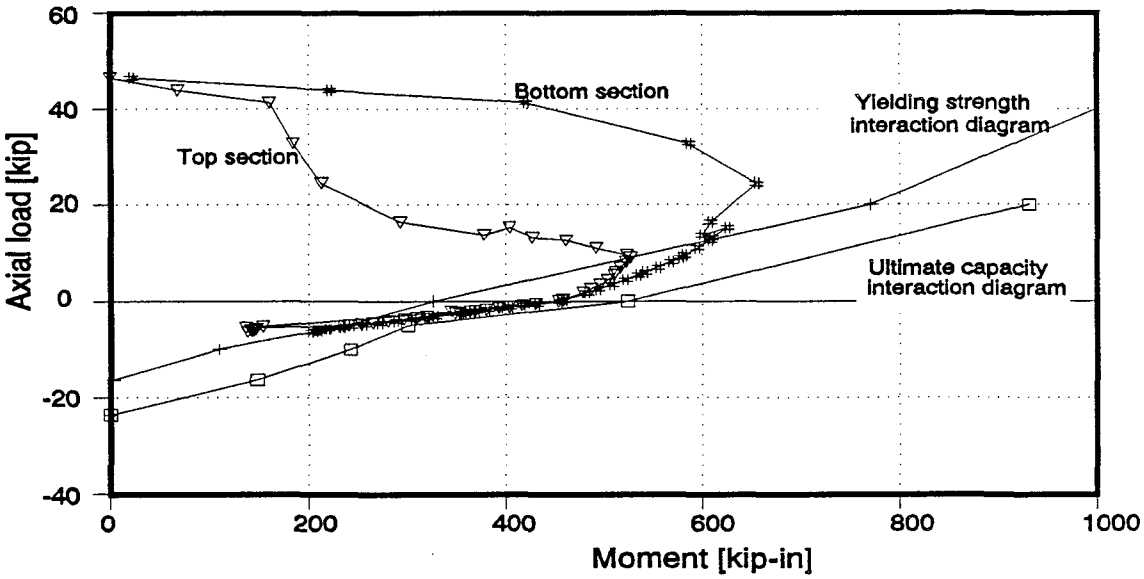

Figure 10.15: Specimen 1a: Predicted moment-axial force history for the end sections of the 1st story center pier, southward loading

In summary, the analysis indicated that the southward lateral load capacity of Specimen 1a would be governed by a mechanism in which the column develops its axial yielding capacity and the base of the wall develops its flexural capacity. The pier mechanism would not develop because the top end of the extreme pier would be far from reaching its flexural capacity. These results are in very good agreement with the experimental results, as described in Section 7.1.1. and as shown in Fig. 7.2.

10.3 Analysis of Specimen 2d Using Computer Program SCAM

10.3.1 General. The same general assumptions stated for the analysis of Specimen 1a were made in this case. Constant vertical loads included 30.5 kips on the top of each wall at the roof level, and 6.5 kips on the top of each wall at the 2nd floor level. The lateral movement of the roof at the top of the center pier was used as the specified degree of

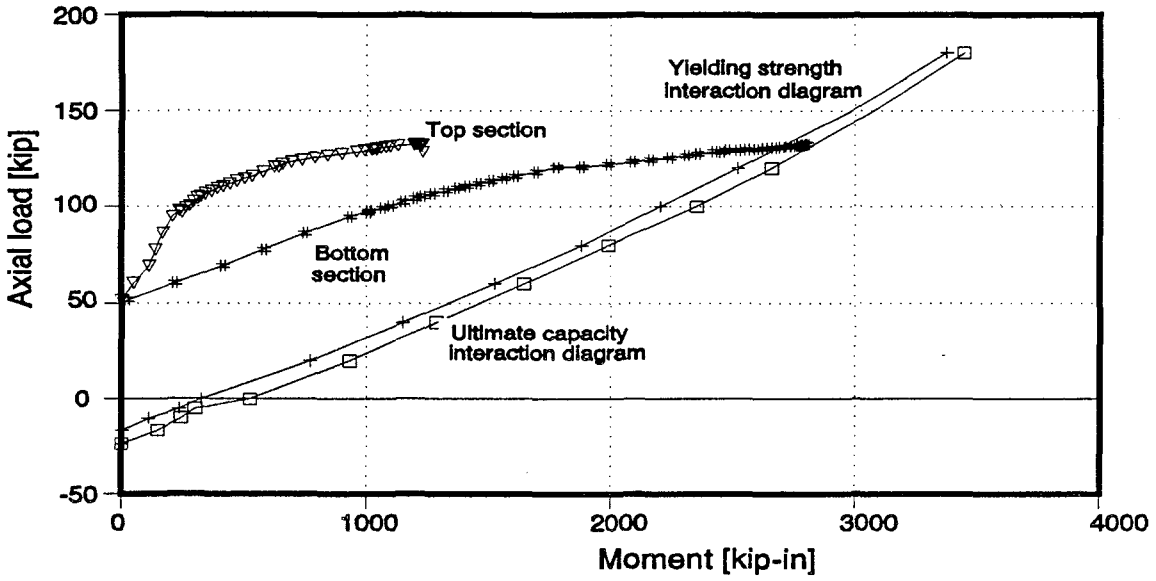

Figure 10.16: Specimen 1a: Predicted moment-axial force history for the end sections of the 1st story extreme pier, southward loading

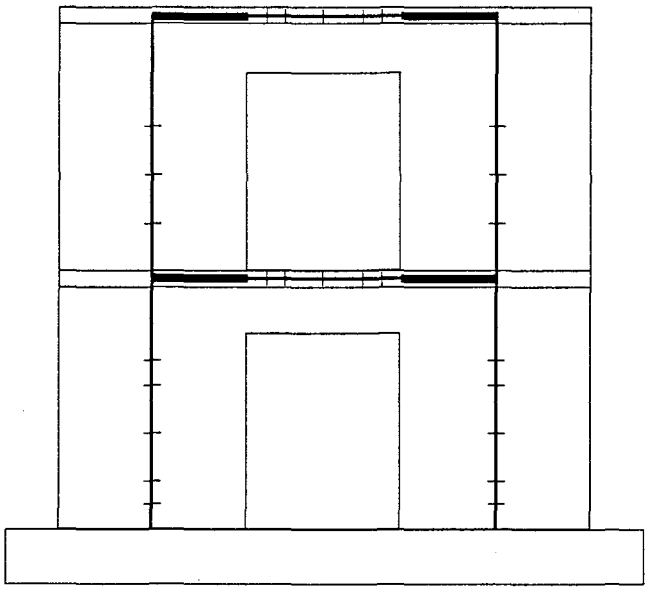

Figure 10.17: Model for Specimen 2d

freedom. A constant increment of 0.01 in. was used to define the displacement history of this specified degree of freedom. The specimen was analyzed for a distribution of equal lateral loads applied at the top of each wall in both floor levels.

10.3.2 Model of the Structure. Fig. 10.17 shows the model used to analyze Specimen 2d. Elements with rigid end portions were used to model the connections. The model was assumed rigidly connected to the floor through the foundation beam. A larger number of elements was used to model the members expected to suffer large inelastic deformations, such as the ends of the 1st story walls and the lintels.

10.3.3 Materials and Force-Deformation Relationships. Measured strengths of the materials used to build the specimen, as described in Chapter 3, were used in the analysis. The properties of the Grade 60 reinforcing steel used in these calculation are described in Table 3.7. A masonry compressive strength f_m' = 3100 psi was used, and concrete compressive strength was f_c' = 5300 psi. A modulus of elasticity for the masonry E_m = 750 f_m' was used. A modulus of elasticity for the concrete E_c = 57,000 $\sqrt{f_c'}$ was used. Moduli of rupture for masonry and concrete equal to 4 $\sqrt{f_m'}$ and 4 $\sqrt{f_c'}$ respectively were used. The stress-strain behavior of the masonry and concrete was modeled using the curve given by Kent and Park for unconfined concrete [33].

10.3.4 Results of the Analysis for Specimen 2d. Because of its symmetry, it was necessary to analyze Specimen 2d in one direction only. The analytical results are compared with the test results for northward loading. The predicted base shear-roof displacement history of Specimen 2d, obtained using SCAM, is shown in Fig. 10.18. Fig. 10.19 shows the comparison between the predicted response and experimental results for the envelope of the 1st peaks of the response for Specimen 1a when loaded to the North. Run time in the 386/25 computer was about 30 minutes.

As shown in Fig. 10.18, the predicted lateral load capacity was 96.9 kips at a roof displacement of 0.59 in. Those predicted values did not agree well with the observed values of 111.4 kips and 0.98 in. respectively. As shown in Fig. 10.19, the predicted response agreed very well with the experimental results at the initial part of the curve, but it ended at a maximum displacement of about 0.75 in., far less than the experimentally observed value. Reasons for these discrepancies are discussed in Section 10.4. As discussed earlier, the sudden drop in predicted capacity is due to the fact that element flexural resistance was assumed to drop abruptly to zero at unconfined masonry compressive strains exceeding 0.003.

Fig. 10.20 shows the moment-axial load history for the section at the base of each wall. Initial moments and axial forces in the walls are due to the vertical loads. As the loading process progressed, the axial load of each wall was being modified due to overturning. The axial load and the moment acting on the base of the compression wall increased until eventually reaching the ultimate flexural capacity of the section, point that defined the predicted lateral force capacity for this specimen. The axial load at the base

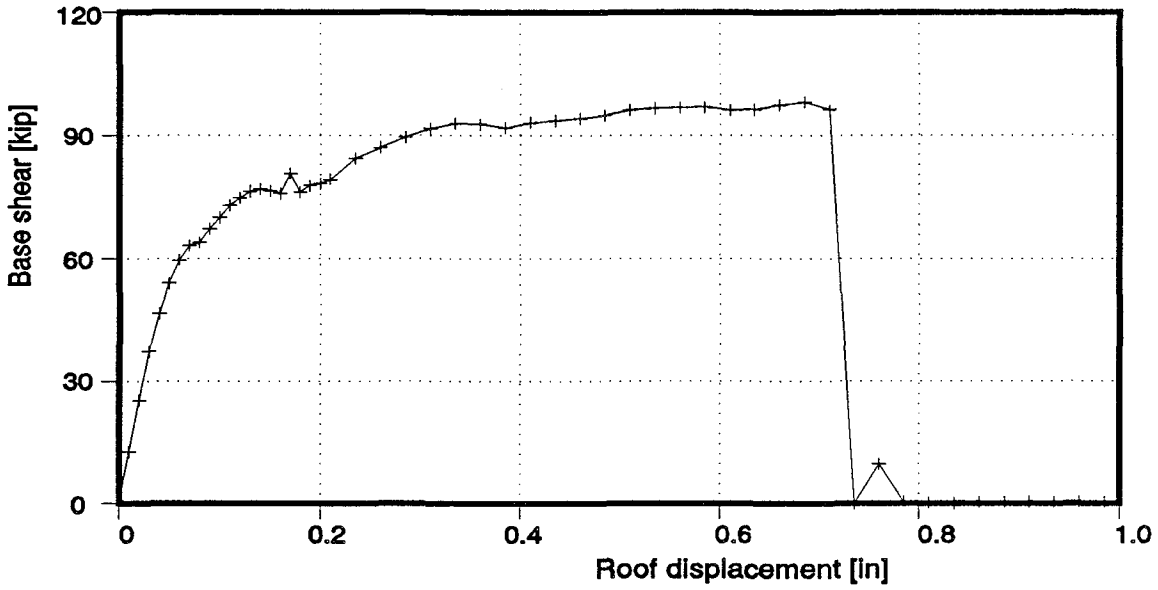

Figure 10.18: Specimen 2d: Predicted base shear-roof displacement history obtained using SCAM

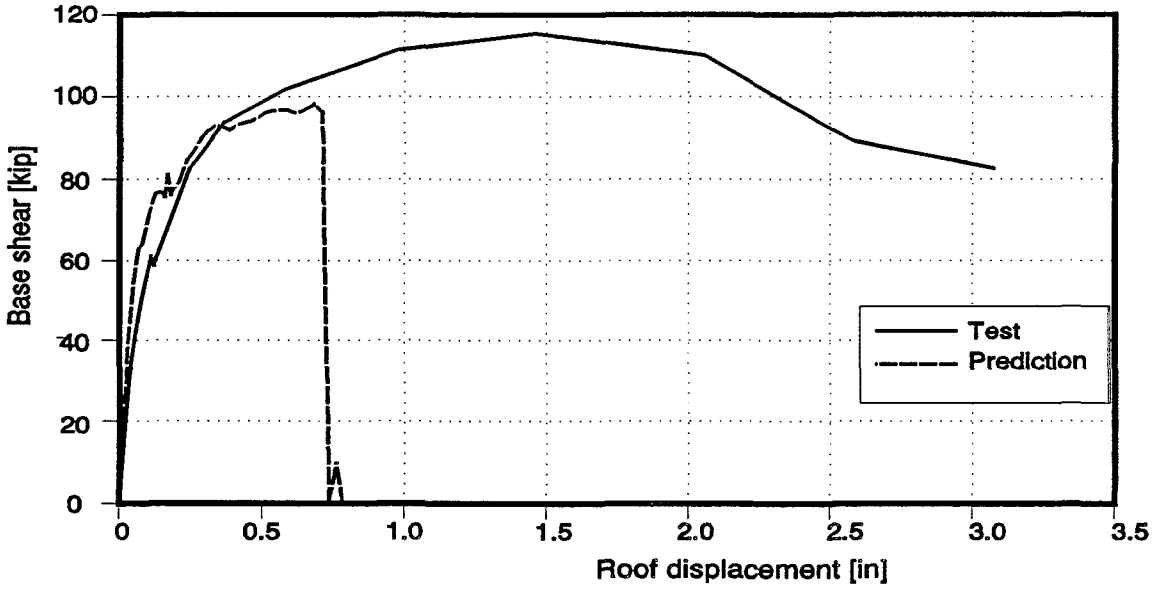

Figure 10.19: Specimen 2d: Comparison between the predicted response and experimental results for the envelope of the 1st peaks of the response, northward loading

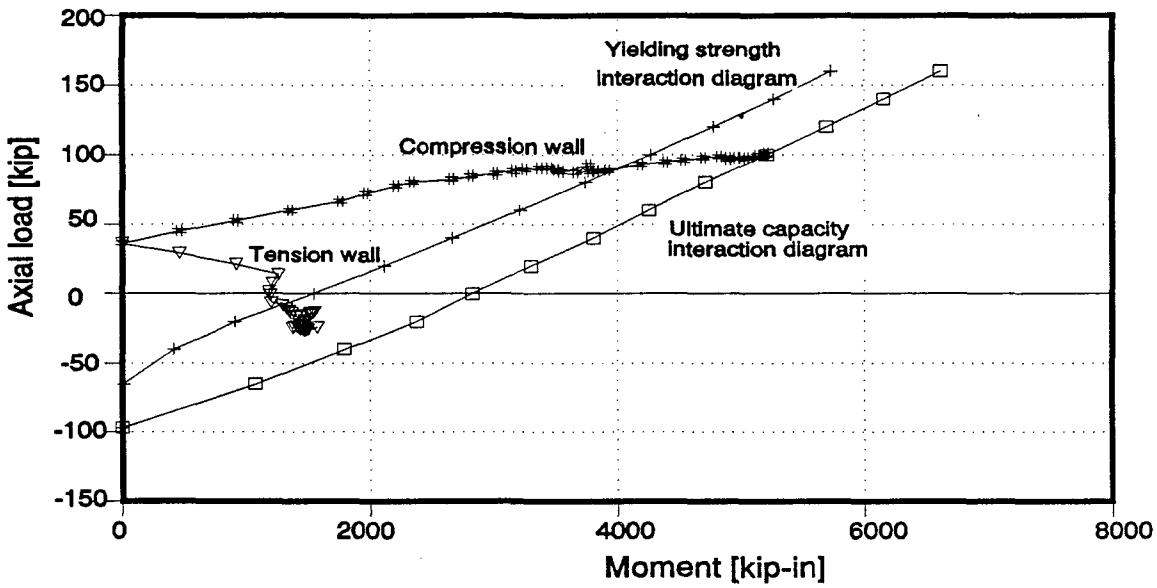

Figure 10.20: Specimen 2d: Predicted moment-axial force history for the sections at the bases of the walls

of the tension wall decreased, and the section eventually developed its yielding strength, but did not reach its flexural capacity.

Results for the lintels showed a similar behavior for both of them. End sections developed their flexural capacities only at the connection with the compression wall.

In summary, at the point when the analysis indicated that the specimen would suffer a drastic reduction of its lateral strength, only the compressed wall had developed its flexural capacity, and the lintels had developed their flexural capacities only at one end. This damage progression is clearly not enough to define a collapse mechanism for this type of structure, and the predicted response is clearly incomplete.

10.4 Evaluation of Results Obtained with the Computer Program SCAM

The computer program SCAM was able to model the response of masonry wall specimens up to drift levels of about 0.4%. The program operation was based on moment-curvature curves which ended at an assumed maximum masonry strain of 0.003. The program was therefore unable to follow the specimens' behavior past drift levels corresponding to those maximum strains.

Predicted response was generally stiffer than the observed response. Maximum lateral capacities were estimated within about 10%. Drift at maximum capacity was

underestimated. Observed collapse mechanism were accurately predicted. The solution algorithm remained stable, even when element capacities were dropping. The model fulfilled its requirements as a design tool for predicting collapse mechanisms and corresponding capacities.

These results are generally consistent with the assumptions and limitations of the program: the program was not originally intended as a pure analysis tool. The program could be expected to underestimate the lateral drifts, for the following reasons:

1) Moment-curvature relationships used were consistent with a flexural cracking value of $4\sqrt{f_m'}$ based on the experimental observations of Specimen 2a. If this value exceeded the actual one, the program would underestimate the cracked, elastic deformations of the specimen.

2) The program does not have a connection element capable of following the bond degradation of flexural reinforcement at the base of the specimens. This leads to underestimates of deformation.

3) The program does not have a connection element capable of modeling sliding shear behavior. This also leads to underestimates of deformations.

The program could be expected to overestimate capacity slightly because its estimate of element flexural capacity is based on moment-curvature curves for monotonically increasing curvatures. An exception to this, observed for Specimen 2d, was due to the fact that large curvatures (corresponding to strains in excess of the assumed maximum) occurred in the lintels of both stories.

The program did not calculate maximum drifts beyond about 0.4%, far less from the experimentally observed values. It must be emphasized that this is due only to the masonry reaching its assumed maximum compressive flexural strain of 0.003, and not to any problem with the solution algorithm. Based on work performed in this and other TCCMAR tasks [47], it did not seem justified to use a larger value of the maximum strain during the design process. However, if larger maximum strain values had been used, the program's solution algorithm would have accommodated them. Also, maximum strains much larger than 0.003 could have been inconsistent with the small-deformation assumptions used in the program.

If the computer program SCAM were to be extended as a general analysis tool for masonry wall specimens, the following limitations would have to be overcome:

1) Moment-curvature relationships for unconfined sections, obtained by methods such as the RCCOLA computer program, are stopped at some conventionally defined point corresponding to a maximum strain in the masonry, usually 0.003. However, observations of the actual failure mechanism (Section 9.5) reveals that this point does not necessarily correspond to the maximum

deformations. After failure of the original section, a reduced section with lower strength but with some residual deformation capacity will remain active. This reduced section is defined by the progression of the masonry crushing and reinforcement fracture inside the original section. Some studies are necessary to obtain moment-curvature relationships that include this behavior.

2) The relationship between element deformations and strains would have to be revised to permit large deformations.

3) An interface element would have to be added to model bond degradation and sliding shear behavior at the wall base, in addition to rocking about the compression corner of the wall element.

The program would, however, still be limited by its idealization of masonry elements as lines following the mid-sections of those elements. The general solution algorithm is stable even for descending branch behavior. It could be implemented in finite element programs for analyzing masonry walls.

10.5 Proposed Shear Strength Analytical Model for Masonry Walls

To analyze the behavior of the specimens tested as part of this work, a model was needed to represent the shear capacity of masonry walls and piers. As mentioned in Chapter 2, there has been extensive discussion of how to evaluate shear capacity of masonry elements. Several expressions for calculating shear capacity of masonry walls have been recently proposed [1,7,8,10,20,22]. Most are empirical, and include in different ways, some or all the aspects influencing shear strength of masonry walls.

However, it was believed by this author that further analyses were needed to improve that model and/or propose a new one to predict shear capacity of masonry walls. A first step was to analyze the degree of agreement of the existing models with available experimental results. Based on the obtained conclusions, a new model was proposed. Finally, results obtained with the new model were compared with experimental data. A complete description of the development of the proposed expression and the corresponding calculations is given in Appendix C of this work.

The proposed model uses the conventional approach of representing the shear strength after diagonal cracking V_n as the summation of the residual strength of the masonry V_m plus the contribution of the transverse steel V_s.

The contribution of the transverse reinforcement V_s to the shear strength can be expressed as:

$$V_s = \alpha \frac{A_h}{ht} td f_y = \alpha \rho_h td f_y \qquad (150.15)$$

Where:

α	=	Transverse reinforcement effectiveness ratio
A_h	=	Total transverse reinforcement area in the height of the wall
t	=	Wall thickness
h	=	Wall height
d	=	Effective depth of wall cross-section
f_y	=	Yielding strength of transverse reinforcement
$\rho_h = A_h/th$	=	Transverse reinforcement ratio

From the analysis of available experimental data, a value of $\alpha = 0.4$ was determined as the most appropriate.

As described in Section 2.3.2, the masonry contribution V_m to the shear strength is the residual masonry shear strength after diagonal cracking. V_m is provided by shear transfer at the compression toe of the wall, by aggregate interlock between the faces of the diagonal crack, and by dowel action of the longitudinal reinforcement crossing the diagonal crack. The following parameters affecting V_m have been identified: the compressive strength of the masonry f_m' the aspect ratio of the wall, usually represented by the M/Vd ratio; the axial stress level f_a; and the longitudinal reinforcement ratio ρ_v.

The neutral axis depth c at the critical section, as calculated from usual principles for the section under combined flexure and axial load, and the ratio of the acting moment to flexural capacity M/M_n for that section, were chosen to represent the above factors affecting V_m. The proposed expression for V_m is therefore of the following form:

$$V_m = C_m \frac{c}{d} \frac{M}{M_n} td \sqrt{f_m'} \qquad (10.4)$$

The value of the constant $C_m = 18$ was determined from the experimental data.

Based on these results, the following equation is proposed to evaluate the shear strength of a fully grouted masonry wall:

$$V_n = V_m + V_s \qquad (10.5)$$

Where:

$$V_m = 18 \frac{c}{d} \frac{M}{M_n} td \sqrt{f_m'} \quad \textbf{(10.6)}$$

$$V_s = 0.4 \rho_h f_y td \quad \textbf{(10.8)}$$

As described in Appendix C, results obtained with the proposed model compared very well with available experimental data for masonry walls failing in shear.

11. SUMMARY, CONCLUSIONS AND RECOMMENDATIONS

11.1 Summary

The objectives of this study, part of Task 3.1(c) of the TCCMAR Program, were to examine how the in-plane seismic resistance of multistory reinforced concrete masonry walls is affected by floor-wall joints, wall openings, and floor elements. To that end, six full-scale concrete masonry specimens, reinforced and fully grouted, were constructed and tested in the laboratory. Two of the specimens, known as Type 1, represented a shear wall of a two-story building with door and window openings. The rest of the specimens, known as Type 2, represented a pair of coupled walls of a two-story building, each coupled by a different floor system, with and without lintels.

The specimens were tested under quasi-static, reversed cyclic lateral loads applied in the plane of the walls at the second-floor and roof level. All of them but Specimens 2b and 2c were also loaded vertically by constant loads representing gravity loads on the coupling slabs' tributary areas. To analyze potential problems of lateral instability, Specimen 1a was subjected to out-of-plane displacements simultaneously with the in-plane displacements during the last cycles of loading.

Test results for each specimen included load-deflection data, strains in reinforcement, and sufficient information to compute deformations and to analyze the behavior of the specimen and its critical regions.

The specimens behaved generally as intended in design. Under many cycles of reversed loading, the response was stable up to story drift ratios as high as 0.7% to 1.0%. The energy dissipated per cycle did not degrade significantly, even at the maximum story drift levels. Failure was ductile, in that inelastic action was restricted to those elements designed to respond in a predominantly flexural mode.

Maximum capacities and overall behavior of the specimens were well predicted by the analysis of the expected collapse mechanisms. An analytical inelastic model developed during this work, and based on beam and column elements, showed reasonably good results in predicting the load-deformation behavior of the specimens and their critical elements.

11.2 Conclusions

11.2.1 General Design Approach. Based on the test results and analytical predictions, a general design approach is proposed for coupled and perforated reinforced concrete masonry walls subjected to seismic loads. This approach involves the following steps:

1) Select a stable collapse mechanism for the wall, characterized by reasonable inelastic deformation demand in hinging regions. Using that collapse mechanism, predict the lateral load capacity of the wall in terms of its flexural capacity in hinging regions. This process can be facilitated using collapse analysis programs such as that developed for this research.

2) Using general plane-section theory to describe the flexural behavior of reinforced masonry elements, provide sufficient flexural capacity and flexural ductility in hinging regions.

3) Using a capacity design philosophy, provide wall elements and connections with sufficient shear and shear transfer capacity respectively, to resist the shears consistent with the development of the intended collapse mechanism. Calculate the shear capacity of masonry elements, and the shear transfer capacity between adjacent elements, using expressions developed in this and previous research. An appropriate strength reduction factor must be considered in calculating nominal shear capacities of the elements.

4) Using reinforcement details developed and tested in this and previous research, detail the wall reinforcement to develop the necessary strength and inelastic deformation capacity in the critical regions.

11.2.2 Design Guidelines. Successful implementation of this general design approach requires that inelastic deformations and associated damage be compatible with design assumptions at each region of the specimen, allowing for uncertainties in loads and capacities. To meet this requirement, the following specific design guidelines should be followed:

1) Walls designed according to a pier-based design philosophy or a coupled wall-based philosophy, can each perform satisfactorily as described above. Pier-based walls were not observed to be susceptible to out-of-plane instability in these tests. However, selection of the desired collapse mechanism should include considerations of required local deformations associated with assumed overall drift level.

2) Strain demands in flexural reinforcement at hinging regions should be compared with available strain capacity under reversed cyclic loading. If strain demand is excessive, inelastic drift should be reduced, or wall bases should be shortened. To decrease the reinforcement strain associated with inelastic rotations, longitudinal reinforcement can be de-bonded in hinging regions. This is particularly useful at bases of long walls.

3) In computing the flexural capacity of coupling elements similar to those tested here, the effective width of the slab should be at least as great as the actual 6.5 ft. width

used for these specimens. This is important in order to get correct estimates of collapse capacity and associated shear demands.

4) Lap splices should be carefully located, considering the following factors:

   a) Lap splices at critical regions can lead to premature splitting failure if large-diameter bars are used. Whatever the bar diameter, lap splices at critical regions limit the yielded length of flexural reinforcement and increase the strain demand for a given drift level.

   b) Extensions of splices which inadvertently increase flexural capacity of adjacent critical regions should be avoided.

5) To enhance wall stability and retard fracture of longitudinal reinforcement, sliding shear should be resisted by shear keys at wall bases.

6) In carrying out the capacity design of masonry elements for shear, shear resistance should be calculated using the methods developed and evaluated here, as described in Section 10.5 and Appendix C. A strength reduction factor of 0.85 or less should be used in shear design of masonry elements.

7) End anchorages in shear reinforcement should be detailed using 180-degree hooks around the extreme flexural reinforcement. If a given combination of bar diameter and wall thickness do not permit standard bend radii, it is better to use smaller bend radii and retain the 180-degree hook.

8) Shear capacity of coupling elements depends on the geometry, reinforcement, and axial load of the element. The floor slab-lintel assemblages tested here had shear capacities exceeding the capacity of the web alone.

9) Connections between precast floor slabs and walls had minimum reinforcement, consisting of welded wire fabric placed in the 2-in. topping. This detail performed satisfactorily as discussed above.

10) Seismic behavior of perforated masonry shear walls is dependent on the integrity of the masonry and grout. Use of a grouting admixture was crucial to grout integrity.

To further improve the performance of masonry walls designed according to the guidelines proposed here, further investigation is needed in the following areas:

1) Factors affecting early fracture of extreme longitudinal reinforcement in long walls with light flexural reinforcement.

2) Factors affecting progressive deterioration of the lintel-wall and lintel-column connections.

3) Effects of high levels of overturning axial forces on the coupled walls as a result of excessive flexural capacity of the lintels.

11.2.3 Analytical Approaches for Design. The behavior and lateral load capacity of the specimens studied here were in general agreement with the methods used to predict lateral capacity and collapse mechanism. The following analytical procedures are recommended for design of complex masonry walls:

1) A simple plastic analysis of trial collapse mechanisms provides a very good estimate of a wall's lateral load capacity. However, the selection of the correct mechanism can be difficult for highly indeterminate walls.

2) To automate this procedure, the solution algorithm and the line element model used were incorporated into the computer program SCAM to perform a sequential collapse analysis for masonry walls. This approach was appropriate for predicting the response of masonry wall structures within the range of validity of the moment-curvature relationships used.

11.3 Recommendations for Implementation

The design approach, specific design guidelines, and analytical tools studied and developed here should be used in design of perforated and coupled wall masonry structures. The design approach should be incorporated into masonry design codes.

11.4 Recommendations for Further Research

1) In this work, only the overall characteristics of the response of the specimens were analyzed. Further analyses are needed to study the individual response of each component of the specimens. Instrumentation data include sufficient information to perform this task. Complete data are available to the research community.

2) Implementation of improved models for the moment-curvature relationships for masonry sections are needed. The new models should consider the residual deformation capacity of the reduced section after the original section is damaged.

3) The proposed model for shear strength of masonry walls needs to be verified using experimental results other than those against which it was calibrated.

4) A minimum ratio of distributed flexural reinforcement is needed to control inelastic rotations at the base of the walls, to prevent fracture of the extreme bars, and to enhance sliding shear resistance, especially at the wall-foundation connection. Some research is needed to relate the requirement for a minimum longitudinal reinforcement with the requirements that the wall's flexural capacity be limited to insure ductile behavior.

5) Studies are needed to determine the minimum requirements for transverse reinforcement needed at lintel-column joints to resist the unbalanced forces associated with the development of the flexural capacities of the elements connected by the joint.

6) Studies are needed to determine the reinforcement details at the lintel-wall connection, needed to prevent the local damage detected during the tests of Specimens 2c and 2d.

7) The design approach and design guidelines developed here are expected to be generally applicable to grouted clay masonry as well as grouted concrete masonry. Specific aspects of material properties and flexural and shear behavior may differ, and they should be verified experimentally.

APPENDIX A

DESIGN OF TYPE 1 PERFORATED WALL SPECIMENS

A.1 Introduction

In this Appendix, design of the two Type 1 Specimens of the TCCMAR Program Task 3.1(c), single walls with door and window openings (Fig. A.1), is described, and the results obtained are discussed, with emphasis on the differences between the design philosophies [31]. Lateral load resisting elements were provided with enough flexural and shear strength to satisfy code type requirements. All the wall elements were then re-designed to satisfy the requirements consistent with the development of the expected collapse mechanism. In both cases, the wall capacity was assumed to be controlled by flexural behavior. According to a capacity design philosophy, elements were provided with shear capacities larger than shear forces associated with the development of flexural strength of the system.

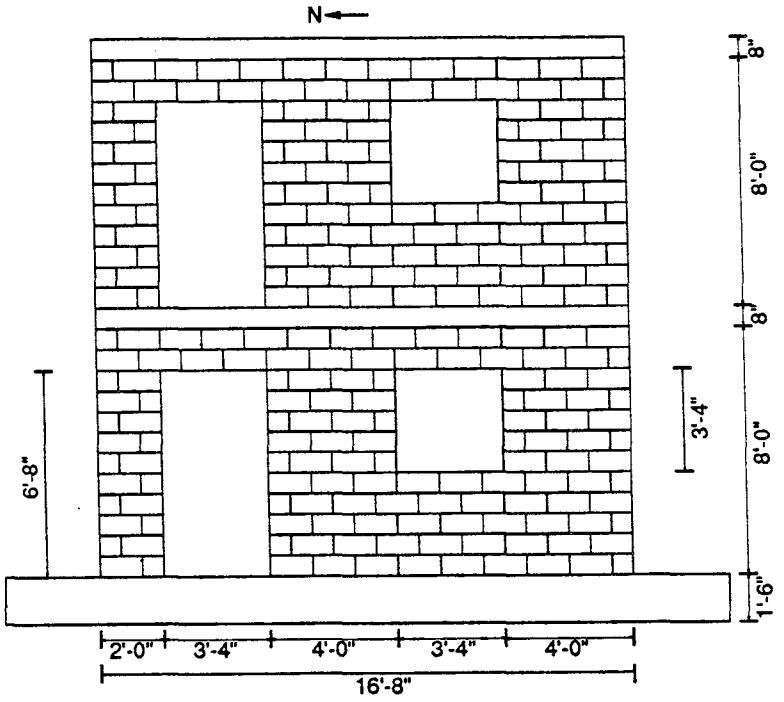

Figure A.1: Type 1 Specimen.

A.2 Design Criteria

A.2.1 Materials. Estimated values of the material properties were based on the results of previous tests in the same project [13,32].

Reinforcement

Grade 60 reinforcing steel was used to built the specimens. Based on the results of previous tests, the following steel properties were used (Fig. A.2): f_y = 72 Ksi, E_s = 29,000 Ksi, ϵ_{sh} = 0.5%, E_{sh} = 1320 Ksi, f_u = 114 Ksi, and ϵ_u = 12%.

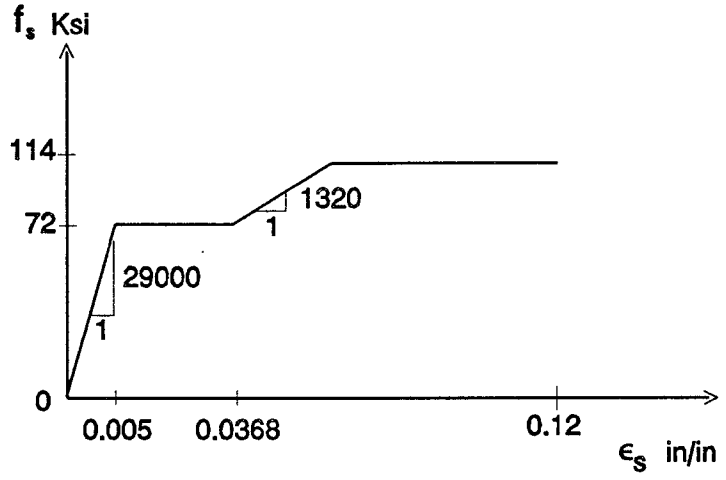

Figure A.2: Reinforcing steel properties used in design.

Masonry

Masonry compressive strength f'_m = 2000 psi was used. The stress-strain behavior of the masonry was modeled using the curve given by Kent and Park for unconfined concrete [21].

Concrete

A concrete compressive strength f'_c = 4000 psi was used. The stress-strain behavior of the concrete was modeled using the curve given by Kent and Park for unconfined concrete [21].

A.2.2 Loads. In order to use consistent criteria throughout the project, Type 1 Specimens were designed for gravity and lateral loads specified in the 1985 UBC [34], acting on the wall as part of the prototype building [35]. The tributary width of the wall in the

prototype building was taken as 20 ft. The specimens were loaded vertically by constant loads representing the gravity loads on the wall's tributary area.

Gravity Loads

Wall: Wall density = 121 pcf
Wall weight = 6.3 Kips/Story

Floors:

Dead Load:	Precast plank + topping	74 psf
	Partitions	20 psf
	Floor finish	5 psf
	HVAC	8 psf
	TOTAL	107 psf
Live Load:	On the full area	50 psf
	Reduction	7 psf
	TOTAL	43 psf
Total Floor:	Distributed	150 psf

Total Load per floor = 0.15 x (16.67' x 20') = 50.0 Kips

Lateral Loads (for UBC Zone 4)

$$V_{base} = ZIKCSW \qquad \textbf{(A.3)}$$

Where Z = 1.0
I = 1.0
K = 1.33
CS = 0.14
W = 2 (0.107 x 20 x 16.67 + 6.3) = 83.9 Kips

$$V_{base} = 15.6 \text{ Kips}$$

A.3 Code Design

The code-type design was the same for both specimens. Essentially, an allowable stress design was performed when the walls were subjected to the service loads.

A.3.1 Design Criteria. Allowable stresses design as prescribed in 1985 UBC [34] was performed. Seismic shear forces were amplified by a factor of 1.5 and allowable stresses were increased by 1/3 when seismic forces were included in service loads. Material properties were: F_s = 24 Ksi; E_s = 29,000 Ksi; f_m' = 2000 psi; E_m = 750 f_m' = 1500 Ksi; $F_b = f_m' / 3$ = 667 psi; $n = E_s/E_m$ = 19.3

A.3.2 Vertical Load Distribution. The center pier was assumed to take 1/2 of the total gravity load above its level (55.4 Kips); the lateral elements, 1/4 each (27.7 Kips).

A.3.3 Lateral Force Distribution. Analysis based on the uncracked elastic properties of the elements indicated that 48% of the base shear would be taken by each pier, and 2% taken by the column. To take into account the effect of cracking and the increase in stiffness of the downwind pier due to the higher compressive forces induced by overturning moment, it was assumed that the downwind pier would take 3/4 of the base shear [35].

A.3.4 Flexural Design of Piers. The most heavily loaded pier was designed first. It was assumed the pier was in double curvature and size #3 bars were used as jamb bars. The code forces acting on that pier were:

V = $3/4V_{base}$ = 11.7 Kips
M = $VL/2$ = (11.7 K)(40")/2 = 234 Kip-in
N = 27.7 Kips (Gravity load only)

Assuming that plane sections remain plane, that materials behave elastically, that masonry takes no tensile stresses, and that the maximum stress in the masonry is equal to F_b ($k > k_b$) when the axial load is conservatively taken equal to the gravity load of 27.7 Kips, and by imposing compatibility of deformations, the tensile stress in the reinforcing steel f_s and the maximum allowable moment M_a for the section were calculated:

f_s = 21.9 Ksi < F_s = 24 Ksi *O.K.*
M_a = 603 Kip-in
$1.33M_a$ = 802 Kips > $1.5M$ = 351 Kips-in *O.K.*

A.3.5 Shear Design of Piers. The service level shearing stress f_v, amplified by a factor of 1.5 as per code seismic provisions, was compared with the allowable stress F_v increased by 1/3 and calculated assuming the shear reinforcement takes all shear:

f_v = (11.7 x 1000)/(5.63 x 38.1) = 54.5 psi
M/Vd = $L/2d$ = 40/(2 x 43.4) = 0.46

F_v = $\frac{1}{2}(4 - M/Vd)\sqrt{f'_m}$ = $\frac{1}{2}(4 - 0.46)\sqrt{2000}$ = 79.2 psi
$F_{v\,max}$ = $(120 - 55\,M/Vd)$ = (120 - 55 x 0.46) = 94.7 psi *O.K.*
$1.33F_v$ = 105.6 psi > $1.5f_v$ = 81.8 psi *O.K.*

The required area of transverse reinforcement at each course was:

A_v = $sV/F_s\,d$ = 8 x (1.5 x 11.7)/(1.33 x 24 x 43.4) = 0.1 in^2

To satisfy this requirement, minimum transverse reinforcement of 1#3 at each course was provided.

A.3.6 Minimum Reinforcement Requirements.

Flexural reinforcement ratio = $2\#3/A_g$ = 2(0.11)/(47.63 x 5.63) = 0.00082 > Min ratio = 0.0007 *O.K.*

Transverse reinforcement ratio = 1#3/(8 x 5.63) = 0.0024 > Min ratio = 0.0007 *O.K.*

Total reinforcement ratio = 0.00082 + 0.0024 = 0.0032 > Min ratio = 0.002 *O.K.*

Maximum reinforcement spacing ≈ 40" < Maximum allowed = 48" *O.K.*

Minimum bar size = #3 = Minimum allowed *O.K.*

A.3.7 Flexural Design of the Base of the Wall. It was conservatively assumed that the base of the wall would take all the base shear and overturning moment, and that the wall would take 3/4 of the total gravity load. Only #3 jamb bars were considered in computing the allowable stresses for the section. The forces acting on the wall were:

V = V_{base} = 15.6 Kips
M = 15.6 x (204 + 100) = 4742 Kip-in
N = 3/4(2 x 6.3 + 2 x 50) = 84.5 Kips

The tensile stress in the reinforcing steel f_s and the maximum allowable moment M_a for the section were calculated as previously described:

f_s = 23.6 Ksi < F_s = 24 Ksi *O.K.*
M_a = 6924 Kip-in
$1.33M_a$ = 9209 Kip-in > $1.5M$ = 7113 Kip-in *O.K.*

A.3.8 Shear Design of the Base of the Wall. Because of the low level of the service shearing stress f_v in the base of the wall, minimum transverse reinforcement was required at this stage of the design.

The final design of the walls, described in the next sections of this report, was completed based on the previously calculated actual lateral load capacity of the specimens according to the different design philosophies.

A.4 Capacity Design

A.4.1 General. Each structural element of the walls was designed to resist the forces associated with the lateral load capacity of the specimen. Those elements expected to develop large inelastic deformations were provided with shear capacities larger than the shear forces associated with the development of their flexural strengths.

A.4.2 Capacity Design Criteria

Flexural behavior and design. As previously mentioned, the flexural behavior of reinforced concrete masonry elements was modeled using the general methodology developed for reinforced concrete sections under eccentric axial load. Flexural capacity of the masonry member sections were calculated using the RCCOLA computer program [39] considering a maximum compressive masonry strain of 0.003.

Shear behavior and design. Because of good agreement with results of tests performed on pier specimens similar to those analyzed here [38], it was decided to use the shear strength model proposed by Blondet et al. [20]. In that model, the cracking strength v_{cr0} of the masonry in the absence of axial stresses is:

$$\begin{aligned} v_{cr0} &= (3.5 - 1.75\, M / Vd)\sqrt{f_m'} \qquad \text{for} \quad M/Vd \le 1 \\ v_{cr0} &= 1.75\sqrt{f_m'} \qquad\qquad\qquad\quad \text{for} \quad M/Vd > 1 \end{aligned} \tag{A.2}$$

The influence of axial compressive stress f_a is included based on a principal stress criterion:

$$v_{cr} = \sqrt{v_{cr0}^2 + \frac{v_{cr0} f_a}{1.5}} \tag{A.8}$$

The shear strength v_n is taken as the sum of the contributions of the masonry, v_{cr}, and the transverse reinforcement, $½v_s$. The latter is calculated assuming that only 1/2 of the

steel is effective in resisting shear. If ρ_h is the transverse reinforcement ratio, the shear strength will be:

$$v_n = v_{cr} + \frac{1}{2}v_s = v_{cr} + \frac{1}{2}\rho_h f_y \qquad \text{(A.9)}$$

Because the end sections of the flexural elements may be subjected to large rotations, wide cracks were expected to develop at those locations. It was necessary to check the interface shear transfer capacity at these sections. The resisting mechanism is provided by aggregate interlock and by dowel action. Reinforcement normal to the sliding plane produces clamping force necessary to develop aggregate interlock action and provides dowel action. The interface shear capacity V_f is usually computed using traditional concepts of shear friction:

$$V_f = \mu (N + A_s f_y) \qquad \text{(A.10)}$$

where is the friction coefficient, A_s is the distributed reinforcement normal to the sliding plane, and N is the net axial load acting on the wall. Previous experimental results obtained in the same project [13,32] showed that the coefficient of friction could be taken equal to one.

Each element was provided with enough shear capacity to resist the shearing forces associated with the development of the collapse mechanism. It was assumed the shear strength mechanism would govern the behavior of sections where plastic hinges would not develop. The contribution of masonry to the shear strength was always considered in addition to that of the transverse reinforcement. Shear behavior of plastic hinging was assumed to be essentially a problem of interface shear transfer. Sections in which plastic hinges were expected to develop were checked for sufficient interface shear transfer capacity. Because the flexural capacities of the elements were calculated considering the overstrength due to the strain hardening of the reinforcement, no understrength factors ϕ were used in calculating shear capacities.

A.5 Design of Specimen 1a

A.5.1 General. Specimen 1a was designed for a base shear of 172 Kips, as determined from preliminary calculations of the lateral load capacity of the system. Each element of the specimen was designed to resist the forces associated with that base shear capacity.

A.5.2 1st Story Extreme Pier. Longitudinal reinforcement of the pier was #3 jamb bars. This element was expected to develop plastic hinges at both ends. Forces associated with the collapse mechanism were calculated as:

Axial force N_{p2} = 80.5 Kips (Compression)
Bending moment = Section flexural capacity = M_{p2} = 1931 Kip-in
Shear force V_{p2} = $2M_{p2}/40$ = 96.5 Kips

Shear Design

V_u = V_{p2} = 96.5 Kips
M/Vd = 0.46
f_a = 80.5 x 1000/(47.63 x 5.63) = 300 psi
v_{cr0} = (3.5 - 1.75 x 0.46)$\sqrt{}$2000 = 2.69$\sqrt{}$2000 = 120 psi (Eq. A.2)
v_{cr} = $(120^2 + 120 \times 300/1.5)^{1/2}$ = 196 psi (Eq. A.3)
v_s = $\rho_h f_y$ = 72000 ρ_h

Shear capacity $V_n = (v_{cr} + \frac{1}{2}v_s)bd = (196 + \frac{1}{2}72000\,\rho_h)(5.63 \times 43.4)$

Setting $V_n = V_u$, the required ρ_h = 0.56 % was obtained
Use 1#3 + 1#4 @ each course

Check: ρ_h = 0.69 % *O.K.*
V_n = 108 Kips > V_u = 96.5 Kips *O.K.*

Interface Shear Transfer

V_f = $\mu(N + A_s f_y)$ = 1.0(80.5 + 0.22 x 72) = 96.3 Kips *O.K.*

A.5.3 1st Story Center Pier. Longitudinal reinforcement of this pier was #3 jamb bars. Forces associated with the collapse mechanism were:

Axial force N_{p1} = 54.6 Kips (Compression)
Bending moment = Section flexural capacity = M_{p1} = 1511 Kip-in
Shear force V_{p1} = $2M_{p1}/40$ = 75.6 Kips

Shear Design

V_u = V_{p1} = 75.6 Kips
M/Vd = 0.46
f_a = 54.6 x 1000/(47.63 x 5.63) = 204 psi
v_{cr0} = (3.5 - 1.75 x 0.46)$\sqrt{}$2000 = 2.69$\sqrt{}$2000 = 120 psi (Eq. A.2)
v_{cr} = $(120^2 + 120 \times 204/1.5)^{1/2}$ = 175 psi (Eq. A.3)

Using the same transverse reinforcement as in the extreme pier:

v_s = $\rho_h f_y$ = 72000 x 0.69% = 497 psi
Shear capacity $V_n = (v_{cr} + \frac{1}{2}v_s)bd$ = (175 + ½497)5.63 x 43.4 = 104 Kips *O.K.*
Use 1#3 + 1#4 @ each course

Interface Shear Transfer

V_f = $\mu(N + A_s f_y)$ = 1.0(54.6 + 0.22 x 72) = 70.4 Kips *O.K.*

A.5.4 1st Story Column. Flexural reinforcement of this element was 2#3 bars. As assumed in the preliminary collapse mechanism analysis, when the specimen loaded to the right reached its capacity, the column was subjected exclusively to a tensile axial force equal to its axial tensile capacity. It was necessary to check the element for the case of load to the left. Following the same procedure, it was assumed that the extreme tension pier was able to develop its full tensile axial capacity, and that the column was subjected to a compressive force equal to its gravity load plus the transmitted force. Since the extreme pier and column had the same longitudinal reinforcement and were subjected to the same gravity loads, the maximum compressive force in the column resulted in the same value of the compressive force on the extreme pier. The forces acting on the column were:

Axial load N_c	=	80.5 Kips (Compression)
Bending moment	=	Section flexural capacity = M_c = 744.4 Kip-in
Shear force V_c	=	$2M_c/80$ = 18.6 Kips

Shear Design

V_u	=	V_c = 18.6 Kips
M/Vd	>	1.0
f_a	=	80.5 x 1000/(23.63 x 5.63) = 605 psi
v_{cr0}	=	$1.75\sqrt{2000}$ = 78 psi (Eq. A.2)
v_{cr}	=	$(78^2 + 78 \times 605/1.5)^{1/2}$ = 194 psi (Eq. A.3)

Masonry shear capacity $V_{cr} = v_{cr}bd$ = 196 x 5.63 x 19.4/1000 = 21.4 Kips

$V_{cr} > V_u$ *O.K.*

Use 1#3 each course. Use same reinforcement for 2nd story column

Interface Shear Transfer

$V_f = \mu(N + A_s f_y)$ = 1.0(80.5 + 0.22 x 72) = 96.3 Kips *O.K.*

A.5.5 2nd Story Extreme Pier. Longitudinal reinforcement of this pier was #3 jamb bars. Forces acting on the pier were:

Axial force due to overturning moment, assumed equal to one half of that acting on the 1st story extreme pier = ½ 52.8 = 26.4 Kips.

Axial force due to gravity loads, assumed equal to one quarter of the total gravity load at the top of the element plus its own weight = 24.2 Kips.

Total axial force N_{p2} = 24.2 + 26.4 = 50.6 Kips (Compression)

It was assumed that the bottom section develops its full flexural capacity:

$M_{bot} = M_{p2}$ = 1444 Kip-in

The moment at the top section, M_{top}, is limited by the flexural capacity of the lintel, which must be smaller than M_{bot}. It was assumed that

$M_{top} = ½ M_{p2}$ = 722 Kip-in.

Shear force was $V_{p2} = 1.5M_{p2}/40$ = 54.2 Kips = 63% of the story shear

Shear Design

V_u = V_{p2} = 54.2 Kips
M/Vd = 0.61
f_a = 50.6 x 1000/(47.63 x 5.63) = 189 psi
v_{cr0} = (3.5 - 1.75 x 0.61)$\sqrt{2000}$ = 2.43$\sqrt{2000}$ = 109 psi (Eq. A.2)
v_{cr} = $(109^2 + 109 \times 189/1.5)^{1/2}$ = 160 psi (Eq. A.3)
v_s = $\rho_h f_y$ = 72000 ρ_h
Shear capacity $V_n = (v_{cr} + ½v_s)bd$ = (160 + ½72000 ρ_h)5.63 x 43.4

Making $V_n = V_u$, the required ρ_h = 0.18 % is obtained
Use 1#4 @ each course. Use same reinforcement for 2nd story center pier.

Check: ρ_h = 0.44 % *O.K.*
V_n = 78 Kips = 90% of the story shear *O.K.*

Interface Shear Transfer

$V_f = \mu(N + A_s f_y)$ = 1.0(50.6 + 0.22 x 72) = 66.4 Kips *O.K.*

A.5.6 Base of the Wall. The base of the wall was designed to resist the forces associated with the ultimate capacity of the 1st-story piers as shown in Fig. A.3. Longitudinal reinforcement was provided by the pier jamb bars continuous through the wall base and anchored to the base beam. Extra reinforcement was added as needed. The extra

pier bars were cut below the base of the piers so that no additional flexural capacity was added to those elements. Forces on the wall base were (Fig. A.3):

Axial force N_w = 54.6 + 80.5 + 4.3 = 139.4 Kips (Compression)

Shear force V_w = Specimen capacity = 172 Kips

Bending moment M_w = 1511 + 1931 + (80.5 - 54.6)(44) + (75.5 + 96.5)(40) = 11,462 Kip-in

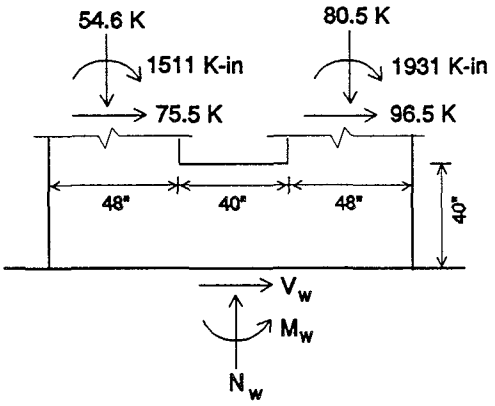

Figure A.3: Forces acting on the wall at base of Specimen 1a.

Flexural Design

$M_u = M_w$ = 11,462 Kips

Adding 4#4 uniformly distributed at the base:

M_n = 13,650 Kip-in > M_u = 11,462 Kip-in *O.K.*

Transverse Reinforcement Design Design of the transverse reinforcement was governed by the design of the drag bars needed to take the pier shears into the base of the wall. The critical location were the compression toe of the extreme pier. As previously described, it was assumed that the pier shear V_u would be taken by the reinforcement at the two top courses of the wall base.

Required reinforcement area / course = $V_u/2f_u$ = 96.5/(2 x 114) = 0.42 in²/course
Practical limitation: no more than 2#4 per course = 0.40 in².

Use 2#4 @ every course

Interface Shear Transfer

$V_f = \mu(N + A_s f_y)$ = 1.0(139.4 + 1.24 x 72) = 229 Kips *O.K.*

A.5.7 2nd Floor Horizontal Member. The 2nd floor horizontal member between piers was designed to resist the forces associated with the ultimate capacity of 1st and 2nd story piers as shown in Fig. A.4. Forces acting on the end section of the horizontal element were:

Axial force N_h = 96.5 - 54.2 = 42.3 Kips (Compression)
Shear force V_h = 80.5 - 50.6 = 29.9 Kips
Bending moment M_h = 1931 + 1444 + (96.5 + 54.2)(64/2) - 29.9(48/2) = 7480 Kip-in

Flexural Design For the given axial force, the flexural capacity M_n of the section reinforced using 2#4 at each course was 6610 Kip-in. Since this is the maximum practical

reinforcement, it was necessary to accept some degree of flexural failure of this element.

Use 2#4 @ each course

Transverse Reinforcement Design Design of the transverse reinforcement was not governed by the shear associated with the flexural capacity of the horizontal element, but rather by the forces associated with the pier capacities:

$V_u = V_h$ = 29.9 Kips
$M/Vd >$ 1.0
v_{cr0} = 1.75 $\sqrt{2000}$ = 78 psi (Eq. A.2)

Shear capacity neglecting axial stress contribution:

$V_n = (v_{cr0} + \frac{1}{2}v_s)bd$ = (78 + ½72000 ρ_h)x (5.63 x 61.6)

Setting $V_n = V_u$, the required ρ_h = 0.03% is obtained

Use 1#4 @ every other cell

Check: ρ_h = 0.22 % *O.K.*
½V_s = 27.7 Kips *O.K.*

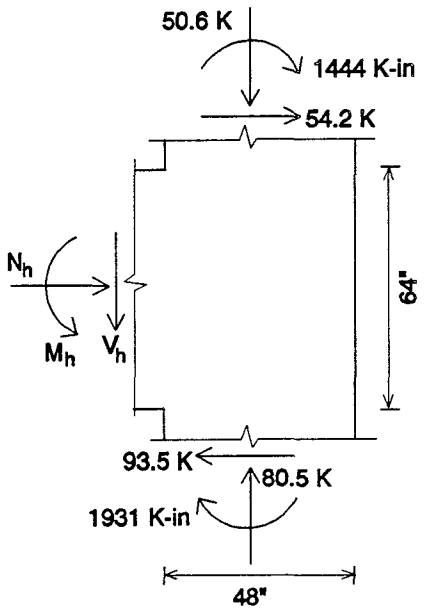

Figure A.4: Forces acting on 2nd floor horizontal member-pier connection of Specimen 1a

Interface Shear Transfer Neglecting axial force contribution:

$V_f = \mu A_s f_y$ = 1.0(8 x .4)72 = 230.4 Kips *O.K.*

A.5.8 Roof Lintel between Piers. The roof lintel between piers was designed to resist forces from the 2nd story extreme pier as described in Sect. A.5.5. From equilibrium of forces, as shown in Fig. A.5, forces at the end of the lintel were:

Axial force N_l = 54.2 Kips (Compression)
Shear force V_l = Force transmitted through the lintel = 26.4 Kips
Bending moment M_l = ½ 1444 + 54.2 x 12 - 26.4 x 24 = 739 Kip-in

Flexural Design The flexural capacity of the section M_n was calculated neglecting the axial force and considering the welded wire fabric in the topping, approximately 0.5 in². Using 1#4 plus WWF at the top and 2#4 at the bottom, flexural capacities were M_n = 620 Kip-in and M_n = 957 Kip-in when the bottom and top fibers were in tension respectively.

Use 1#4 + WWF @ top and 2#4 @ bottom

Transverse Reinforcement Design Design of the transverse reinforcement was not governed by the shear associated with the flexural capacity of the horizontal element, but rather by the forces associated with the pier capacities:

$V_u = V_l = 26.4$ Kips
$M/Vd > 1.0$
$v_{cr0} = 1.75\sqrt{2000} = 78$ psi (Eq. A.2)

Shear capacity neglecting axial stress contribution:

$V_n = (v_{cr0} + \frac{1}{2}v_s)bd = (78 + \frac{1}{2}72000\ \rho_h)(5.63 \times 21.63)$

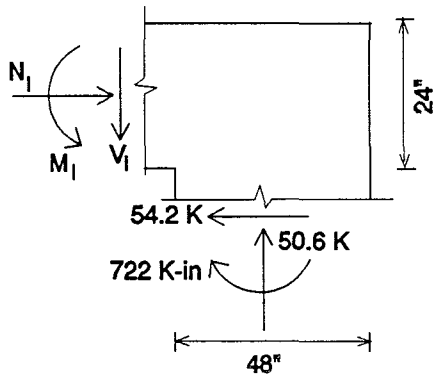

Figure A.5: Forces acting on the roof lintel-pier connection of Specimen 1a

Setting $V_n = V_u$, the required $\rho_h = 0.39$ % is obtained

Use #3 U tie @ every cell

Check: $\rho_h = 0.49$ % *O.K.*
$V_n = 30.9$ Kips *O.K.*

Interface Shear Transfer Neglecting axial force contribution:

$V_f = \mu A_s f_y = 1(3 \times 0.2 + 0.5) \times 72 = 79.2$ Kips *O.K.*

Use same reinforcement for both roof lintels

A.5.9 2nd Floor Lintel. The 2nd floor lintel was designed to resist the force transmitted through the coupling system when the specimen reaches its capacity.

Flexural Design Longitudinal reinforcement was provided as a continuation of the longitudinal reinforcement of the 2nd floor horizontal element (2#4 @ each course).

Transverse Reinforcement Design Using the same reinforcement as in roof lintel, #3 U ties @ every cell, the shear capacity V_n was also 30.9 Kips.

Note the total shear capacity of both lintels between the column and the piers is 2 x 30.9 = 61.8 Kips = 117 % of maximum transmitted force through the wall. *O.K.*

Interface Shear Transfer Neglecting axial force contribution:

$V_f = \mu A_s f_y = 1(6 \times 0.2 + 0.5) \times 72 = 122.4$ Kips *O.K.*

A.6 Design of Specimen 1b

A.6.1 General. Specimen 1b was designed for a lateral load capacity of 130 Kips, which corresponded to the case of lateral loads acting to the right. Each element of the specimen was designed to resist the forces associated with that case. Some of the elements were checked for the case of load to the left.

A.6.2 Roof Lintel-Column Connection. Longitudinal reinforcement of the column was 3#5 bars. This element was expected to develop a plastic hinge at the top section for either direction of the lateral load. Lintel top reinforcement was 1#3 plus the WWF 6x6 No.6 at the topping. Lintel Bottom reinforcement was 1#3. For the case of the specimen loaded to the right, forces on the column and roof lintel, as shown in Fig. A.6, were:

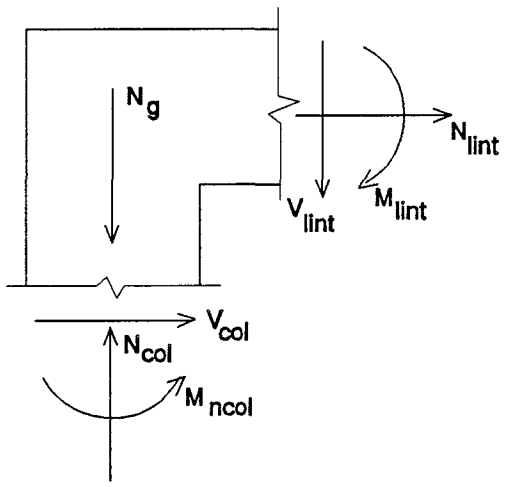

Figure A.6: Forces acting on the roof-lintel connection of Specimen 1b

N_{col}	=	27.3 Kips (Tension)
M_{col}	=	Section flexural capacity = 437 Kip-in
V_{col}	=	10.9 Kips (Assuming double curvature)
M_{lint}	=	208 Kip-in < Section flexural capacity = M_{s1} = 267 Kip-in
V_{lint}	=	V_r = 30.0 Kips

Forces acting on the column and the lintel for the case of the specimen loaded to the left were:

N_{col}	=	26.4 Kips (Compression)
M_{ncol}	=	Section flexural capacity = 752 Kip-in
V_{col}	=	17.9 Kips (Assuming double curvature)
M_{lint}	=	682 Kip-in < Section flexural capacity = M_{s2} = 991 Kip-in
V_{lint}	=	V_r = 23.7 Kips

Shear Design of the 2nd Story Column

V_u	=	V_{max} = 17.9 Kips (Case of column under compression)
M/Vd	>	1.0
f_a	=	26.4 x 1000/(23.63 x 5.63) = 198 psi
v_{cr0}	=	1.75 $\sqrt{2000}$ = 78 psi (Eq. A.2)
v_{cr}	=	$(78^2 + 78 \times 198/1.5)^{1/2}$ = 128 psi (Eq. A.3)
v_s	=	$\rho_h f_y = 72000\ \rho_h$

Shear capacity $V_n = (v_{cr} + \frac{1}{2}v_s)bd = (128 + \frac{1}{2}72000\,\rho_h)5.63 \times 20.0$

Setting $V_n = V_u$, the required $\rho_h = 0.09$ % is obtained

Use 1#4 @ each course

Check: $\rho_h = 0.44$ % *O.K.*

$V_n = 32.4$ Kips $> V_u = 17.9$ Kips *O.K.*

Check case of column under tensile forces: consider $v_{cr} = 0$

$V_n = 18.0$ Kips $> V_u = 10.9$ Kips *O.K.*

Interface Shear Transfer of the 2nd Story Column

$V_f = \mu A_s f_y = 1 \times 3 \times 0.30 \times 72 = 64.8$ Kips *O.K.*

Shear Design of Roof Lintel

$V_u = 31.5$ Kips (Shear associated with flexural capacity of lintel)

From Sect. A.5.8, using #3 U tie @ every cell, the lintel shear capacity V_n was 30.9 Kips. Since the contribution of the slab was not considered, this value was conservative. *O.K.*

Interface Shear Transfer of Roof Lintel

$V_f = \mu A_s f_y = 1.0(2 \times 0.11 + 0.5)72 = 51.8$ Kips *O.K.*

A.6.3 2nd Floor Lintel-Column Connection. Longitudinal reinforcement in the columns was 3#5 bars in both stories. Columns were not expected to develop plastic hinges at the connection with the 2nd floor lintel. Lintel top reinforcement was 1#3 plus the WWF 6x6 gauge 6 at the topping. Lintel bottom reinforcement was 1#3. Given the axial forces acting on the 2nd story column and the plastic moments at the 2nd floor lintel, forces acting on the 1st story column could be calculated from Figs. A.7 and A.8 for the cases of load to the right and load to the left respectively.

Forces Acting on the 2nd Floor Lintel-Column Connection for the Case of the Specimen Loaded to the Right (Fig. A.7)

Forces from 2nd story column:

N_2 = 27.3 Kips (Tension)

M_2 < Section flexural capacity $M_{n2} = 437$ Kip-in

V_2 = $(437 + M_2)/80$

Forces from 2nd floor lintel:

M_{lint} = Section flexural capacity = M_{s1} = 267 Kip-in
V_{lint} = 31.5 Kips

Forces from 1st story column:

N_1 = $N_2 + V_{lint} - N_g = 27.3 + 31.5 - 2.7 =$ 56.1 Kips (Tension)
M_1 < Section flexural capacity = 273 Kip-in
V_1 = $(273 + M_1)/80$

Mechanism condition (from equilibrium at the connection):

$M_1 + M_2 > 468$ Kip-in

Capacity condition:

$M_1 + M_2 < 710$ Kip-in

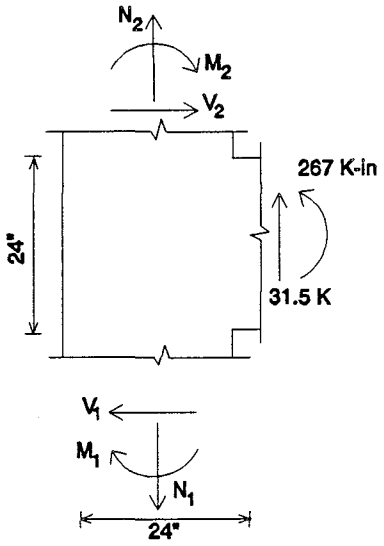

Figure A.7: Forces acting on the 2nd floor lintel-column connection of Specimen 1b for the case of load to the right

It was perfectly possible to satisfy both conditions simultaneously, i.e., the combined flexural strength of the columns above and below the connection was large enough to induce the formation of the plastic hinge in the lintel.

To estimate V_1:

$$V_1 = (273 + M_1)/80 \approx [273 + (273)(468/710)]/80 = 5.7 \text{ Kips}$$

Forces Acting on the 2nd Floor Lintel-Column Connection for the Case of the Specimen Loaded to the Left (Fig. A.8)

Forces from 2nd story column:

N_2 = 26.4 Kips (Compression)
M_2 < Section flexural capacity M_{n2} = 752 Kip-in
V_2 = $(752 + M_2)/80$

Forces from 2nd floor lintel:

M_{lint} = Section flexural capacity = M_{s1} = 991 Kip-in
V_{lint} = 31.5 Kips

Forces from 2nd story column:

N_1 = $N_2 + V_{lint} + N_g$ = 26.4 + 31.5 + 2.7 = 60.6 Kips (Compression)
M_1 < Section flexural capacity = 890 Kip-in
V_1 = $(890 + M_1)/80$

Mechanism condition (from equilibrium at the connection):

$M_1 + M_2 > 976$ Kip-in

Capacity condition:

$M_1 + M_2 < 1642$ Kip-in

It was perfectly possible to satisfy both conditions simultaneously, i.e., the combined flexural strength of the columns above and below the connection was large enough to induce the formation of the plastic hinge in the lintel.

To estimate V_1:

V_1 = $(890 + M_1)/80 \approx [890 + (890)(976/1642)]/80$ = 17.7 Kips

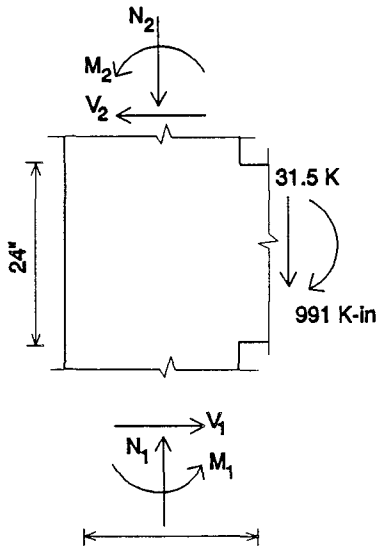

Figure A.8: Forces acting on the 2nd floor lintel-column connection of Specimen 1b for the case of load to the left

Shear Design of the 1st Story Column

V_u = V_{max} = 17.7 Kips (Case of column under compression)
M/Vd > 1.0
f_a = 60.6 x 1000/(23.63 x 5.63) = 456 psi
v_{cr0} = $1.75\sqrt{2000}$ = 78 psi (Eq. A.2)
v_{cr} = $(78^2 + 78 \times 456/1.5)^{1/2}$ = 173 psi (Eq. A.3)
v_s = $\rho_h f_y = 72000\rho_h$
Shear capacity $V_n = (v_{cr} + \frac{1}{2}v_s)bd = (173 + \frac{1}{2}72000\rho_h)5.63 \times 20.0$
Setting $V_n = V_u$, minimum ρ_h is required

Use 1#4 @ each course

Check case of column under tensile forces: consider $v_{cr} = 0$
V_n = 18.0 Kips > V_u = 5.7 Kips *O.K.*

The rest of the design of the column and lintel was the same as in the previous case.

A.6.4 1st Story Piers. Since no large inelastic deformations were expected, design of the 1st story piers was based on elastic behavior using a *VL/M* ratio of 0.6 [42]. It was assumed that the case of load to the right governed design:

Total base shear	=	130 Kips
Shear taken by column	=	5.7 Kips
Shear taken by wall at base	=	130 - 5.7 = 124.3 Kips

Two approaches were used to determine forces taken by piers:

Approach 1 The extreme pier was assumed to resist all the axial load transmitted through the wall. Because that pier was laterally stiffer, it was assumed to take 3/4 of the base shear.

Approach 2 After some degree of inelastic action has been developed, both piers were assumed to have the same stiffness and to take the same axial load and shear.

The piers were reinforced using #3 jamb bars continuous through the wall and anchored to the base beam. As required by design, additional flexural reinforcement was added in such a way that the flexural capacity at the base of the wall was not increased.

Forces Acting on 1st Story Extreme Pier, Approach 1

N_{p2}	=	Gravity Load + Total force transmitted through the wall
	=	54.6 + 61.5 = 116.1 Kips (Compression)
V_{p2}	=	3/4 Shear at wall base = 3/4 (124.3) = 93.2 Kips
M_{p2}	=	$V_{p2}\, L/0.6$ = 93.2 x 40/0.6 = 6213 Kip-in

Flexural Design of the 1st Story Extreme Pier, Approach 1 Diameter of additional reinforcement was limited by the size of the cells and by anchorage requirements. It was determined that #6 was the maximum acceptable size. Adding 1#6 on each cell, the flexural capacity of the pier was:

M_{n2} = 4647 Kip-in = 75 % of required capacity

It was not possible to satisfy the calculated flexural demand on this pier. However, it must be noted that the required moment was calculated using a very conservative value of the ratio *VL/M* = 0.6. On the other hand, if the same reinforcement were used in both 1st story piers, there would be some remaining capacity in the center pier and redistribution of forces would occur.

Shear Design of the 1st Story Extreme Pier, Approach 1

V_u = V_{p2} = 93.2 Kips
M/Vd = 1/0.6 > 1.0
f_a = 116.1 x 1000/(47.63 x 5.63) = 433 psi
v_{cr0} = 1.75 $\sqrt{2000}$ = 78 psi (Eq. A.2)
v_{cr} = $(78^2 + 78 \times 433/1.5)^{1/2}$ = 169 psi (Eq. A.3)
v_s = $\rho_h f_y$ = 72000 ρ_h
Shear capacity $V_n = (v_{cr} + \frac{1}{2}v_s)bd = (169 + \frac{1}{2}72000\ \rho_h)5.63 \times 43.4$

Setting $V_n = V_u$, the required ρ_h = 0.58 % is obtained
Use 1#3 + 1#4 @ each course

Check: ρ_h = 0.69 % *O.K.*
V_n = 102 Kips > V_u = 93.2 Kips *O.K.*

Interface Shear Transfer of the 1st Story Extreme Pier, Approach 1

$V_f = \mu(N + A_s f_y) = 1[116.1 + (6 \times 0.44 + .22)72] = 322$ Kips *O.K.*

Forces Acting on 1st Story Piers, Approach 2 The following calculations are valid for both 1st story piers.

N_{p2} = Gravity Load + ½ Total force transmitted through the wall
= 54.6 + ½61.5 = 85.4 Kips (Compression)
V_{p2} = ½ Shear at wall base = ½124.3 = 62.2 Kips
M_{p2} = $V_{p2}L/0.6$ = 62.2 x 40/0.6 = 4147 Kip-in

Flexural Design of the 1st Story Piers, Approach 2 Using the same additional reinforcement as in the previous case, 1#6 in each cell, the flexural capacity of the piers was:

M_{n2} = 4465 Kip-in > M_{p2} = 4147 Kip-in *O.K.*

Shear Design of the 1st Story Piers, Approach 2

V_u = V_{p2} = 62.2 Kips
M/Vd = 1/0.6 > 1.0
f_a = 85.4 x 1000/(47.63 x 5.63) = 318 psi
v_{cr0} = 1.75 $\sqrt{2000}$ = 78 psi (Eq. A.2)
v_{cr} = $(78^2 + 78 \times 318/1.5)^{1/2}$ = 150 psi (Eq. A.3)
Use 1#3 + 1#4 @ each course

Check: ρ_h = 0.69 % *O.K.*
V_n = 97 Kips > V_u = 62.2 Kips *O.K.*

Forces Acting on 1st Story Center Pier, Approach 1 The 1st story center pier was reinforced in the same way as the extreme pier.

N_{p1} = Gravity Load = 54.6 Kips (Compression)
V_{p1} = ¼ Shear at wall base = ¼ (124.3) = 31.1 Kips
$M_{p2} = V_{p2}L/0.6$ = 31.1 x 40/0.6 = 2073 Kip-in

Flexural Design of the 1st Story Center Pier, Approach 1

M_{n2} = 4231 Kip-in *O.K.*

Shear Design of the 1st Story Center Pier, Approach 1

M/Vd = 1/0.6 > 1.0
f_a = 54.6 x 1000/(47.63 x 5.63) = 204 psi
v_{cr0} = 1.75 $\sqrt{2000}$ = 78 psi (Eq. A.2)
v_{cr} = $(78^2 + 78 \times 433/1.5)^{1/2}$ = 129 psi (Eq. A.3)
V_n = $(v_{cr} + ½v_s)bd$ = (0.129 + ½72 x 0.0069)5.63 x 43.4 = 92 Kips *O.K.*

Comments on the 1st Story Pier Design

Total pier shear capacity, Approach 1 = 102 + 92 = 194 Kips
Total pier shear capacity, Approach 2 = 2 x 97 = 194 Kips
Note that even though the individual capacities of the elements were different, the total shear capacity was the same.

Since the results of Design Approach 1 for the extreme pier showed that the pier could not be provided with the required flexural capacity, some level of damage was expected at the base of this element. However, redistribution of forces was expected and the collapse mechanism would not be altered.

A.6.5 2nd Story Piers. Design of 2nd story piers was based on the same assumptions as in 1st story pier case. Design approach 1 was used.

Total story shear = 65 Kips
Shear taken by column = 9 Kips
Shear taken by piers = 65 - 9 = 56 Kips
Shear taken by extreme pier V_{p2} = ¾ 56 = 42 Kips
Axial load on extreme pier N_{p2} = Gravity Load + Transmitted Force = 47.7 + 30.0 = 77.7 Kips (Compression)

$M_{p2} = V_{p2}L/0.6$ = 42 x 40/0.6 = 2800 Kip-in

The pier was reinforced using #3 jamb bars. As required by design, 1#4 was added in each cell.

Flexural Design of the 2nd Story Piers

M_{n2} = 3153 Kip-in *O.K.*

Shear Design of the 2nd Story Piers

M/Vd = $1/0.6 > 1.0$

f_a = $77.7 \times 1000/(47.63 \times 5.63) = 290$ psi

v_{cr0} = $1.75\sqrt{2000} = 78$ psi (Eq. A.2)

v_{cr} = $(78^2 + 78 \times 290/1.5)^{1/2} = 146$ psi (Eq. A.3)

Use 1#3 @ every course

V_n = $(v_{cr} + \frac{1}{2}v_s)bd = (0.146 + \frac{1}{2}72 \times 0.0024)5.63 \times 43.4 = 57$ Kips

O.K.

A.6.6 Wall at Base. Longitudinal reinforcement of the wall at base, as previously defined, was provided by the pier #3 jamb bars continuous through the wall at base and anchored to the base beam. Extra longitudinal reinforcement added to the piers was discontinued so the flexural capacity of the wall at base was not increased.

Design of the transverse reinforcement was governed by the design of the drag-bars needed to transfer the pier shear force into the wall at base as previously described. Since the maximum pier shear was about the same as in Specimen 1a case, the solution described in Sect. A.5.6 was adopted.

Interface Shear Transfer of the Wall at Base

$V_f = \mu(N + A_s f_y) = 1(170.8 + 0.44 \times 72) = 202$ Kips *O.K.*

A.6.7 2nd Floor Horizontal Member. The 2nd floor horizontal member was designed to resist the forces transmitted from the 1st and 2nd story piers calculated using Design Approach 1. Forces acting on the end section of the horizontal element were obtained in the same way as described in Sect. A.5.7 and Fig. A.4:

Axial force N_h	=	48 Kips (Compression)
Shear force V_h	=	38 Kips
Bending moment M_h	=	5585 Kip-in

Same design used in Specimen 1a case, 2#4 at each course as longitudinal reinforcement and 1#4 @ every other cell as transverse reinforcement, was found to be adequate to resist these forces.

A.6.8 Roof Lintel between Piers. The roof lintel between piers was designed to resist forces from 2nd story extreme pier as described in Sect. A.6.5. Forces acting on the end section of the lintel were obtained in the same way as described in Sect. A.5.8 and Fig. A.5:

Shear force V_l	=	Max. shear force = 31 Kips
Bending moment M_l	=	1360 Kip-in

Flexural Design The flexural capacity of the section M_n was calculated neglecting the axial force and considering the welded wire fabric in the topping, approximately 0.5 in^2. Using 1#3 + WWF at the top, 1#4 at the center, and 1#3 + 1#5 at the bottom, flexural capacity is M_n = 1280 Kip-in. Since the axial load was not considered, this is a conservative value. *O.K.*

Transverse Reinforcement Design Same design adopted for Specimen 1a (Sect. 5.8), #3 U tie @ every cell, was adopted.

APPENDIX B
COMPUTER PROGRAM FOR SEQUENTIAL COLLAPSE ANALYSIS OF MASONRY SHEAR WALLS

The purpose of this Appendix is to describe the computer program SCAM, developed to analyze the nonlinear response of masonry shear walls subjected to monotonically increasing loads.

B.1 General

SCAM is a computer program developed to analyze the nonlinear response of a masonry wall subjected to an arbitrary distribution of monotonically increasing loads. The program idealizes the wall as an assemblage of line elements connected by rigid joints. The program performs an inelastic step-by-step analysis using the tangent stiffness properties of the structure. Tangent stiffnesses are calculated during each step using the force-deformation curves of the elements. The solution algorithm is based on a displacement-controlled scheme, which makes the solution process stable, even when tangent stiffnesses are zero or negative. Output information includes the force-displacement curve for the specified degree of freedom used to control the process, force-deformation curves for the end sections of each element, and the values of the force and displacement vectors at each step of the process.

The prescribed displacement history of an arbitrarily specified degree of freedom is used to control the process. The incremental displacement of this specified degree of freedom, defined as part of the prescribed displacement history, must be small enough to permit the convergence of the solution algorithm.

Any arbitrary distribution of nodal forces that includes the force corresponding to the specified degree of freedom can be used. However, the pattern of the distribution cannot be modified during the process; that is, the ratio between each force and the force on the specified degree of freedom must remain constant.

B.2 Beam-Column Element

B.2.1 Element. The computer program SCAM uses a beam-column element with constant cross-sectional area, constant effective shear area, linearly varying moment of inertia along its length, and rigid end sections parallel to the element. The element and the local and global degrees of freedom at each end node are shown in Fig. B.1.

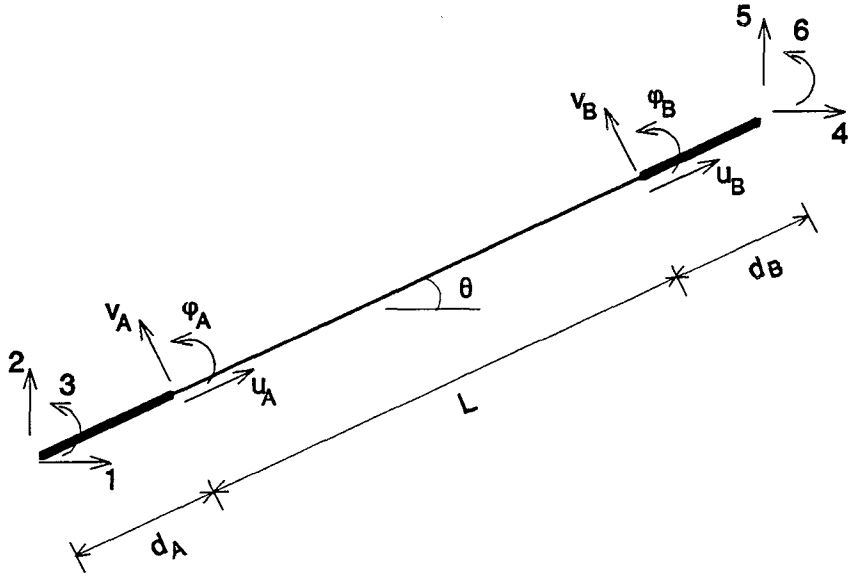

Figure B.1: SCAM beam-column element

B.2.2 Stiffness Matrix. The elemental stiffness matrix $\boldsymbol{k}$ in local coordinates is given by:

$$\boldsymbol{k} = \begin{bmatrix} \boldsymbol{k_A} & \boldsymbol{k_{AB}} \\ \boldsymbol{k_{BA}} & \boldsymbol{k_B} \end{bmatrix}$$

The elements of each submatrix are:

$$k_{A11} = k_{B11} = -k_{AB11} = -k_{BA11} = \frac{EA}{L}$$

$$k_{A22} = -k_{AB22} = -k_{BA22} = k_{B22} = \frac{C_3}{D}(\alpha - 1)^2 \ln\alpha$$

$$k_{A23} = -k_{AB32} = -k_{BA23} = k_{A32} = \frac{C_2}{D}(\alpha - 1)(\alpha - 1 - \ln\alpha)$$

$$k_{AB23} = -k_{B23} = k_{BA32} = -k_{B32} = \frac{C_2}{D}(\alpha - 1)(\alpha \ln\alpha - \alpha + 1)$$

$$k_{A33} = \frac{C_1}{D}\left[(\alpha - 2)^2 - 1 + 2\ln\alpha - \frac{\beta}{3}(\alpha - 1)^3\right]$$

$$k_{AB33} = k_{BA33} = \frac{C_1}{D}\left[\alpha^2 - 2\ln\alpha - 1 - \frac{\beta}{3}(\alpha - 1)^3\right]$$

$$k_{B33} = \frac{C_1}{D}\left[-3\alpha^2 + 4\alpha - 1 + 2\alpha^2 \ln\alpha + \frac{\beta}{3}(\alpha - 1)^3\right]$$

Where:

$$\alpha = \frac{I_A}{I_B}$$

$$\beta = \frac{12 I_A (1 + \nu)}{A_v L^2}$$

$$D = \ln\alpha\left[(\alpha + 1) + \frac{\beta}{3}(\alpha - 1)^2\right] - 2(\alpha - 1)$$

$$C_1 = \frac{EI_A}{L}$$

$$C_2 = \frac{2EI_A}{L^2}$$

$$C_3 = \frac{2EI_A}{L^3}$$

Where:

A: Cross-sectional area of element

A_v: Effective shear area of element

I_A, I_B: Cross-sectional moments of inertia at ends of the element

E, ν: Modulus of elasticity and Poisson's modulus of the material

L: Clear span of the element (excluding the rigid ends)

The elemental stiffness matrix in global coordinates K is:

$$K = L^T k L$$

Where L is the displacement transformation matrix:

$$L = \begin{bmatrix} L_A & \\ & L_B \end{bmatrix}$$

$$L_A = \begin{bmatrix} \cos\theta & \sin\theta & 0 \\ -\sin\theta & \cos\theta & d_A \\ 0 & 0 & 1 \end{bmatrix} \qquad L_B = \begin{bmatrix} \cos\theta & \sin\theta & 0 \\ -\sin\theta & \cos\theta & d_B \\ 0 & 0 & 1 \end{bmatrix}$$

Where:

d_A, d_B: Lengths of the rigid ends

θ: Inclination of the element

B.3 Solution Algorithm to Determine Incremental Displacements and Forces

The problem to be solved during each step can be stated in the following form: given the tangent stiffness matrix calculated at the end of the previous step, find an incremental displacement vector such that:

a) The vector component corresponding to the specified degree of freedom is equal to the prescribed value, and

b) The associated incremental force vector contains non-zero components only in some specified degrees of freedom.

The solution algorithm for the incremental forces and displacements for the n^{th} step is described in the following paragraphs:

a) Initial values for the step n:

$\boldsymbol{K}^{n-1}$: Tangent stiffness matrix, calculated using equivalent elastic properties for each element with the deformations obtained during the previous step.

$\boldsymbol{r}^{n-1}$: Cumulative nodal displacement vector calculated during the previous step.

$\boldsymbol{P}^{n-1}$: Cumulative nodal force vector associated with $\boldsymbol{r}$ and calculated during the previous step.

$\boldsymbol{P}'^{n-1}$: Cumulative nodal force vector that includes unbalanced forces. This vector has been calculated at the end of the previous step using the internal deformations associated with $\boldsymbol{r}^{n-1}$.

b) An arbitrary incremental displacement vector $\Delta\boldsymbol{r}$ is taken. The component Δr_j, which corresponds to the displacement increment in the specified degree of freedom j, must be equal to the prescribed displacement increment.

c) The incremental force vector $\Delta\boldsymbol{P}$ associated with $\Delta\boldsymbol{r}$ is calculated as:

$$\Delta\boldsymbol{P} = \boldsymbol{K}^{n-1}\,\Delta\boldsymbol{r}$$

Since $\Delta\boldsymbol{r}$ is probably not the solution for this step, it will be necessary to correct $\Delta\boldsymbol{P}$ to eliminate the nodal forces corresponding to all degrees of freedom except the specified ones.

d) Define a vector $\delta\boldsymbol{P}$ to correct $\Delta\boldsymbol{P}$ such that the corrected vector $\Delta\boldsymbol{P}^*$ is:

$$\Delta\boldsymbol{P}^* = \Delta\boldsymbol{P} + \delta\boldsymbol{P} = \left\{ \begin{array}{c} \textit{Forces only} \\ \textit{in specified} \\ \textit{degrees of freedom} \end{array} \right\}$$

If the unbalanced forces ($P'^{n-1} - P^{n-1}$) are included in the correction vector δP, its components will be:

$$\delta P_k = -\Delta P_k - (P'^{n-1}_k - P^{n-1}_k) \qquad \textit{for a DOF } k \textit{ with no force}$$

$$\delta P_j = \Delta P_o - (P'^{n-1}_j - P^{n-1}_j) \qquad \textit{for the specified DOF } j$$

$$\delta P_m = -\Delta P_m - (P'^{n-1}_m - P^{n-1}_m) + \alpha_m (\Delta P_j + \Delta P_o)$$

for a DOF whose force is related by α_m with the force at the specified DOF j

e) For an arbitrary value of ΔP_o:

$$\boldsymbol{\delta r} = \left[\boldsymbol{K}^{n-1}\right]^{-1} \boldsymbol{\delta P}$$

The correct solution for this step is such that δr_j is zero, i.e, the incremental displacement of the specified degree of freedom is maintained constant and equal to the prescribed value.

f) If δr_j is different from zero, take a new value for ΔP_o and repeat steps from (d) to (f) until the process converges.

If δr_j is close enough to zero to satisfy a given tolerance criterion, calculate cumulative displacement and force vectors for the step $n+1$:

$$\boldsymbol{r}^n = \boldsymbol{r}^{n-1} + \Delta \boldsymbol{r}^* = \boldsymbol{r}^{n-1} + \Delta \boldsymbol{r} + \boldsymbol{\delta r}$$

$$\boldsymbol{P}^n = \boldsymbol{P}^{n-1} + \Delta \boldsymbol{P}^* = \boldsymbol{P}^{n-1} + \Delta \boldsymbol{P} + \boldsymbol{\delta P}$$

B.4 Internal Forces and Deformations

The cumulative displacement and force vectors, calculated at the end of the process described in the previous Section, have been calculated with the tangent stiffness properties determined at the end of the previous step. Because of the nonlinear behavior of the elements, it is necessary to check for unbalanced forces resulting from changes in stiffness during the step. To do this, deformations of the elements are calculated at the end of the step, and by using force-deformation relationships, internal forces are calculated for each element. Nodal forces are then re-calculated using the internal forces. The calculation of deformations and internal forces is described in this Section.

Deformations of the elements of the structure can be calculated from the cumulative nodal displacement vector $\boldsymbol{r}^n$. Since the calculation of the axial deformations and forces is a straightforward process, the discussion of this Section will be centered on flexural and shear deformations. Since for this program the flexural force-deformation characteristics of the elements are given in the form of moment-curvature relationships for the sections,

it is necessary to determine the distribution of curvatures in terms of the given nodal displacements.

B.4.1 State of Deformations at a Section. Since the object of this study, masonry walls, are usually squat elements, shear deformations are an important contributing part to the total deformations of the wall. In this section, the contribution of shear deformations in a beam-column element is analyzed.

Fig. B.2 shows the shear deformations at a beam-column element of length L subjected to pure shear forces. θ is the rotation of the element axis, and Δ_v is the relative deflection between the ends of the element.

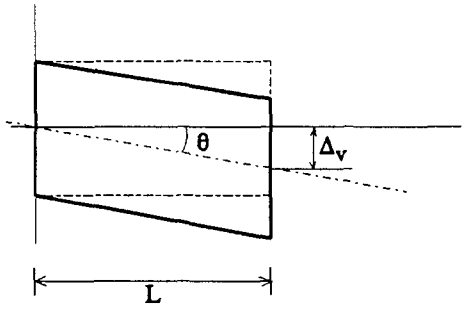

Figure B.2: Shear deformations

Fig. B.3 shows the state of deformations at a section at a position x along the axis of a beam subjected to bending moment and shear force simultaneously. v is the total deflection of section in direction perpendicular to its axis, φ is the flexural rotation of the section, and θ is the shear rotation of the axis of the beam.

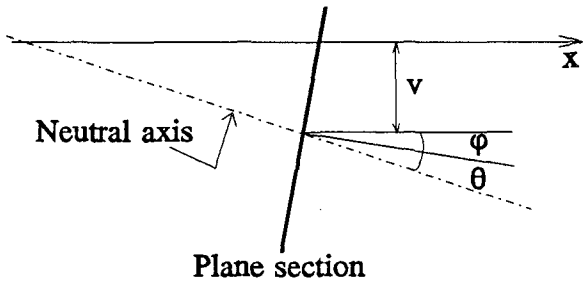

Figure B.3: Deformations at a section

It is usually assumed in beam theory that the plane sections remain normal to the neutral axis, that is, the shear deformations are negligible. However, as seen in Fig. B.3, if shear deformations are important, this assumption is no longer valid, and the slope $\partial v/\partial x$ of the neutral axis is given by:

$$\frac{\partial v}{\partial x} = \varphi + \theta$$

B.4.2 Element Deformations in Terms of Nodal Displacements. Given the total nodal displacements v_A and v_B, and the flexural nodal rotations φ_A and φ_B, it is usually assumed that the rotation at a section is equal to the slope of the neutral axis there. Deflections along the span of the element can be interpolated in terms of the nodal displacements using a third-order polynomial function in x. The variation of curvature in the span, given by the second derivative of the deflection function, is therefore linear. This is the exact solution for an elastic structure subjected to loads only at the nodes, producing linear variation of moments along the elements, and with negligible shear deformations.

However, as previously discussed, when shear deformations become important, the flexural rotations differ from the slope of the neutral axis. By imposing this condition, the process outlined above can still be used to calculate the end curvature of the elements as:

$$\phi_A = 2\left[\frac{3(v_B - v_A - \Delta_v)}{L^2} - \frac{(\varphi_B + 2\varphi_A)}{L}\right]$$

$$\phi_B = 2\left[-\frac{3(v_B - v_A - \Delta_v)}{L^2} + \frac{(\varphi_A + 2\varphi_B)}{L}\right]$$

Where:

ϕ_A, ϕ_B: Curvatures at the A and B ends respectively

Δ_v: Total shear deflection between the ends of the element

B.4.3 Calculation of Elemental Deformations and Internal Forces. As previously discussed, to determine the end curvatures of the element it is necessary to know the shear deformation in advance, which can be easily calculated if the shear force and shear force-shear deformation relationships are available. Since the final objective of this step is to calculate internal forces, the shear force is still unknown and the calculation of the curvatures is not a straightforward process. The problem can be solved by successive iterations for each element, according to the following steps:

a) An arbitrary value of the shear deformation Δ_v is assumed. The associated shear force is calculated using the corresponding relationships between shear force and shear deformations.

b) End curvatures are calculated using the given value of the shear deformation.

c) End moments are calculated using the end curvatures and the moment-curvature relationships.

d) The shear force is re-calculated by equilibrium in the element.

e) Shear forces calculated in steps (a) and (d) are compared. If the difference is small enough to satisfy a given tolerance criterion, the assumed value for the shear deformation was the correct solution. If the difference is important, the process must be repeated using a different value for the shear deformation.

The deformations and internal forces calculated during the last step of the iteration process are the solution of the problem.

B.5 Unbalanced Forces

Using the internal forces determined as described in the previous Section, the nodal force vector at the end of the step n can be re-calculated as P'^{n}. The unbalanced force vector is the difference between this vector and the cumulative force vector P^{n}, calculated using the tangent stiffness matrix at the beginning of the step. The unbalanced force vector is carried on to the next step and eliminated as described in Section B.3.

B.6 Organization of SCAM

Each step of the above process is performed by one or more subroutines. The general organization of the computer program SCA is shown schematically in the flow chart of Fig. B.4, and is described in this Section.

B.6.1 Reading of Input Data. Input data are read in the Main Program and in the subroutines INDAT and INLOAD. Data include:

a) General data

b) Structure model data: Joint coordinates; supports conditions; element properties, including initial elastic element properties

c) Force deformation characteristics of the elements, including moment-curvature and axial force-deformation curves

d) Initial static load conditions

A complete description of the input is given in Section B.7.

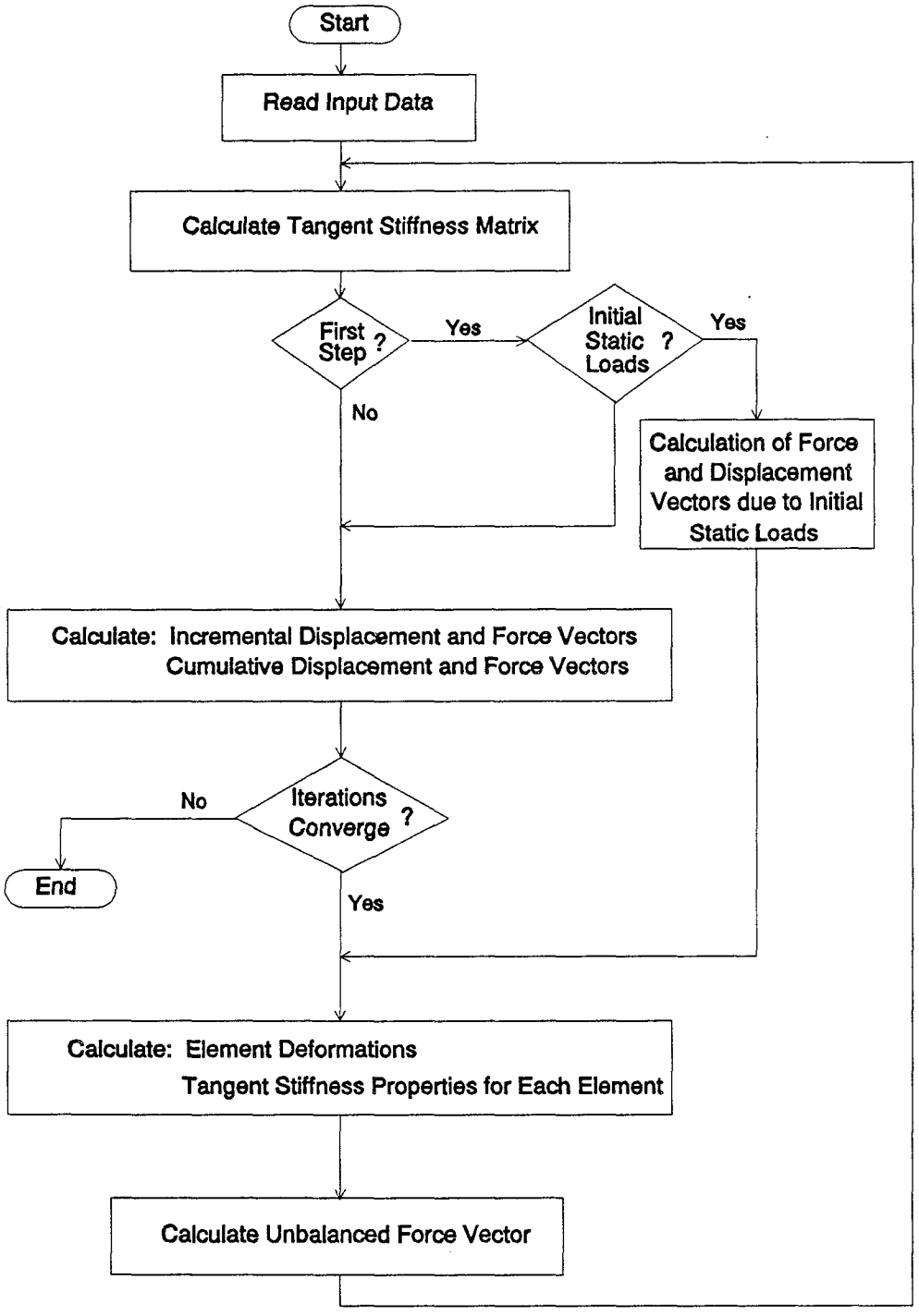

Figure B.4: Flow Chart of Computer Program SCAM

B.6.2 Computation of Tangent Stiffness Matrix. The general organization of the calculation of the tangent stiffness matrix is shown in Fig. B.5.

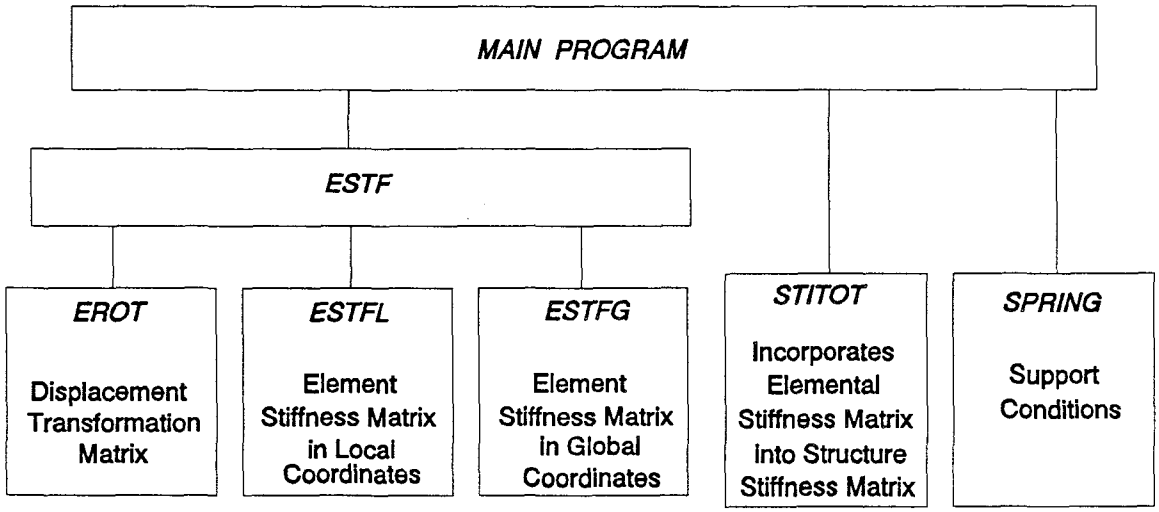

Figure B.5: Organization of tangent stiffness matrix calculations

Elastic initial properties from the data input are used to calculate the tangent stiffness matrix during the first step. Equivalent elastic stiffness properties calculated using the elements' force-deformation curves are used in the next steps. The following is a description of each subroutine.

EROT: Calculates the displacement transformation matrix RLA and RLB, as described in Section B.2.2.

ESTFL: Calculates the element tangent stiffness matrix in local coordinates KLA, KLB, KLAB, and KLBA, as described in Section B.2.2.

ESTFG: Calculates the element tangent stiffness matrix in global coordinates K, as described in Section B.2.2.

STITOT: Incorporates the element stiffness matrix into the structure tangent stiffness matrix KTOT, stored in banded form.

SPRING: Incorporates support conditions to KATOT. Spring constant values are added to the elements of the main diagonal of KATOT corresponding to DOF with elastic support conditions. Large value of the spring constant is used for rigid supports.

B.6.3 Computation of Initial Displacements. Nodal displacement and force vectors associated with an initial static arbitrary distribution of loads are calculated. This step, performed only once at the beginning of the loading process using the elastic initial properties of the structure, involves the following subroutines:

INLD: Reads input data for loads and incorporates nodal loads PX, PY, and M into the cumulative force vector PTOT.

SYMSOL: Calculates the cumulative displacement vector DTOT associated with the static initial loads.

B.6.4 Computation of Incremental Displacement and Force Vectors. The incremental nodal displacement and force vectors for each step are calculated by the subroutine INCR, according to the solution algorithm described in Section B.3:

a) The initial incremental displacement vector DD is taken equal to the DD obtained in the previous step times a factor FACT, equal to 1 for the first iteration step.

b) The incremental displacement at the specified degree of freedom DD(NSPDOF) is set equal to the specified increment SPDIS.

c) The force vector DP associated with DD is calculated as DP = (KTOT)(DD).

d) The correction vector DP1, needed to eliminate forces corresponding to degrees of freedom other than the specified ones in DP, is calculated. DP1(NSPDOF) = DP0, an arbitrary value. Unbalanced forces (PTOT1 - PTOT) are added to DP1.

e) The displacement vector DD1 associated with DP1 is calculated using the subroutine SYMSOL.

f) If DD1(NSPDOF) is small enough compared SPDIS to satisfy a given tolerance criterion, the process converged and:
DD = DD + DD1
DP = DP + DP1
DTOT = DTOT + DD
PTOT = PTOT1 + DP

g) If DD1(NSPDOF) is not small compared with SPDIS, a new value od DP0 is calculated using the bi-section iteration method and steps (d) to (g) are repeated.

h) If the number of iterations is larger than an upper limit, the process starts again from step (a) using a smaller value of FACT.

i) If FACT is smaller than a lower limit, the process is stopped.

B.6.5 Computation of Element Deformations and Tangent Stiffness. Flexural, shear and axial deformations at the ends of each element, and equivalent tangent stiffness properties to use in the next step, are calculated by the subroutine FODE, using the cumulative nodal displacement vector DTOT, as described in Section B.4.3:

a) An initial value is assumed for the element shear force SHFRC.

b) Given the cumulative displacement vector DTOT, the element displacement vector in local coordinates DELOC is calculated using the subroutine EROT to determine the transformation of coordinates matrix RL.

c) The axial deformation AXDEF is calculated, and using the subroutine AXFD, the axial force AXFRC is calculated.

d) Knowing the axial force AXFRC, the subroutine MC1 determines the moment-curvature curves to use for this element.

e) Using the assumed value for the shear force SHFRC, the shear deformation SHDEF is calculated using the subroutine SHFD.

f) End curvatures PHI1 and PHI2 are calculated considering corrections by shear deformation, as described in Section B.4.2.

g) End moments M1 and M2 are calculated by subroutine MC2.

h) Shear force is recalculated by equilibrium using M1 and M2.

i) Steps (e) to (h) are repeated until the error in the calculation of the shear force is small enough to satisfy a given tolerance criterion. Bi-section method is used to determine the new value of SHFRC to start the new iteration.

j) If iterations do not converge to a solution, the process goes back to the calculation of a new incremental displacement vector DD (Section B.6.4) using a smaller increment of the specified DOF displacement SPDIS.

k) If the iterations converge to a solution, the equivalent tangent stiffness properties are calculated by the subroutine FLSTF.

A description of some of the subroutines involved in this process is given in the following paragraphs.

AXFD: For a given value of the axial strain AXDEF, this subroutine calculates the axial force AXFRC and the equivalent cross-section area A. The axial force-axial strain curve used by this subroutine is shown in Fig. B.6.

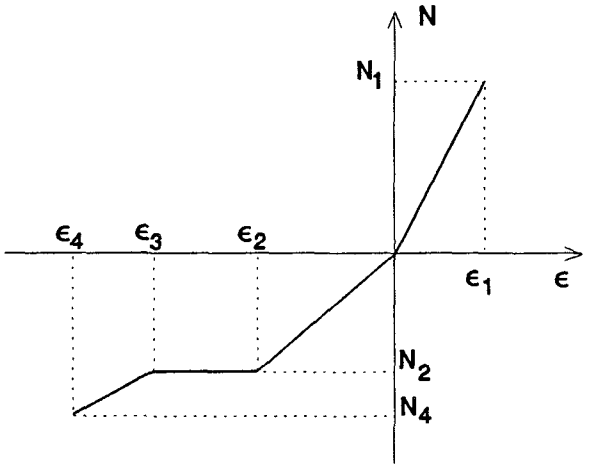

Figure B.6: Axial force-deformation curve used in subroutine AXFD.

This curve was chosen to represent the behavior of reinforced concrete and masonry elements under axial loads. Under compressive forces, the behavior is approximately linear up to an stress of about 70% of f'_c or f'_m. Since it is not usual to find such a high stresses in real elements under pure axial loads, it seems reasonable to use that point as N_1-ϵ_1. Under tensile forces, it can be assumed the behavior is fully governed by the reinforcement. Thus, ϵ_2 corresponds to ϵ_y, ϵ_3 to ϵ_{sh}, and ϵ_4 to ϵ_u, and the N forces are those associated with the yielding and ultimate capacity of the reinforcement.

Assuming the modulus of elasticity remains constant, the axial tangent stiffness is represented by the equivalent cross-section area A, which in terms of the slope of the force-deformation curve at any particular point is:

$$A = \frac{1}{E}\left(\frac{\Delta N}{\Delta \epsilon}\right)$$

SHFD: The inelastic effects on the shear force-deformation relationship have been included by using an equivalent effective shear area AV in the usual elastic expression for the shear force-shear deformation relationship. This effective area has been assumed to be proportional to the neutral axis depth CNU of the section:

$$SHDEF = \frac{SHFRC * L}{G * AV}$$

$$AV = CNU * TW$$

Where G is the shear modulus of the material and TW is the web thickness.

FLSTF: This subroutine calculates the tangent flexural stiffnesses at the ends of an element. Given a set of moment-curvature curves for each section and the axial load acting on that section, the subroutine interpolates between the two curves with the closest axial loads to find the slope at a given curvature level. Fig. B.7 shows a typical set of moment-curvature curves used by this subroutine.

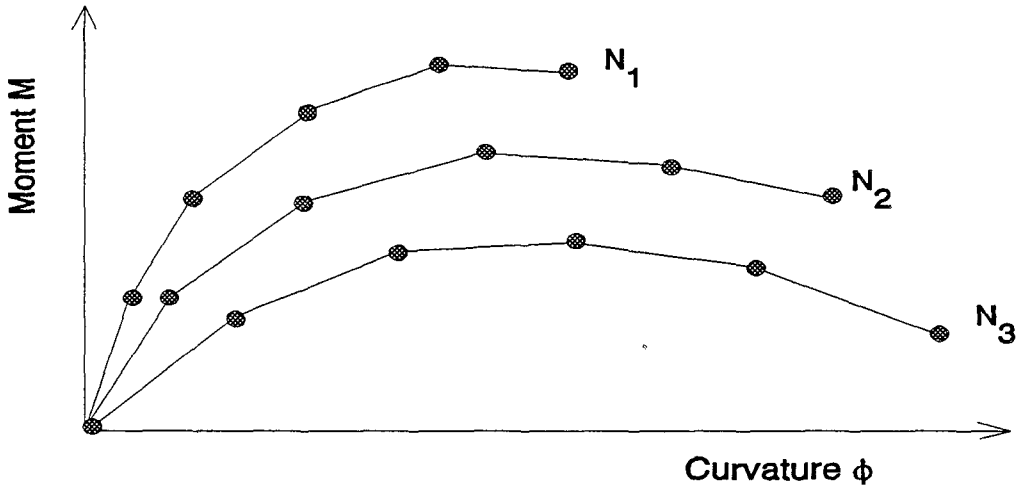

Figure B.7: Typical moment-curvature curves used in subroutine FLSTF

Assuming that the modulus of elasticity remains constant during the process, the equivalent moment of inertia I for each end of the element is calculated in terms of the slope of the moment-curvature curve:

$$I = \frac{1}{E}\left(\frac{\Delta M}{\Delta \phi}\right)$$

B.6.6 Computation of Unbalanced Forces. Using the internal forces for each element, the cumulative force vector is calculated as PTOT1 by the subroutine ASSG with the usual techniques in structural analysis. The unbalanced forces determined from the difference between PTOT1 and PTOT are eliminated by correcting the incremental displacement vector during the next step.

B.6.7 Printing of Results. Results for each step are printed at the end of the step by subroutine PPRINT. Load-displacement histories are printed at the end of the process by subroutine PPRINT2.

B.7 Input for Program SCAM

Numerical input data are supplied in free format. Within each line, data are separated by spaces or by commas. Alpha numeric data must be entered in the specified format.

1) Title: One line

TITLE (A72): Name of the problem

2) Control Information and General Data: One line containing 11 data

NJ: Number of nodes

NE: Number of elements

NSP: Number of nodes with some displacement restrain (supports)

NHEL: Number of elements with initial hinges at one or two ends

NSEC: Number of different types of flexural sections.
This indicates the number of sets of moment-curvature curves. If the same unsymmetrical section will be subjected to moments of different sign in different zones of the structure, it must be entered as two different sections.

NAXSEC: Number of different types of axial sections.

NCODL: Initial load control code
0: No initial loads
1: Initial loads

NSPDOF: Specified Degree of Freedom whose displacement history will control the process.

SPDIS1: Displacement increment for the specified DOF

NPREL: Number of the degrees of freedom, in addition to the specified one, that will be subjected to external loads

NRSPD: Number of regions in the displacement history of the specified DOF with different factors amplifying SPDIS1 (Refer to Fig. B.8)

3) Output Control Information: One line containing 6 data. Each data is a code indicating whether a part of the output will be printed or not.
For each code: 0: No printing of output
1: Print output

NCDGEN: General data input echo

NCDJE: Element property input echo

NCDMC: Force-deformation input echo

NCD1: Incremental displacement and force vectors

NCD2: Cumulative displacement and force vectors

NCD3: Element forces and deformations

4) Moment-Curvature Curves: General Data: NSEC + 1 lines

4.1) One Line:

NPTMAX: Number of points of each moment-curvature curve. This is a unique number for all curves

4.2) NSEC Lines: Each line contains 2 values:

Integer: Number identifying section type, less than or equal to NSEC

NCURV: Number of moment-curvature curves for this type of section

5) Node Coordinates: NJ lines, each containing 2 values. Node coordinates must be entered in sequence, starting from the first node

X: X coordinate

Y: Y coordinate

6) Support Conditions: NSP lines, each containing 4 values.

NJOSP: Number of the node with some displacement restrain

KX: Spring constant in X-direction. If totally restrained, use 1.E15

KY: Spring constant in Y-direction. If totally restrained, use 1.E15

KG: Rotational spring constant. If totally restrained, use 1.E15

7) Element Properties: NE lines, each containing 13 values

N1: Node number at end A

N2: Node number at end B

A: Cross-sectional area

AV: Cross-sectional effective shear area

I: Cross-sectional moment of inertia

TW: Web thickness

E: Modulus of elasticity

SNU: Poisson's modulus

D1: Rigid portion length end A

D2: Rigid portion length end B

NSCOD: Type of flexural section

NSAXCOD: Type of axial section

NELCOD: Code indicating inelastic action of the element:
- 0: Element remains elastic with the initial properties unchanged. No force-deformations output will be available for this element
- 1: Element will behave inelastically and its stiffness properties will be modified during the process

8) Hinged Elements: NHEL lines, each containing 2 values. Omit if NHEL = 0

NJHEL: Number of the hinged element

NJOHEL: Code indicating hinging condition:
- 1: Hinge at initial end
- 2: Hinge at final end
- 3: Hinges at both ends

9) Specified DOF Displacement History: NRSPD lines, each containing 2 values. Refer to Fig. B.8. Omit if NRSPD = 1

FACSPD: Factor that amplifies SPDIS1

LIMSPD: Upper limit of the specified DOF displacement for which FACSPD is valid

10) Incremental Load Distribution: NPREL lines, each containing 2 values. Omit if NPREL = 1

NNPREL: Number of the loaded DOF

PREL: Ratio between load in NNPREL DOF and load in the specified DOF

11) Moment-Curvature Data: -NSECx[2 + NCURVx(NPTMAX + 1)] total lines
-Steps (11.1) to (11.3) must be repeated for each section, making a total of [2 + NCURVx(NPTMAX + 1)] lines for each section
-Data must be input in sequential order, starting from the first section
-Refer to Fig. B.9 for an example

11.1) One Line:

TITL (A72): Name of the section type

11.2) One Line:

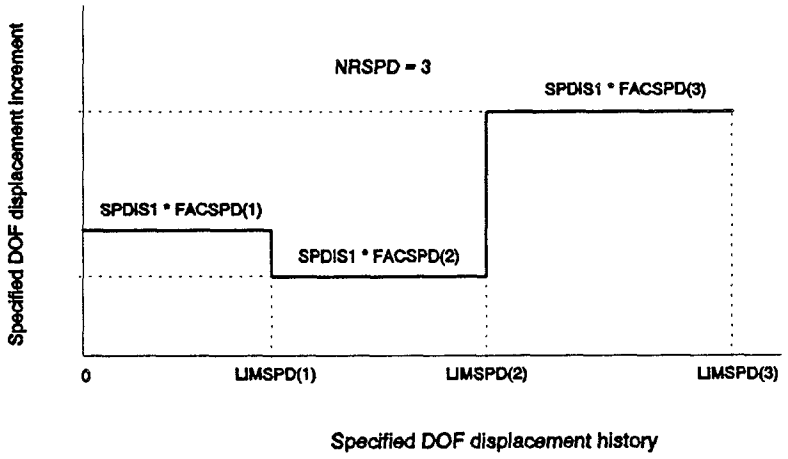

Figure B.8: Example of specified DOF displacement history.

Integer: Number of the section type

11.3) NCURVx(NPTMAX + 1) Lines: -Steps (11.3.1) to (11.3.2) must be repeated NCURV times for each section

11.3.1) One Line:

LOAD: -Axial load for the particular moment-curvature curve
-Compressive force is positive
-Curves must be input in sequential order, starting from the highest axial load

11.3.2) NPTMAX Lines: -Each line contains a moment-curvature point and the corresponding value of the neutral axis depth
-Points within each curve must be input in sequence, starting from the lowest curvature value

MOMPT: Moment

PHIPT: Curvature

CNUPT: Neutral axis depth

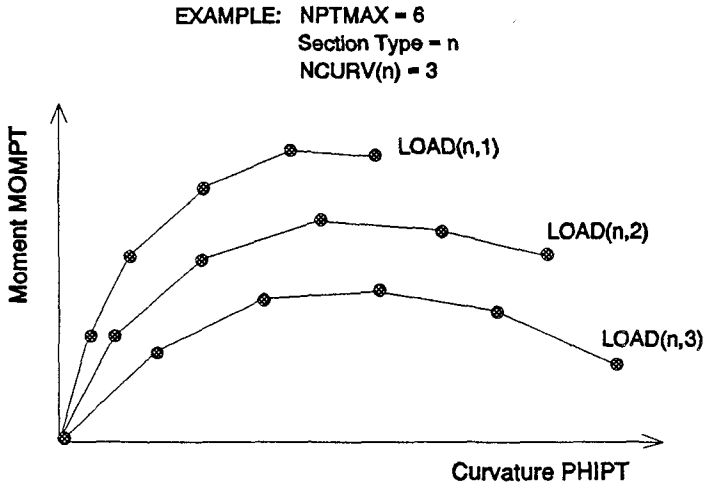

Figure B.9: Example of moment-curvature data

12) Axial Force-Deformation Data: -NAXSECx6 lines
-Steps (12.1) to (12.3) must be repeated for each section, making a total of 6 lines for each section
-Data must be input in sequential order, starting from the first section
-Refer to Fig. B.10

12.1) One Line:

TITL (A72): Name of the section type

12.2) One Line:

Integer: Number of the section type

12.3) Four Lines: -Each line contains 2 values corresponding to one point of the axial force-deformation curve (refer to Fig. B.9)

AXDPT: Axial deformation (in/in), tension is positive

AXFPT: Axial force, tension is positive

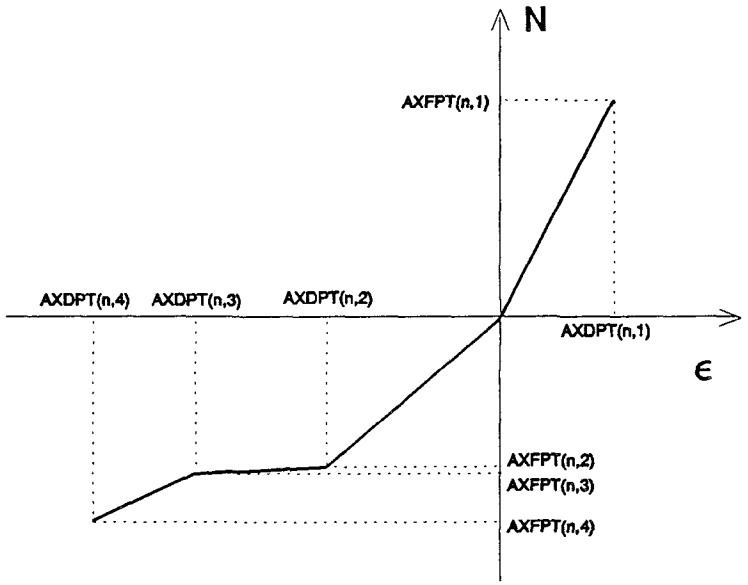

Figure B.10: Axial force-deformation input

APPENDIX C
SHEAR STRENGTH MODEL FOR MASONRY WALLS

C.1 General

To analyze the behavior of the specimens tested as part of this work, a model was needed to represent the shear capacity of masonry walls and piers. As mentioned in Chapter 2, there has been extensive discussion on how to evaluate shear capacity of masonry elements. Several expressions for calculating shear capacity of masonry walls have been proposed recently [1,7,8,10,20,22]. Most are empirical, and include in different ways, some or all the aspects influencing shear strength of masonry walls.

To illustrate the differences among the results obtained, the shear capacity of a typical pier of the Type 1 specimens was evaluated using the different existing expressions [1,10,20], and compared with the 1988 UBC [19] strength design recommendations for masonry walls. The pier was analyzed assuming an M/Vd ratio of 0.46 (contra flexure point at mid-height), axial stress of 300 psi, and using #3 jamb bars as longitudinal reinforcement. Since this analysis was performed in advance of the tests of the specimens, assumed material properties were used: f'_m = 2000 psi; and f_y = 72 ksi. The results are shown in Fig. C.1 for different values of the transverse reinforcement ratio. Minimum values of all curves correspond to the minimum transverse reinforcement ratio of 0.07%, as prescribed by the 1988 UBC [19] for fully reinforced walls. The dot in each curve indicates the maximum transverse reinforcement ratio found in the experimental work on which the analytical model was based on.

As shown in Fig. C.1, significant differences exist among the results of the different models to compute the shear strength of the pier, especially for high values of the transverse reinforcement ratio.

To select an appropriate analytical model for the piers of the Type 1 specimens, the different existing models were evaluated using the results of tests performed on pier specimens similar to those of the Type 1 specimens. Ratios of predicted shear strength to measured shear strength were calculated for each model. At the time those analyses were performed, the shear strength models of Matsumura [10], Blondet et al. [20], and Hidalgo and Lüders [7] were available. Results, given in Ref. [38], showed that the model proposed by Blondet et al. had the best agreement with the experimental results. As described in Appendix A, piers of Type 1 specimens were designed using that model.

However, it was believed by this author that further analyses were needed to improve that model and/or propose a new one to predict shear capacity of masonry walls. A first step was to analyze the degree of agreement of the existing models with available experimental results. Based on the obtained conclusions, a new model is proposed here. Finally, results obtained with the new model are compared with experimental data.

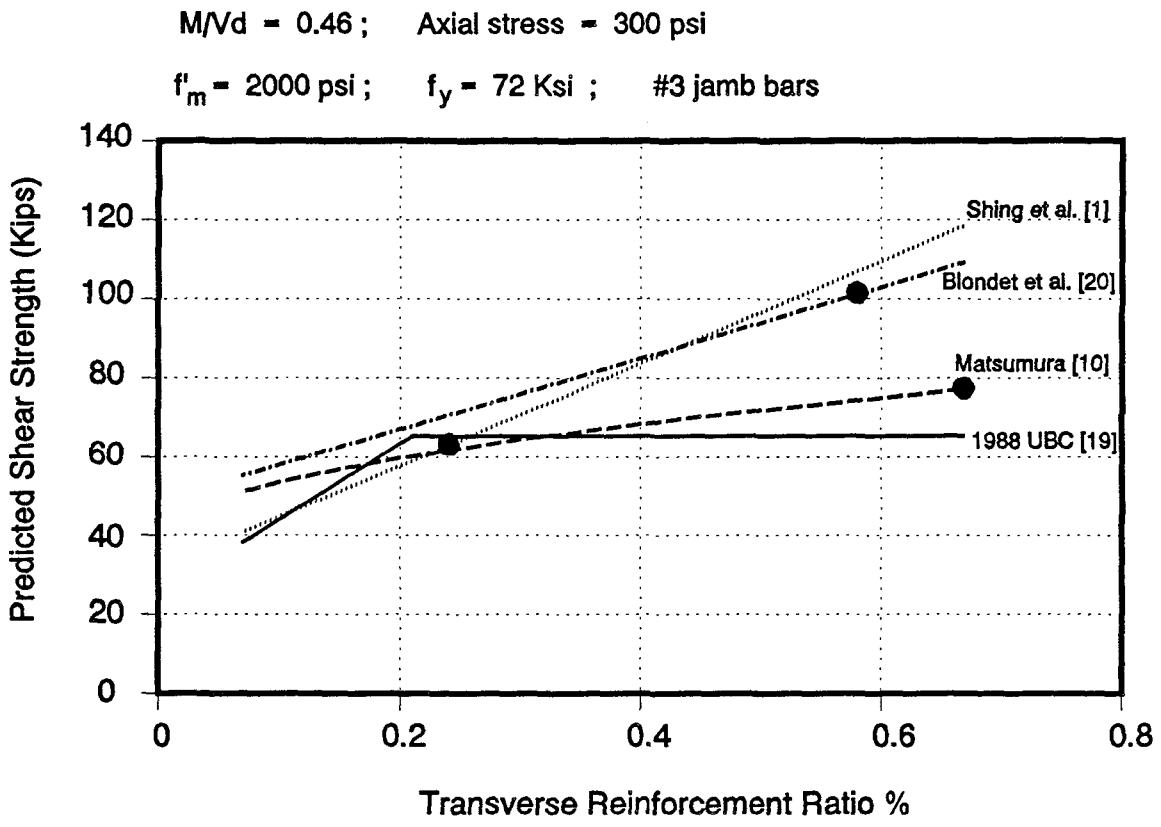

Figure C.1: Predicted shear strength of Type 1 Specimen pier.

Experimental data selected for this study included only results from tests on fully grouted concrete masonry walls, with enough transverse reinforcement to prevent a brittle shear failure; that is, their ultimate shear capacity was larger than diagonal cracking strength. In all cases, transverse reinforcement had 180-degree hooks around extreme longitudinal reinforcement. Of each set of results, only those walls showing a shear mode of failure were considered. Data were taken from tests performed at The University of California, Berkeley [12], in Japan by Matsumura [10], and at The University of Colorado by Shing [4]. Additional tests results obtained at Berkeley [43,44] were not considered because they did not satisfy the conditions previously mentioned. Detailed descriptions of the specimens and test results are given in the references above, and are not be repeated here. Test results and calculations are summarized at the end of this Appendix.

C.2 Analysis of Existing Models

Experimental results were compared with predicted values obtained with some of the existing models. Results are discussed with emphasis on each one of the factors governing the shear capacity of masonry walls.

Models studied included the 1988 UBC [19] provisions for strength design of masonry walls, the model proposed by Blondet et al. [20], the model of Matsumura [9], and the model proposed by Shing et al. [1]. All the models, described at the end of this Appendix, use the approach of representing the shear strength after diagonal cracking V_n as the summation of the residual strength of the masonry V_m plus the contribution of the transverse steel V_s.

$$V_n = V_m + V_s \tag{C.1}$$

To compare the degree of agreement of each model with the experimental results, ratios of the predicted shear strength to the measured shear strength were calculated. Plots of the strength ratios versus the transverse reinforcement ratio, defined as the ratio of the total transverse reinforcement area to the vertical cross-section area, are shown in Figs. C.2 through C.5. In those figures, the mean value and the 90% and 10% fractile values are indicated by dashed lines. Statistical results of those calculations are given in Table C.1.

Table C.1 Statistical summaries of ratios of predicted shear strength to measured shear strength

Model	Mean value	Coefficient of Variation %	Maximum	Minimum
1988 UBC [19]	0.70	15.7	0.97	0.41
Blondet et al. [20]	0.85	10.3	1.04	0.65
Matsumura [9]	1.02	10.2	1.21	0.84
Shing et al. [1]	0.90	13.4	1.09	0.62

Based on the discussion of the shear strength mechanism of reinforced masonry walls given in Section 2.3.2, the results of the strength ratio calculations will be analyzed in the following sections.

C.2.1 Transverse Reinforcement Contribution to Shear Strength. As discussed in Section 2.3.2, shear strength V_s is provided by the tensile capacity of the horizontal steel crossing the diagonal crack (Fig. 2.8). The effectiveness of the transverse reinforcement in resisting shear forces can be expressed in terms of the ratio between the V_s actually developed and the total shear capacity if all the bars crossing the diagonal crack were able to reach the yielding point.

The 1988 UBC [19] expression for V_s [19] is based on the assumption that all the transverse reinforcement crossing a 45-degree diagonal crack will eventually yield, as in the case of reinforced concrete elements. As seen in Fig C.2, the ratios of predicted strength

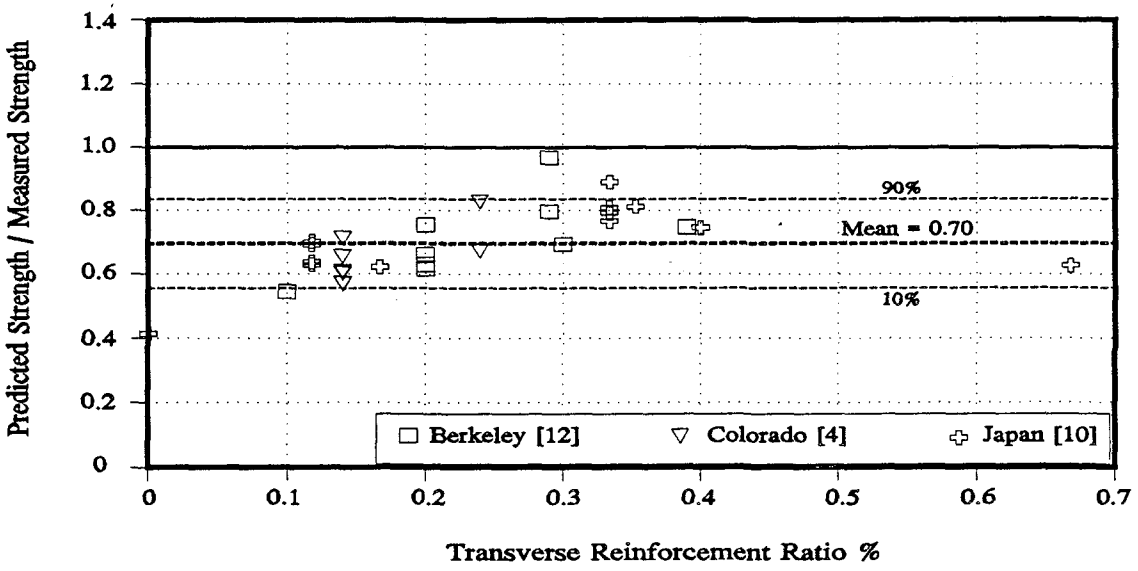

Figure C.2: Ratios of predicted shear strength to measured strength. 1988 UBC [19] strength design equations for masonry walls.

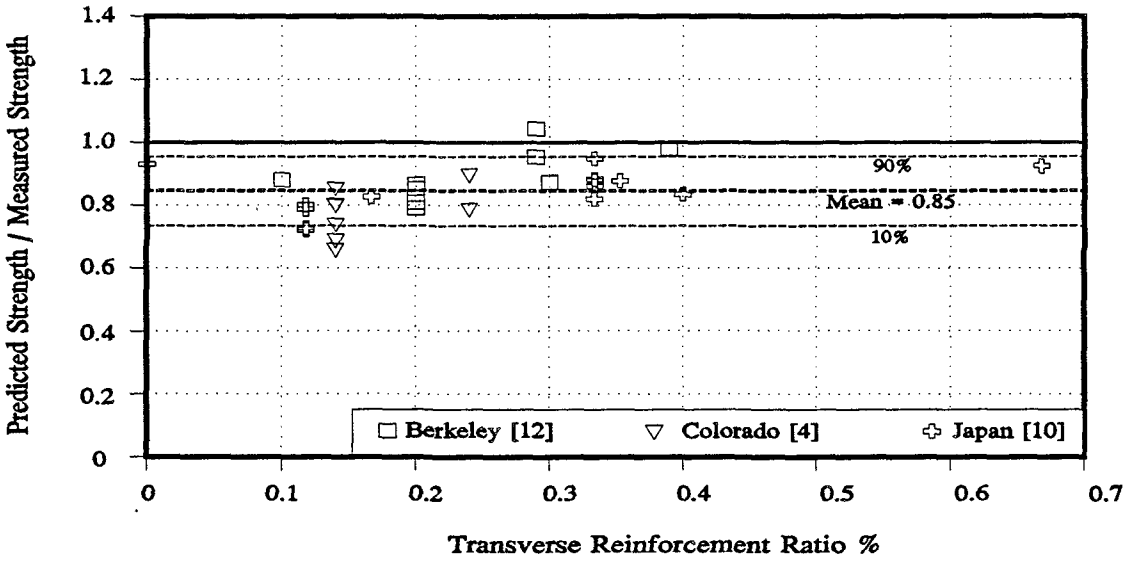

Figure C.3: Ratios of predicted shear strength to measured strength for model of Blondet et al. [20].

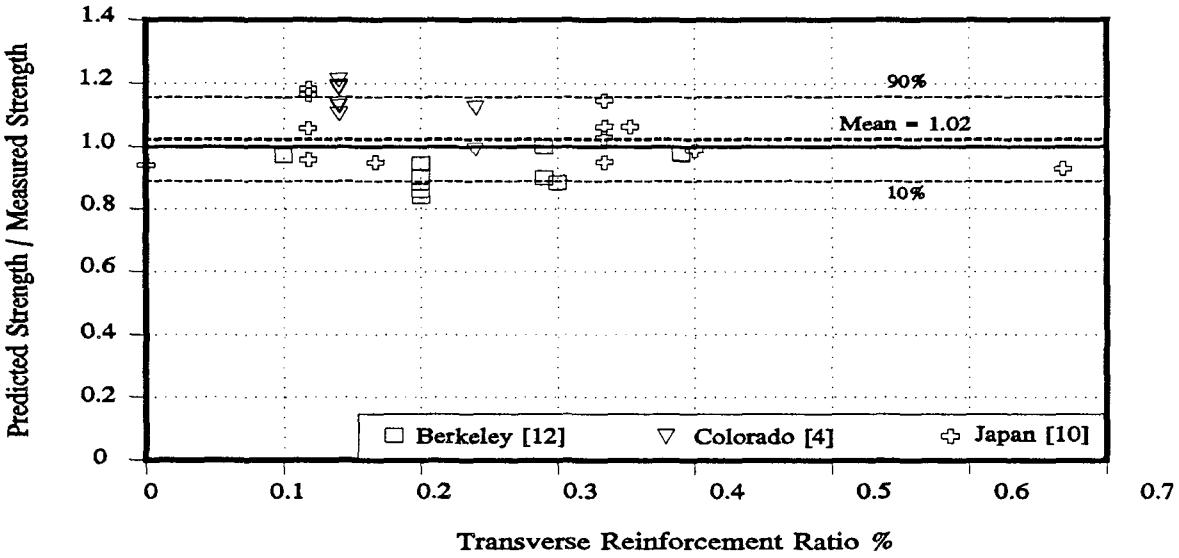

Figure C.4: Ratios of predicted shear strength to measured shear strength for model of Matsumura [9].

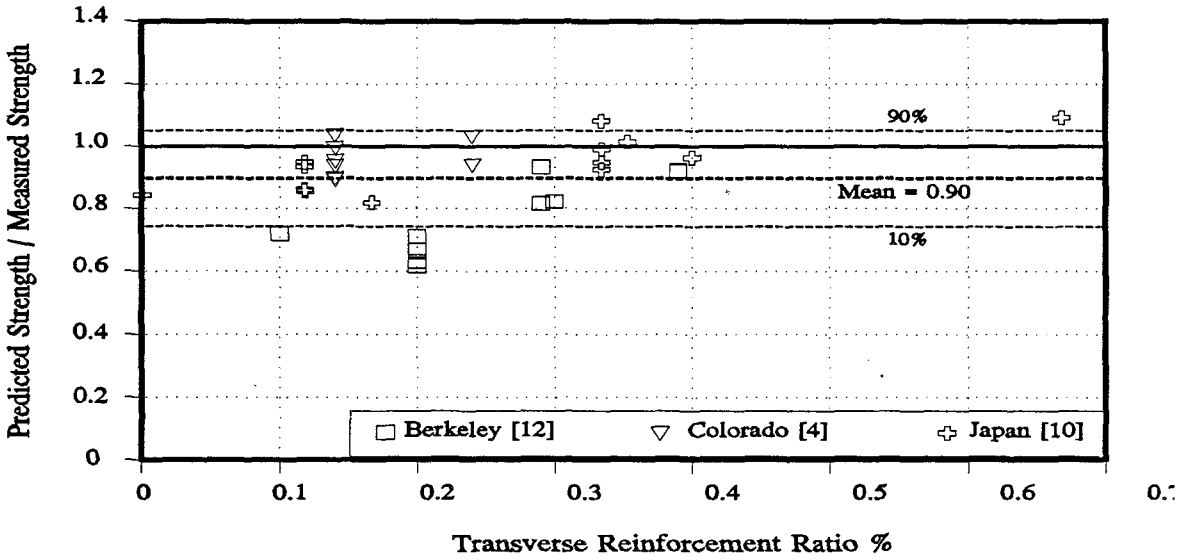

Figure C.5: Ratios of predicted shear strength to measured shear strength for model of Shing et al. [1].

to measured strength calculated using the 1988 UBC recommendations, tend to increase as the transverse reinforcement ratio increases. These results suggest that the contribution of the transverse reinforcement to the shear strength of reinforced masonry walls is overestimated by those recommendations. Because 1988 UBC limits the maximum available shear strength, the recommendations seem to be conservative for large values of the transverse reinforcement ratio.

Blondet et al. [20] assumed that the transverse reinforcement effectiveness is a constant equal to 50%. As seen in Fig C.3, the ratios of predicted strength to measured strength are more uniformly distributed with respect to the transverse reinforcement ratio than in the previous case. However, the strength ratios still tend to increase for higher values of the transverse reinforcement ratio, which suggests that contribution of steel is overestimated in that range.

Matsumura [9] assumed that the contribution of the transverse steel is proportional to the square root of the transverse reinforcement ratio. The transverse reinforcement effectiveness ratios for all the walls of this study, calculated with this model, are shown in Fig. C.6. From that figure, it is clear that Matsumura's model lacks an upper limit for the steel contribution at the range of low transverse reinforcement ratios, as the effectiveness ratios become larger than one. This conclusion is verified by examining Fig. C.4. Strength ratios tend to be larger for low ratios of transverse reinforcement, which confirms that this model overestimates the steel contribution to the shear strength in that range.

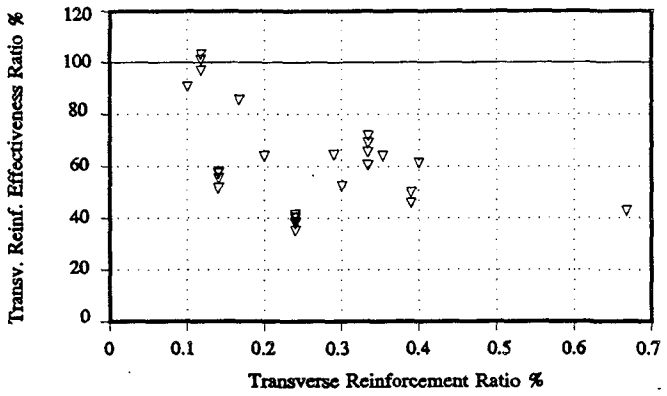

Figure C.6: Effectiveness of transverse reinforcement, model of Matsumura.

Shing et al. [1] assumed that the steel contribution effectiveness decreases as the spacing s between transverse bars is increased. As the transverse reinforcement ratio usually increases as s decreases, the effectiveness ratio of the transverse reinforcement becomes larger for higher reinforcement ratios. As shown in Fig. C.7, the effectiveness ratio is practically constant at approximately 70% for transverse reinforcement ratios larger than 2%. As shown in Fig. C.5, strength ratios tend to increase with transverse reinforcement ratio.

C.2.2 Masonry Contribution to Shear Strength. As described in Section 2.3.2, the masonry contribution V_m to the shear strength is the residual masonry shear strength after diagonal cracking. V_m is provided by shear transfer at the compression toe of the wall, by aggregate interlock between the faces of the diagonal crack, and by dowel action of the

longitudinal reinforcement crossing the diagonal crack. The following parameters affecting V_m have been identified: the compressive strength of the masonry f'_m; the aspect ratio of the wall, usually represented by the M/Vd ratio; the axial stress level f_a; and the longitudinal reinforcement ratio ρ_v. The existing models consider the contribution of some or all of these parameters, usually in a semi-empirical way.

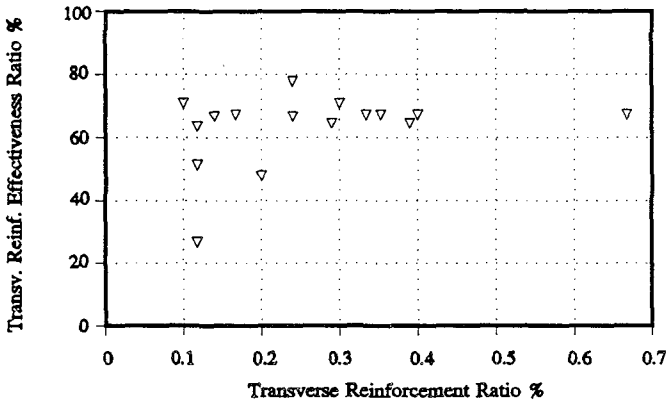

Figure C.7: Effectiveness of transverse reinforcement, model of Shing et al.

C.3 Proposed Shear Strength Model for Reinforced Concrete Masonry Walls

Based on the discussions regarding the shear strength mechanism given in Section 2.3.2, and on the analysis of the existing models, a new shear strength model for masonry walls has been proposed. The new model uses the conventional approach of representing the shear strength after diagonal cracking V_n as the summation of the residual strength of the masonry V_m plus the contribution of the transverse steel V_s.

C.3.1 Transverse Reinforcement Contribution to Shear Strength. From the analysis of the existing models, it was concluded that if a minimum ratio of transverse reinforcement is provided and a maximum spacing between transverse rebars is maintained, the effectiveness of the transverse steel can be assumed constant, with a value of 0.5 or less.

The contribution of the transverse reinforcement V_s to the shear strength can be expressed as:

$$V_s = \alpha \frac{A_h}{ht} td f_y = \alpha \rho_h td f_y \qquad \text{(C.2)}$$

Where:

α	=	Transverse reinforcement effectiveness ratio
A_h	=	Total transverse reinforcement area
t	=	Wall thickness
h	=	Wall height
d	=	Effective depth of wall cross-section
f_y	=	Yielding strength of transverse reinforcement
ρ_h	=	A_h/th = Transverse reinforcement ratio

To determine an appropriate value of α, the expression of the shear strength of the masonry wall can be conveniently written as:

$$\frac{v_n}{f_y} = \frac{v_m}{f_y} + \alpha \rho_h \qquad \text{(C.3)}$$

Where:

$v_n = V_n/td$ = Average shear strength

$v_m = V_m/td$ = Average masonry contribution to the shear strength

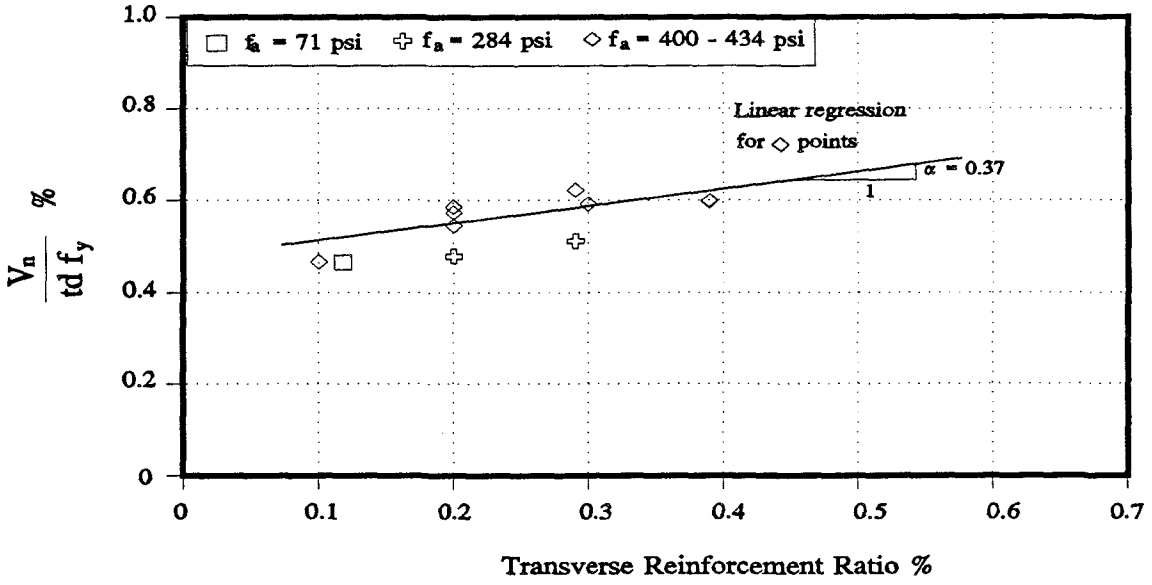

Figure C.8: Shear strength of masonry walls with M/Vd = 0.60 - 0.62.

To eliminate the influence of the other parameters on the shear strength, test data were arranged in groups of specimens of the same properties. Figs. C.8 and C.9 show the results obtained for walls with *M/Vd* ratios between 0.60 and 0.62, and 0.82 respectively. In both cases, the results have been arranged by different levels of axial stresses. Available data for other *M/Vd* ratios were in small quantities that did not permit valid results to be obtained. The series with the largest number of points in each plot was used to fit an straight line using a linear regression technique. Because the form in which the data have been represented, the slope of this line is directly the transverse reinforcement effectiveness ratio. Results of the linear regression analyses are given in Table 2, and the lines have been plotted in Figs. C.8 and C.9.

From these results, a transverse reinforcement effectiveness ratio of about 0.4 seems to be adequate.

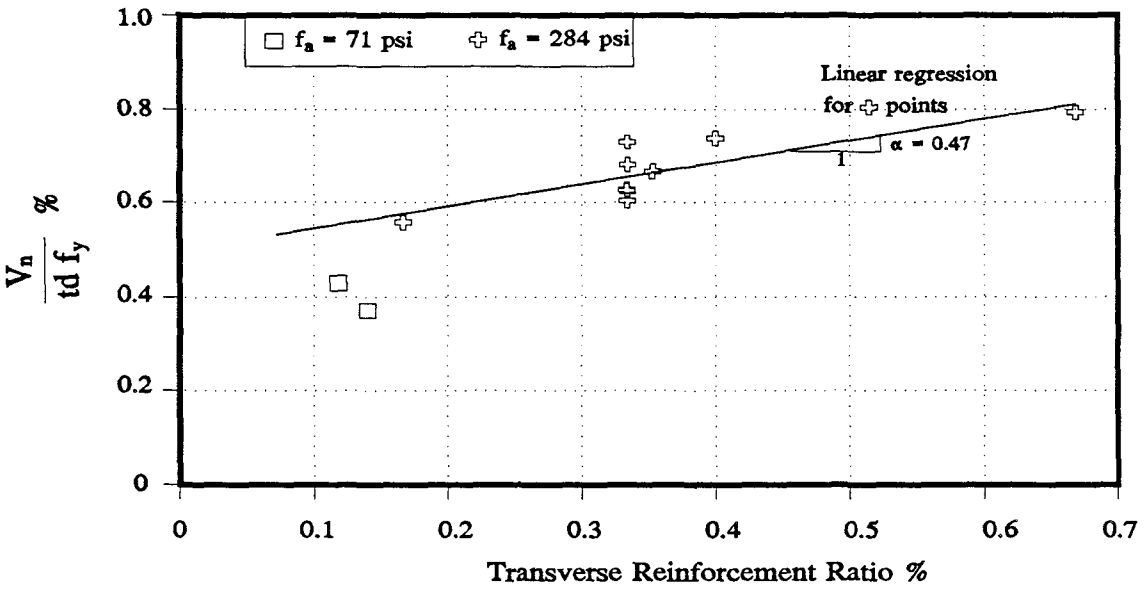

Figure C.9: Shear strength for masonry walls with M/Vd = 0.82.

Table C.2 Transverse reinforcement effectiveness α calculated from linear regression analyses.

M/Vd	Axial stress f_a psi	Number of data points	Slope α	Correlation coefficient
0.60 - 0.62	400 - 437	8	0.37	0.61
0.82	284	9	0.47	0.64

C.3.1 Masonry Contribution to Shear Strength. It was the intention of this author to select a single parameter involving all the mechanisms that govern the masonry residual shear strength. To do that, shear resisting mechanisms were related to the conditions existing at the section subjected to the maximum level of bending moment, which is usually the base of the wall.

For a critical section already cracked due to reversal loading cycles, the mechanism of shear transfer at the compression toe can be visualized as a problem of force transfer by friction between two surfaces. The strength developed by that mechanism of shear transfer will depend on the level of clamping forces in the compression toe. The normal stress level in the compression toe, which defines the extent of the clamping forces, depends on the

axial force acting on the wall, on the level of flexural stresses in the compression toe, and on the size of that area. The neutral axis depth c at the base section, as calculated from usual principles for the section under combined flexure and axial load, and the ratio of the acting moment to flexural capacity M/M_n for that section, represent adequately both parameters: the size of the compression toe, and the axial stress level.

The aggregate interlock effect depends essentially on the opening of the diagonal crack, which in turn depends on the axial stress level and the reinforcement in that zone. The influence of the transverse reinforcement in this mechanism has already been considered in V_s. The amount of longitudinal reinforcement can be also represented by the neutral axis depth c of the wall section.

The aspect ratio of the wall, which is usually expressed in terms of the M/Vd ratio, indicates the relationship between the shear acting on the wall and the bending moment at the critical section. It can be reasonably assumed that this ratio remains constant for sections in elements close to develop their capacity. Since the neutral axis depth depends directly on the moment, the M-V relationship can be expressed in terms of c.

An additional parameter considered in this study was the moment-shear capacity interaction. The mechanism governing the flexure-shear interaction is still unknown. While the flexural capacity development is a mechanism involving some definite critical sections of the wall, the shear strength mechanism involves either the complete element, or the interstory height of the wall.

The available experimental evidence has shown that the influence of the shear stress level on the flexural capacity of the wall's critical sections is insignificant. Due to shear deformations, the plane-section assumption is not longer valid for high levels of forces. However, the flexural capacity is not affected.

The shear capacity of the wall ia also affected by the level of flexural damage. Flexural cracks extending to the web of the wall are likely to reduce the residual shear capacity of the masonry. This fact was noted by Priestley [23] who suggested that the masonry shear capacity should be reduced according to the level of ductility demand on the wall. Based on this considerations, the neutral axis depth c for the critical section, at the time the shear failure occurs, was used as the parameter to represent the shear-flexure interaction.

In summary, the neutral axis depth c, and the ratio of the acting moment to flexural capacity M/M_n at the critical section, are the parameters chosen to represent the residual masonry shear strength V_m. The proposed expression for V_m is therefore of the following form:

$$V_m = C_m \frac{c}{d} \frac{M}{M_n} td\sqrt{f'_m} \quad \text{(C.4)}$$

The value of the constant C_m was determined from the experimental data. The flexural capacity M_n and the neutral axis depth c of the critical section, for the given level of axial load at shear failure, were calculated using the RCCOLA computer program [39]. The bending moment M at the critical section at shear failure was calculated using the given M/Vd ratio. V_s, calculated using Eq. C.2, was subtracted from V_n to obtain V_m and calculate C_m for each point. This process was repeated for different values of α in Eq. C.2, ranging from 0 to 1. The average C_m and the standard deviation were computed for the entire series of data, for each α. As shown in Fig. C.10, the coefficient of variation is minimized

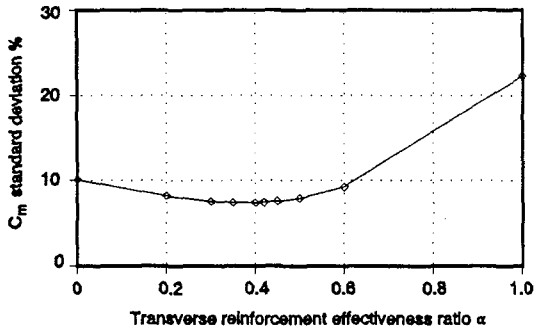

Figure C.10: Standard deviation of C_m calculations.

for α = 0.4, which is the same value previously estimated for the transverse reinforcement effectiveness ratio.

Based on these results, the following equation is proposed to evaluate the shear strength of a reinforced concrete fully grouted masonry wall:

$$V_n = V_m + V_s \quad \text{(C.5)}$$

Where:

$$V_m = 18 \frac{c}{d} \frac{M}{M_n} td\sqrt{f'_m} \quad \text{(C.6)}$$

$$V_s = 0.4\ \rho_h f_y\ td \quad \text{(C.7)}$$

C.4 Analysis of the Proposed Shear Strength Model for Reinforced Concrete Masonry Walls

To compare the degree of agreement of the proposed shear strength model with the experimental results, ratios of the predicted shear strength to the measured shear strength were calculated and plotted, as shown in Fig. C.11.

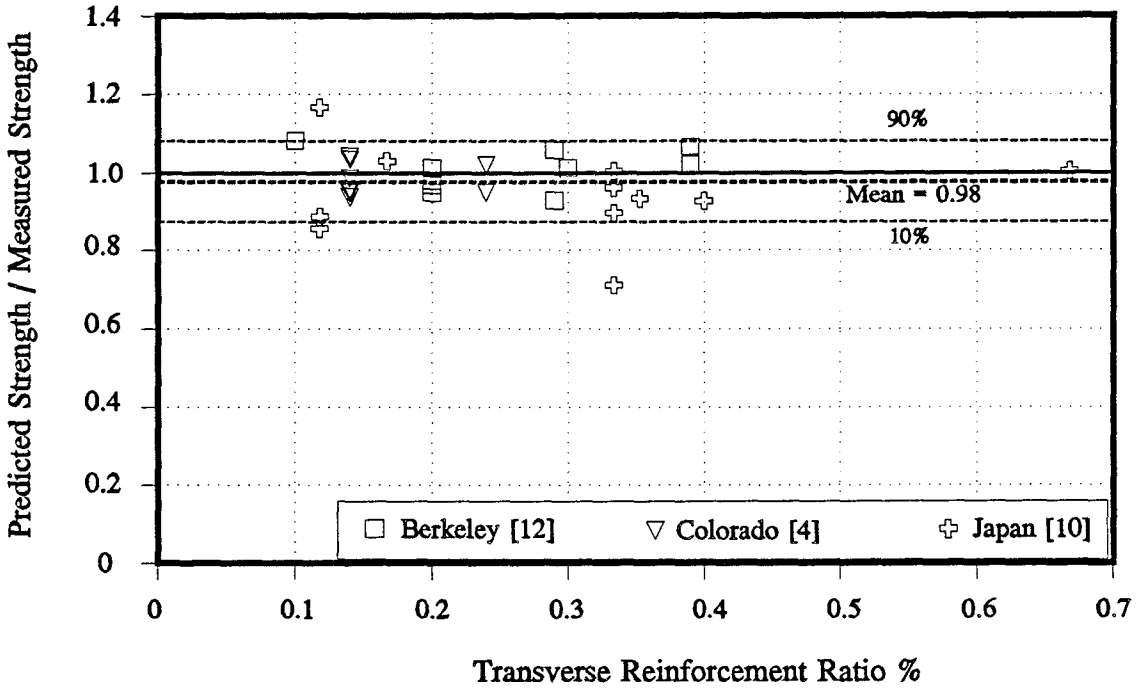

Figure C.11: Predicted shear strength to measured shear strength ratios for proposed shear strength model.

The mean value of the strength ratio distribution was 0.98, and the standard deviation was 8.3% of the mean. The maximum and minimum values were 1.17 and 0.71, and the 90% and 10% fractiles were 1.08 and 0.87 respectively.

A simple examination of Figs. C.11 and C.2 to C.5 shows that the strength ratio distribution of the proposed model is more uniform than those of the existing models. The ratios tend to be closer to the mean value and they do not show a tendency to vary with the transverse reinforcement ratio.

REFERENCES

1 Shing, P. B., Schuller, M., Hoskere, V. S., and Carter, E., "Flexural and Shear Response of Reinforced Masonry Walls," *ACI Structural Journal*, V. 87, No. 6, Nov-Dec 1990.

2 Ghosh, S. K. and Markevicius, V. P., "Design of Earthquake Resistant Shearwalls to Prevent Shear Failure," *Proceedings*, Fourth U. S. National Conference on Earthquake Engineering, Palm Springs, California, May 20-24, 1990.

3 Shing, P. B., Klamerus, E. W., and Schuller, M. P., "Behavior of Single-Story Reinforced Masonry Shear Walls Under In-Plane Cyclic Lateral Loads," *Proceedings*, Fourth Meeting of the U.S.-Japan Joint Technical Coordinating Committee on Masonry Research, San Diego, California, October 17-19, 1988.

4 Shing, P. B., Schuller, M., and Hoskere, V. S., "In-Plane Resistance of Reinforced Masonry Shear Walls," *Journal of Structural Engineering*, ASCE, V. 116, No. 3, March 1990.

5 Shing, P. B., Noland, J. L., Klamerus, E., and Spaeh, H., "Inelastic Behavior of Concrete Masonry Shear Walls," *Journal of Structural Engineering*, ASCE, V. 115, No. 9, Sept., 1989.

6 Yancey, C. W. C. and Lew, H. S., "Influence of Horizontal Reinforcement on the Shear Resistance of Masonry Walls," *Proceedings*, 21st Joint Meeting of the Panel on Wind and Seismic Effects, May, 1989.

7 Hidalgo, P. and Lüders, C., "Shear Strength of Reinforced Masonry Walls under Earthquake Excitation," *Proceedings*, Third U.S. National Conference on Earthquake Engineering, Charleston, South Carolina, August 24-28, 1986.

8 Lüders, C. and Hidalgo, P., "Mathematical Models for the Prediction of the Seismic Behavior of Reinforced Masonry Walls," *Proceedings*, Fourth U.S. National Conference on Earthquake Engineering, Palm Springs, California, May 20-24, 1990.

9 Matsumura, A., "Shear Strength of Reinforced Hollow Unit Masonry Walls," *Proceedings*, Second Meeting of the Joint Technical Coordinating Committee on Masonry Research, U.S - Japan Cooperative Research Program, Keystone, Colorado, Sept. 8 -10, 1986. 1987.

10 Matsumura, A., "Shear Strength of Reinforced Hollow Unit Masonry Walls," *Proceedings*, Fourth North American Masonry Conference, Los Angeles, California, August 16-19, 1987.

11 Woodward, K. and Rankin, F., *Influence of Aspect Ratio on Shear Resistance of Concrete Block Masonry Walls*, Pub. NBSIR 84-2993, National Bureau of Standards, U.S. Department of Commerce, January 1985.

12 Sveinsson, B. I., McNiven, H. D., and Sucuoglu, H., *Cyclic Loading Tests of Masonry Single Piers, Vol 4 - Additional Tests with Height to Width Ratio of 1*, EERC Report No. UCB/EERC-85/15, University of California, Berkeley, California, 1985.

13 Merryman, K. M., Leiva, G., Antrobus, N., and Klingner, R. E., "In-Plane Seismic Resistance of Two-Story Concrete Masonry Coupled Shear Walls," *U.S.-Japan Coordinated Program for Masonry Building Research Report No. 3.1(c)-1, PMFSEL Report No. 89-3*, The University of Texas at Austin, Austin, Texas, 1990.

14 Priestley, M. J. N., "Seismic Resistance of Reinforced Concrete-Masonry Shear Walls with High Steel Percentages," *Bulletin of the New Zealand National Society for Earthquake Engineering*, Vol. 10, No. 1, March, 1977.

15 Priestley, M. J. N., "Ductility of Unconfined Masonry Shear Walls," *Bulletin of the New Zealand National Society for Earthquake Engineering*, Vol. 14, No. 1, March, 1981.

16 Priestley, M. J. N., "Ductility of Confined Concrete Masonry Shear Walls," *Bulletin of the New Zealand National Society for Earthquake Engineering*, Vol. 15, No. 1, March, 1982.

17 Priestley, M. J. N. and Elder, D. McG., "Cyclic Loading Tests of Slender Concrete Masonry Shear Walls," *Bulletin of the New Zealand National Society for Earthquake Engineering*, Vol. 15, No. 1, March, 1982.

18 Kariotis, J., Personal Communication, June, 1990.

19 *Uniform Building Code*, 1988 Edition, International Conference of Building Officials, Whittier, California, 1988.

20 Blondet, J. M., Mayes, R. L., Kelly, T., Villablanca, R., and Klingner, R. E., "Performance of Masonry Structures in the Chilean Earthquake of March 3, 1985: Implications for U.S. Design Practice," Report to the National Science Foundation (Grant No. ECE-8613264), *PMFSEL Report No. 89-2*, University

of Texas at Austin and Computech Engineering Services, Inc. (Berkeley, California), June 1989.

21 Park, R. and Paulay, T., *Reinforced Concrete Structures*, John Wiley & Sons, NY, 1975.

22 Priestley, M. J. N., "Seismic Design of Concrete Masonry Shear Walls," *ACI Journal*, V. 83, No. 1, Jan-Feb 1986.

23 Priestley, M. J. N., "The Role of Research in the Formulation of Masonry Design Procedures," *Proceedings*, Fourth North American Masonry Conference, Los Angeles, California, August 16-19, 1987.

24 ACI-ASCE Committee 422, "Response of Concrete Buildings to Lateral Forces," (ACI 422R-88), American Concrete Institute,Detroit, Michigan, 1988.

25 Antrobus, N., "Development and Construction of Masonry Shear Walls Specimens," M.S. Report, The University of Texas at Austin, May, 1988.

26 Woodward, K. A. and Jirsa, J. O., "Design and Construction of a Floor Wall Reaction System," *CESRL Report No. 77-4*, December, 1977.

27 Porter, M. L., "Sequential Phased Displacement (SPD) Loading for TCCMAR Testing," Report presented at the Second Meeting of the Joint Technical Coordinating Committee on Masonry Research, U.S.- Japan Coordinated Program for Masonry Building Research, Keystone, Colorado, September, 1986.

28 Paulay, T. and Taylor, R. G., "Slab Coupling of Earthquake-Resisting Shearwalls," *ACI Journal*, V. 78, No. 11, March-April 1981.

29 Schwaighofer, J. and Collins, M. P., "Experimental Study of the Behavior of Reinforced Concrete Coupling Slabs," *ACI Journal*, V. 74, No. 3, March 1977.

30 Paulay, T., "The Design of Ductile Reinforced Concrete Structural Walls for Earthquake Resistance," *Earthquake Spectra*, Vol. 2, No. 4, 1986.

31 Leiva, G., Merryman, K. M., and Klingner, R. E., "Design Philosophies for Two-Story Concrete Masonry Walls with Door and Window Openings," *Proceedings*, Fifth North American Masonry Conference, University of Illinois at Urbana-Champaign, Illinois, June 1990.

32 Leiva, G. and Klingner, R. E., "Status Report: TCCMAR Task 3.1(c): In-Plane Seismic Resistance of Two-Story Concrete Masonry Walls with Openings,"

Joint Technical Coordinating Committee on Masonry Research, Boulder, Colorado, Jan. 1990.

33 Kent, D. C., and Park, R., "Flexural Members with Confined Concrete," *Journal of the Structural Division*, ASCE, V. 97, No. ST7, July 1971.

34 *Uniform Building Code*, 1985 Edition, International Conference of Buildings Officials, Whittier, California, 1985.

35 Klingner, R. E., "TCCMAR Task 3.1(c): In-Plane Seismic Resistance of Two-Story Concrete Masonry Walls with Openings," Boulder, Colorado, September 11, 1987.

36 *Plastic Design in Steel, a Guide and Commentary*, Joint Committee of the Welding Research Council and the American Society of Civil Engineers, 2nd Edition, ASCE, 1971.

37 Englekirk, R.E. and Hart, G.C., *Earthquake Design of Concrete Masonry Buildings: Volume 2 - Strength Design of One-to Four-Story Buildings*, Prentice-Hall, New Jersey.

38 Leiva, G. and Klingner, R. E., "Design of Type 1 Perforated Wall Specimens," Seventh Meeting of the U.S. - Japan Joint Technical Coordinating Committee on Masonry Research, Port Ludlow, Washington, August 1990.

39 Farahany, M., "User-Oriented Computer Program for Flexural Behavior of General Reinforced Concrete Sections," M. Sc. Thesis, The University of Texas at Austin, December 1983.

40 *PCI Design Handbook, Precast and Prestressed Concrete*, Third Edition, Prestressed Concrete Institute, Chicago, Illinois, 1985.

41 *Building Code Requirements for Reinforced Concrete (ACI 318-83)*, ACI Committee 318, American Concrete Institute, Detroit, 1989.

42 Klingner, R. E., "Report of Two-Story Wall Working Group," Boulder, Colorado, Jan. 18, 1990.

43 Chen, S. J., Hidalgo, P. A., Mayes, R. L., Clough, R.W., and McNiven, H. D., *Cyclic Loading Tests of Masonry Single Piers, Vol 2 - Height to Width Ratio of 1*, EERC Report No. UCB/EERC-78/28, University of California, Berkeley, California, 1978.

44 Hidalgo, P. A., Mayes, R. L., McNiven, H. D., and Clough, *Cyclic Loading Tests of Masonry Single Piers, Vol 3 - Height to Width Ratio of 0.5*, EERC Report No. UCB/EERC-79/12, University of California, Berkeley, California, 1979.

45 Leiva, G., Merryman, K. M., Antrobus, N., and Klingner, R. E., "In-Plane Seismic Resistance of Two-Story Masonry Concrete Coupled Walls," *Proceedings*, Fifth North American Masonry Conference, University of Illinois at Urbana-Champaign, Illinois, June 1990.

46 Noland, J., "1990 Status Report: US Coordinate Program for Masonry Building Research," *Proceedings*, Fifth North American Masonry Conference, University of Illinois at Urbana-Champaign, Illinois, June 1990.

47 Assis, G. F., Hamid, A. A., and Harry, H. G., "Material Models for Grouted Block Masonry," *U.S.-Japan Coordinated Program for Masonry Building Research Report No. 1.2(a)-2*, Drexel University, Philadelphia, Pennsylvania, 1989.